Biodegradable and Bioresponsive Core-Multishell Nanocarriers for the Delivery of Drugs into Skin

Inaugural-Dissertation
to obtain the academic degree
Doctor rerum naturalium (Dr. rer. nat.)

submitted to
the Department of Biology, Chemistry and Pharmacy
of Freie Universität Berlin

Karolina Anna Walker
from Zabrze, Poland

2018

The research presented in this thesis was carried out from June 2014 to July 2018 under the supervision of Prof. Dr. Rainer Haag at the Institute of Chemistry and Biochemistry - Organic Chemistry of the Freie Universität Berlin.

1st reviewer: Prof. Dr. Rainer Haag
2nd reviewer: PD Dr. Kai Licha
Date of defense: 16.08.2018

Acknowledgements

I'd like to thank Prof. Rainer Haag for being my supervisor, and for his trust and support throughout my time as a PhD student.

I'd also like to thank Dr. Kai Licha for being the second referee of this work, and for the scientific advice during my projects.

Embedded in the SFB 1112 "Nanocarrier", I've met great collaboration partners during my doctoral work. Prof. Annika Vogt is thanked for being a great teacher, supervisor and role model. The collaboration with her and her group, especially Dr. Fiorenza Rancan, is the part of my doctoral work that I will always remember as the blueprint of interdisciplinary work. Prof. Axel Neffe is thanked for his challenging and helpful questions. As a student member in the integrated research training group of the SFB 1112 advisory board, I'm thankful for having experienced a professional, constructive, and open-minded atmosphere. Also, the students of the SFB 1112 are thanked for the great time we spent during research meetings and beyond.

I am truly grateful for the support, perfect measurements and countless consulting time of the NMR department of the BCP Core Facility BioSupraMol, namely Prof. Andreas Schäfer, Anja Peuker and Bettina Zeisig.

The AG Haag family, former and current members, are thanked for the great working atmosphere. Special thanks go to my lab family Dr. Sumati Bhatia, Antara Sharma, Pallavi Kiran, Dr. Lingyan Gao, Qingcai Zhao, Yong Hou, Dr. Pradip Dey, and the best hood friend ever, Dr. Fang Du.

Thanks to the lunch group, Friday seminar (happened too rarely), and special lunch groups for the interesting work-related, and non-work-related discussion.

Special thanks go to my friends I've met during the Haag time: Dr. Silke Heinen, Dr. Laura Vossen, Dr. Olaf Wagner, and Dr. Sabine Reimann. Dr. Michael Unbehauen is thanked for being the best office-friend ever, for picking up every line of song I'm mumbling and laughing at my silly jokes during dark times of working madness. Dr. Emanuel Fleige is thanked for having been a great teacher and friend who introduced me to the world of CMS chemistry. I'm grateful for having met many generations of AG Haag members, who will all remain an integral part and great memory of my AG Haag time.

Also, I want to thank my first chemistry teacher Frau Schönthaler. With the very first school lesson in chemistry and the opening question “What is chemistry?” she evoked my fascination for science and paved the way for chemistry being the basis of my professional development.

My parents and sister are thanked for always having supported and believed in me, their love, and for being understanding whenever chemistry needed to come first. My in-laws are thanked for being loving supporters and for always looking out for me and my vitamin supply.

To my husband Matthias Walker: words cannot express my deep gratefulness for your support, love, understanding, and countless ways, how you made this doctoral work possible. Thank you.

Table of Contents

List of Abbreviations

2D	Two-dimensional
3D	Three-dimensional
CAC	Critical aggregation concentration
CAL B	Candida antarctica lipase B
CARS	Coherent anti-Stokes Raman spectroscopy
cLSM	Confocal laser scanning microscopy
CMC	Critical micelle concentration
CMS	Core-multishell
DCM	Dichloromethane
DDS	Drug delivery system
D_f	Degree of functionalization
D_h	Hydrodynamic diameter
DLC	Drug loading content
DLS	Dynamic light scattering
DMF	Dimethylformamid
DNA	Desoxyribonucleic acid
dPG	Dendritic polyglycerol
Dx or DXM	Dexamethasone
EM	Electron microscopy
EPR	Electron Paramagnetic Resonance
FDA	US Food and Drug Administration
FITC	Fluoresceine
FLIM	Fluorescence Lifetime Imaging Microscopy
FRET	Förster resonance energy transfer
FTIR	Fourier-transform infrared spectroscopy
GPC	Gel-permeation chromatography
GSH	Glutathione
GSSG	Glutathione-disulfide
hPG	Hyperbranched poly (poly(glycerol)
HPLC	High performance liquid chromatography
HPMA	N-(2-hydroxypropyl)-methacrylamide
IR	Infrared
L-PGA	Poly(Lglutamic acid)
LC	Liquid chromatography
LSM	Laser scanning microscopy

MeOH	Methanol
MMP	Matrix metalloprotease
M_n	Number average molecular weight
mPEG	Methoxy poly(ethylene glycol)
M_w	Weight average molecular weight
MWCO	Molecular weight cut-off
NMR	Nuclear magnetic resonance
NP	Nanoparticle
NR	Nile red
OCL	Oligocaprolactone
osCMS	Oxidation-sensitive CMS
oxCMS	Oxidized CMS
PAA	Poly(aspartic acid)
PCA	3-(carboxy)-2,2,5,5-tetramethyl-1-pyrrolidinyloxy
PCL	Poly (Poly(caprolactone)
PDI	Polydispersity
PEG	Poly(ethylene glycol)
PGA	Poly(glycolic acid)
PLA	Poly(lactic acid)
PPS	Poly(propylene sulfide)
RC	Regenerated cellulose
ROMBP	Ring-opening multibranching polymerization
ROS	Reactive oxygen species
rsCMS	Reduction-sensitive CMS
SC	Stratum corneum
SEM	Scanning electron microscopy
SERS	Surface enhanced Raman spectroscopy
siRNA	Single interfering desoxyribonucleic acid
TAC	Tacrolimus
TCEP	tris(2-carboxyethyl) phosphine
TEM	Transmission electron microscopy
TEMPO	2,2,6,6-tetramethyl-1-piperidinyloxy
T_g	glass transition temperature
UV-Vis	Ultraviolet-visible spectroscopy
wt	Weight

1 Introduction

1.1 Stimuli-Responsive Polymeric Drug Delivery

1.1.1 Polymeric Drug Delivery Systems

Drug delivery aims at enhancing the efficacy of drugs by increasing their solubility and specifically delivering them to the targeted site of action. The need for drug delivery initially resulted from the nature of small drugs: after first pass metabolization, the bioavailability of the drug is significantly lowered when compared to the applied dose. The active drug is then passed to the circulatory system, distributed throughout the whole body, and finally cleared by the liver and kidney. High clearance rates require frequent dosing of the drug, and the additional lack of specificity by the drug often results in side and adverse effects. Ringsdorf postulated the concept of polymer-drug conjugates in the 1970ies, where the attachment of low molecular weight drugs to linear polymeric scaffolds was designed to increase circulation times in the body.[1] Introduction of a targeting unit to the same polymeric backbone, such as receptor-specific antibodies, allows specific delivery of the polymer-drug conjugate to the targeted site of action. Driven by the developments in the field of polymer synthesis, this basic understanding of a polymer therapeutic was extended to more sophisticated polymer-drug conjugates. It now comprises the attachment of drugs to homo- and copolymers of various architectures, such as linear, brush-like, hyperbranched, and dendritic (Fig 1).[2] These conjugates can either transport their cargo as a unimer, or self-assemble into supramolecular assemblies, such as micelles or liposomes.

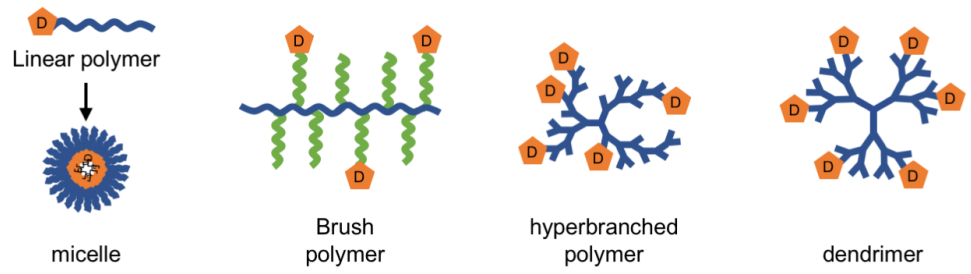

***Fig. 1**: Various types of polymer-drug conjugates; from left to right: self-assembled micelle from linear polymer-drug conjugates; brush-type polymer-drug conjugate; hyperbranched polymer-drug conjugate; dendrimer-drug conjugate.*

Another approach to enhance the circulation and uptake are supramolecular complexes: drug delivery systems of drug guests and physically or affinity-mediated crosslinked hosts forming a highly ordered supramolecular complex.[3] These systems use supramolecular motifs for both the formation of the supramolecular 3D structure and the encapsulation of drugs on the molecular level, where the drug is coordinated to the binding motif by hydrophobic interactions, H-bonding, or electrostatic interactions. The supramolecular polymer is formed in most cases by either stacks of molecules, held together by „ordered hydrogen bonding",[3] or by $\pi - \pi$

interaction of small building blocks, or (self-)complimentary units, which crosslink into a network. The binding of the drug takes place on a molecular level, and so the polymer can be adapted, independently of the drug, to biomedical needs, such as responsiveness or solubility.

Polymer-drug conjugates, connected through either a chemical bond or physical interactions, need to be adapted to their field of application. Choosing from - but not being limited to - linear to dendritic, homo- to copolymer, hydrophilic, hydrophobic, or amphiphilic oligo- or polymers often leaves the right choice at the stage of an educated guess. Inspired by the naturally occurring and highly adaptive micelle, the dendrimer was initially synthesized as its integral analog.[4] Reiterative, step-wise synthesis of dendrimers using a divergent approach, i.e., from core to shell, with high conversions at each step (>99.9%) yielded perfectly branched polymers.[5] With each cycle of synthetic steps, a so-called generation is added to the precursor dendrimer, and the space needed for attachment of the new generation with full conversion becomes more limited, the higher the generation is.[4] The empty space in between the branches were recognized as perfect voids for the encapsulation of small molecules. This finding, termed “dendritic box” by E. W. Meijer,[4] is a cornerstone of unimolecular micelles and the first example of polymeric nanocarriers (Fig. 2A). Selective functionalization of their terminal groups yields so called core-shell type dendrimers. When the dendritic core and its shell differ in polarity, the unimolecular micelle (Fig. 2B) is amphiphilic and thus resembles the self-assembled micelle in terms of polarity. Going beyond the core-single shell dendrimer, Radowski et al. developed the core-multishell nanocarrier. This carrier is based on a hyperbranched core, replacing the dendritic core, and is surrounded by an amphiphilic double shell, thus resembling the polarity gradient of a liposome (Fig. 2C).[6-7]

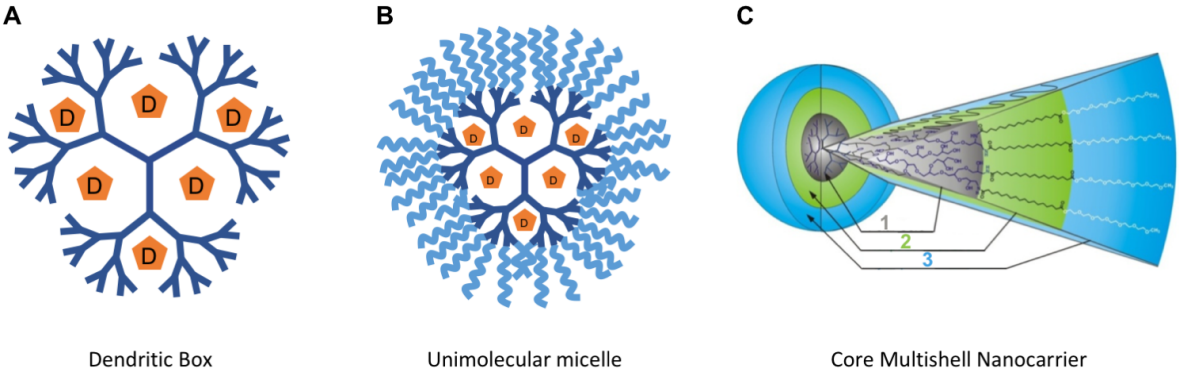

Fig. 2: *Drug delivery devices based on dendritic polymers;* ***A****: Dendritic box, as suggested by E.W. Meijer;* ***B:*** *amphiphilic unimolecular micelle;* ***C****: Core Multishell CMS nanocarrier, as published by M. Radowski (1: polar hyperbranched polymer core; 2: hydrophobic inner shell; 3: hydrophilic outer shell).* ***C****: Adapted with permission from Fleige, E et al., Aggregation Phenomena of Host and Guest upon the Loading of Dendritic Core-Multishell Nanoparticles with Solvatochromic Dyes.* Macromolecules ***2012,*** 45 *(23), 9452-9459.[8] Copyright 2018, American Chemical Society.*

CMS delivery systems enhance water-solubility of new and already existing drugs and provide the opportunity for easy encapsulation.[7, 9] The single nanotransporters, called unimers, have a typical size of 8–10 nm and form larger aggregates upon loading with guest molecules above

a certain critical aggregation concentration.[6, 8] These aggregates are stable even upon filtration and size exclusion chromatography, and they contribute to the transport of guest molecules by entrapping them between the single unimers.

1.1.2 Stimuli-Responsiveness in Drug Delivery

Stimuli-responsive drug delivery systems are designed to release their guest at the targeted site of action in a triggered fashion. The release mechanism of the drug from the polymeric carrier depends on the mode of transport. In case of stimuli-responsive polymer-drug conjugates, the bond between drug and carrier is designed to be responsive.[10-11] Hence, the stimulus causes cleavage of the responsive bond between drug and carrier and releases the drug (Fig. 3A). Nanocarriers with physically entrapped drugs release their cargo upon stimulus-caused changes of the intrinsic chemical properties of the nanocarrier. To do so, the polymeric scaffold can either be cleaved itself, leading to a release of the locked-in drug (Fig. 3B), or it can change its polarity or charge, leading to a repulsion of the drug from the carrier (Fig. 3C).

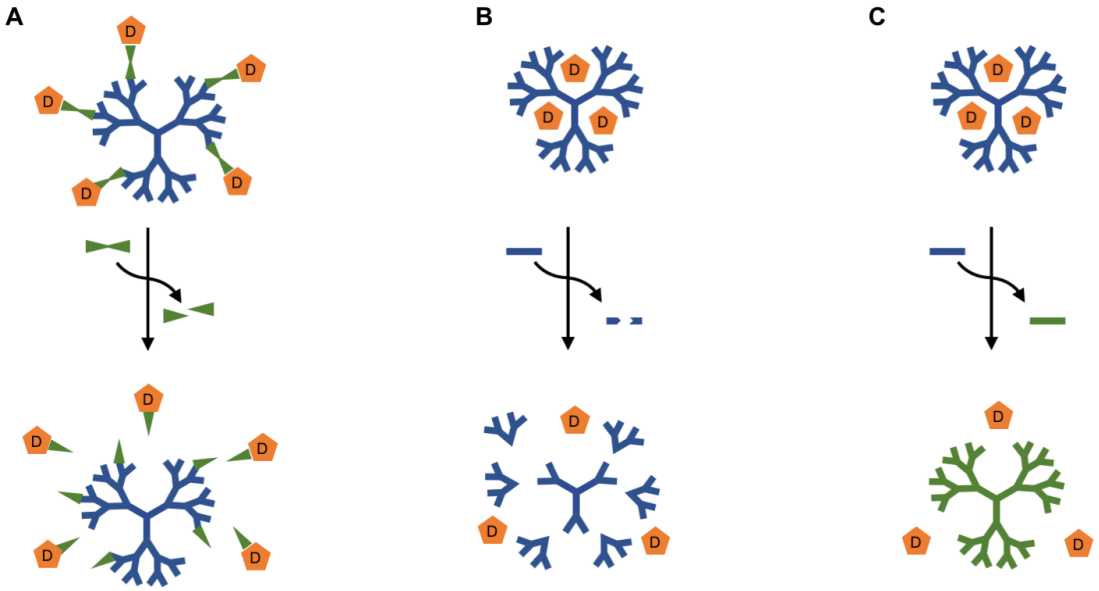

Fig. 3: *Triggered release of drug upon stimulus;* ***A****: polymer-drug conjugate with stimulus-responsive linker; drug is released upon cleavage of linker* ***B:*** *biodegradable dendrimer with encapsulated drug; drug is released upon degradation of polymer;* ***C****: stimulus-responsive dendrimer with encapsulated drug; drug is released upon change in physico-chemical properties of polymer, e.g., polarity or charge.*

In case of self-assembled supramolecular DDS, an external stimulus can trigger the disassembly of the carrier, leading to a release of the drug. When a drug delivery system is referred to as being stimulus-responsive, the release mechanism, and thus the stimulus, needs to be specific for the pathological features of the targeted disease. Independent of the mode of transport, either conjugated or physically entrapped, the designed drug delivery system's features for specific response all rely on the same stimuli-responsive functional groups. Exogenous stimuli are mostly of physical nature, and they include light, magnetic fields, ultrasound, and temperature gradients.[12] Endogenous stimuli are related to biochemical

markers, such as pH value, enzymes, ionic strength, and redox potentials.[13] The three major stimuli relevant for this thesis are discussed in the following.

pH-Responsiveness

Acidic pH value of the extracellular space is a common pathological factor associated with both inflammation and cancer. It indicates a change in metabolism compared to a normal, healthy state. Low pH values in cancerous tissue, typically of pH 6-7,[14] results from a high rate of lactate secretion from anaerobic glycolysis, accompanied by the overproduction of protons.[15] Thus, the stimulus-responsiveness to pH value mostly refers to acidic conditions. If a cleavage of a specific bond under acidic environment is envisioned for a pH sensitive nanocarrier, hydrolytically-cleavable groups are chosen. These include for example acetals, ketals, and imines. A change in pH value can also be used to change a polymer's intrinsic properties, leading to a repulsion of physically entrapped drugs. This has been reported for the "dendritic box", where a poly(propylene imine) shows protonation-dependent behavior. Upon protonation of its tertiary amines in the inner sphere, encapsulated pyrene is released in dependence of the pH value (Fig.3).[4, 16] The pH value as stimulus is used for the triggered release of drugs, but can furthermore be used for designing special properties of the nanocarrier, such as degradation after drug release. This will be discussed in detail in chapter *1.4.1 Forms of Biodegradability*.

Enzyme-Responsiveness

For the design of an enzyme-responsive DDS, the right match of enzyme and responsive functional group is sufficient for a successful enzyme-responsive system. Containing an ester-bond makes the DDS cleavable by esterase, an amide can be cleaved by a lipase. However, enzyme-triggered DDS for the targeted treatment at the site of disease need to be selectively responsive to pathological overexpression of enzymes. Cancer is among all targeted diseases the pathological state which is cited most in the field of enzyme-responsive DDS. Overexpressed enzymes associated with cancer are lysosomal proteases (cathepsins), extracellular proteases (matrix metalloproteases, MMP),[17] β-glucoronidase, and carboxyl-esterases.[10] Peng and Kopecek reported a polymer-drug conjugate based on N-(2-hydroxypropyl)-methacrylamide (HPMA) and doxorubicin as a drug.[18] The copolymer, connected via an tetrapeptide linker, carried additionally a tumor-directing and cell penetration enhancing iRGD motif, which was conjugated through a MMP-degradable peptide linker. The tetrapeptide linker between polymer and drug is sensitive to cathepsin B, a further enzyme specifically overexpressed in the lysosome of cancer cells.[10] The conjugate showed enhanced accumulation and penetration in cancer cells, as shown in 2D and 3D prostate cancer cells. After uptake into cells, the MMP-degradable tripeptide was cleaved by lysosomal MMP and doxorubicin was released in the lysosome.[18] This example, like many others, shows the potential of polymer-drug conjugates for preventing side effects in chemotherapy.

Redox-Responsiveness

Research on redox-responsive DDS mostly make use of the difference in redox potential between the extracellular and the intracellular space. Glutathione is the major redox buffer in organisms, and the state of the glutathione-glutathione disulfide (GSH/GSSG) equilibrium decides whether the environment is reductive (GSH) or oxidative (GSSG). Cytoplasm has a reductive environment, as its reductive capacity is 100-1000-fold higher than the extracellular space.[19] This difference in GSH content is used as the trigger for redox-stimulated changes of DDS, and disulfide linkages are used to introduce this redox-responsiveness. Due to the response stimulated in the cytoplasm, most research on redox-responsiveness in drug delivery focuses on releasing drugs, siRNA, DNA and proteins inside the cell.[20-21] Reduction-sensitive polymer-drug conjugates have been reported by the group of Kataoka. They synthesized an iminothiolane-modified poly(ethylene glycol)-block-poly(l-lysine) micelle for the transport of siRNA in its inner cavity. The micelle was core-crosslinked via disulfide bond formation, and thus the micelle remained stable during the cellular uptake mechanism. Once inside the cell, the disulfide groups were degraded and the micelle fell apart, releasing its cargo siRNA. Using this approach, a 100-fold higher transfection efficacy of siRNA was reached, compared to non-crosslinked micelles of the same type.[22] The redox-responsiveness of polymers is discussed in detail in chapter *1.3.3 Redox-Responsive Polymers.*

1.2 Skin Diseases and the need for Dermal Drug Delivery

1.2.1 Anatomy of the Skin in Healthy and Diseased State

Skin is the largest organ of the human body, and it covers an area of approximately 2 m^2.[23] Being the interface between the body and the external environment, its most important role is to act as a barrier and to regulate the inward and outward flow of matter. Differentiating cells grow outwards, from the deepest layer, the dermis, to the outermost layer, the epidermis. The outermost epidermal layer, stratum corneum (SC), is the major component of the barrier. It consists of corneocytes, which are aggregated keratin filaments, enclosed by a cornified envelope, surrounded by multiple stacks of highly organized lamellar bilayers (Fig. 4). Water molecules are retained by the barrier, preventing excessive water loss, and lipid-soluble molecules of low molecular weight can pass the lipid layer. This “composite material”[24] with a barrier function was described with the “brick and mortar” model in 1983 by P. M. Elias.[25] The combination of geometrically highly ordered tetraidekaedric corneocytes allowing dense packing, embedded in an intercellular lamellar bilayer matrix consisting of hydrophobic lipids, provides an efficient physico-chemical barrier. The lipids, mainly free fatty acids, ceramides, and cholesterol,[26] organize into hydrophobic and hydrophilic domains (Fig. 4),[27-28] and furthermore, the presence of aqueous regions has been postulated.[29-30] In pathological states, the skin barrier structure is changed and thus its function is negatively affected.[31] During

inflammatory skin disease, e.g., atopic dermatitis and psoriasis, the physico-chemical barrier is impaired due to changes in the biosynthesis of the stratum corneum,[32] including its lipid composition and organization.[33] The microbiome, which dictates chemical properties like surface pH and presence or absence of enzymes, is also affected by the inflammation.

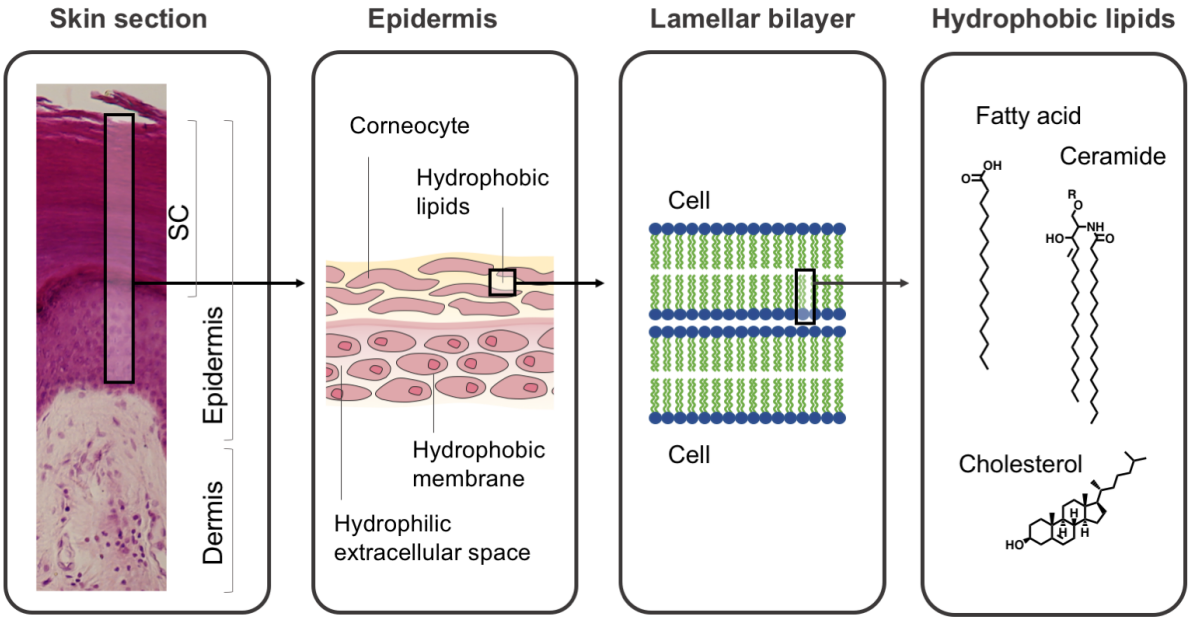

Fig. 4: *Anatomy of the skin; Section of skin with stratum corneum (SC), epidermis, and dermis (from top to bottom); the epidermis consists of the stratum corneum, comprising corneocytes embedded in hydrophobic lipids, and the viable epidermis, containing hydrophobic and hydrophilic spaces; the lamellar bilayer consisting of mainly free fatty acids, ceramides, and cholesterol. Skin sections adapted with permission according to CC-BY-SA 3.0, as described at http://creativecommons.org/licenses/by-nc-sa/3.0/ from WVSOM Meissner's corpuslce.jpg, ©Mikael Häggström, by Wbensmith.*

1.2.2 Dermal Drug Delivery: Pathways, Limitations, and Chances

Topical diseases, such as atopic dermatitis and psoriasis, are quite efficiently treated with small molecular weight corticosteroids, but their long-term application can lead to severe side effects, such as skin thinning or diseased blood vessels.[34] Treatment by high-molecular weight drugs, such as proteins, are limited by their poor penetration into skin and hence show only limited success in therapy. Both problems could be circumvented by combination with polymeric nanocarriers. Targeted delivery of drugs to the site of disease would allow a selectivity of therapy, sustained release from a drug delivery depot in the skin would make frequent dosing redundant, and the increased solubility of poorly-soluble drugs might increase the efficacy of drugs with inefficient formulations. For a successful topical treatment of epidermal malignancies, the difference between lesional and non-lesional skin is of great importance. In lesional skin, the skin barrier is impaired, which can be used as a penetration pathway for nanocarriers. The lipid bilayer of stratum corneum is used for diffusion of lipophilic substances, and the extent of penetration is governed by the polarity and size of the substance. Two penetration pathways have been identified as the major routes of nanoparticles into the skin: the intercellular pathway and the transcutaneous pathway (Fig. 5).[30] The latter is represented by natural openings into the stratum corneum, such as hair follicles. They reach

into the dermis, and act as depots for bigger substances.[35-37] Using this depot function of the hair shaft, more substance can be stored and it can persist ten times longer in the follicle than in the depot of stratum corneum.[38-40]

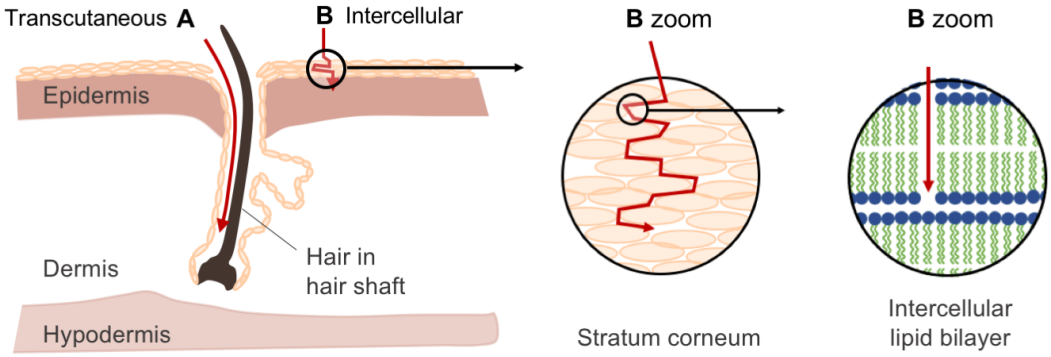

***Fig. 5**: Penetration pathways of nanoparticles into the skin; **A**: transcutaneous pathway via the hair shaft, reaching deeper skin layers; **B**: Transcellular pathway with zoom into stratum corneum with corneocytes and zoom into intercellular space in between corneocytes.*

It was found that hard particles applied topically on healthy skin remain in the stratum corneum, while soft, deformable ones penetrate deeper SC layers. In disrupted skin, increased uptake was observed.[36, 41] Generally, physical properties, including size and shape, have been hypothesized to influence the penetration properties, especially of hard and inorganic nanoparticles. TiO_2 and ZnO, [42-43] Au,[44] Ag,[45] and other inorganic nanoparticles of different sizes and shapes have shown no overcoming of healthy skin barrier, but accumulation in hair follicles or upper layers of SC. As discussed by Cevc and Vierl, publications claiming successful penetration of SC probably observed simple diffusion of their nanoparticles due to overhydration of the skin, resulting in widened pores.[30] Organic, soft nanoparticles are governed by their deformability. Liposomes are hypothesized to squeeze through smaller pores, while retaining their transport properties. Furthermore, they can both fuse with themselves, forming an extended continuous lipidic phase,[46-48] and fuse with cell lipids and thus deliver their cargo directly into cells.[49] Intrinsic deformability and structure integrity of unimolecular micelles, dendrimers and core-(multi-) shell architectures make these nanocarriers appear as a dermal drug delivery class on their own. The Vogt group studied the penetration pathway of CMS nanocarriers in disrupted human skin, and observed accumulation in hair follicles and localization in the lipid bilayer of SC.[50] However, their penetration mechanism is still under investigation. Due to their size and solvent-dependent behavior, dendrimers are argued to work as penetration enhancers,[30] but a proof of concept study is still missing. Soft organic nanocarriers enhance the penetration of their carried guest molecules, but the analysis of the nanocarriers' fate after delivery has not been performed. Furthermore, the studies published on the fate of nanocarriers have been performed using Franz cell tests with porcine skin. The tested skin in a Franz cell set-up is heated to 60 °C for removal of stratum corneum prior to the application of the tested formulation, which is criticized

for changing the skin properties (disruption of liposomal structures, widened pores). Furthermore, the bottom of the skin layer is in constant contact with water, acting as the acceptor medium (Fig. 6). However, the constant contact with water is suspected to lead to increased diffusion of agents,[51] followed by their translocation through the skin from the skin surface to the bottom, driven by capillary forces. Together, these factors leave critics to doubt the reliability of results obtained by Franz cell tests.

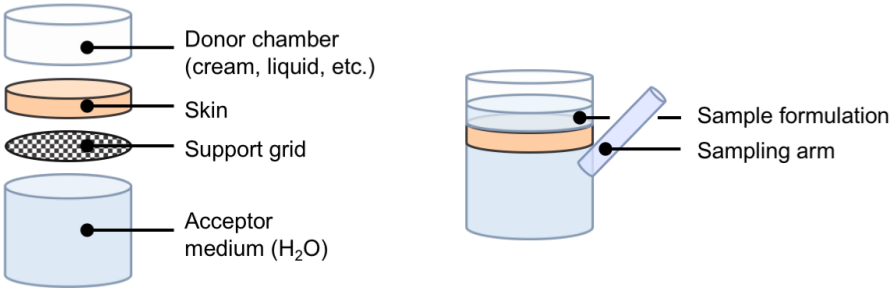

***Fig. 6**: Set-up of a in vitro static diffusion testing system (Franz cell). The tested skin is mounted on a grid, placed on the acceptor compartment and topped with a donor chamber. The receptor medium is liquid, and hence the skin is in contact with a liquid throughout the test. The tested substance is placed on the skin as the respective formulation. Picture adapted from Chilcott, R.; Price, S., Principles and practice of skin toxicology. John Wiley & Sons: 2008.*

Even if penetration pathways of nanocarriers are elucidated and understood on healthy skin, the scenario for diseased skin with an impaired skin barrier might be different. To mimic the diseased state, the stratum corneum is removed by repetitive adhesion and removal of adhesive tape (so called tape stripping),[52] treatment by penetration enhancers,[53] or it is mechanically opened by punching holes using micro needles.[54] Increased penetration of drugs from nanocarriers tested on diseased skin was shown in numerous publications,[55-56] an investigation of the nanocarriers' fate is only rarely performed. In studies, where UV irradiation and mechanical disruption was used to mimic inflamed skin, solid nanocarriers were found in the viable epidermis.[57-59] Even though no data is available on the penetration of diseased skin by polymeric nanocarriers, it is assumed that similarly to solid nanoparticles, nanocarriers will penetrate diseased skin deeper than non-diseased skin. Long-term treatment with polymeric drug delivery systems might hence lead to accumulation-related toxicity, especially in lesional skin with increased immune response. Biodegradable nanocarriers, which degrade upon endogenous pathological stimuli in the skin to biocompatible fragments, might be advantageous for preventing side effects, especially in the treatment of lesional skin.[31, 55] Biodegradable nanocarriers are discussed in *1.4.2 Biodegradable Hyperbranched Polymers, and the* response of polymers to pathological changes in skin are discussed in *1.3.3 Redox-responsive Polymers.*

1.3 Redox Reactions in Biological Systems

1.3.1 Definition of the Redox Potential in Biological Environment

Redox state is a concept that is widely used in the field of responsive materials for biomedical applications. It is used as a general term describing the oxidative or reductive environment of a cell. However, the term *redox couple* historically refers to "the ratio of the interconvertible oxidized and reduced form of a specific redox couple"[19], and thus reflects a relative value. In turn, the redox environment of a "linked set of redox couples" of a defined biological environment (cell compartment, fluid, tissue) is the sum of the products of the reduction potential and reducing capacity of the considered linked redox couples, as suggested by Schafer and Buettner.[19] The cell has a range of redox couples, e.g., Ubiquinone $CoQ/CoQ^{\cdot-}$, $NADP^+$/NADPH, Thioredoxin TrxSS/TRx$(SH)_2$ and Glutathione GSSG/2GSH. The last three couples are thermodynamically interconnected, whereas NADPH is the source of energy for both the thioredoxin and the glutathione couple. Instead of measuring all connected redox couples, it is sufficient to quantify one representative.[19] As the GSSG/2GSH couple provides most reductants in a cell, it is the major redox buffer of the cell. Its redox state thus indicates the overall redox environment of the cell. To have full knowledge of the redox state of this couple, absolute concentrations are needed. Absolute concentrations of the reductant, i.e., GSH, determine the reduction capacity: If 1% of overall glutathione is oxidized to GSSG, then a GSH concentration of 10 mM (9.9 mM GSH, 0.1 mM GSSG) results in a higher reduction capacity than with 1 mM GSH (0.99 mM GSH, 0.01 mM GSSG). In a cell, the reduction capacity differs strongly depending on the cell compartment. The ratio of GSH/GSSG in the endoplasmatic reticulum has a ratio of 1:1 to 3:1, while the cytosolic level is at 100:1. The comparably high concentration of GSH in the cytosol of 1-10 mM is maintained by antioxidant enzymes (see Fig.7).

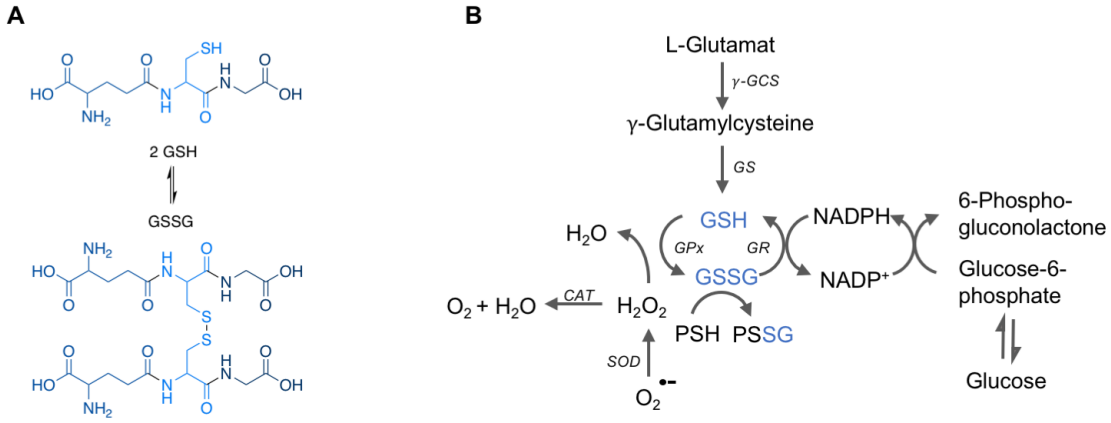

Fig. 7**: **A**: Tripeptide glutathione (GSH) in equilibrium with its dimeric form GSSG; **B**: Relationship between antioxidant enzymes and glutathione; CAT: catalase; γ-GCS: γ-glutamylcysteine synthetase; GS: glutathione synthetase; GPx: glutathione peroxidase; GR: glutathione reductase; SOD: superoxide dismutase. Figure **B** reproduced and adapted from Schafer, F. Q.; Buettner, G. R., Redox environment of the cell as viewed through the redox state of the glutathione disulfide/glutathione couple.* Free Radical Biology and Medicine ***2001, 30 *(11), 1191-1212. [19], Copyright 2018, with permission from Elsevier.*

The antioxidant enzymes keep the GSSG/2GSH redox couple in a nonequilibrium steady state. Considering short periods of time where the set of redox pairs and their ratios do not change, the reduction potential of each half-cell can be calculated with the Nernst equation at non-standard conditions:

$$\Delta E = \Delta E^{\circ} - \frac{RT}{nF} \ln Q$$

With ΔE° being the electromotive force under standard conditions, gas constant R, temperature T, number of exchanged electrons n, Faraday constant F and the mass action expression Q:

$$Q = \frac{[GSH]^2}{[GSSG][H^+]^2}$$

The reduction potential is the measure for the tendency of a chemical species to be reduced. The glutathione half-cell reduction is pH-dependent:

$$GSSG + 2\,H^+ + 2\,e^- \rightarrow 2\,GSH$$

The pH value influences the half-cell potential. This change can be calculated with a simplified Nernst equation:

$$E_{pH} = E^{\circ} - \frac{59.1\ mV}{n} \log \frac{[GSH]^2}{[GSSG][H^+]^2}$$

With $E^{\circ} = +180\ mV$ for GSSG/2GSH, the reduction potential at pH 7.4 at 25 °C and [GSH]=[GSSG]=1 M, the reduction potential is $E_{pH7.4} = -233.7\ mV$.

In vivo, the cytosolic concentration of GSH is 1-11 mM, while the GSH/GSSG ratio is 100:1. This in vivo situation is often mimicked in vitro by using 10 mM glutathione in buffer at pH 7.4 or in water (remark: 10 mM GSH in water has a pH of 4.5). However, the nonequilibrium steady state of the GSSG/2GSH couple in vivo is enabled by enzymes, and thus GSH cannot make any use of its reducing capacity when used in vitro in absence of enzymes. [60] Nevertheless, when GSH is used as a biologically relevant reducing agent for disulfide cleavage studies, thiol-disulfide exchange between the tested disulfide and GSH is observed. As argued by Misra, this might be due to the oxidative effect of GSH. Upon reaction of deprotonated GS^- with reactive oxygen species (ROS), a radical $GS^{\cdot}$ species is formed, which in turn reacts with disulfides in a free radical mechanism.[61]

Measurements of thiol/disulfide redox couples are often performed by methods that disrupt cell integrity.[62] Therefore, differences in redox states between cell compartments are not captured. Furthermore, biochemical methods using chemosensors,[63] or quantitative western blot methods require alkylation of free thiol species (GSH), thus dynamic changes in the redox

couple are omitted.[62] The lack of spatiotemporal resolution in the analysis of redox couples poses a major problem in assessing the redox status of the cell and its compartments. The role of glutathione is still discussed, as its function spans from reduction of disulfides, hydroperoxides, sulfenic acids, and nitrosothiols, over detoxification, to the synthesis of iron–sulfur clusters, and steroids. It furthermore affects oxidative protein folding and redox signaling.[64] In this context, the GSSG/2GSH ratio and its redox potential is not proven to be causing these biological events, but might instead be a concomitant biochemical marker of changes in the redox metabolism.[60]

1.3.2 Redox Environment in Healthy and Diseased Skin

Reactive oxygen species (ROS) include radical oxygen species, e.g., superoxide $O_2^{\cdot -}$, hydroxyl radical $HO\cdot$, and non-redical species, e.g., H_2O_2.[65] Together with antioxidants, such as glutathione, they represent the redox-mediating species of the organism (Fig. 8). Upon post-translational oxidation of proteins by ROS, protein structures and functions are modified, leading to initiation of signaling cascades and processes, spanning from cell proliferation to apoptosis.[66]

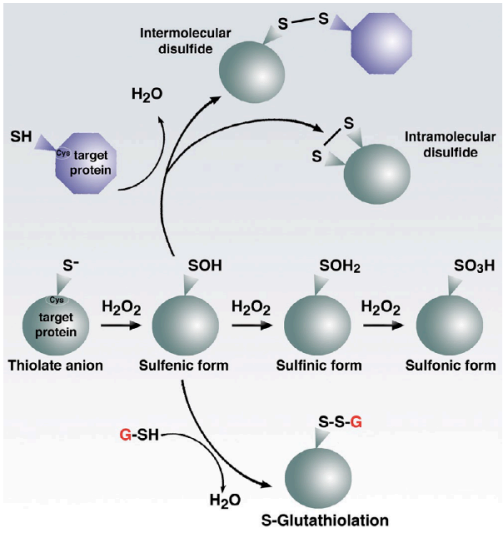

Fig. 8: Redox-depending signaling, mediated by H_2O_2/H_2O and the GSSG/2GSH redox couples. Reproduced with permission from Finkel, T., Signal transduction by reactive oxygen species. *J Cell Biol* **2011,** *194* (1), 7-15, under a CC-BY-SA 3.0 licence, as described at http://creativecommons.org/licenses/by-ncsa/3.0/).

Formation of ROS in skin is an integral part of skin metabolism, and upon exposure to external stimuli (UV light, heat) or after induced inflammation, the increased ROS levels are neutralized by antioxidants. However, the redox balance is destabilized in a state of chronic inflammation.[65] In healthy skin, epidermal differentiation is accompanied by a natural thiol and disulfide gradient,[67] and so thiols are abruptly oxidized to disulfides at the junction between stratum corneum and the viable epidermis.[68] Sulfhydryl oxidase is found across the epidermis, but its highest activity was found in stratum granulosum.[68] In murine stratum corneum, a steep increase of glutathione from the outer to the deeper layers was found.[69] In human skin, GSH regenerating glutathione reductase in the viable epidermis was found in higher amounts, compared to dermis. During chronic inflammatory skin diseases, such as psoriasis, atopic dermatitis, and contact dermatitis, the skin exhibits changes in its biochemical and physical characteristics, e.g., physical skin barrier, and enzymatic activity.[70] Inflammatory mediators and cell infiltrates generate oxidative stress, consuming antioxidants. Psoriatic skin exhibits reduced levels of thiols, accompanied by increased oxidative stress in lesional tissue.[71] The impaired redox

balance could be used as a trigger for redox-stimulated release of drugs from dermal drug delivery systems. The enclosed manuscript “Redox-sensitive Nanocarriers for Pronounced Release of Drugs in Inflammatory Skin Diseases” shows how a pathological redox environment is generated in ex vivo human skin and how reduction- and oxidation-sensitive CMS nanocarriers could be used for targeted treatment of inflammatory skin conditions.

1.3.3 Reduction- and Oxidation-Sensitive Functional Groups

Pathological tissue shows upregulation and downregulation of redox-mediators, such as ROS or GSH, as discussed above. Pathological biomarkers are commonly used as diagnostic readout for quantification of the state of disease, but also offer the possibility of being utilized as disease-specific triggers for stimulus-responsive behavior. This is especially interesting for the field of polymeric drug delivery, where site-specific triggered release of a transported cargo is desired. To this end, a trigger-responsive functional group is introduced as a covalent link between drug and carrier, or into the chemical structure of the carrier alone. The responsiveness to reductive or oxidative biochemical triggers can lead to bond rupture, as encountered in polymer-drug conjugates, or to a change in the physico-chemical properties of the carrier, such as a change in polarity. Most research in the field of reduction-sensitive materials focuses on the use of disulfide linkages.[12, 21, 72-73] Disulfides are especially of interest where increased levels of GSH are expected, such as in the cellular cytosol. Disulfide rearrangement between the GSH thiolate and the disulfide leads to formation of a new disulfide and a thiol (Fig. 9). In vivo, thiol-disulfide exchange resulting in disulfide scission or isomerization is mediated by disulfide oxidoreductases.[74] An alternative to reducible disulfides are reducible diselenides. Beld reported a diselenide-containing glutathione (GSe-SeG) and compared its redox potential and biological activity towards a protein. The Se-Se bond is 7 kcal/mol stronger than S-S in GSSG, and the redox potential of the GSe-SeG/2GSeH couple is reported by be 150 mV lower than GSSG/2GSH.[75] Thus, the SeSe bond is more stable, compared to disulfide, and thus stable for potentially longer periods in biological environment.[76] In contrast to the limited range of reducible bonds, oxidation-responsive bonds and groups offer a more diverse choice.[77-79]

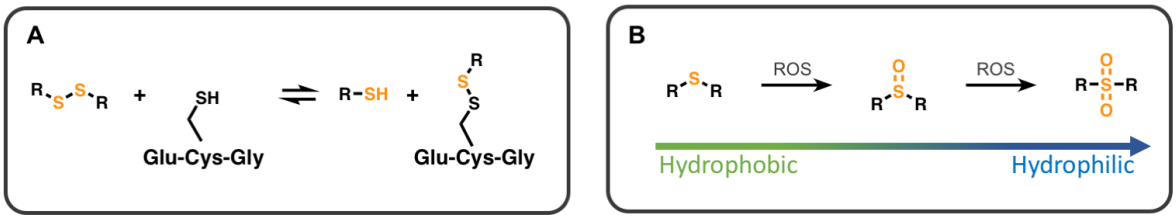

***Fig. 9: A**: Reductive scission of a disulfide bond by the tripeptide glutathione; **B**: Oxidation of a sulfide to sulfoxide and sulfone by reactive oxygen species (ROS).*

Sulfides and Selenides are oxidized in two steps by reactive oxygen species to sulfoxides and sulfones, or selenoxides and selenones, respectively. In line with the difference in behavior

between diselenides and disulfides, it is easier to oxidize selenides compared to sulfides.[80-81] Another oxidation-sensitive group based on sulfur is the thioketal group. It is oxidized in a non-reversible fashion and cleaves to a thiol and a ketal moiety. Further motifs used as oxidation-responsive groups, leading to bond scission, are phenyl boronic acids, proline, aryl oxalate esters, and ferrocene.[79, 81] In vivo, oxidation of the respective sensitive group occurs upon reaction with H_2O_2, metabolized from O_2 in the cytochrome chain or by enzymes.[82] In vitro, the oxidative environment is mimicked by incubation with aqueous H_2O_2 solutions.

1.3.4 Redox-responsive Polymers and Drug Delivery Systems

When pathological states are accompanied by chemical markers, a polymeric drug delivery system can be designed to feature a stimulus-triggered response to such a marker. Depending on the stimulus-responsive group, the triggered response on molecular level can either lead to bond scission, or to a change in the polymers physico-chemical properties, translating to a macroscopic change of the polymer structure. During chronic and acute inflammation, the redox balance is destabilized,[65] and so pathological changes in concentrations and gradients of oxidative ROS species and reductants, e.g., GSH, are reported. Using polymers, which are responsive to these pathological changes in the biochemical environment, drug delivery systems for the triggered release at inflammatory sites can be obtained. The following section focusses on sulfur-based redox-responsive polymers.

Reduction-Sensitive Polymers

In the field of polymeric drug delivery systems, redox-responsive polymers are utilized to provide site-specific release of the transporter cargo at the site of disease. Reduction-sensitive polymers are designed to respond to increased levels of biological reductants, e.g., GSH. Thus, polymers containing reduction-sensitive disulfide moieties account for most reported reduction-sensitive polymers.[20-21, 72, 83] Disulfides are either introduced as a cleavable linker in between polymeric building blocks or by crosslinking thiolated polymers (Fig. 10). Thiolation of block-copolymers by small organic molecules, e.g., cysteamine or thioglycolic acid, is used to crosslink micelles, which increases their stability in non-reductive environment. Many groups report increased stability of polyplexes, i.e., cationic micelles complexing genetic material, when the core has been crosslinked by disulfide formation between terminal thiol groups,[84-85] or by crosslinking incorporated free thiol residues in the polymeric backbone.[86] Once the polyplex has been taken up by the cell, the enhanced reductive environment mediated by the cytosolic level of GSH cleaved the disulfide, and the micelle disassembled and thus released its transported genetic material. In unimolecular micelles, research has focused on incorporation of cleavable disulfides into the backbone of the hyperbranched core building block, allowing controlled degradation and drug release in the reductive environment of cell cytosol.[87-88] Crosslinking strategies by disulfide formation has also been used to synthesize reduction-sensitive nano- and hydrogels,[89-90] and polymer-drug conjugates which are

connected via disulfide bonds.[91] De Vries et al. recently published a self-assembled cyclodextrin polymer, surrounded by a disulfide crosslinked polymeric shell. The reduction-sensitive shell prevented premature release of encapsulated drug, and live cell imaging experiments showed controlled cytosolic delivery of the payload.[92]

Thiolation of polymers renders thiomers, a special class of polymers.[93] Their ability to form disulfide groups with other thiol-containing scaffolds is exploited in their application as mucus penetrating polymer.[83] Mucus is a hydrogel, consisting of cysteine-rich glycoproteins. Thiomers form disulfide bonds with itself, but also to the cysteines of the mucus, and thus are mucoadhesive. Additional mucolytic papain molecules on the backbone of the thiomer allows for dynamic disulfide bond formation and scission, and so the thiomer can penetrate mucus.[94] The combination of free thiols and disulfide bonds due to intramolecular reactions make thiomers a hybrid class of redox-responsive polymers.

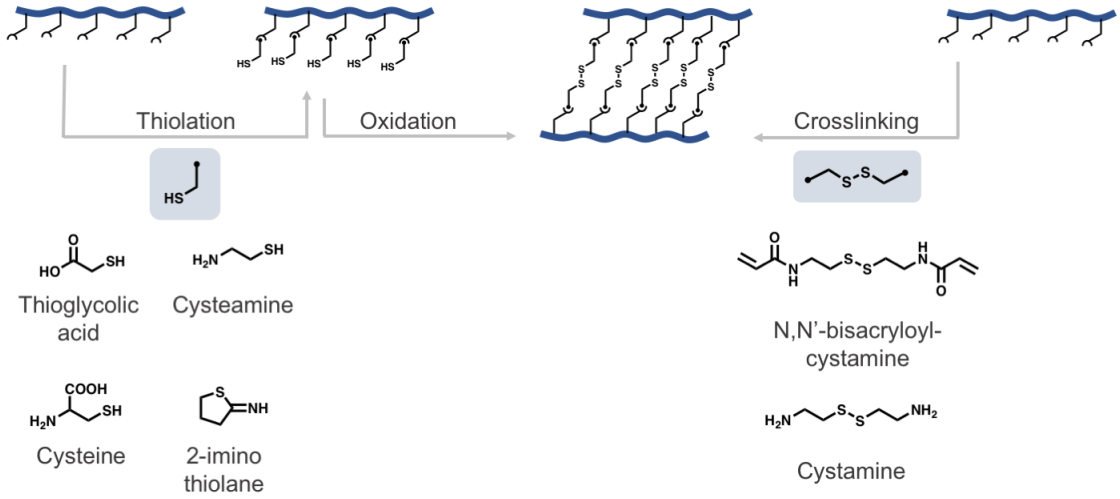

***Fig. 10**: Synthetic strategies for the synthesis of disulfide-containing polymers via thiolation or crosslinking with disulfide-containing molecules.*

Oxidation-Responsive Polymers

Responsiveness of sulfur-based materials towards oxidation has been reported for polysulfides, including both main-chain polysulfides and side-chain polysulfides. Main-chain polysulfides are syntheiszed by chain polymerization via ionic ring-opening polymerization of, e.g., episulfides, or by step polymerization, using thiols or alkali metals sulfides and halides, or thiols and olefins (Fig. 11). The first polysulfide-based nanoparticle reported to show oxidation-dependent behavior was a nanoparticle based on polypropylene sulfide (PPS).[95] Hubell and coworkers synthesized a triblock copolymer PEG-PPS-PEG, and a nanoparticle based on this material disassembled upon treatment with 10 % H_2O_2. PPS is hydrophobic, and upon oxidation of the sulfides to sulfoxides, the polarity of the C-S bond switches to a more polar one,[96] leading to an overall change from hydrophobic to hydrophilic. The change in the PPS polarity macroscopically destabilized the vesicles, resulting in a transformation to wormlike micelles, and ultimately “non-associating unimolecular micelles”.[95] The oxidation-

responsive behavior was shown in numerous publications, where drugs were released upon oxidation from PPS-PEG copolymer-based delivery architectures, e.g., in self-assembled micelles,[97-99] nanoparticles,[100] or from PEG-PPS-PEG copolymer-based polymersomes.[101-103] Besides their triggered release at elevated ROS levels, polysulfide-based delivery systems were reported to show a therapeutic effect as radical scavengers themselves. In studies on cellular levels of ROS compounds, curcumin-loaded PPS microspheres lowered cellular ROS levels of macrophages after 24 h treatment. A comparison to the treatment with non-loaded PPS microspheres revealed lowered levels of ROS as well, though less pronounced as with loaded particles.[104]

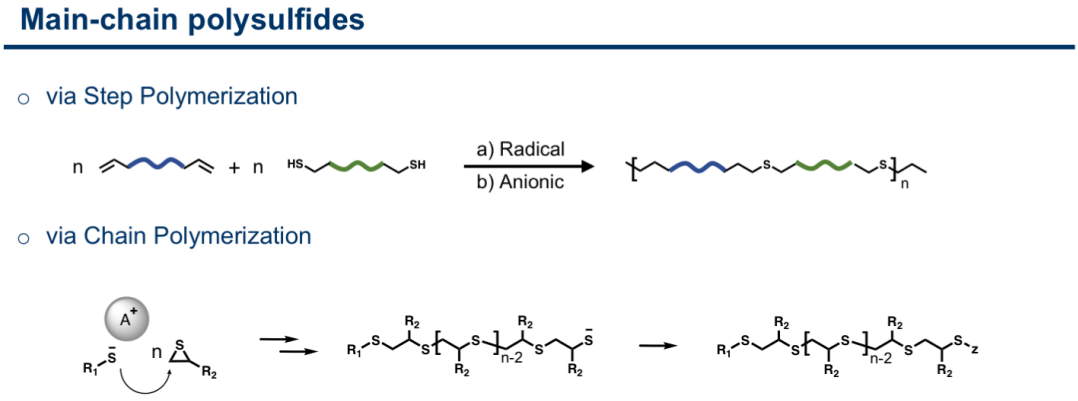

***Fig. 11**: Synthetic strategies for obtaining main-chain polysulfides; step polymeriaztion can be performed either by free radical polymerization (Thiol-ene) or by anionic chain polymerization using a catalyst (Thiol Michael Addition); Chain polymerization by anionic ring opening polymerization of episulfides yields polysulfides; side reactions are not shown.*

In analogy to methionine-rich proteins, polymers with thioethers in their side chain are oxidation-responsive and the change in polarity from hydrophobic to hydrophilic can translate to an overall structural change of the polymer.[105] In biology, the methionine thioether is hypothesized to be an antioxidant, buffering high ROS levels and preventing unwanted cysteine oxidation.[106-107] Methionine oxidation in enzymes and proteins result in conformational changes, [105] driven by the changed order of polar and non-polar residues.[108-109] In a work by Herzberger et al., an amphiphilic block-copolymer of PEG and a side chain-functionalized polyether comprising a thioether was synthesized and formed self-assembled micelles with a size of 9-15 nm in water.[110] Incubation of the micelles in a 1 % H_2O_2 solution led to oxidation of thioethers to sulfoxides, followed by disassembly of the micelles (Fig. 12). The oxidation was studied using ^{1}H NMR techniques and revealed a comparably fast oxidation, leading to full oxidation within 2.5 h at 37 °C or within 6 h at room temperature. In comparison, PEG-PPS polymersomes are oxidized in a 10 % H_2O_2 solution within 10 h.[95] Tirelli et al. reported an auto accelerated oxidation of PPS by H_2O_2, resulting from the H_2O_2 access to the thioether groups, depending on the content of already oxidized sulfoxides.[111] The more sulfoxides are present, the more hydrophilic is the polymeric scaffold and thus H_2O_2 has a

facilitated access to the thioethers, and oxidation gets accelerated. Sigmoidal shapes of kinetic curves indicate such behavior.

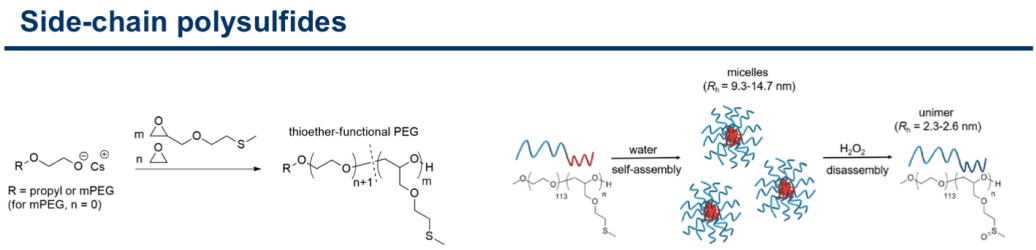

Fig. 12: *Side-chain polysulfide synthesized via anionic ring opening polymerization. Self-assembled micelles disintegrate upon oxidation by H2O2 and release their transported guest molecules. Adapted with permission from Herzberger, J. et al., Oxidation-Responsive and "Clickable" Poly(ethylene glycol) via Copolymerization of 2-(Methylthio)ethyl Glycidyl Ether.* J Am Chem Soc ***2016,*** 138 *(29), 9212-9223.*[110] *Copyright 2018, American Chemical Society.*

This behavior was also observed by Herzberger et al. for the case of side-chain polysulfides.[110] In line with published data, Herzberger reported oxidation by H_2O_2 leading to sulfoxides, while oxidation with the stronger oxidant hypochlorite gave sulfones.[112] In vivo, hypochlorite is generated from H_2O_2 and chloride anions by peroxidases. When oxidizing PPS with in situ generated hypochlorite using oxidases, in analogy to the in vivo situation, oxidation is much faster. It is hypothesized that in vivo, presence of enzymes might further accelerate oxidation events which are observed in vitro.[113] The release of drugs from polysulfide-based self-assembled architectures is based on the disassembly of the vehicle upon oxidation. However, oxidation of a polysulfide-based unimolecular micelles or nanogels does not necessarily lead to disruption of the architecture. Instead, the solubility switch from the hydrophobic sulfide to the hydrophilic sulfoxide or sulfone results in changes of the polymeric microenvironment: polymeric networks, e.g., nanogels, can swell and thus release their encapsulated guest, while solubility changes within unimolecular micelles might either lead to tightly locked in or quickly expelled drugs. D'Arcy et al. investigated the kinetics of linear polysulfide oxidation, and they observed two main influences: the polarity of the hydrophobic domain (the polymer composition) and local steric hindrance (linear vs. branched polymers).[114] Branched polymers showed a slower response to oxidation comapred to linear polymers and the speed of oxidation increases with rising hydrophilicity.[115]

1.4 Hyperbranched Biodegradable Polymers

1.4.1 Forms of Biodegradability

The term "biodegradable polymer" in public discussions is strongly associated with plastic-based packing materials. Self-explanatory, the word "biodegradable", consisting of degradation and biology, states the intended purpose of using such materials: degradation of a polymer in a biological environment. However, the conditions under which a polymer should degrade, differ strongly, depending on the field of application. Thus, the characteristic

biodegradability of a material should meet the requirements of the intended use. In the following, the term biodegradable will refer to materials with hydrolytically or enzymatically cleavable bonds, leading to erosion of the polymer. Though desirable, biodegradation of polymers does not necessarily lead to products which can be eliminated by the body.[116] The field of biomaterials spans from bulk polymers, e.g., used as implants, to nanoscopic unimolecular micelles. Despite their different shapes and functions, the materials used in this broad area should meet a minimum set of requirements to qualify for being biodegradable: the materials should not trigger an inflammatory response and have a reasonable degradation time. Furthermore, their degradation should give non-toxic products.[117] Polymeric drug delivery systems coined “biodegradable” include systems based on fully degradable, meaning degradable up to the smallest units, e.g., monomers, but also systems comprising a degradable linker, allowing for erosion to smaller polymer or oligomer fragments.[118] Biodegradable bonds used as linkers include hydrolytically cleavable groups, e.g., esters, imines, acetals, ketals, phosphoesters and enzymatically cleavable groups, e.g., amides.[117-118] Based on these groups, numerous biodegradable polymers have been synthesized and their use for polymeric drug delivery has been discussed in many reviews.[117-119]

The mechanism of degradation depends on intrinsic factors, e.g., the polymer’s chemistry, molecular weight, morphology, and on external factors, e.g., temperature and pH.[120] Most biodegradable polymers are degraded by hydrolysis, enzymatic reactions and oxidation.[121] In the following, polymers comprising multiple degradable groups in their polymeric backbone will be discussed, while copolymers connected with a biodegradable linker will be excluded.

Hydrolytic Degradation

The kinetics of the hydrolytic cleavage of an acid-sensitive group generally depend on the type of the acid-labile group, but it can vary strongly depending on the respective polymer. Among others, hydrophobic-hydrophilic balance, side groups, and water solubility can affect the speed of cleavage. When the acid-labile groups are located on the aliphatic polymer backbone, accessibility of the groups by water molecules governs the hydrolysis.[120] Poly-α-esters are aliphatic polymers with hydrolytically degradable ester groups in their polymer backbone. Theoretically, all polyesters are biodegradable, but when the polyester is used in biomedical applications and thus is intended to degrade within a reasonable period, the aliphatic chains should be short.[122] Poly(lactic acid) (PLA) and poly(glycolic acid) (PGA) are degraded to lactic acid and glycolic acid, respectively. These are natural metabolites and can be metabolized by the citric acid cycle to CO_2 and H_2O.[123] Thus, both polymers are FDA-approved biodegradable, or more specifically, bioresorbable, polymers which are used as sutures and for drug delivery.[124] After this success, researchers focused on synthesizing new materials based on aliphatic polyesters, especially poly(ε-caprolactone) (PCL). It degrades to ε-hydroxy caproic acid, and the rate of degradation is generally slower than those reported for PLA and

PGA.[124] Values of degradation rates are generally reported by groups working on biodegradable bulk polymers for implants, sutures and materials for fracture fixation, among others.[117] Degradation times of 50 days (PGA, 40 kDa) up to two years (PLA, 300 kDa) are reported, which for the intended application can be considered reasonable.[121] However, the degradation time for polyester-based nanoscopic drug delivery systems cannot be predicted based in the data obtained from bulk polymers. Further hydrolytically degradable organic polymers are polyphosphoesters,[125] poly(ortho esters), polyacetals, polyanhydrides, and polycarbonates (mainly enzymatically). Degradation products of polyesters, namely small molecular weight acids, can lead to an inflammatory response at the site of inflammation.[126].

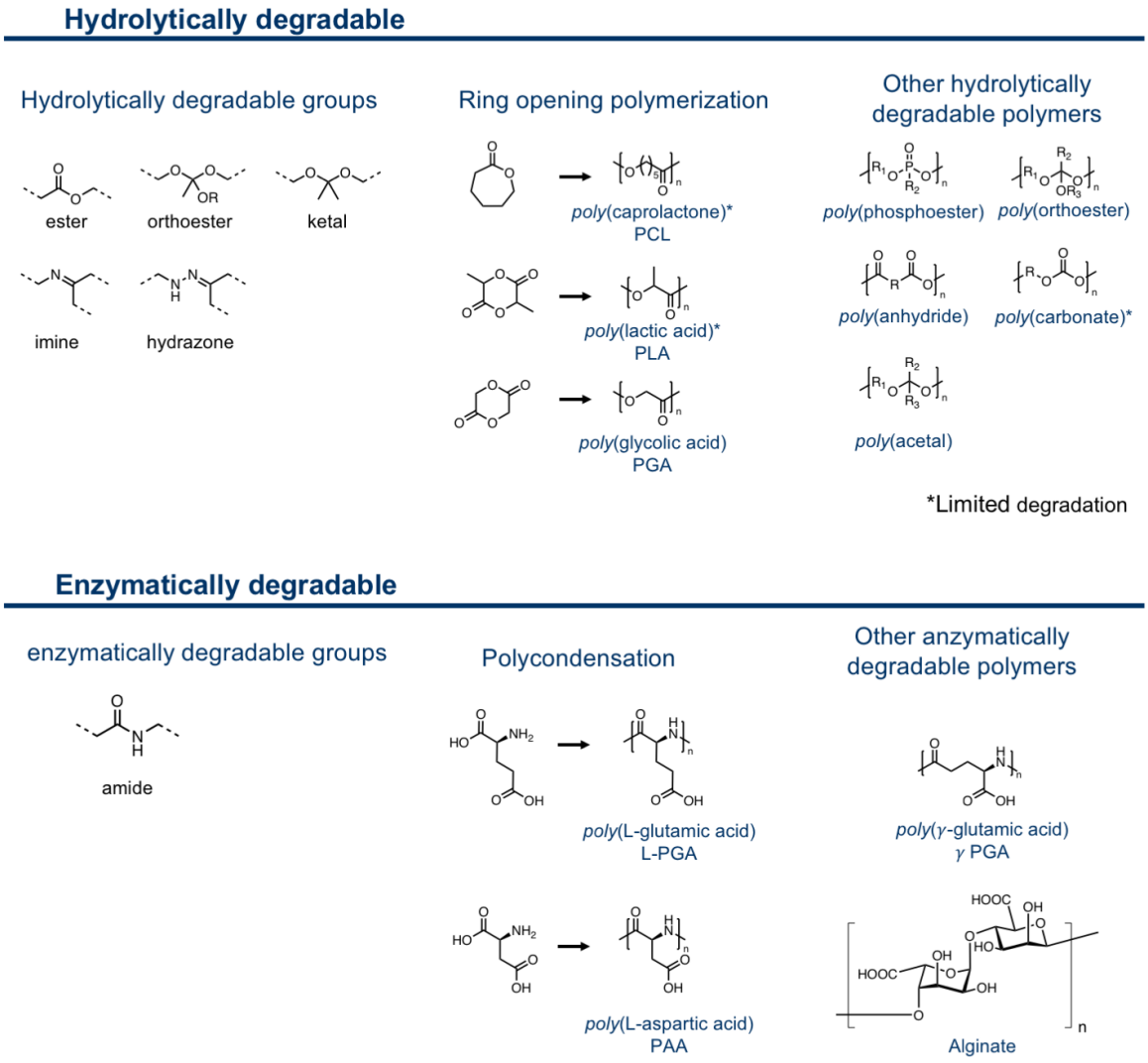

***Fig. 13**:* Overview on commonly employed hydrolytically and enzymatically degradable linkers and polymers in polymeric drug delivery.

Enzymatic Degradation

Enzymatic degradation by hydrolysis is catalyzed by hydrolases, among others including peptidases, esterases, phosphatases, and glycosidases. Degradation of bulk polymers by enzymes occurs under surface erosion, i.e., the degradation from the surface to the core of a bulk material. Limited by its size, the enzyme cannot penetrate deeper into the polymer matrix.

In contrast, enzymatic degradation of nanoscopic drug delivery systems is not limited to surface erosion, but might as well occur under bulk erosion, i.e., a simultaneous degradation of the scaffold throughout the whole nanoparticle. The mechanism is governed by the composition, polarity, and architecture of the scaffold. Generally, enzymatically-degradable polymers are also hydrolytically degradable, but their rate of hydrolysis is too low at physiological conditions to be considered as relevant.[117] Natural polymers, such as proteins (collagen, gluten, elastin), and polysaccharides (cellulose, alginate, chitosan) are enzymatically degradable and used as bio-sourced biodegradable materials in drug delivery.[120, 122] Synthetic polymers, which can be degraded by humans, include poly(L-glutamic acid) (L-PGA) and poly(aspartic acid) (PAA). They belong to the polymer class of synthetic poly(amino acids), and are the first promising candidates as biomaterials of this class. Previous polymers were not suitable due to their high crystallinity, slow degradation, and immunogenicity.[117] L-PGA can be synthesized as a linear polymer, or grafted from a branched multifunctional core.[88] Due to its negatively charged backbone, it has shown promising results in DNA delivery,[127] and layered with cationic polymers into layer-by-layer nanospheres, it can transport cationic and anionic payloads.[128-129] Xu et al.. tested the degradation of a PGA hydrogel, containing disulfide links. In vitro degradation in presence of elastase and 1 mM GSH, the hydrogel degraded completely within two hours. In vivo studies were performed in mice by subcutaneous injection of the hydrogel. Here, the gel was completely degraded after 12 days, whereas a comparable PGA hydrogel without disulfide bonds remained stable even after one month.[130]

A few PCL-containing medical devices got approved by the FDA, namely a coating for stents (SynBiosys®), a bioresorbable suture (Monocryl®, approval recalled due to insterile production), and a long-term implant delivery device (Capronor®).[131] Even though PCL is considered as a generally biodegradable polymer, its degradation rate is very low. Nevertheless, PCL is communicated as an FDA-approved biodegradable polymer throughout literature, and so many publications can be found where the authors assume biodegradation of their PCL-containing drug delivery system, without giving clear evidence thereof. The scope of biodegradability under physiological conditions is strongly overestimated. Changing the polymer's connectivity, architecture, molecular weight or substitution pattern changes the crucial factors affecting the degradation profile, such as crystallinity, glass transition temperature T_g, molecular weight, and water solubility.

1.4.2 Biodegradable Hyperbranched Polymers

The physico-chemical behavior of polymers is not only dependent on the constitution, but also their architecture. Polymer architecture spans from linear to highly branched, i.e., dendritic. With increase in branching, as shown in Fig. 14, four categories of polymer architecture can be differentiated: linear polymers, branched polymers, hyperbranched polymers, and

dendrimers. The densely packed branches of hyperbranched and dendritic systems offer multiple functional groups with a maximum density on one single molecule. Compared to linear polymers, branched polymers are restricted in the movement of single segments by their branching points. Thus, whenever entanglement plays a role, branched polymers exhibit special properties: low viscosity, low crystallinity, enhanced solubility.[132-133]

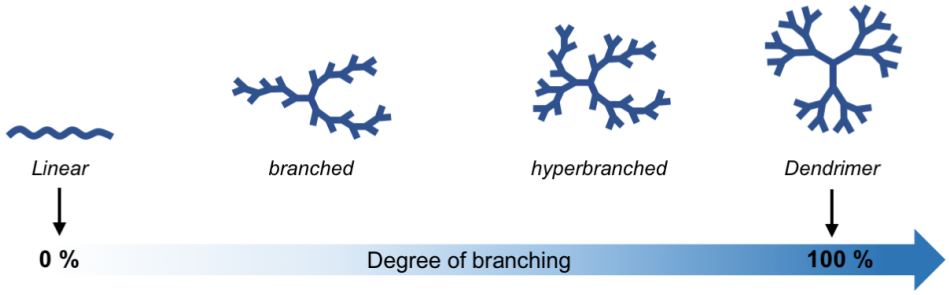

***Fig. 14**: Polymers with increasing degree of branching. Per definition, linear polymers have a degree of branching (DB) of 0 %, while Dendrimers are maximally branched and DB = 100 %.*

Being maximally branched, dendrimers are considered as perfect architectures. However, their synthesis is often based on a multistep approach, including purification of intermediates at each stage of the synthesis. This synthetic effort limits their applicability. In contrast, hyperbranched polymers can be synthesized in one pot reactions, and despite being the imperfect version of dendrimers, their physico-chemical properties can comply with those of dendrimers.[134-135] The synthesis of hyperbranched polymers can be based on various types of monomers and reactions. To achieve branching, one monomer must have at least three reaction sites. Self-reactive monomers of the type AB_x ($x \geq 2$), combining two different reactive groups in one monomer, were the first monomers used for the synthesis of hyperbranched polymers.[136] In the 1990ies, the alternative approach using an A_2+B_x ($x \geq 3$) combination was established. Even though AB_x type monomers need to be synthesized prior to a polymerization, they dominate the synthesis of hyperbranched polymers. These polymers can be used in polycondensation reactions, step growth polyaddition of the Michael type, and in ring opening multibranching polymerization (ROMBP).[136] Hyperbranched polyesters are the major class of polymers in the field of biodegradable hyperbranched polymers, and their most known and successful representative is the Boltorn type aliphatic polyester (Fig.15). Based on bismethylolpropionic acid, an AB_2 monomer, it is synthesized in a step growth polycondensation reaction. The degradation of Boltorn polymers was shown in various publications.[137] Reul et al. tested the degradation of a 19 kDa Boltorn H40 polymer and compared it to a Boltorn with additionally grafted lipophilic chains, and a Boltorn grafted with lipophilic chains and PEG chains. Degradation by hydrolysis was performed at neutral pH 7.4, and while the modified Boltorn polymers did not show degradation, the crude Boltorn H40 degraded by 7 % within 24 h and 30 % within 28 days.[138] Copolymerization of the AB_2 bismethylolpropionic acid monomer in combination with the ring opening polymerization of ϵ-

caprolactone gave a hyperbranched polyester with longer aliphatic segments in between the ester units, which was also shown to work under enzymatic catalysis.[139-140] Anhydro sugars, monomers of the type AB_4, can be polymerized via ROMBP to hyperbranched glycopolymers,[141] whereas step-wise polymerization of cyclic N-carboxyanhydrides and successive protection/deprotection steps of amino acids give hyperbranched polyamides.[142] Alternatively, polycondensation of diamines (A_2) and trimesic acids (B_3),[143] or the thermal self-condensation of an AB_2 amino acid hydrochloride, e.g., lysine hydrochloride with unequal reactivities of the amine groups,[144] give hyperbranched polyamides. Hyperbranched polyphosphoesters are obtained by self-condensing ring-opening polymerization, e.g., from 2-(2-hydroxyethoxy)ethoxy-2-oxo-1,3,2-dioxaphospholane.[145] Degradation studies using a polyphosphoester-based hydrogel disproved the expectation of this polymer to be a fast degrading scaffold. Immersed in solution at pH 4.0, 60 % of the polymer was degraded after 15 days.[146]

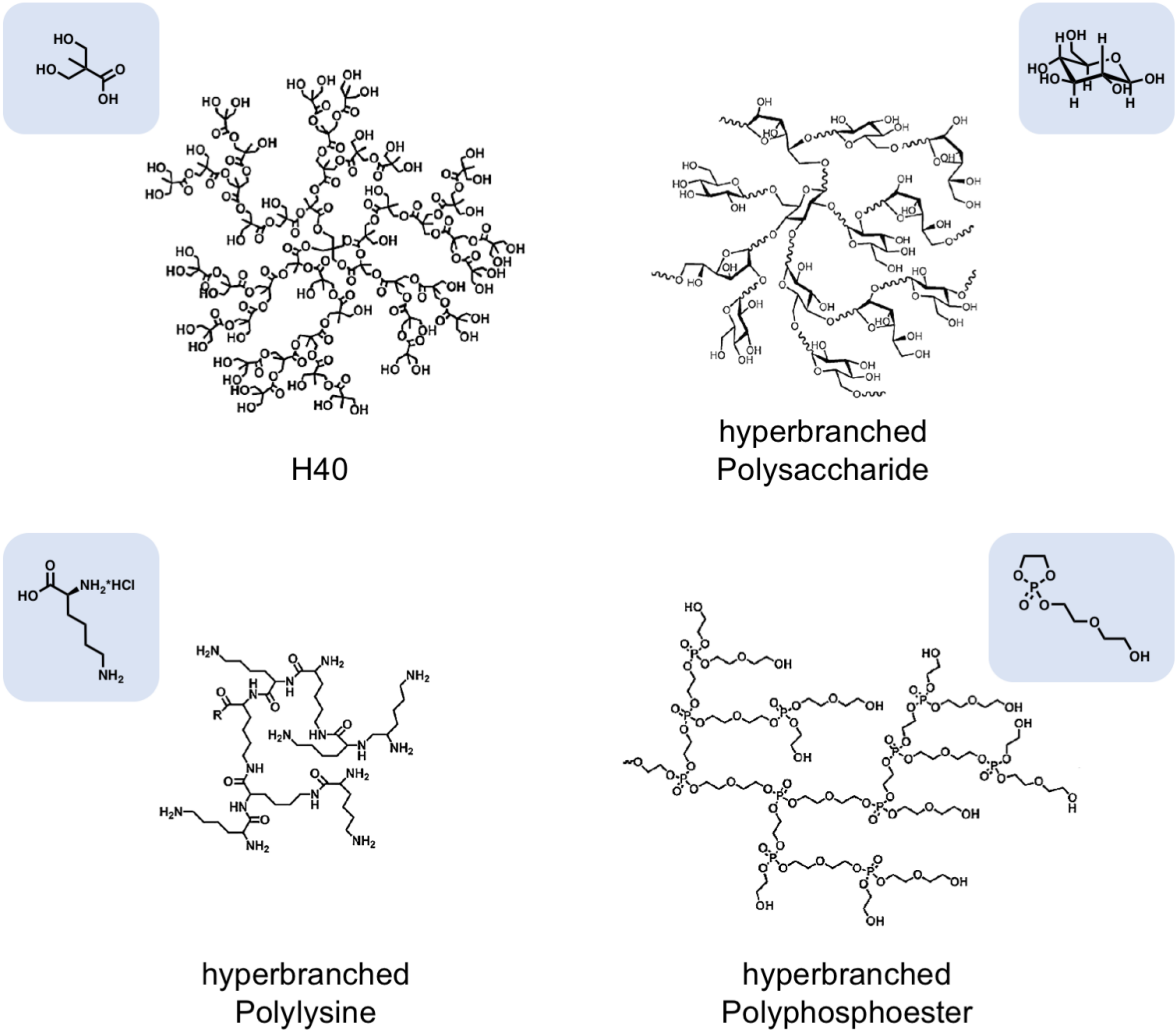

Fig. 15**: Representatives of biodegradable hyperbranched polymer and their parent monomers. Reproduced from Wang, D. et al., Bioapplications of hyperbranched polymers.* Chemical Society Reviews ***2015, 44 *(12), 4023-4071, Ref. [147] with permission from The Royal Society of Chemistry.*

In summary, the choice of the right hyperbranched biodegradable polymer strongly depends on the application and the targeted polymer performance. If used as a branching scaffold for unimolecular core (multi-) shell nanocarriers, the hyperbranched core molecule is expected to be the last sphere to be degraded, if enzymatic degradation is expected. If the (multi-)shell is to be shed off by enzymatic degradation or hydrolytic cleavage, the core should be designed to remain water-soluble, as the enzymatic degradation of hydrophobic polymers is very limited. Hydrolysis of biodegradable polymers at physiologically relevant acidic pH, i.e., pH 5.5, is surprisingly slow, and many hyperbranched polymers reported to be biodegradable were tested either in strongly acidic conditions (up to pH 2.0) or biologically irrelevant basic conditions (up to pH 11). Toxicity of degradation products and degradation fragments also needs to be considered thoroughly. If acidic products are formed, they might induce inflammatory response at placed that are weakly vascularized, e.g., the epidermis.

1.5 Analysis of Nanocarrier Penetration, Release, and Degradation

1.5.1 Release of Drugs and Degradation of Nanocarriers

Accumulation of nanocarriers in tissue, e.g., specific skin layers, might lead to toxicity, especially when treating pathological tissue. Understanding this relationship means investigating the nanocarrier's fate during and after delivery of the drug. The first step towards assessing the nanocarrier performance is simulation of the in vivo situation in an in vitro environment. This is especially performed for the characterization of drug release profiles and possible degradation of the nanocarrier. The release of drugs can be tested with a dialysis set up, where a dialysis bag, containing the nanocarrier and its encapsulated drug, is immersed in the respective solvent. The dialysis membrane molecular weight cut off should be chosen in an appropriate size range, i.e., a size where the drug can penetrate the membrane while the nanocarrier is retained inside the dialysis bag. Also, the combination of the solvent volumes and the compound concentrations inside the bag and its surrounding volume should maintain so called sink conditions. At sink condition, the concentration of the diffusing compound (drug) over the complete dialysis volume is 5 to 10-fold lower than the compound's solubility in the tested solvent. Sink conditions are maintained to exclude diffusion driven by precipitation of an insoluble compound. Schwartzl et al. recently published a model that supports the suitability of dialysis set up for the determination of the release kinetics of the drug dexamethasone from CMS nanocarriers. It was found that it is necessary to perform an equilibration release experiment, where the drug diffusion through the membrane is quantified in absence of the nanocarrier. When the drug diffusion rate is substracted from the drug diffusion in presence of the nanocarrier, the drug retaining effect of the nanocarrier can be determined.[148] Drug release from nanocarriers can also be tested in ex vivo human skin using intradermal microdialysis tubes, which are placed in different depths of skin to determine the penetration

depth and kinetics of the drug.[149] Degradation of nanocarriers, either upon hydrolytic or enzymatic cleavage, is performed in vitro by incubation of the nanocarrier in the respective environment. Analysis of degradation products can be based e.g., on their molecular weight, determined by size exclusion chromatography, or on molecular analysis by spectroscopy or spectrometry, e.g., NMR techniques, or mass spectrometry. When samples are taken frequently, analysis of each time sample give degradation kinetics. Screening penetration pathways of nanocarriers requires advanced techniques, which will be discussed in the following section.

1.5.2 Penetration Pathways by Label-free Techniques

Label free techniques include electron microscopy (SEM, TEM), vibrational spectroscopy and microscopy (FTIR, IR, Raman, SERS, CARS), as well as X-ray spectromicroscopy and diffraction. Light microscopy is applicable whenever the contrast between the nanoparticles and its surrounding matrix is big enough. Thus, light microscopy is mostly applied for inorganic nanoparticles. Electron microscopy (EM) based techniques are used on surfaces, and hence analysis of the localization of NPs is performed on thin skin sections. Transmission EM detects electron-dense areas, and thus, mainly inorganic and metallic NPs can be visualized.[150] Atomic force microscopy was used to detect NPs within the collagen network of human skin cryosections.[151] X-ray spectromicroscopy has a spatial resolution of a few nm, and its high chemical selectivity allows suppression of the skin absorption whilst detecting the drug's specific absorption. With this technique, the spatial distribution of the drug dexamethasone within ex vivo human skin sections was analyzed.[152] Fourier-transformed infrared spectroscopy (FTIR) of stratum corneum sheets, obtained by tape stripping, was used to determine the quantitative distribution of polymeric vesicles in human stratum corneum. However, the IR absorption of water in skin limits this technique to analysis of SC.[31] Furthermore, the comparability of tape stripping and IR measurement of the tape strips is limited due to non-standardized protocols of application and measurement.[153] Non-invasive quantification of Raman active NPs in vivo can be assessed with Raman spectroscopy. To obtain penetration profiles, overlapping Raman spectra of skin components and the NP of interest are deconvoluted. Using confocal Raman spectroscopy, penetration profiles in skin depths up to 5 µm can be detected.[154]

1.5.3 Penetration Pathways by Label-based Techniques

Encapsulation of fluorescent molecules into nanocarriers or covalent labeling of nanocarriers with fluorescent dyes allows for spatial resolution of drugs and their parent nanocarriers. Using a pair of adjacently attached fluorescent molecules, the transfer of energy from one excited dye molecule to the other can be used in FRET experiments to determine, e.g., the cleavage of a chemical bond (Fig.16). This technique was used by Krüger et al. to kinetically resolve the cleavage of a hydrolytically cleavable bond.[155] The FRET pair dye molecules were coupled to

the polymer, and while transfer of energy is only possible within the Förster resonance distance which, in this case, complies when the bond is intact, the increase in fluorescence reported the prohibited energy transfer and thus the scission of the connecting bond.

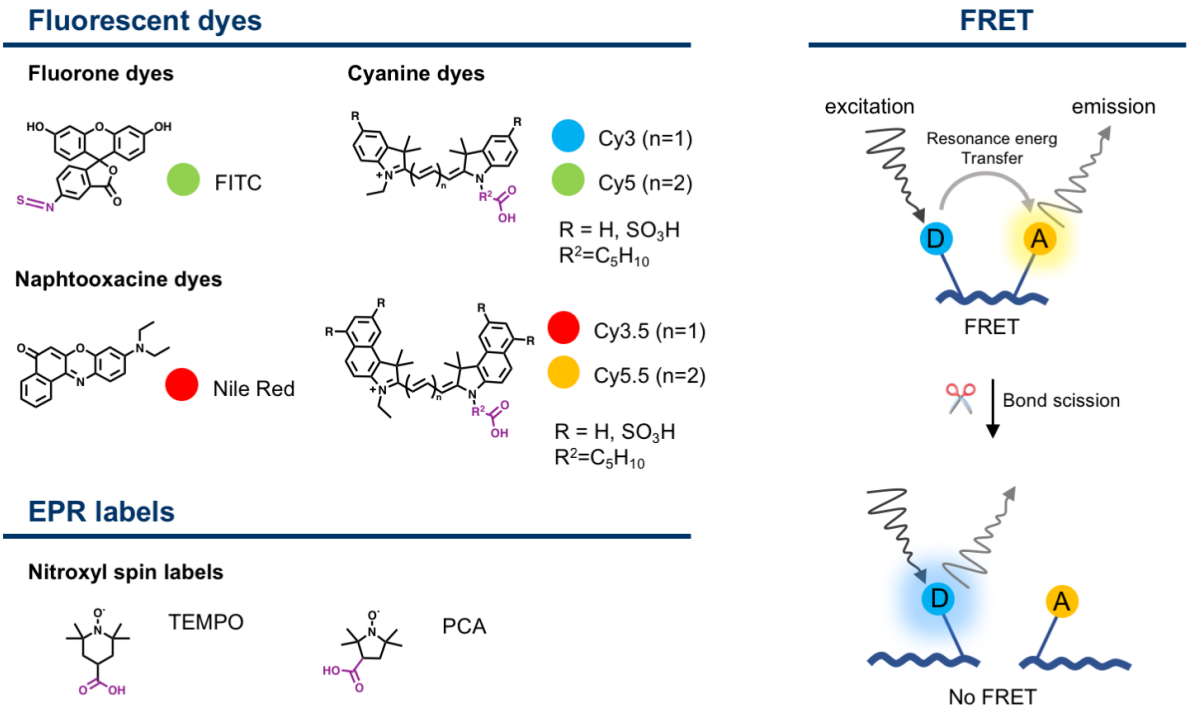

***Fig. 16**: Various types of labels used for label-based techniques described in this chapter; fluorescent dyes are used as fluorescent model drugs, or as fluorescent labels when attached via linkers (highlighted in purple); EPR labels can be attached to a nanoparticle and report the polarity of the environment; FRET= Förster Resonance Energy Transfer; In a FRET pair, a donor fluorescent dye (D) is excited and transfers energy to an acceptor (A) fluorescent dye, when A is within the Förster distance to D; A emits light; The transfer is interrupted, when the connecting bond is broken, and A leaves the Förster Resonance distance; D emits light.*

While most fluorescence-based analysis methods (transmission microscopy, confocal microscopy) measure the intensity and hence the concentration of the fluorescent probe, Fluorescence Lifetime Imaging Microscopy (FLIM) adds information on the chemical environment of the fluorescent molecule. The combination of a confocal laser scanning microscope and a time-correlated photon counter gives excited state fluorescence decay traces as the readout. Due to the sensitivity of the fluorescence lifetime to its chemical environment, more detailed information can be assessed, e.g., drug distribution within the nanocarrier. Time-resolved anisotropy measurements report drug binding and release from nanocarriers, and their aggregation behavior.[156] Similar information can be obtained from Electron Paramagnetic Resonance Measurements (EPR). This method requires labeling of the drug or the carrier with a spin label, e.g., nitroxide-based molecules with an unpaired electron (Fig.16). The unpaired electron is sensitive to the polarity of its environment and thus a spin-labelled drug molecule inside a nanocarrier can report changes of its environment upon its release from the carrier by diffusion,[157] or due to degradation of the carrier.

2 Objectives

Polymeric drug delivery systems aim at overcoming the limited applicability of poorly soluble drugs by entrapping the drug in a solubility-enhancing polymeric environment. Among the vast diversity of polymeric drug delivery systems, dendritic nanocarriers are considered as universal systems, as their architecture offers many benefits. The internal voids, the nanocarrier size, and flexibility are tunable by design, thus allowing for optimization of nanocarrier properties for specific drugs and controlled release adapted to the aimed biological target. Carrier-based drug delivery systems can provide penetration enhancement across the skin barrier and protection of sensitive compounds. Drug release can be modified to achieve high local concentrations at the site of action and reduction of side effects by site-specific targeting, while chemical modifications of the nanocarrier can lead to a controlled or triggered release.

For this PhD work, we envisioned the development of CMS nanocarriers towards efficient penetration into skin, triggered release, and controlled biodegradability at physiological conditions. The carrier should follow the concept of the CMS nanocarrier. All carriers should have the following characteristics: 1) defined particle size, 2) increased transport capacity compared to established pharmaceutical formulations, 3) targeted drug release and 4) efficient synthesis.

The first focus was to develop a biodegradable CMS nanocarrier. After penetration of the CMS into skin, a possible accumulation of the carrier might lead to an inflammatory response, especially when treating diseased skin. Preventing an accumulation-related toxic effect, the new CMS nanocarrier is supposed to degrade to ideally non-toxic products after delivery of the transported drug. To this end, polyesters as the basic polymer for the biodegradable CMS were hypothesized to hydrolytically degradable in skin at physiological pH values of 5.0 – 5.5. Keeping the typical composition of a CMS nanocarrier and its water-soluble outer shell mPEG, its core and inner shell building blocks needed to be exchanged for polyester-based alternatives. A hyperbranched polyester suiting as the core molecule needed to be synthesized, as well as a linear polyester as the inner shell. Assembled to a CMS, the biodegradable version of the CMS was supposed to meet the performance standards of the established CMS in terms of encapsulation and transport.

Aiming at a triggered release of drugs by pathologically upregulated chemical markers, the redox environment of inflamed skin was chosen as the targeted stimulus for a stimulus-responsive CMS nanocarrier. The goal was to synthesize redox-sensitive CMS nanocarriers for enhanced release in inflamed areas of the skin. Here, our hypothesis consisted of two parts: Firstly, inflammation leads to high levels of oxidative stress expressed in high levels of reactive oxygen species (ROS) in the stratum corneum. We hypothesized that the introduction of thioether moieties in CMS nanocarriers will lead to an oxidation-sensitive nanocarrier (osCMS),

releasing encapsulated cargo in oxidative environment of inflamed stratum corneum. The release is based on the oxidation of the thioether group to sulfoxides, which translates to a change in polarity of the inner shell from hydrophobic to hydrophilic. Secondly, the natural gradient in glutathione and glutathione reducing enzymes with increasing concentrations in dependence on the penetration depth in the skin can be used as a release trigger. We intended to introduce disulfide groups in the inner sphere of the CMS nanocarriers as the glutathione-sensitive moiety, which would react with the free thiol of glutathione, leading to a cleavage of the CMS nanocarrier and the release of the encapsulated cargo. The rate of cleavage of reduction-sensitive CMS (rsCMS) will increase with increasing glutathione and glutathione reducing enzymes, and hence with increasing penetration depth. As in the first project, the general structure and the outer shell of CMS were not to be changed, whereas a synthetic strategy needed to be found for synthesizing rsCMS and osCMS. The complementary set of CMS needed to be as similar as possible, and so the inner shell of rsCMS and osCMS was intended to have a same length. Furthermore, the synthetic strategies were supposed to lead to maximal conversions of the core molecule's terminal functional groups, translating to a CMS nanocarrier with a maximum density of arms.

Understanding and visualizing the penetration pathway of CMS nanocarriers and their encapsulated or released guest molecules was a further goal of this PhD work. Typically, fluorescent dyes, i.e., nile red, are used as model drugs to study the penetration behavior of CMS nanocarriers using fluorescence microscopy. However, fluorescent dyes are different from real drugs in terms of their molecular weight and polarity. The ideal case would be to characterize the release from a CMS nanocarrier and the penetration route of a clinically relevant drug, such as dexamethasone. However, labelling the drug with a fluorescent dye changes the drug's intrinsic properties, and its uptake and release from nanocarriers would not be comparable to the label-free situation. Electron-paramagnetic-resonance-active nitroxide-based labels are comparably small, and labelling of a drug with these labels might give drugs with only minor changes of their properties. Hence, the drug dexamethasone was supposed to be labelled at its primary hydroxy group, and a suitable robust labelling technique needed to be found.

3 Publications and Manuscripts

3.1 Polyester-Based, Biodegradable Core-Multishell Nanocarriers for the Transport of Hydrophobic Drugs

“A water-soluble, core-multishell (CMS) nanocarrier based on a new hyperbranched polyester core building block was synthesized and characterized towards drug transport and degradation of the nanocarrier. The hydrophobic drug dexamethasone was encapsulated and the enzyme-mediated biodegradability was investigated by NMR spectroscopy. The new CMS nanocarrier can transport one molecule of dexamethasone and degrades within five days at a skin temperature of 32 °C to biocompatible fragments.”

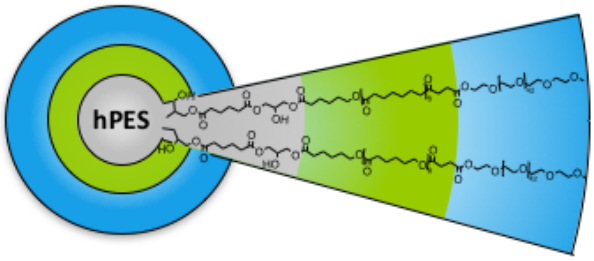

This chapter was published in:

Walker, K.A.; Stumbé, J.-F.; Haag, R. Polyester-Based, Biodegradable Core-Multishell Nanocarriers for the Transport of Hydrophobic Drugs. *Polymers* **2016**, *8*, 192.

https://doi.org/10.3390/polym8050192

Contribution:

Conception, synthesis, and analysis of the nanocarrier, experiments on performance and degradation behavior. Writing and editing of manuscript and its graphics, revision of manuscript and galley proof as well as communication with the editor.

polymers

MDPI

Article

Polyester-Based, Biodegradable Core-Multishell Nanocarriers for the Transport of Hydrophobic Drugs

Karolina A. Walker [1], Jean-François Stumbé [2] and Rainer Haag [2,*]

[1] Institute of Chemistry and Biochemistry, Freie Universität Berlin, Takustr. 3, 14195 Berlin, Germany; karolina.walker@fu-berlin.de

[2] Laboratoire de Photochimie et d'Ingénierie Macromoléculaires, Université de Haute Alsace, 3 rue Alfred Werner, 68093 Mulhouse Cedex, France; jean-francois.stumbe@uha.fr

* Correspondence: haag@chemie.fu-berlin.de; Tel.: +49-030-8385-2633

Academic Editors: André Laschewsky and Sebastien Lecommandoux
Received: 26 February 2016; Accepted: 3 May 2016; Published: 14 May 2016

Abstract: A water-soluble, core-multishell (CMS) nanocarrier based on a new hyperbranched polyester core building block was synthesized and characterized towards drug transport and degradation of the nanocarrier. The hydrophobic drug dexamethasone was encapsulated and the enzyme-mediated biodegradability was investigated by NMR spectroscopy. The new CMS nanocarrier can transport one molecule of dexamethasone and degrades within five days at a skin temperature of 32 °C to biocompatible fragments.

Keywords: nanocarrier; biodegradable; polyester

1. Introduction

A main objective for polymeric nanocarriers is to increase the solubility of hydrophobic and poorly water-soluble drugs. The idea to use nanocarriers originates from the mimicry of micellar architectures, which are self-assembled constructs made of amphiphiles. Inspired by micelles, the first attempts to mimic this architecture with polymeric structures was made in the late 1980s [1]. Apart from their good performance in terms of loading efficacy, both architectures can disassemble below a critical micellar concentration [2,3]. This drawback can be resolved by creating a micelle, as visualized in Figure 1, which is covalently linked at its focal point [4]. Although there have been advances in the field of unimolecular micelles, which are based upon hyperbranched and dendritic core molecules, such as hyperbranched poly(ethylene imine), hyperbranched polyglycerol, or hyperbranched polyester Boltorn™, little progress has been made in biodegradable systems [5,6]. The majority of published work focuses on solubilizing drugs in water-soluble nanocarriers. This feature of water solubility is introduced to the branched nanocarrier scaffold mostly by covalently attaching biocompatible poly(ethylene glycol) (PEG), which serves as the outer shell of the nanocarrier [7].

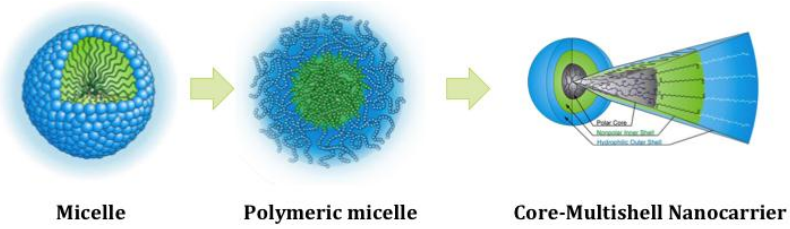

Figure 1. Evolution of nanocarriers, which has led to core-multishell nanocarriers. Adapted from PhD thesis M.Radowski and reprinted with permission from E. Fleige, B. Ziem, M. Grabolle, R. Haag, U. Resch-Genger, *Macromolecules* **2012**, 45, 9452–9459 [8]. © Copyright 2012 American Chemical Society.

Our motivation was to create a biodegradable nanocarrier for the encapsulation of hydrophobic drugs, such as dexamethasone. As previously reported poly(ε-caprolactone) is a well-suited material for the entrapment or encapsulation of dexamethasone, we chose this linear, potentially biodegradable polymer to be a building block for the work presented here, as shown in Figure 2 [9,10]. Combining our expertise in the synthesis of hyperbranched polymers and synthesizing universal nanocarriers for the transport of drugs, our aim was to synthesize a biodegradable polyester-based core-multishell nanocarrier (CMS) for the encapsulation of dexamethasone [5,6,11]. In this paper we will show the synthesis of a CMS based on a hyperbranched polyester (shown in Figure 2) that acts as a multifunctional initiator for the ring-opening polymerization of ε-caprolactone (ε-CL) in a grafting-from approach, which is terminated by a methoxy poly (ethylene glycol) (mPEG) chain to introduce the feature of water solubility. The synthesis comprises a surprising, and not often discussed, ring opening of glycidol by the terminal carboxylic acid groups of the core. This leads to the introduction of hydroxyl groups at the surface of the inner core and will be discussed based on detailed analysis. We studied how the polyester architecture can transport the drug dexamethasone and the degradation behavior of the CMS nanocarrier.

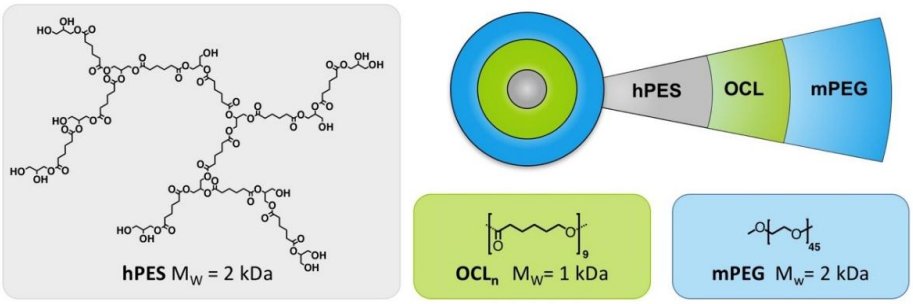

Figure 2. Building blocks and schematic representation of water-soluble CMS nanocarriers based on polyesters.

2. Materials and Methods

2.1. Materials

Adipic acid (Fluka Analytical, Steinheim, Germany), dibutyltin dilaurate (DBTL, Merck KGaA, Darmstadt, Germany), Tin(II) 2-ethylhexanoate ($Sn(Oct)_2$, 92.5%–100%), glycidol (Sigma Aldrich, Steinheim, Germany), 1-(3-dimethylaminopropyl)-3-ethylcarbodiimide hydrochloride (EDC, ⩾99%, Carl Roth GmbH + Co. KG, Karlsruhe, Germany), 4-(dimethylamino)-pyridin (4-DMAP, 99%, Acros Organics, Acros Organics, Beel, Belgium), poly (ethylene glycol) methyl ether (mPEG, M_n ~2000 g·mol^{-1}, Sigma Aldrich, Steinheim, Germany), and succinic anhydride (Acros Organics, Beel, Belgium) were used without further purification. ε-Caprolactone (ε-CL, 97%, Sigma Aldrich, Steinheim, Germany) was dried over ground CaH_2 (Sigma Aldrich) and distilled using cryogenic distillation prior to reaction. Solvents were purchased as HPLC grade and used without further purification. Anhydrous solvents were either purchased as ultra-dry solvents from Acros Organics, or taken from a MBraun MB SPS-800 solvent purification system. CAL B lipase, which is immobilzed on acrylic resin, was purchased from Sigma Aldrich. Dialysis was performed in benzoylated cellulose dialysis tubes from Sigma-Aldrich (width: 32 mm, MWCO = 1000 g/mol). Ultrafiltration was performed in a Millipore solvent-resistant stirred cell (47 mm diameter, 300 mL volume) with Millipore-regenerated cellulose membranes (47 mm diameter) and nitrogen pressure set between four to five bar. Reactions were performed under dry conditions using a Schlenk line, Schlenk flasks, and argon as the inert gas.

2.2. Characterization

2.2.1. Nuclear Magnetic Resonance Spectroscopy

^{1}H NMR and ^{13}C NMR spectra were recorded on a Bruker AMX 500 (Bruker Corporation, Billerica, MA, USA), Jeol ECP 500 (JEOL (Germany) GmbH, Freising, Germany), or a Bruker Avance 400 spectrometer (Bruker Corporation, Billerica, MA, USA) (at 295 K). Inverse-gated ^{13}C NMR and overnight measurements spectra were recorded on a Bruker Avance 500 spectrometer, or a Bruker Avance III 700 (Bruker Corporation, Billerica, MA, USA). Tetramethylsilane was used for internal calibration at 125 MHz with complete proton decoupling. Degree of branching was evaluated by inverse-gated ^{13}C NMR according to Frey *et al.*, as shown in Equation (A4) in the Appendix [12].

2.2.2. TAV and THV

Total acid values TAV and total hydroxyl values THV were determined based on ^{1}H NMR spectroscopy (see Appendix).

2.2.3. Gel Permeation Chromatography

GPC measurements in THF were performed with highly-dilute fractions eluting from a SEC system consisting of an Agilent 1100 solvent delivery system (Agilent Technologies, Santa Clara, CA, USA) with isopump, manual injector, and an Agilent 1100 differential refractometer. Three 30 cm columns were used (PLgel Mixed C, Agilent Technologies, Santa Clara, CA, USA, 5 µm particle size) to separate polymer samples. The mobile phase was THF and the flow rate was 1.0 mL· min^{-1}. The columns were held at room temperature. For each measurement, 100 µL of a sample of 15 or a 5 mg mL^{-1} solution was injected. WinGPC Unity from PSS was used to acquire data from the seven scattering angles (detectors) and the differential refractometer. Molecular weights and molecular-weight distributions were compared with poly(methyl methacrylate) (PMMA) standards (PSS, Mainz, Germany).

GPC in DMF data was obtained by measurements using a Shimadzu (Kyoto, Japan) liquid chromatography (LC) set up with degasser, pump, auto sampler, column oven, and differential refractometer. Three PolarSil columns (PSS Polymer Standards Service GmbH, Mainz, Germany; PolarSil 8 mm × 300 mm, 100, 1000, 3000 Å with 5 µm particle size) using DMF with 0.3% LiBr and 0.6% acetic acid as the mobile phase at a flow rate of 1 mL· min^{-1} were used to analyze polymer samples. The columns were operated at 40 °C with the RI detector set to the same temperature. The calibration was performed by using polystyrene standard (PSS, Mainz, Germany). Samples were measured at a concentration of 10 mg· mL^{-1} injecting 100 µL. LC solution software from Shimadzu was used for data acquirement and interpretation.

2.2.4. Dynamic Light Scattering

DLS experiments were performed using a Malvern Zetasizer Nano instrument (Malvern Instruments Ltd, Worcestershire, UK) equipped with a He-Ne laser (633 nm) using backscattering mode (detector angle 173°). The CMS nanocarriers were dissolved in dH_2O, mixed by a Vortex shaker for 2 min, followed by filtration using a 0.45 µm RC syringe filter. 100 µL of the filtered solution was added to a disposable Plastibrand®micro cuvette (Brand GmbH + Co KG, Wertheim, Germany) with a round aperture. The autocorrelation functions of the backscattered light fluctuation were analyzed using Zetasizer DLS software from Malvern Instruments Ltd (Worcestershire, UK) to determine the size distribution by intensity and volume. The measurements were performed at 25 °C, equilibrating the system on this temperature for 120 s. Mean diameter values were obtained from four different runs.

2.2.5. High Pressure Liquid Chromatography

HPLC measurements for the analysis of dexamethasone content was performed on a Knauer Smartline-HPLC system with an internal UV absorption detector (λ = 254 nm), equipped with a Gemini RP C18 column (Phenomenix, 250 nm × 4.6 mm, particle size: 5 µm) and run with an acetonitrile-water (40:60) mixture as the mobile phase at a flow rate of 1.0 mL· min^{-1} under isocratic regime. The data were analyzed with Chromgate software (Knauer, Berlin, Germany). A calibration curve of dexamethasone was obtained by measuring dexamethasone in an acetonitrile-water (40:60) mixture in the concentration range of 0.004–2 mg· mL^{-1}.

2.2.6. Infrared Spectroscopy

IR-spectra were obtained from a Nicolet Avatar 320 FT-IR spectrometer (Thermo Fisher Scientific Inc., Waltham, MA, USA) operating from 4000–400 cm^{-1}, equipped with a Smart Orbit ATR accessory with a diamond crystal.

2.3. Synthesis

2.3.1. Synthesis of Hyperbranched Polyester hPES **1**

At room temperature, adipic acid (39.9 g, 273 mmol, 1.2 eq) was charged into a three-neck glass vertical reactor, equipped with a mechanical stirrer and a Liebig condenser. After adding pre-dried glycerol (20.9 g, 228 mmol), the bulk monomer mixture was heated to 150 °C. Under stirring at 150 rpm, a 0.6 mL of a stock solution of DBTL in toluene (100 ppm) was added to the molten monomers using a syringe. The reaction temperature was increased to 160 °C. After 1 h at 160 °C, the formed volatiles were removed by cryo distillation and collected in a round-bottom flask. The removal of volatiles was repeated every hour. With proceeding reaction time, the frequency of volatile removal was increased to once per every 10 min. Conversion of the reaction was controlled by determination of the ratio of unreacted to total amount of acid groups, using ^{1}H NMR spectroscopy. When conversion almost reached the maximum conversion P_A as determined by the Flory Equation, the reaction was stopped by complete removal of the volatiles and cooling the reactor to room temperature. The viscous product hPES **1** was obtained without any further purification as a light yellow viscous solid and dissolved in THF for easier handling. Product was characterized via ^{1}H NMR, IG ^{13}C NMR, and GPC in THF (see Table A1 and Figure A6).

2.3.2. Synthesis of Polyesterol hPES-OH **2**

30 mL of a solution of hyperbranched polyester hPES **1** in THF (c = 347 mg· mL^{-1}, 10.41 g, 19 mmol COOH) was charged into a Schlenk flask. Residual catalyst DBTL (1.3 mg, 3.9 µmol) from the original product hPES **1** was used to catalyze the reaction; no further catalyst was added. After solubilization in 10 mL DMF under stirring at RT, the flask was heated to 85 °C. THF was removed from the mixture under controlled reduced pressure using cryo distillation. Within the limits of ^{1}H–NMR, no residual THF was detected. After that, the mixture was heated to 110 °C. Glycidol (1.25 mL, 1.388 g, 19 mmol, 1 eq) was added dropwise to the stirring yellow solution during a time period of 10 min using a syringe. The reaction mixture was stirred at 110 °C for 120 min, afterwards at RT overnight. Due to the incompleteness of the reaction, the reaction was heated to 110 °C again and more glycidol (0.1 mL, 20 mmol in total) was added dropwise to the stirring reaction mixture. The reaction was stirred at 110 °C for 5.5 h and afterwards allowed to cool down to RT. The viscous product was obtained without further purification and stored in DMF. Product was characterized via ^{1}H NMR, IG ^{13}C NMR, and GPC in DMF (see Figure A7).

2.3.3. Synthesis of Linear Di-Block Copolymer hPES-OCL$_9$-OH **3**

In a Schlenk flask pre-dried macroinitiator hPES-OH **2** (2 g, 10.6 mmol OH) was dissolved in freshly-distilled ε-caprolactone (6.18 g, 54 mmol) at 60 °C and two drops of Sn(Oct)$_2$ were added to the stirring mixture, followed by an increase of the temperature to 125 °C. The bulk mixture was stirred at 125 °C for 18 h. Purification was performed by dissolving the crude reaction mixture in DCM in high dilution and precipitation in a high excess of ice-cold MeOH under vigorous stirring. The dispersion was separated from the formed gel, solvent was removed under reduced pressure, and the received solid was redissolved in DCM in high dilution. Another precipitation was performed by adding the DCM solution drop-wise into vigorously stirred ice-cold diethyl ether. The mixture was separated by centrifugation at 4000 min^{-1} for 1 min, and the supernatant was collected. After drying the separated supernatant under reduced pressure, the received solid was once again purified using dialysis in DCM (benzoylated RC membrane, MWCO = 1000 g/mol, 7 h) for removal of Sn(Oct)$_2$ and traces of ε-caprolactone. A white wax-like solid product was obtained after removal of solvent under reduced pressure (2.69 g, yield: 33%). The product was characterized via ^{1}H NMR, IG ^{13}C NMR, and GPC in DMF (see Figure A8).

2.3.4. Functionalization of mPEG-OH

To a solution of pre-dried mPEG (4.786 g, 2.5 mmol) in a mixture of 10% anhydrous DMF in anhydrous THF (28 mL) in a 50 mL Schlenk flask, 4-DMAP (0.44 g, 3.8 mmol, 1.5 eq), TEA (0.5 mL, 3.8 mmol, 1.5 eq), and succinic anhydride (1.2 g, 12.5 mmol, 5 eq) were added under stirring at RT. After stirring at RT for three days, unreacted precipitated starting material was removed from the solution and the solution was dried under reduced pressure. The crude product was purified by precipitation from DCM solution into ice-cold, 10-fold excess of Et$_2$O. The formed precipitate was filtered off using a glass filter (P4), redissolved in DCM, and precipitated once more following the same procedure. The collected precipitate was dried under high vacuum and 3.5 g (1.67 mmol, yield: 70%) of pure product were obtained. The product was characterized via ^{1}H NMR, IG ^{13}C NMR, and GPC in DMF.

2.3.5. Synthesis of Core Multishell Nanocarrier hPES-OCL$_9$-PEG-OMe **4**

In a dried 25 mL Schlenk flask, solid mPEG-COOH (1.110 g, 0.529 mmol, 1.1 eq) was added at RT to a stirring solution of hPES-OCL$_9$-OH **3** (304 mg, 0.48 mmol OH) in 6 mL anhydrous DMF. After the addition of 4-DMAP (0.016 g, 0.106 mmol, 20 mol %), EDCl (0.110 g, 0.574 mmol, 1.1 eq) was added at 0 °C. The reaction mixture was stirred for 10 min at 0 °C, and then allowed to reach RT by removing the ice bath. After 20 h of stirring at RT, the crude product was purified via extensive ultrafiltration (DMF, MWCO = 10,000 g/mol), followed by repeated fractionation. For this purpose, the impure product was dissolved in DCM and yielded a clear solution. Hexane was added to the clear solution at RT until cloudiness appeared. The cloudy dispersion was heated to obtain a clear solution, followed by the addition of hexane to obtain a dispersion. The warm solution was allowed to reach RT and centrifuged (1 min, 3900 min^{-1}) to separate into a stable dispersion and sediment. The dispersion was dried and refractionated following the above-described procedure. The progress of purification was monitored using GPC in DMF. After six cycles of refractionation and removal of solvent under reduced pressure, followed by drying at high vacuum, a white solid product was obtained (0.116 g, yield: 12%). The product was characterized via ^{1}H NMR, IG ^{13}C NMR, and GPC in DMF (see Figure A8).

2.3.6. Encapsulation of Dexamethasone in CMS Nanocarrier

Encapsulation of dexamethasone was performed using the film method uptake [8], in which dexamethasone solubilized in ethanol was dried under reduced pressure at 40 °C, which created a dry film at the bottom of the vial. The dry film was subsequently dissolved in a double amount of CMS nanocarrier in dH$_2$O at a concentration of 10 mg· mL^{-1}. The mixture was stirred for 22 h at 1200 min^{-1}

and RT and, afterwards, filtered using a 0.45 µm PTFE syringe filter to remove excess dexamethasone. The size of the loaded CMS nanocarriers was determined using a DLS measurement of the aqueous solutions after filtration. The determination of dexamethasone content via HPLC was performed either by aqueous solution after filtration, to which acetonitrile (ACN/dH_20 4:6) was added prior to measurement, or the samples were first freeze-dried and then redissolved in an acetonitrile-water (4:6) mixture before measurement. The amount of dexamethasone in the CMS solution was determined by HPLC measurement relative to a dexamethasone calibration curve. As dexamethasone has some solubility in water, a blank sample was prepared to determine the natural solubility of dexamethasone in water. Therefore, a solution of dexamethasone in water was prepared in a procedure analog to the film method uptake. The solubility of the drug obtained from this blank control was subtracted from the nanocarrier results in order to obtain the effective loading. The values obtained from HPLC measurements of dexamethasone-loaded CMS were inserted in the following equation, which led to the loading capacity (LC):

$$\text{Loading capacity } (LC) = \frac{n\,(\text{encapsulated dexamethasone})}{n\,(\text{nanocarrier})} \times 100 \quad (1)$$

2.3.7. Degradation of CMS Nanocarriers

Acidic degradation of CMS nanocarriers was studied by incubation of 2 mL of a CMS nanocarrier solution (10 mg· mL^{-1}) in acetate buffer (pH 5.0) at 32 °C and constant stirring at 500 rpm. At defined time points, samples of 100 µL were withdrawn and freeze-dried in 1.5 mL Eppendorf tubes. The obtained lyophilisates were dissolved in DMSO-d_6. Insoluble salts were separated by centrifugation at 4000 U· min^{-1} for 1 min, and the supernatant was analyzed by ^{1}H NMR spectroscopy. For studying enzymatic degradation, samples were prepared for each time point as follows: 0.5 mL of a CMS nanocarrier solution (5 mg· mL^{-1}) in 0.1 M PBS buffer (pH 7.4) was prepared in a 1.5 mL Eppendorf tube, and 200 wt % with respect to the polymer of immobilized CAL B was added, followed by 5 µL of n-butanol. The samples were incubated at 32 °C in an incubator shaker (New Brunswick Scientific Co. Int., Enfield, CT, USA). Samples were withdrawn at defined time points, frozen with liquid nitrogen, and kept in a freezer. After all the samples were obtained, the samples were allowed to thaw, and the immobilized enzymes were separated from the aqueous solution by centrifugation at 4000 U· min^{-1} for 1 min. The supernatant was transferred to a 1.5 mL Eppendorf tube, and combined with 0.5 mL dH_2O used for washing the separated resin. The resin-free aqueous solution was freeze-dried, and the obtained lyophilisate was dissolved in DMSO-d_6. After the insoluble salts were separated by centrifugation (4000 U· min^{-1}, 1 min), the supernatant was analyzed via ^{1}H NMR spectroscopy. As a control for both experiments, degradation of CMS nanocarriers in 0.1 M PBS buffer (pH 7.4) was performed in the absence of enzyme by incubation of 1 mL of a CMS nanocarrier solution (10 mg· mL^{-1}) in 0.1 M PBS buffer (pH 7.4) at 32 °C and constant stirring at 500 rpm. At defined time points, samples of 100 µL were withdrawn and freeze-dried in 1.5 mL Eppendorf tubes. The obtained lyophilisates were dissolved in DMSO-d_6. Insoluble salts were separated by centrifugation at 4000 U· min^{-1} for 1 min, and the supernatant was analyzed by ^{1}H NMR spectroscopy.

3. Results and Discussion

3.1. Synthesis of Hyperbranched Polyester

Based on previous work of Stumbé *et al.*, hyperbranched polyester hPES **1** was synthesized, as shown in Scheme 1, by polycondensation of a 1.2:1 molar ratio of adipic acid and glycerol at 160 °C and catalyzation with dibutyltin dilaurate [13]. NMR spectroscopy, which is the key for evaluating the hyperbranched polymer's structure, was used during the polymerization process to control the polymerization conversion, and to provide information about the extent of branching. The first step to control the polymerization via NMR was to predict the theoretical polymerization conversion P_A

before reaching the gel point. This value could be calculated based on Flory's theory of gelation and led to a P_A value of 0.79 for a molar ratio of 1.2:1 (diacid:triol) [14].

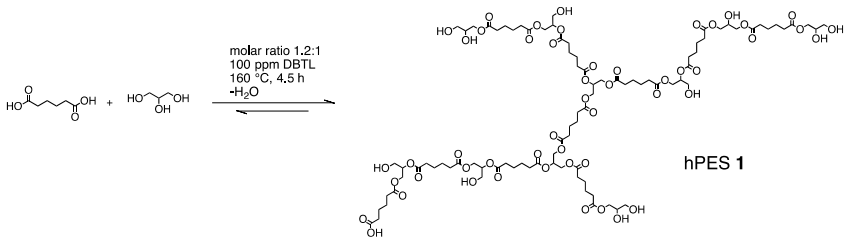

Scheme 1. Synthesis of hyperbranched polyester hPES **1** used for the synthesis of CMS nanocarriers as a branching scaffold.

The conversion P was monitored by ^{1}H NMR spectroscopy based on the conversion of acid to ester groups, *i.e.*, the ratio between the integral of the methylene next to the acid at 2.2 ppm and the integral of the methylene next to the ester at 2.3 ppm. The calculated P value of 0.83 is slightly higher than the P_A value of 0.79. The reason might be the underestimation of the reactivity difference of primary and secondary alcohol functional groups of glycerol in Flory's theory. Information about the degree of branching is extracted from inverse-gated ^{13}C NMR (IG ^{13}C NMR). The degree of branching (DB) of a hyperbranched polymer contributes the most to an understanding of the polymers' architecture, because it reflects the perfection of the branching, which is essential for evaluating the structural similarity to dendritic systems. DB values range from 0 for linear systems to 1 for perfectly-branched dendrimers [15]. In hPES **1**, glycerol is the trifunctional branching unit (B_3) and, thus, mainly responsible for the extent of branching. If the trifunctional branching unit has equal reactivities at every reactive end group, full branching is achieved at every step. In reality, the primary alcohol groups of glycerol are reported to have high reactivity, while the secondary alcohol shows reduced reactivity [16]. This difference in reactivity leads to the formation of different types of distinguishable glycerol units. Glycerol can react in three modes: at one primary and one secondary alcohol group forming a $\mathbf{L_{1,2}}$ unit, at both primary alcohol groups forming a $\mathbf{L_{1,3}}$ unit, and it can react with all three functional groups, which leads to a branching unit **D**. Terminal glycerol units can either have one free primary and one free secondary alcohol group that produce a $\mathbf{T_{1,2}}$ unit or two free primary alcohol groups, which form $\mathbf{T_{1,3}}$, as shown in Figure 3. According to previously published detailed analysis, and as supported by HMQC-NMR spectroscopy, the signals of the five types of glycerol units obtained by IG ^{13}C NMR spectroscopy can be assigned, leading to the DB value as defined by Frey *et al.* [12,13,17]. Based on the spectrum shown in Figure 3, a DB value of 0.52 was calculated for product hPES **1**. Values for total acid and total hydroxyl values were obtained by ^{1}H NMR spectra analysis. The majority of free functional groups are represented by free hydroxyl groups with a percentage of 56%, compared to the overall amount of free functional groups. Molecular weights were determined by GPC measurements in THF and showed two peaks with values of 3.7×10^7 and 1600 g·mol^{-1} in M_w.

*3.2. Modification of hPES **1** to Uniform Diol Endgroups*

In order to obtain a monofunctional branched polyester scaffold, hPES **1** was modified with glycidol via ROP, which yielded hPES-OH **2**. The benefit of using glycidol is that the risk of transesterification during the process is omitted and the number of hydroxyl groups increases rapidly, as one ring-opening process yields two hydroxyl groups in the first ring opening step. The new approach in this synthesis is that glycidol reacts with carboxylic acids, instead of hydroxyl groups. Reactions between carboxylic acids and glycidol have not been reported in literature yet. Nevertheless, there are some reports of comparable reactions with epoxide moieties and carboxylic

acids, which took place under metal-mediated catalysis. The reported catalysts for the ring-opening reactions of epoxides initiated by carboxylic acids are generally limited to Lewis acid catalysts, such as $FeCl_3$, tetrabutylammonium chloride and bromide, and $Ce(OTf)_4$ [18–21]. In the case of glycidol, the combination of the high ring strain of the epoxide and the polarity of the carbon-oxygen bonds makes the ring prone to nucleophilic attack. The ring-opening reactions can be catalyzed under acidic or basic conditions, but can also take place at high temperatures initiated by any weak nucleophile. The latter case is called thermally-induced, ring-opening reaction of glycidol [22]. Based on the above-mentioned literature, we hypothesized that DBTL as Lewis acid mediates a ring-opening of glycidol initiated by carboxylic acid of hyperbranched polyesters. Hyperbranched polyester hPES **1** with an total acid value of 1.8 mmol carboxylic acid groups per gram polyester was modified with equimolar amounts of glycidol per hydroxyl group of hPES **1**, aiming at a modification of one glycidol per carboxylic acid. We chose the polar aprotic solvent DMF as solvent, since preliminary results showed that it performed best for this type of ring-opening reaction. The reactions were performed at a bath temperature of 110 °C for two hours and afterwards at room temperature overnight. The reaction progress was monitored by ^{1}H NMR, which showed the disappearance of the methylene signal next to the free carboxylic acid as well as the proton signal of terminating carboxylic acid groups. We paid special attention to the expected changes of several structural units as well as the possibility of the shown side reaction, as shown in Scheme 2.

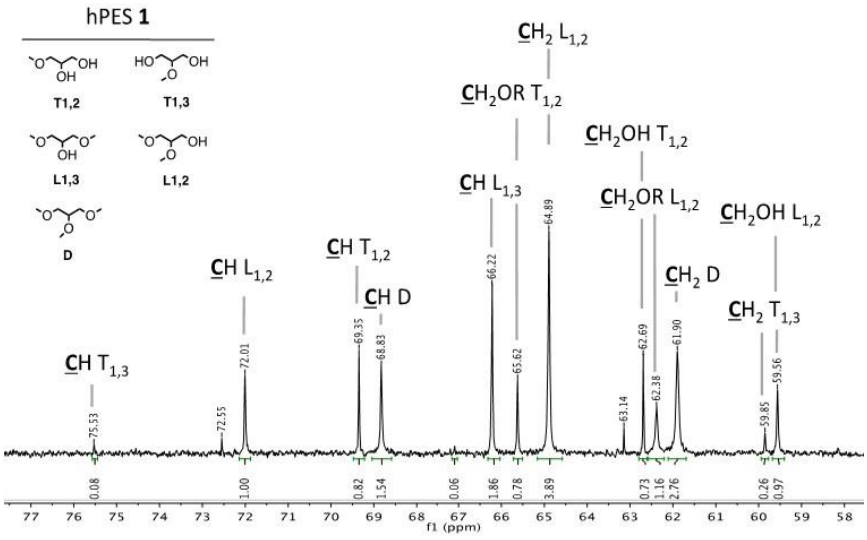

Figure 3. Extract of an IG ^{13}C NMR spectrum of hPES-OH **2** that is crucial for evaluation of DB and shows the assignment of methine ***C***H and methylene ***C***H2 signals of various glycerol units.

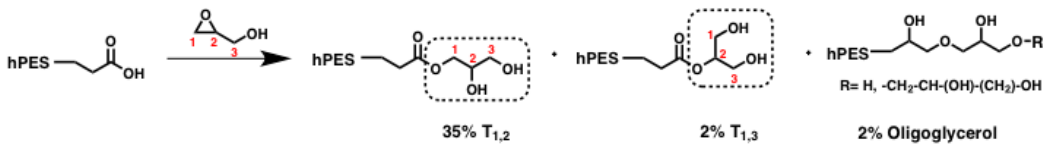

Scheme 2. A simplified scheme of polyester modification by ring-opening reaction of glycidol; crucial units for NMR evaluation are highlighted in boxes; %: abundance of species relative to abundance of all glycidol units.

^{1}H and inverse-gated ^{13}C NMR spectra were measured and checked for a change in methine and methylene signals of the various glycerol units. In summary, the amount of esterified carboxylic acid

units increased by a factor of 2.5 compared to the esterified carboxylic acid units before the modification, while full modification of carboxylic acids could not be achieved. The degree of functionalization of carboxylic acids is D_f (COOH) = 0.83. The ring-opening of glycidol did not only take place at C1 carbon atom, which led to a new $T_{1,2}$ unit, but also at the C2 carbon atom, which formed $T_{1,3}$ units. Formation of oligoglycerols only took place to a low extent.

3.3. ε-Caprolactone Polymerization Using hPES-OH **2** in Grafting from

Having hyperbranched polyester hPES-OH **2** at hand, there were two options to synthesize a core-multishell nanocarrier: either by synthesizing the amphiphilic double-shell and attaching it via a grafting-to approach, or using the hydroxyl groups of hPES-OH **2** as initiators for a polymerization, aiming at the grafting-from approach. As previous trials with grafting to approaches led to low functionalization of the hyperbranched template, and removal of unreacted amphiphilic double-shell building blocks turned out to be quite tedious, we decided to use the grafting-from approach. As already discussed in other publications, multiple hydroxyl groups on one branched scaffold allow the polymerization to simultaneously take place at ideally all accessible hydroxyl groups [23,24]. This concept of a so-called macroinitiator was used in our herein-presented work to polymerize ε-caprolactone in a tin-catalyzed ring opening polymerization. We aimed for an oligocaprolactone with five repeating units per free OH groups, but as calculated based on ^{1}H NMR spectroscopy we, instead, obtained nine repeating units (see Figure 4). The number of repeating units was calculated based on a comparison of methylene CH_2^E, at 3.98 ppm and methylene neighboring terminal alcohol groups $CH_2^{E\Omega}$ at 3.36 ppm, which was obtained by ^{1}H NMR spectroscopy. In order to investigate whether ring opening occurred at both species of hydroxyl groups of the core's glycerol units, namely, primary and secondary, we integrated the individual methine CH signals via IG ^{13}C NMR and compared their abundance as shown in Table A3. We could show that polymerization occurred at both primary and secondary hydroxyl groups, and the degree of functionalization was D_f (OH) = 0.67 (for NMR spectra, see Figure A9).

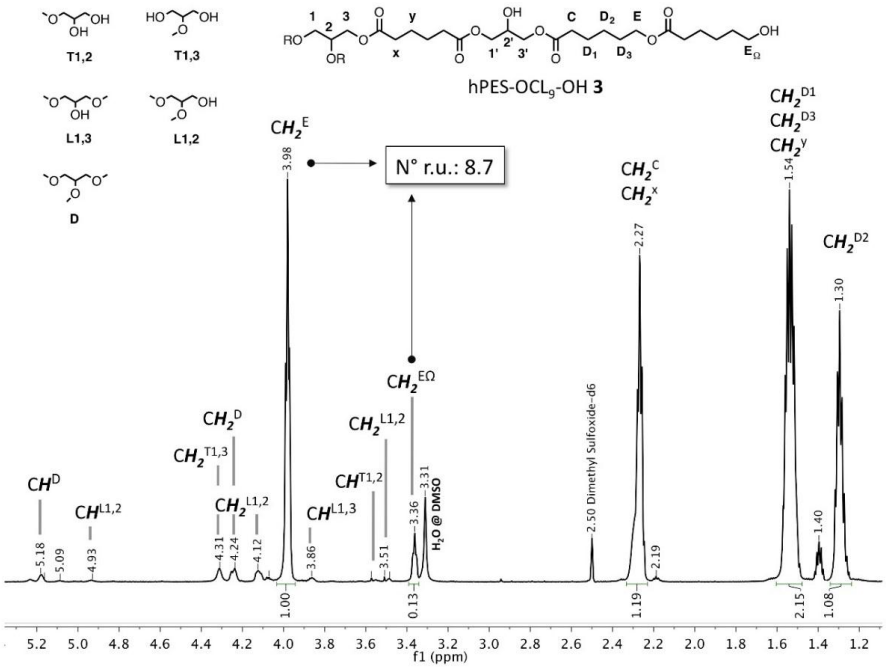

Figure 4. ^{1}H NMR of hPES-OCL$_9$-OH **3** showing peak assignment and crucial methylene signals for determination of number of repeating units of caprolactone.

3.4. Synthesis of CMS Nanocarrier

The attachment of succinic acid anhydride-modified mPEG outer shell was accomplished by ester bond formation using modified Steglich type conditions, as shown in Scheme 3 [25,26]. We used the water soluble carbodiimide coupling reagent EDC and catalytic amounts of 4-(dimethylamino)-pyridin (4-DMAP) in anhydrous DMF for the ester bond formation, which was followed by a multistep purification approach consisting of extraction and ultrafiltration to remove starting material and low-functionalized CMS nanocarriers. We used ultrafiltration membranes with a molecular weight cutoff of 10 kDa, which yielded a product with a quite narrow molecular weight distribution of M_w/M_n = 1.1. The decreasing PDI from the precursor hPES-OH **2** and hPES-OCL9-OH **3** to the final product hPES-OCL$_9$-mPEG 4 reflects the effort put into the purification procedure. While hPES-OH **2** was not purified, hPES-OCL$_9$-OH **3** was purified by precipitation and dialysis, removing products with very high and very low functionalization. The impact of purification on the PDI can be observed especially in the final product hPES-OCL$_9$-mPEG **4**, where a combination of ultrafiltration and precipitation was performed. As described in Materials and Methods, the ultrafiltration desks had a molecular weight cutoff of 10 kDa and, hence, allowed the removal of low molecular weight compounds. To further narrow down the molecular weight distribution, fractionation was performed. This strategy consisting of precipitation and dissolution including heat-chill cycles lead to the removal of high molecular weight side-products. The initial PDI of 1.2 obtained after ultrafiltration was therefore decreased to 1.1. In addition to the impact of the purification, it is known and has been reported in the literature that the PDI of CMS nanocarriers is often lower than the PDI of the core or core-single shell precursors [24,27]. Owing to both the multistep synthesis and the extensive purification procedures, the overall yield was 12%. ^{1}H NMR measurements of the purified product **4** were analyzed with respect to increasing the ester neighboring methylene signals, which revealed an esterification efficacy of oligocaprolactone's hydroxyl groups of D_f (CL) = 0.7. Furthermore, we could show that 55% of present mPEG chains were attached to terminal caprolactone and 45% of mPEG chains reacted with internal glycerol units. The M_n of the final CMS nanocarrier as calculated by NMR of 30 kDa is similar to the findings from GPC measurement, which were obtained by comparison to linear polymer standards. Table 1 summarizes the characteristics of the CMS nanocarrier and its building blocks. The degree of branching increased from 0.41 (hPES-OCL-OH **3**) to 0.52, which matches well the observation that mPEG-COOH reacted with the internal glycerol hydroxyl groups. The size of the CMS nanocarriers in dH$_2$O was determined by DLS measurements and showed a hydrodynamic diameter of 28 nm in the volume distribution. The size indicates aggregation behavior of the CMS nanocarriers, which has been observed before [8,28–30].

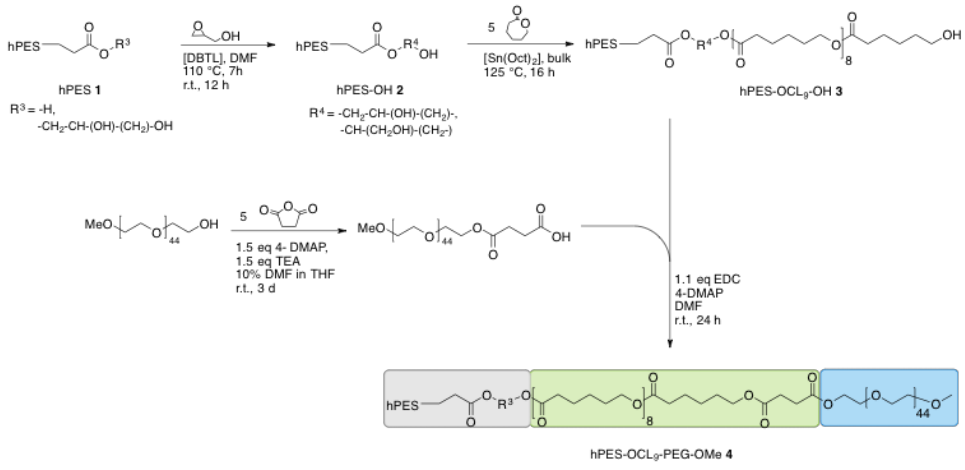

Scheme 3. Synthesis of CMS nanocarrier and its building blocks.

Table 1. Comparison of physical characteristics of CMS with its macroinitiator and intermediate.

Compound	D_f [a]	DB [a]	M_n [b]	M_w/M_n [b]
hPES-OH **2**	0.83	0.41	900 [b]	2.7 [b]
hPES-OCL$_9$-OH **3**	0.67	0.74 [c]	5,150 [d]	1.7 [d]
hPES-OCL$_9$-mPEG **4**	0.7 [e]	0.52	27,900 [d]	1.1 [d]

[a] determined via NMR; [b] GPC in THF, Pullulan standards; [c] based on overnight ^{13}C NMR measurements; [d] GPC in DMF, PS standards; and [e] D_f of terminal caprolactone hydroxyl groups.

3.5. Encapsulation of Dexamethasone in CMS Nanocarriers

In order to elaborate whether polyester-based CMS nanocarriers are suitable for hydrophobic drugs, synthesized CMS nanocarriers were tested for the encapsulation of dexamethasone. Dexamethasone is an approved glucocorticoid drug used for its anti-inflammatory and immune suppressant effect. Due to its hydrophobic nature, it has a low water solubility of c = 0.08 mg· mL^{-1} that limits its application. Therefore, solubilizing dexamethasone in water-soluble nanocarriers is of great interest and might increase its significance as a used drug. The encapsulation of dexamethasone is performed according to the film-method uptake. For example, a dry film of 50 wt % dexamethasone is dissolved in a stock solution of CMS in dH_2O and the dispersion is stirred for 22 h at 1200 rpm, which is followed by filtration using a syringe filter. The filtration process removes big crystals of dexamethasone, while dexamethasone-loaded CMS as well as the water-soluble fraction of dexamethasone pass the filter. Analysis by HPLC combined with an internal UV absorption detector was used to determine the concentration of dexamethasone. The overall concentration of dexamethasone of the CMS nanocarrier sample is c = 0.182 mg· mL^{-1}. This value roughly correlates to one molecule of encapsulated dexamethasone per CMS nanocarrier after deducting the drug's natural solubility.

3.6. Acidic and Enzymatic Degradation of CMS Nanocarriers

In order to mimic the conditions in skin, degradation of CMS nanocarriers was investigated in both acidic and enzymatic environments at 32 °C. For creating an acidic environment, CMS nanocarriers were solubilized in an acetic acid buffer of pH 5.0, while the enzymatic degradation study was performed using non-specific lipase expressed from Candida Antarctica (CAL B) and immobilized on acrylic resin [31,32]. Both studies were performed for five days and sampled at defined time points. A control experiment at pH 7.4 in the absence of enzyme was performed simultaneously and showed no degradation. The hydrolysis of ester bonds leading to formation of carboxylic acids was monitored by ^{1}H NMR spectroscopy in DMSO-d$_6$. While the signal intensity of methylene-neighboring ester bonds at 2.3 ppm decreased, the intensity of methylene neighboring carboxylic acids at 2.2 ppm increased, as depicted in Figure 5. After one day of incubation, a new peak at 2.24 ppm appeared, which is the signal of cleaved succinic acid. Even though the integral of this signal does not allow for isolated integration of the peak at 2.3 ppm, the disappearance of the ester-neighboring methylene is clearly visible. Table 2 gives the values of the individual integrals for each time point, as well as the percentage of cleaved ester bonds. After five days of enzymatic degradation, nearly all ester bonds are degraded (for full spectrum, please see Figure A10). In contrast to the successful enzymatic degradation, no degradation was observed in acidic environment at pH 5.0, even after seven days.

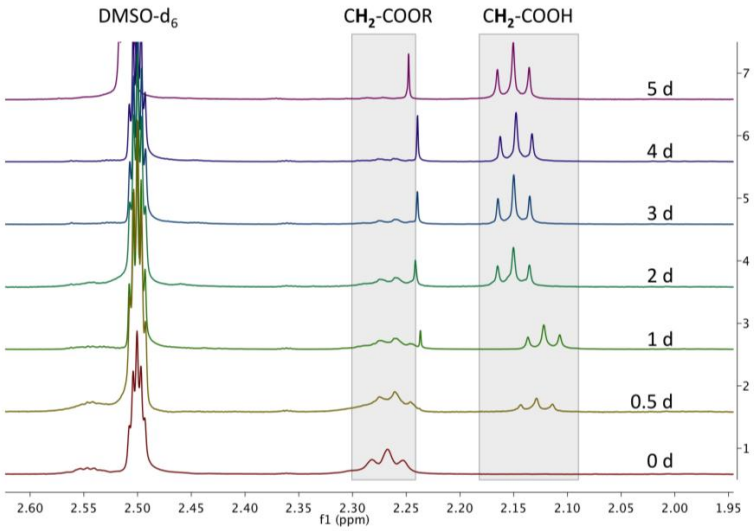

Figure 5. Overlay of magnified ^{1}H NMR spectra in DMSO-d_6 of CMS nanocarriers after incubation with CAL B at 32 °C at various time points during a five-day study; simultaneous decrease of –C**H$_2$**–COOR at 2.27 ppm and increase of –C**H$_2$**–COOH at 2.15 ppm.

Table 2. Degree of degradation of CMS nanocarriers by incubation with CAL B.

Incubation time (Days)	Ratio C*H*$_2$–COOR: C*H*$_2$–COOH	Degree of degradation (%)
0	1:0	0
0.5	1:0.3	24
1	1:0.4	30
2	1:4.3	81
3	1:5.2	84
4	1:6	86
5	1:22	96

4. Conclusions

A hyperbranched polyester was synthesized in a bulk polycondensation based on adipic acid and glycerol, catalyzed by the tin catalyst DBTL. The obtained branched scaffold with a degree of branching of 0.41 and a rather low molecular weight of M_n = 900 Da was modified with glycidol in a ring-opening reaction in the presence of the tin catalyst. The obtained scaffold was further used as a macroinitiator for the ring-opening polymerization of ε-caprolactone. Based on ^{13}C NMR spectroscopy, we showed that the polymerization of ε-caprolactone was initiated by both primary and secondary hydroxyl groups of mainly terminal glycerol units, which led to oligocaprolactone chains with about nine repeating units and an overall degree of functionalization of 0.67. After functionalization of the obtained scaffold with mPEG–COOH linear chains via ester bond formation using modified Steglich type conditions followed by purification, we obtained CMS nanocarriers with a M_n of 28,000 Da and a low dispersity of 1.1. While 60% of all attached mPEG chains were bound to caprolactone chains ends, another 40% were attached to internal glycerol hydroxyl groups. The obtained water-soluble CMS nanocarrier was used for the encapsulation of the hydrophobic drug dexamethasone using the film method uptake and resulted in a transport capacity of one molecule dexamethasone per CMS nanocarrier. Furthermore, we performed degradation studies showing almost full degradation within five days at 32 °C, mediated by lipase, while degradation in acidic environment at pH 5.0 within seven days at 32 °C was not observed.

Acknowledgments: This work was supported by the SFB 1112 (Sonderforschungsbereich 1112—Nanocarrier). We want to thank Andreas Schäfer for advice in NMR spectroscopy, Florian Paulus and Cathleen Schlesener for GPC measurement and Marleen Selent for HPLC analysis. Additionally we want to thank Bala Naga Satyanarayana Thota for helpful scientific discussion.

Author Contributions: Karolina A. Walker, Jean-François Stumbé and Rainer Haag conceived and designed the experiments; Karolina A. Walker performed the experiments; Karolina A. Walker analyzed the data; Jean-François Stumbé contributed reagents and analysis tools; Karolina A. Walker wrote the paper.

Conflicts of Interest: The authors declare no conflict of interest.

Abbreviations

The following abbreviations are used in this manuscript:

NMR	nuclear magnetic resonance
PEG	poly(ethylene glycol)
CMS	core-multishell nanocarrier
ε-CL	ε-caprolactone
mPEG	methoxy poly(ethylene glycol)
$Sn(Oct)_2$	Tin(II) 2-ethylhexanoate
DBTL	dibutyltin dilaurate
EDC	1-(3-dimethylaminopropyl)-3-ethylcarbodiimide hydrochloride
4-DMAP	4-(dimethylamino)-pyridin
MWCO	molecular weight cut-off
TAV	total acid value
THV	total hydroxyl value
GPC	gel permeation chromatography
SEC	size-exclusion chromatography
PMMA	poly(methyl methacrylate)
HPLC	high pressure liquid chromatography
hPES	hyperbranched poly (ester)
eq.	equivalents
IG	inverse-gated
DCM	dichloromethane
MeOH	methanol
TEA	triethylamine
Et_2O	diethyl ether
DMF	dimethylformamide
dH_2O	deionized water
ACN	acetonitrile
LC	loading capacity
P_A	conversion of polymerization at gel point
DB	degree of branching
HMQC	Heteronuclear multiple-quantum correlation spectroscopy
ROP	ring opening polymerization
PCL	poly(ε-caprolactone)
r.u.	repeating units
rpm	revolutions per minute
DMSO	dimethyl sulfoxide
M_w	weight average molecular weight
M_n	number average molecular weight

Appendix

A.1. Synthesis of Hyperbranched Polyester (hPES **1***)*

At room temperature, adipic acid (39.9 g, 273 mmol, 1.2 eq) was charged into a three-neck glass vertical reactor, equipped with a mechanical stirrer and a Liebig condenser. After adding pre-dried glycerol (20.9 g, 228 mmol), the bulk monomer mixture was heated to 150 °C. Under stirring at 150 rpm, a 0.6 mL of a stock solution of DBTL in toluene (100 ppm) was added to the molten monomers using a syringe. The reaction temperature was increased to 160 °C. After 1 h at 160 °C, the formed volatiles

were removed by cryo-distillation and collected in a round-bottom flask. The removal of volatiles was repeated every hour. With proceeding reaction time, the frequency of volatile removal was increased to once per every 10 min. Conversion of the reaction was controlled by determining the ratio of the unreacted acid groups to the total amount of acid groups, using ^{1}H NMR spectroscopy. When the conversion almost reached the maximum conversion P_A. as determined by Flory Equation, the reaction was stopped by completely removing the volatiles and cooling the reactor to RT. The viscous product hPES **1** was obtained without any further purification as a light yellow, viscous solid and dissolved in THF for easier handling.

^{1}H NMR (400 MHz, DMSO-d$_6$): δ = 12.00 (s, 1H, R–COO**H**), 5.18 (m, 1H, C**H**^{D}), 4.94 (m, 1H, C**H**^{L1,2}), 4.72 (m, 1H, C**H**^{T1,3}), 4.26–4.23, 4.14–4.12 (2 m, 4H, C**H$_2$**^{D}), 4.23–4.07 (m, 2H, C**H$_2$**^{L1,2}), 4.03, 3.89 (2 m, 4H, C**H$_2$**^{T1,3}), 3.98 (m, 4H, C**H$_2$**^{L1,3}), 3.86 (m, 1H, C**H**^{L1,3}), 3.63 (q, 1H, C**H**^{T1,2}), 3.49–3.40 (m, 4H, C**H$_2$**^{T1,3}), 3.49–3.48 (m, 2H, C**H$_2$**^{L1,2}), 3.55–3.26 (m, 2H, C**H$_2$**^{T1,2}), 2.30 (m, 2H, –C**H$_2$**–COOR), 2.20 (m, 2H, –C**H$_2$**–COOH), 1.52 (m, 4H, ROOC–CH$_2$–(C**H$_2$**)$_2$–CH$_2$–COOR) ppm. Abbreviations in accordance with Figure A1.

IG ^{13}C NMR (400 MHz, DMSO-d$_6$): δ = 174.42–174.34 (m, 1H, HOO**C**–(CH$_2$)$_4$–COO–CH$_2$–(CHOR)–(CH$_2$OR)), 172.88–172.08 (m, HOO**C**–(CH$_2$)$_4$–COO–CH$_2$–(CHOH)–(CH$_2$OR), HOOC–(CH$_2$)$_4$–**C**OO–CH$_2$–(CHOH)–(CH$_2$OR), HOOC–(CH$_2$)$_4$–**C**OO–CH$_2$–(CHOR)–(CH$_2$OR), (CH$_2$OR)–(CHOR)–CH$_2$–OO**C**–(CH$_2$)$_4$–**C**OO–CH$_2$–(CHOR)–(CH$_2$OR)), 75.53 (s, 1 C, **C**H ^{T1,3}), 72.01 (s, 1 C, **C**H^{L1,2}), 69.35 (s, 1 C, **C**H^{T1,2}), 68.83 (s, 1 C, **C**H^{D}), 66.22 (s, 1 C, **C**H^{L1,3}), 65.62 (s, 1 C, **C**H$_2$–OR^{T1,2}), 64.89 (s, 1 C, **C**H$_2$^{L1,2}), 62.69 (**C**H$_2$–OH^{T1,2}), 62.38 (s, 1 C, **C**H$_2$–OR^{L1,2}), 61.90 (s, 1 C, **C**H$_2$^{D}), 59.85 (s, 1 C, **C**H$_2$^{T1,3}), 59.56 (s, 1 C, **C**H$_2$–OH^{L1,2}), 33.44–32.93 (m, 2 C, ROCO–**C**H$_2$–(CH$_2$)$_2$ –**C**H$_2$–COOR), 24.10–23.67 (m, 2 C, ROCO–CH$_2$–(**C**H$_2$)$_2$–CH$_2$–COOR) ppm. Abbreviations in accordance with Figure A1.

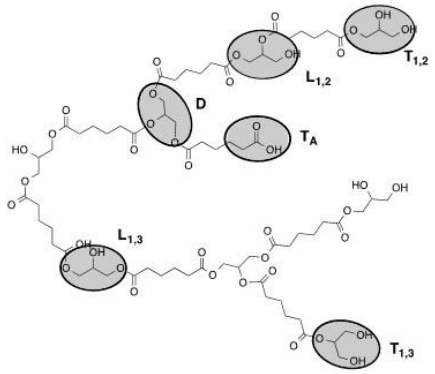

Figure A1. Structural units of hPES **1**.

Table A1. Molecular weight distribution of hPES **1**.

Peak No.	M_n	M_w	M_w/M_n
1	3.4 × 10^7 Da	4.2 × 10^7 Da	1.2
2	300 Da	1,600 Da	5

DB: 0.52

GPC (THF)

TAV: 1.80 mmol COOH/g polymer

THV: 2.25 mmol OH/g polymer

IR: ν = 3458.71, 2948.63, 1729.83, 1455.03, 1416.46, 1381.75, 1166.72, 1135.87, 1078.01, 1061.62, 943.02, 754.031 cm^{-1}.

A.2. Synthesis of Polyesterol hPES-OH **2**

30 mL of a solution of hyperbranched polyester **hPES 1** in THF (c = 347 mg·mL^{-1}, 10.41 g, 19 mmol COOH) was charged into a Schlenk flask. The residual catalyst DBTL (1.3 mg, 3.9 µmol) from the original product **hPES 1** was used to catalyze the reaction; no further catalyst was added. After solubilization in 10 mL DMF under stirring at RT, the flask was heated to 85 °C. THF was removed from the mixture under controlled reduced pressure using cryo-distillation, and the completeness of the THF removal was controlled by ^{1}H NMR. After THF was removed, the mixture was heated to 110 °C. Glycidol (1.25 mL, 1.388 g, 19 mmol, 1 eq) was added drop wise to the stirring yellow solution during a time period of 10 min using a syringe. The reaction mixture was stirred at 110 °C for 120 min, afterwards at RT overnight. Due to the incompleteness of reaction, the reaction was reheated to 110 °C and more glycidol (0.1 mL, 20 mmol in total) was added dropwise to the stirring reaction mixture. The reaction was stirred at 110 °C for 5.5 h and afterwards allowed to cool down to RT. The viscous product was obtained without further purification and stored in DMF.

^{1}H NMR (500 MHz, DMSO-d$_6$): δ = 7.95 (s, DMF), 5.18 (s, 1 H, C***H***^{D}), 4.94 (s, 1 H, C***H***^{L1,2}), 4.72 (q, 1 H, C***H***^{T1,3}), 3.86–4.26 (m, 13 H, C***H***^{L1,3}, C***H***$_2{}^{T1,2}$, C***H***$_2{}^{L1,3}$, C***H***$_2{}^{L1,2}$, C***H***$_2{}^{D}$), 3.63 (q, 1 H, C***H***^{T1,2}), 3.60 (THF), 3.27–3.50 (m, 6 H, C***H***$_2{}'^{T1,2}$, C***H***$_2{}^{T1,3}$, C***H***$_2{}'^{L1,2}$), 3.19, 3.02, 2.89, 2.73 (s, DMF), 2.59, 2.31 (m, 2H, –C***H***$_2$–CO$_2$–R), 2.10–2.12 (m, 2 H, –C***H***$_2$–CO$_2$H), 1.75 (THF), 1.54 (m, 4 H, –OCO–CH$_2$–(C***H***$_2$)$_2$–CH$_2$–COO–) ppm. Abbreviations in accordance with Figures A1 and A2.

IG ^{13}C NMR (500 MHz, DMSO-d$_6$): δ = 174.93–175.04 (CH$_2$–***C***OOH), 172.08–172.85 (CH$_2$–***C***OOR), 75.49 (***C***H^{T1,3}), 72.98, 72.52, 71.97 (***C***H^{L1,2}), 70.52, 69.33 (***C***H^{T1,2}), 68.79 (***C***H^{D}), 67.02 (THF), 66.19 (***C***H^{L1,3}), 65.57 (***C***H$_2$–OR^{T1,2}), 64.85 (s, ***C***H$_2{}^{L1,3}$), 62.68 (s, ***C***H$_2$–OH^{T1,2}), 62.33 (s, ***C***H$_2$–OR^{L1,2}), 61.83 (s, ***C***H$_2{}^{D}$), 59.79 (***C***H$_2{}^{T1,3}$), 59.52 (***C***H$_2$–OH^{L1,2}), 35.75 (DMF), 32.85–33.36 (–OCO–***C***H$_2$–(CH$_2$)$_2$–***C***H$_2$–COO), 30.74 (DMF), 25.13 (THF), 23.62–23.91 (–OCO–CH$_2$–(***C***H$_2$)$_2$–CH$_2$–COO–) ppm. Abbreviations in accordance with Figures A1 and A2.

DB: 0.41

GPC: M_n = 900 Da; M_w = 2400 Da, M_w/M_n = 2.7

TAV: 0.045 mmol COOH/g polymer

THV: 5.3 mmol OH/g polymer

IR: ν = 3384.46, 2938.02, 2871.49, 2332.48, 1732.73, 1660.41, 1439.6, 1409.71, 1383.68, 1250.61, 1167.69, 1137.8, 1091.51, 1054.87, 937.24, 865.88 cm^{-1}.

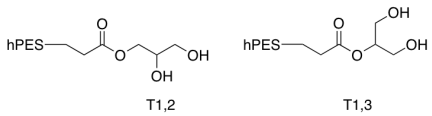

Figure A2. Terminal glycerol units of hPES-OH 2.

A.3. Synthesis of Linear Di-Block Copolymer hPES-OCL$_9$-OH **3**

In a Schlenk flask pre-dried macroinitiator hPES–OH **2** (2 g, 10.6 mmol OH) was dissolved in freshly distilled ε-caprolactone (6.18 g, 54 mmol) at 60 °C and two drops of Sn(Oct)$_2$ were added to the stirring mixture, followed by an increase of the temperature to 125 °C. The bulk mixture was stirred at 125 °C for 18 h. Purification was performed by dissolving the crude reaction mixture in DCM in high dilution and precipitation in a high excess of ice-cold MeOH under vigorous stirring. The dispersion was separated from the formed gel, solvent was removed under reduced pressure, and the received solid was redissolved in DCM in high dilution. Another precipitation was performed by adding the DCM solution dropwise into vigorously stirred ice-cold diethyl ether. The mixture was separated by centrifugation at 4000 min^{-1} for 1 min, and the supernatant was collected. After drying the separated supernatant under reduced pressure, the received solid was once again purified using dialysis in DCM (benzoylated RC membrane, MWCO 1–2 kDa, 7 h) for removal of Sn(Oct)$_2$ and traces of ε-caprolactone.

A white, wax-like solid product was obtained after removing the solvent under reduced pressure (2.69 g, yield: 33%).

^{1}H NMR (500 MHz, DMSO-d_6): δ = 5.18 (C***H***^{D}), 5.09 (new), 4.93 (C***H***^{L1,2}), 4.31 (C***H***$_2^{T1,3}$), 4.24 (C***H***$_2^{D}$), 4.12 (C***H***$_2^{L1,2}$), 3.98 (C***H***$_2^{E}$), 3.86 (C***H***^{L1,3}), 3.57 (C***H***^{T1,2}), 3.51 (C***H***$_2^{L1,2}$), 3.36 (C***H***$_2^{E\Omega}$), 2.27 (m, C***H***$_2^{C}$, C***H***$_2^{X}$), 1.54 (C***H***$_2^{D1}$, C***H***$_2^{D3}$, C***H***$_2^{y}$), 1.40, 1.30 (m, C***H***$_2^{D2}$) ppm. Abbreviations in accordance with Figure A3.

^{13}C NMR (700 MHz, overnight, DMSO-d_6): δ = 172.8, 172.7, 172.4 (various CH_2-***C***OOR), 71.9 (***C***H^{L1,2}), 69.8 (new), 69.3 (***C***H^{T1,2}), 68.8 (***C***H^{D}), 66.1 (***C***H^{L1,3}), 64.7 (***C***H$_2^{L1,3}$), 63.5 (***C***H$_2^{E}$), 62.6 (***C***H$_2$OH^{T1,2}), 62.3 (***C***H$_2$OR^{L1,2}), 61.8 (***C***H$_2^{D}$), 60.5 (***C***H$_2^{E\Omega}$), 59.5 (***C***H$_2$OH^{L1,2}), 33.6 (***C***H$_2^{X}$), 33.3 (***C***H$_2^{C}$), 32.1, 27.8 (***C***H$_2^{D3}$), 25.0, 24.9 (***C***H$_2^{D2}$), 24.4, 24.1 (***C***H$_2^{D1}$) ppm. Abbreviations in accordance with Figure A3.

DB: 0.74

GPC: M_n = 5000 Da, M_w = 8900 Da, M_w/M_n = 1.72

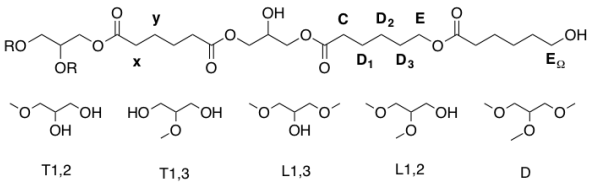

Figure A3. Labelling of atoms and structural units of hPES-OCL$_9$-OH 3 used for NMR description.

A.4. Functionalization of mPEG-OH (mPEG-COOH)

To a solution of pre-dried mPEG (4.786 g, 2.5 mmol) in a mixture of 10% anhydrous DMF in anhydrous THF (28 mL) in a 50 mL Schlenk flask, 4-DMAP (0.44 g, 3.8 mmol, 1.5 eq), TEA (0.5 mL, 3.8 mmol, 1.5 eq), and succinic anhydride (1.2 g, 12.5 mmol, 5 eq) were added under stirring at RT After stirring at RT for three days, the unreacted precipitated starting material was removed from the solution and the solution was dried under reduced pressure. The crude product was purified by precipitation from DCM solution into an ice-cold, 10-fold excess of Et_2O. The formed precipitate was filtered off using a glass filter (P4), redissolved in DCM, and precipitated once more following the same procedure. The collected precipitate was dried under high vacuum and 3.5 g (1.67 mmol, yield: 70%) of pure product were obtained.

^{1}H NMR (500 MHz, DMSO-d_6): δ = 4.21 (t, 2 H, C***H***$_2^{A''}$), 3.73–3.45 (m, 185 H, various C***H***$_2^{A}$), 3.33 (s, 3 H, PEG–O–C***H***$_3$), 2.64–2.58 (m, 4 H, C***H***$_2^{H1}$, C***H***$_2^{H2}$) ppm. Abbreviations in accordance with Figure A4.

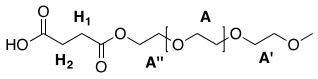

Figure A4. Labelling of atoms of mPEG-COOH used for NMR description.

A.5. Synthesis of Core-Multishell Nanocarrier (hPES-OCL$_9$-PEG-OMe **4***)*

In a dried 25 mL Schlenk flask, solid mPEG–COOH (1.110 g, 0.529 mmol, 1.1 eq) was added at RT to a stirring solution of hPES–OCL$_9$–OH **3** (304 mg, 0.48 mmol OH) in 6 mL anhydrous DMF. After the addition of 4-DMAP (0.016 g, 0.106 mmol, 20 mol %), EDCl (0.110 g, 0.574 mmol, 1.1 eq) was added at 0 °C. The reaction mixture was stirred for 10 min at 0 °C and then allowed to reach RT by removing the ice bath. After 20 h of stirring at RT, the crude product was purified via extensive ultrafiltration (DMF, MWCO < 10 kDa), followed by repeated fractionation. For this purpose, the impure product was dissolved in DCM, which yielded a clear solution. Hexane was added to the clear solution at RT until cloudiness appeared. The cloudy dispersion was heated to obtain a clear solution, followed

by the addition of Hexane to obtain a dispersion. The warm solution was allowed to reach RT and centrifuged (1 min, 3900 min^{-1}) to separate into a stable dispersion and sediment. The dispersion was dried and refractionated following the above-described procedure. The progress of purification was monitored using GPC in DMF. After six cycles of refractionation and removal of solvent under reduced pressure, followed by drying at high vacuum, a white solid product was obtained (0.116 g, yield: 12%).

^{1}H NMR (700 MHz, DMSO-d_6): δ = 5.17 (C***H***^{D}), 4.24 (CH_2^{D}), 4.12 (C***H*****$_2^{L1,2}$**), 3.98 (C***H*****$_2^{E}$**), 3.59–3.40 (various C***H*****$_2^{A}$**, C***H*****$_2^{A''}$**), 3.24 (PEG–OC***H*****$_3$**), 2.27 (C***H*****$_2^{C}$**, C***H*****$_2^{x}$**), 1.54 (C***H*****$_2^{D1}$**,C***H*****$_2^{D3}$**, C***H*****$_2^{y}$**), 1.29 (C***H*****$_2^{D2}$**) ppm. Abbreviations in accordance with Figure A5.

^{13}C NMR (500 MHz, DMSO-d_6): δ = 172.7 (–***C***OOR–), 171.9 (–***C***OOR–), 78.9, 75.3, 71.3 (***C***H^{L1,2}), 69.8 (PEG backbone), 69.6, 68.22 (various ***C***H$_2$, ***C***H$_2$), 69.6 (***C***H^{D}), 63.8 (***C***H$_2^{L1,2}$), 63.5 (***C***H$_2^{E}$), 61.8 (***C***H$_2^{D}$), 58.0 (PEG–O***C***H$_3$), 33.3–33.1 (***C***H$_2^{C}$, ***C***H$_2^{x}$), 28.5 (***C***H$_2^{H1}$, ***C***H$_2^{H2}$), 27.8 (***C***H$_2^{D1}$, ***C***H$_2^{D3}$), 24.9 (***C***H$_2^{D2}$), 24.1 (***C***H$_2^{y}$) ppm. Abbreviations in accordance with Figure A5.

DB: 0.52

GPC: M_n = 27,900 Da, M_w = 31,100 Da, M_w/M_n = 1.11

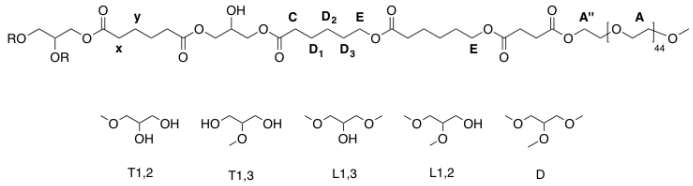

Figure A5. Labelling of atoms and structural units of hPES-OCL$_9$-OH 3 used for NMR description.

A.6. GPC of Hyperbranched Polymers

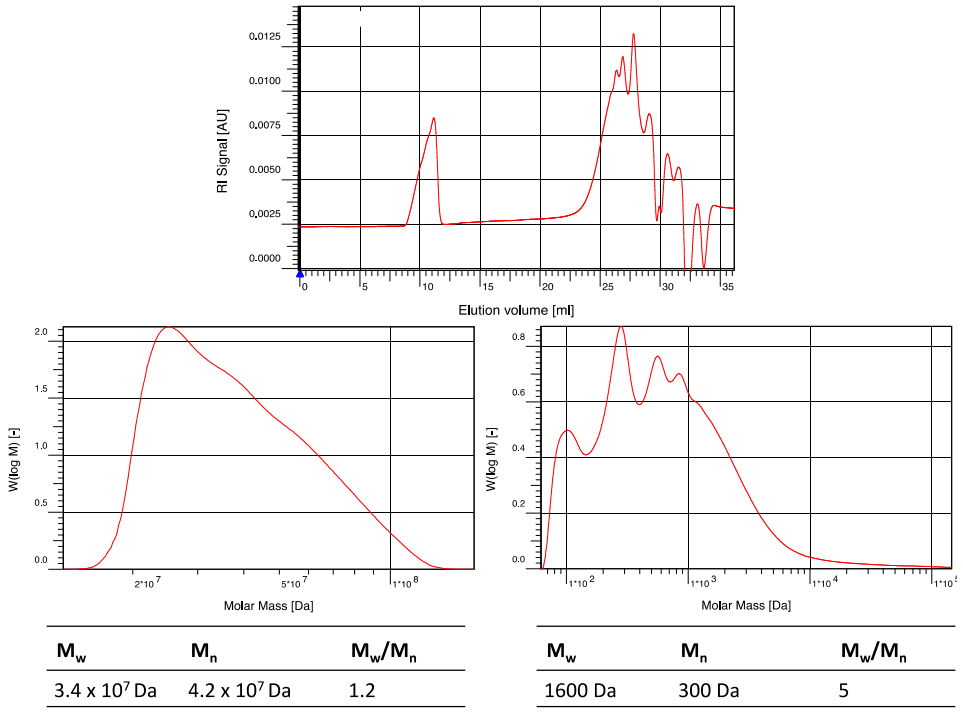

M_w	M_n	M_w/M_n
3.4 x 10^7 Da	4.2 x 10^7 Da	1.2

M_w	M_n	M_w/M_n
1600 Da	300 Da	5

Figure A6. GPC elugram of crude hPES 1 in THF. (Top) full range elugram; *y*-axis: elution volume. (Bottom) detailed elugrams with molecular weights; *y*-axis: molar mass.

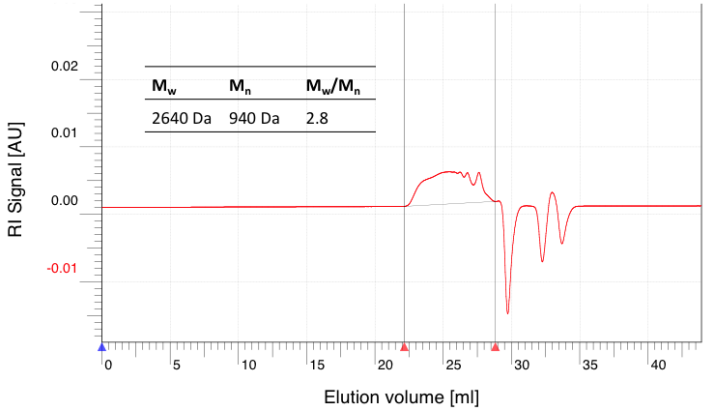

Figure A7. GPC elugram of purified hPES-OH 2 in THF.

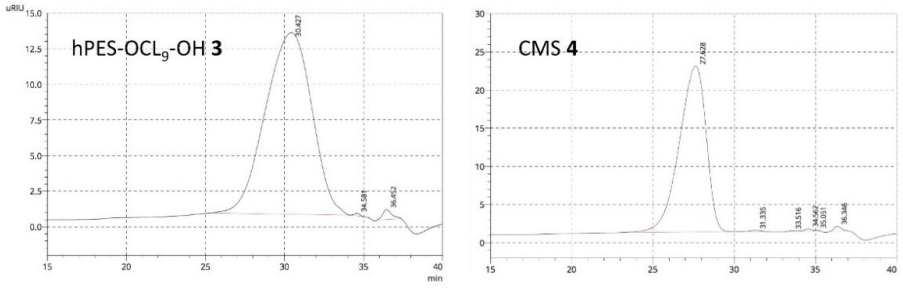

M_w	M_n	M_w/M_n
8900	5153	1.73

M_w	M_n	M_w/M_n
31078	27903	1.11

Figure A8. GPC elugram of purified hPES–OCL9–OH 3 and CMS 4 in DMF.

A.7. Determination of TAV and THV of hPES ***1*** *and hPES-OH* ***2***

To determine the total acid value (TAV) and total hydroxyl value (THV) it is crucial to know the conversion at the respective point of the reaction. Synthesis of hyperbranched polyester **1** consisting of a diacid (A2) and triol (B3) was stopped before reaching the so-called gel point. According to Flory, the gel point is the point when the conversion reaches its maximum before becoming an infinite network [14]. The actual gel point can be predicted as a function of the functionality f and ratio ρ. In our case of adipic acid as A_2 and glycerol as B_3 unit, functionality f is 3, reflecting three functional groups on the branching unit, while ratio $\boldsymbol{\rho}$ is the ratio between the number of A functional groups and the number of B functional groups yields:

$$\rho = \frac{n_{\mathrm{COOH}}}{n_{\mathrm{OH}}} \tag{A1}$$

$n_{COOH,}$ amount of acid groups in mol; $n_{OH,}$ amount of hydroxyl groups in mol.

This theoretical approach does not take into account the difference in reactivity of primary and secondary functional groups of the B_3 trifunctional branching unit. Functionality f can be used to determine the critical value α_c of the branching coefficient α for formation of infinite networks:

$$\alpha_c = \frac{1}{f-1} \tag{A2}$$

f, functionality of branching unit; α_c, critical value of branching coefficient α

In our case for B_3 monomers, f is 3 and α_c consequently 0.5. The connection between functionality f and ratio ρ is as follows:

$$P_A = \left(\frac{\alpha_c}{\rho}\right)^{\frac{1}{2}} \quad \text{(A3)}$$

P_A, conversion at gel point; α_c, critical value of branching coefficient α; ρ, ratio, see above.

Equation (3) allows for prediction of the theoretical conversion P_A at the gel point. For the synthesis of hPES **1** with a ratio of 1.2:1 (A_2:B_3), the value for P_A is 0.79. The conversion during the reaction was monitored by using ^{1}H NMR spectroscopy and analysis of the ratio of C**H$_2$**–COOH (2.3 ppm) versus C**H$_2$**–COOR (2.2 ppm). When the reaction approached the theoretical P_A value, the reaction was stopped and the bulk polymer cooled down to stop the polymerization. After evaluation of the real P value, the TAV and THV were calculated for hPES **1** as follows:

m(adipic acid) = 39.9 g n_0(COOH) = 545 mmol
m(glycerol) = 20.93 g n_0(OH) = 682 mmol
m(polymer) = 52.708 g

Conversion p = (Integral C**H$_2$**–COOH)/(Integral C**H$_2$**–COOH + Integral C**H$_2$**–COOR) = 1/1.21 = 0.83
TAV:
n_t(COOH) = (1−P) × n_0(COOH) = 94.9 mmol
→TAV = 94.9 mmol COOH/52.708 g polymer = 1.80 mmol/g polymer
THV:
n_t(OH) = (1−P) × n_0(OH)= 118.7 mmol
→THV = 118.7 mmol OH/52.708 g polymer = 2.25 mmol/g polymer

Values of TAV and THV of hPES–OH **2** were determined based on the assumption that COOH reacted with glycidol with a conversion of p = 0.97.so that hPES–OH **2** had 2.9% remaining COOH:
n_0(COOH) = 18.7 mmol
n_0(OH) = 26.8 mmol
m(polymer) = 11.918 g
TAV:
n_t(COOH) = (1−P) × n_0(COOH) = 0.5423 mmol
→TAV = 0.5423 mmol/11.918 g polymer = 0.045 mmol COOH/g polymer
THV:
n_t(OH) = n_0(OH) + [(n_0(COOH) − n_t(COOH)) × 2] = 63.1 mmol
→THV = 63.1 mmol OH/11.918 g polymer = 5.3 mmol OH/g polymer

A.8. Determination of Degree of Branching DB

The degree of branching was calculated based on Equation (4), which is the calculation of the DB as published by Frey *et al.* We chose this equation, because Frey states that the original Fréchet Equation (5) overestimates the branching, if small or low branched molecules are considered [12,33].

$$DB = \frac{2\,D}{2\,D + L} \quad \text{(A4)}$$

$$DB = \frac{D + T}{L + D + T} \quad \text{(A5)}$$

Where: T: relative integral of terminal units of type **T$_{1,2}$**, **T$_{1,3}$**, and **T$_A$**.
L: relative integral of linear units of type **L$_{1,3}$** and **L$_{1,2}$**
D: relative integral of dendritic unit **D**.

The relative integrals needed for this calculation are the integrals of methine signals of the various glycerol branching units, as depicted in Figure A9 for the case of hPES 1, hPES-OH 2, and hPES–OCL$_9$–OH 3. The spectra were measured by inverse-gated ^{13}C spectroscopy, because the

obtained carbon peaks were quantifiable. Table A2 summarizes all the relevant data for the calculation of branched products 1, 2, 3, and 4. In the case of product CMS 4, a quantification of methine and methylene signals was not possible.

Table A2. Interpretation of inverse-gated (IG) ^{13}C NMR spectra of hyperbranched polyesters in DMSO-d$_6$. Integral values of –CH– signals of relevant glycerol units for evaluating the degree of branching (DB).

Structure	Integral value			DB
	CH ^{L1,2}	CH ^{D}	CH ^{L1,3}	
hPES **1**	1.00	1.54	1.86	0.52
hPES-OH **2**	0.74	1.00	2.15	0.41
hPES–OCL$_9$–OH **3**	0.16 *	1.00 *	0.54 *	0.74 *

* obtained from overnight ^{13}C NMR measurement, non IG; neither CH ^{L1,2} and CH ^{L1,3} nor CH2 ^{L1,2} and CH2 ^{L1,3} were detected in IG due to the low signal-to-noise ratio.

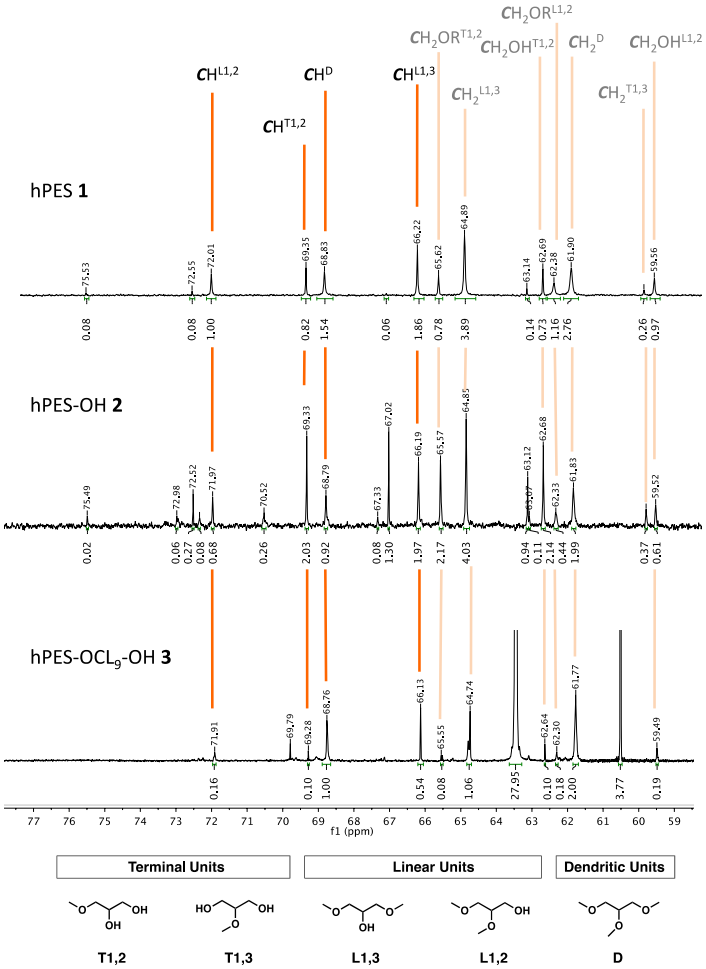

Figure A9. Details of ^{13}C NMR spectra of hPES 1, hPES–OH 2, and hPES–OCL$_9$–OH 3 (top to bottom). Depicted are peaks relevant for calculation of D_f and DB analysis. Five types of glycerol units can be distinguished in the structure of the hyperbranched polyester. For comparability of signal integrals, the value for diacid peaks was set to be identical in hPES 1 and hPES–OH 2.

A.9. Determination of Degree of Functionalization Df

A.9.1. hPES-OH **2**

Hyperbranched polyester hPES **1** with a total acid value of 1.8 mmol carboxylic acid groups per gram polyester was modified with equimolar amounts of glycidol with respect to the amount of hydroxyl groups of hPES **1**, in order to modify one glycidol per carboxylic acid. The reactions were performed at a bath temperature of 110 °C in DMF for two hours; afterwards at room temperature overnight. The reaction progress was monitored by ^{1}H NMR, *i.e.*, the disappearance of the methylene signal next to the free carboxylic acid as well as the proton signal of terminating carboxylic acid groups. We paid special attention to the expected changes of several structural units as well as the possibility of the side reaction shown in Scheme 4.

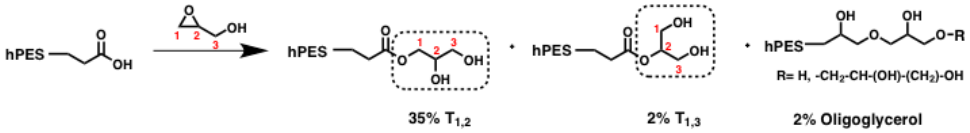

Scheme 4. Simplified scheme of polyester modification by ring-opening reaction of glycidol; crucial units for NMR evaluation are highlighted in boxes. %: abundance of species relative to abundance of all glycerol units.

Even though equimolar amounts of glycidol were used during the reaction, full conversion of all carboxylic acid groups could not be achieved. Evaluation of the methylene signals next to free carboxylic acids versus those next to ester groups after ^{1}H NMR measurements showed that the fraction of carbons from free carboxylic acid decreased from 17.4% before to 2.9% after modification, giving a functionalization degree of D_f (COOH) = 0.83. At the same time, the amount of esterification increased by a factor of 2.5, which was evaluated according to the increased methine peak supplementary inverse-gated ^{13}C NMR spectroscopy. Based on inverse-gated ^{13}C NMR spectroscopy, we can also show that $T^{1,2}$ methine and methylene signals increased by a factor of 2.5 as well, indicating that these newly formed $T^{1,2}$ units arose from reactions with carboxylic acids at the sterically less-hindered C1 atom of glycidol. We can furthermore observe the increase of $T^{1,3}$ methylene signals by a factor of 1.4. Hence, ring-opening of glycidol also occurred on the sterically more-hindered C2 carbon atom, as shown in Scheme 4. The inverse-gated ^{13}C NMR spectra were also checked for further changes of integrals, as we were also interested in the question whether formation of oligoglycerol formation occurred. If terminal glycerol hydroxyl groups initialized ring-opening of glycidol, new signals should have arisen. In fact, three new signals can be found in the region of methine shifts (70.52–72.98 ppm, see Figure A1). With regard to the shift of these signals, they could have resulted from the methylene next to the ether bond between two glycerol units. With an average integral of 0.4, the new signals represent only 2% of the amount of overall carbon signals in the region of glycerol's methine and methylene signals. As this amount is small, the presence of oligoglycerols should not interfere with further reactions and analysis. In summary, terminal carboxylic acid groups of the hyperbranched polyester hPES **1** were modified with glycerol units by in a tin-catalyzed, ring-opening reaction with glycidol. The amount of esterified carboxylic acid units increased by a factor of 2.5 compared to the esterified carboxylic acid units before the modification, while full modification of carboxylic acids could not be achieved. Ring-opening of glycidol did not only take place at C1 carbon atom leading to a new $T^{1,2}$ unit but also at the C2 carbon atom, which formed $T^{1,3}$ units. Oligoglycerols only formed to a certain extent.

A.9.2. hPES-OCL$_9$-OH **3**

Determination of D_f was accomplished based on Equation (6), where the estimated amount of reacted hydroxyl groups of hPES–OCL$_9$–OH **3** is compared to the estimated amount of theoretically-available hydroxyl groups of hPES–OH **2**.

$$D_f = \frac{\text{amount reacted OH of hPES} - \text{OCL}_9 - \text{OH 3}}{\text{amount free OH of hPES} - \text{OH 2}} \quad \text{(A6)}$$

The amounts of hydroxyl groups were estimated based on the integrals in ^{13}C NMR spectra of methine arising from glycerol units, marked with orange lines in Figure A9. The relative abundance of the methine signals was calculated and normalized according to Table A2, which gave the amounts of reacted and free OH grous of hPES–OH 2 and hPES–OCL9—OH 3 that were needed for Equation (A6):

$$D_f = \frac{119 - 39}{119} = 0.67$$

Table A3. Comparison of ^{13}C NMR spectra of hPES–OH 2 and hPES–OCL$_9$–OH 3 as shown in Figure A9 with regard to specific glycerol's methine signals and calculation of their relative abundance, and absolute and normalized amounts of OH and OR groups for calculation of the degree of functionalization D_f.

	hPES–OH 2					**hPES–OCL$_9$–OH 3**				
Signal	CH ^{L1,2}	CH ^{T1,2}	CH^{D}	CH^{L1,3}	all	CH ^{L1,2}	CH ^{T1,2}	CH^{D}	CH^{L1,3}	all
abs. integral value	0.74	2.21	1	2.15	6.1	0.16	0.10	1	0.54	1.80
rel. integral value	12%	36%	16%	35%	100%	9%	6%	56%	30%	100%
amount OH [a]	12	72	-	35	119	6.9 [b]	9.2 [b]	-	23.1 [b]	39.3 [b]
amount OR	-	-	48	-	48	-	-	127 [b]	-	127 [b]

[a] Linear units contributed 1 OH group, terminal units contributed two OH groups, dendritic units contributed three OR groups; [b] The amount of OH and OR groups was normalized by factor $F = 0.77 = (119 + 48)/(39 + 127)$ to maintain a constant sum of OR and OH groups.

A.9.3. CMS Nanocarrier hPES–OCL$_9$–PEG–OMe **4**

Functionalization of terminal caprolactone hydroxyl groups was analyzed via ^{1}H NMR by determining the increase of esterification of caprolactone hydroxyl groups. This was done by comparing the ratio of CH_2^E and CH_2^{C+x} before the reaction to the ratio after the reaction. Since the integral of CH_2^{C+x} remained constant upon functionalization with mPEG–COOH, we could fix this integral value and determine the percental increase of CH_2^E, leading to a value of D_f(CL–OH) = 0.7. To cross check this assumption, the integral of methoxy CH_3 of mPEG was compared to CH_2^{C+x}. This comparison revealed an 80% excess of mPEG chains, which therefore should be attached to internal glycerol hydroxyl groups. The functionalization of internal hydroxyl groups was supported by ^{13}C-NMR of the product, which showed a disappearance of $CH^{L1,2}$ and $CH^{L1,3}$ and indicated that the respective hydroxyl groups reacted with mPEG–COOH. As the abundance of internal glycerol units was too small to allow for quantification, we could not estimate the degree of functionalization of internal glycerol hydroxyl groups based on ^{13}C NMR. Nevertheless, ^{1}H NMR analysis led to the assumption, that roughly 55% of present mPEG–COOH chains were attached to 70% of terminal caprolactone units, while 45% of mPEG–COOH reacted with internal glycerol units.

A.10. Enzymatic Degradation—Full Spectrum

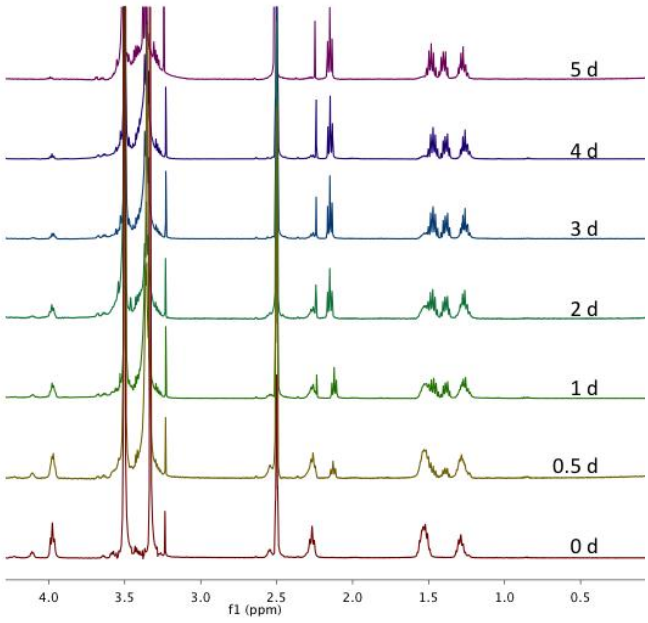

Figure A10. Overlay of magnified ^{1}H NMR spectra in DMSO-d_6 of CMS nanocarriers after incubation with Novozyme® 435 at 32 °C at various time points during a five-day study.

References

1. Miyata, K.; Christie, R.J.; Kataoka, K. Polymeric micelles for nano-scale drug delivery. *React. Funct. Polym.* **2011**, *71*, 227–234. [CrossRef]
2. Kataoka, K.; Kwon, G.S.; Yokoyama, M.; Okano, T.; Sakurai, Y. Block copolymer micelles as vehicles for drug delivery (L & J). *J. Control. Release* **1993**, *24*, 119–132.
3. Kataoka, K.; Harada, A.; Nagasaki, Y. Block copolymer micelles for drug delivery: Design, characterization and biological significance. *Adv. Drug Deliv. Rev.* **2001**, *47*, 113–131. [CrossRef]
4. Newkome, G.R.; Moorefield, C.N.; Baker, G.R.; Saunders, M.J.; Grossman, S.H. Unimolecular micelles. *Angew. Chem. Int. Ed. Engl.* **1991**, *30*, 1178–1180. [CrossRef]
5. Kurniasih, I.N.; Keilitz, J.; Haag, R. Dendritic nanocarriers based on hyperbranched polymers. *Chem. Soc. Rev.* **2015**, *44*, 4145–4164. [CrossRef] [PubMed]
6. Lukowiak, M.C.; Thota, B.N.S.; Haag, R. Dendritic core–shell systems as soft drug delivery nanocarriers. *Biotechnol. Adv.* **2015**, *33*, 1327–1341. [CrossRef] [PubMed]
7. Kadajji, V.G.; Betageri, G.V. Water soluble polymers for pharmaceutical applications. *Polymers* **2011**, *3*, 1972. [CrossRef]
8. Fleige, E.; Ziem, B.; Grabolle, M.; Haag, R.; Resch-Genger, U. Aggregation phenomena of host and guest upon the loading of dendritic core-multishell nanoparticles with solvatochromic dyes. *Macromolecules* **2012**, *45*, 9452–9459. [CrossRef]
9. Wang, X.; Gurski, L.A.; Zhong, S.; Xu, X.; Pochan, D.J.; Farach-Carson, M.C.; Jia, X. Amphiphilic block co-polyesters bearing pendant cyclic ketal groups as nanocarriers for controlled release of camptothecin. *J. Biomater. Sci. Polym. Ed.* **2011**, *22*, 1275–1298. [CrossRef] [PubMed]
10. Krishnan, V.; Xu, X.; Barwe, S.P.; Yang, X.; Czymmek, K.; Waldman, S.; Mason, R.W.; Jia, X.; Rajasekaran, A.K. Dexamethasone-loaded block copolymer nanoparticles induce leukemia cell death and enhance therapeutic efficacy: A novel application in pediatric nanomedicine. *Mol. Pharm.* **2013**, *10*, 2199–2210. [CrossRef] [PubMed]

11. Fleige, E.; Quadir, M.A.; Haag, R. Stimuli-responsive polymeric nanocarriers for the controlled transport of active compounds: Concepts and applications. *Adv. Drug Deliv. Rev.* **2012**, *64*, 866–884. [CrossRef] [PubMed]
12. Frey, H. Degree of branching in hyperbranched polymers. *Acta Polym.* **1997**, *48*, 30–35.
13. Stumbé, J.-F.; Bruchmann, B. Hyperbranched polyesters based on adipic acid and glycerol. *Macromol. Rapid Commun.* **2004**, *25*, 921–924. [CrossRef]
14. Flory, J. Molecular size distribution in three dimensional polymers. I. Gelation. *J. Am. Chem. Soc.* **1941**, *63*, 3083–3090. [CrossRef]
15. Sunder, A.; Hanselmann, R.; Frey, H.; Mülhaupt, R. Controlled synthesis of hyperbranched polyglycerols by ring-opening multibranching polymerization. *Macromolecules* **1999**, *32*, 4240–4246. [CrossRef]
16. Luman, N.R.; Kim, T.; Grinstaff, M.W. Dendritic polymers composed of glycerol and succinic acid: Synthetic methodologies and medical applications. *Pure Appl. Chem.* **2004**, *76*, 1375–1385. [CrossRef]
17. Zhang, T.; Howell, B.A.; Dumitrascu, A.; Martin, S.J.; Smith, P.B. Synthesis and characterization of glycerol-adipic acid hyperbranched polyesters. *Polymer* **2014**, *55*, 5065–5072. [CrossRef]
18. Posner, G.H.; Rogers, D.Z. Organic reactions at alumina surfaces. Mild and selective opening of epoxides by alcohols, thiols, benzeneselenol, amines, and acetic acid. *J. Am. Chem. Soc.* **1977**, *99*, 8208–8214. [CrossRef]
19. Iranpoor, N.; Shekarriz, M.; Shiriny, F. Highly efficient, regio—and stereoselective ring opening of epoxides and thiiranes with $Ce(OTf)_4$. *Synth. Commun.* **1998**, *28*, 347–366. [CrossRef]
20. Iranpoor, N.; Tarrian, T.; Movahedi, Z. $FeCl_3 \cdot 6H_2O$ supported on SiO_2 catalysed ring opening of epoxides with alcohols, acetic acid, water, chloride, bromide and nitrate ions. *Synthesis* **1996**, *12*, 1473–1476. [CrossRef]
21. Khalafi-Nezhad, A.; Soltani Rad, M.N.; Khoshnood, A. An efficient method for the chemoselective preparation of benzoylated 1,2-diols from epoxides. *Synthesis* **2003**, *16*, 2552–2558. [CrossRef]
22. Weiss, M.E.R.; Paulus, F.; Steinhilber, D.; Nikitin, A.N.; Haag, R.; Schütte, C. Estimating kinetic parameters for the spontaneous polymerization of glycidol at elevated temperatures. *Macromol. Theory Simul.* **2012**, *21*, 470–481. [CrossRef]
23. Zhou, Y.; Huang, W.; Liu, J.; Zhu, X.; Yan, D. Self-assembly of hyperbranched polymers and its biomedical applications. *Adv. Mater.* **2010**, *22*, 4567–4590. [CrossRef] [PubMed]
24. Gao, H. Development of star polymers as unimolecular containers for nanomaterials. *Macromol. Rapid Commun.* **2012**, *33*, 722–734. [CrossRef] [PubMed]
25. Steglich, W.; Höfle, G. *N*,*N*-dimethyl-4-pyridinamine, a very effective acylation catalyst. *Angew. Chem. (Int. Ed. Engl.)* **1969**, *8*, 981. [CrossRef]
26. Steglich, W.; Neises, B. Simple method for the esterification of carboxylic acids. *Angew. Chem. Int. Ed. Engl.* **1978**, *17*, 522–523.
27. Fischer, A.M.; Thiermann, R.; Maskos, M.; Frey, H. One-pot synthesis of poly(L-lactide) multi-arm star copolymers based on a polyester polyol macroinitiator. *Polymer* **2013**, *54*, 1993–2000. [CrossRef]
28. Radowski, M.R.; Shukla, A.; von Berlepsch, H.; Böttcher, C.; Pickaert, G.; Rehage, H.; Haag, R. Supramolecular aggregates of dendritic multishell architectures as universal nanocarriers. *Angew. Chem.* **2007**, *46*, 1265–1269. [CrossRef] [PubMed]
29. Fleige, E.; Tyagi, R.; Haag, R. Dendronized core-multishell nanocarriers for solubilization of guest molecules. *Nanocarriers* **2013**, *1*, 1–9. [CrossRef]
30. Fleige, E.; Achazi, K.; Schaletzki, K.; Triemer, T.; Haag, R. Ph-responsive dendritic core-multishell nanocarriers. *J. Control. Release* **2014**, *185*, 99–108. [CrossRef] [PubMed]
31. Kurniasih, I.N.; Liang, H.; Kumar, S.; Mohr, A.; Sharma, S.K.; Rabe, J.P.; Haag, R. A bifunctional nanocarrier based on amphiphilic hyperbranched polyglycerol derivatives. *J. Mate. Chem. B* **2013**, *1*, 3569–3577. [CrossRef]
32. Stefani, S.; Kurniasih, I.N.; Sharma, S.K.; Böttcher, C.; Servin, P.; Haag, R. Triglycerol-based hyperbranched polyesters with an amphiphilic branched shell as novel biodegradable drug delivery systems. *Polym. Chem.* **2016**, *7*, 887–898. [CrossRef]
33. Fréchet, J.M.J.; Hawker, C.J. Hyperbranched polyphenylene and hyperbranched polyesters: New soluble, three-dimensional, reactive polymers. *React. Func. Polym.* **1995**, *26*, 127–136. [CrossRef]

3.2 Radical Stability vs. Temporal Resolution of EPR-Spectroscopy on Biological Samples

“Spin-labeling active compounds is a convenient way to prepare them for EPR spectroscopy with minimal alteration of the target molecule. In this study we present the labeling reaction of dexamethasone (Dx) with either TEMPO (2,2,6,6-tetramethyl-1-piperidinyloxy) or PCA (3-(carboxy)-2,2,5,5-tetramethyl-1-pyrrolidinyloxy) with high yields. According to NMR data, both labels are attached at the primary hydroxy group of the steroid. In subsequent spin-stability measurements both compounds were applied onto HaCaT cells. When the signal of Dx-TEMPO decreased below the detection limit within 3 h, the signal of Dx-PCA remained stable for the same period of time.”

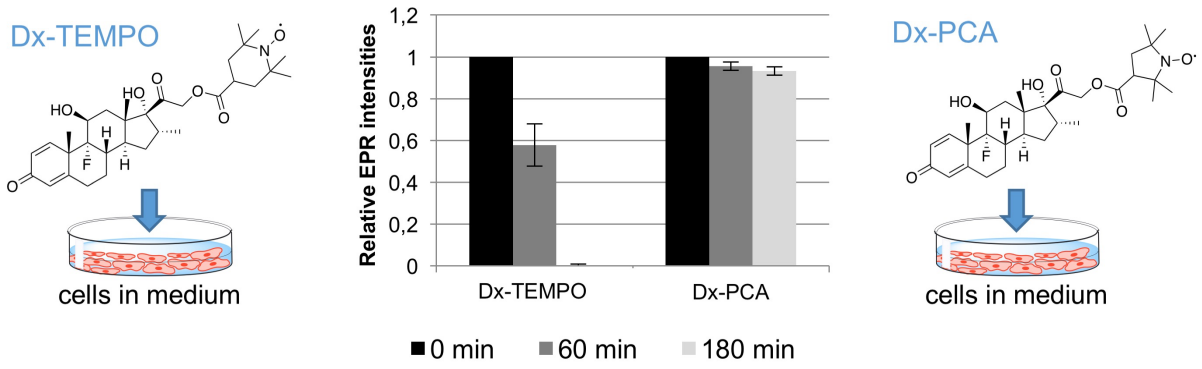

This chapter was published in:

Walker, K. A.;[a] Unbehauen, M. L.;[a] Lohan, S. B.; Saeidpour, S.; Meinke, M. C.; Zimmer, R.; Haag, R., Spin-labeling of Dexamethasone: Radical Stability vs. Temporal Resolution of EPR-Spectroscopy on Biological Samples. *Zeitschrift für Physikalische Chemie* **2018,** *232* (5-6), 883-891.

[a]equal contribution of K.A. Walker and M.L. Unbehauen

https://doi.org/10.1515/zpch-2017-1076

Contribution:

Establishment of synthetic approach and reaction parameters for chemoselective labelling of primary hydroxy group of dexamethasone by spin label PCA. Structural analysis of Dx-PCA conjugate NMR. Writing and editing of manuscript and its graphics, revision of manuscript and galley proof as well as communication with the editor.

DE GRUYTER Z. Phys. Chem. 2018; 232(5–6): 883–891

Karolina A. Walker[a], Michael L. Unbehauen[a], Silke B. Lohan, Siavash Saeidpour, Martina C. Meinke, Reinhold Zimmer and Rainer Haag*

Spin-labeling of Dexamethasone: Radical Stability vs. Temporal Resolution of EPR-Spectroscopy on Biological Samples

https://doi.org/10.1515/zpch-2017-1076
Received November 15, 2017; accepted April 5, 2018

Abstract: Spin-labeling active compounds is a convenient way to prepare them for EPR spectroscopy with minimal alteration of the target molecule. In this study we present the labeling reaction of dexamethasone (Dx) with either TEMPO (2,2,6,6-tetramethyl-1-piperidinyloxy) or PCA (3-(carboxy)-2,2,5,5-tetramethyl-1-pyrrolidinyloxy) with high yields. According to NMR data, both labels are attached at the primary hydroxy group of the steroid. In subsequent spin-stability measurements both compounds were applied onto HaCaT cells. When the signal of Dx-TEMPO decreased below the detection limit within 3 h, the signal of Dx-PCA remained stable for the same period of time.

Keywords: electron spin relaxation; *ex vivo* imaging; labeling; X-band EPR.

Dedicated to: Eckart Rühl on the occasion of his 60th birthday.

1 Introduction

The functionalization of active drugs with so-called spin labels is relevant for drug delivery. In this field, drugs are embedded in drug delivery devices, e.g.

[a]**Karolina A. Walker and Michael L. Unbehauen:** These authors contributed equally to this work.
***Corresponding author: Rainer Haag,** Institute for Chemistry and Biochemistry, Freie Universität Berlin, Takustrasse 3, 14195 Berlin, Germany, e-mail: haag@chemie.fu-berlin.de
Karolina A. Walker, Michael L. Unbehauen and Reinhold Zimmer: Institute for Chemistry and Biochemistry, Freie Universität Berlin, Takustrasse 3, 14195 Berlin, Germany
Silke B. Lohan and Martina C. Meinke: Department of Dermatology, Venerology and Allergology, Center of Experimental and Applied Cutaneous Physiology, Charité – Universitätsmedizin Berlin, Charitéplatz 1, 10117 Berlin, Germany
Siavash Saeidpour: Department of Physics, Freie Universität Berlin, Arnimallee 14, 14195 Berlin, Germany

nanoparticulate polymeric transporter, providing controlled released out of the polymer matrix [1, 2]. For the preclinical investigation of a drug delivery device, we need to understand the release mechanism and kinetics of the drug, as well as its fate after being released. Studies on the fate of encapsulated drugs upon release are usually based on UV-Vis or fluorescence spectroscopy techniques [3]. Both techniques require either the use of UV-Vis-active model drugs, such as Nile Red, or fluorescently labeled drugs [4]. Nevertheless, fluorescent labels can significantly change the physico-chemical properties of the drug within the transporter, because they are complex and often large molecules ($M \geq 300$ g/mol) themselves. Using small labels, e.g. spin labels, minimizes the change of properties, such as the drug's polarity, and biological activity [5]. Spin labels, such as nitroxide-based TEMPO and PCA, are sensitive to their chemical microenvironment and hence are used in biological experiments. The difference between TEMPO and PCA in terms of stability of the radical defines their field of application. TEMPO is less stable than PCA and is consequently more readily reduced to the respective hydroxylamine, while reduction of PCA typically occurs under irradiation [6]. The benefit of using spin labels in the field of drug delivery systems is that their sensitivity gives valuable information on the microenvironment of the drug delivery system surrounding the spin label. Combining the spin label with a drug molecule will therefore give us the way to track the movement of the drug inside and outside of the transporter by time-resolved observations [7, 8]. The drug of interest in our case was the poorly water soluble glucocorticoid dexamethasone (Dx, $\log P = 1.83$), which is widely used as an anti-inflammatory and immunosuppressant agent [9, 10]. The drug molecule contains three hydroxy groups that may potentially serve as functional groups for attaching the carboxylic acid-containing nitroxide-based spin labels TEMPO and PCA (see Scheme 1). With respect to the conjugates' further application in drug delivery, it was of great importance to generate only one regioisomer, hence attaching the spin label at selectively one

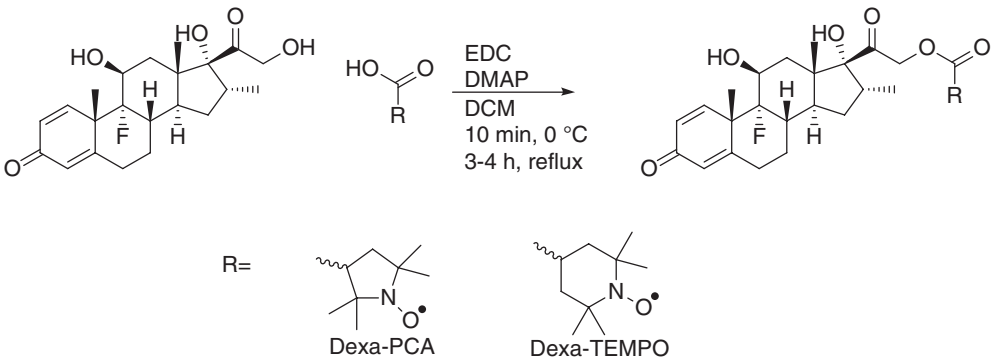

Scheme 1: Synthesis of spin-labeled dexamethasone with either TEMPO or PCA as spin labels.

hydroxy group of the drug. As a single compound, the spin-labeled drug will have a very defined behavior within the polymeric transporter. We present an easy protocol for the selective ester bond formation between the drug's primary hydroxy group and the spin label, and discuss the differences in terms of EPR performance between the two resulting drug conjugates.

2 Results

For the spin-labeling reaction, mild conditions had to be chosen to maintain the spin label's functionality as well as possible. In this regard, the Steglich-type esterification (see Scheme 1) was most promising. This type of reaction involves a carbodiimide, which, in this case, is 1-ethyl-3-(3-dimethylaminopropyl) carbodiimide (EDC) that forms the respective urea scavenging H_2O, the formal side product of this reaction. The acyl-transfer agent 4-dimethylaminopyridine (DMAP) was added to prevent acyl-trapping side products [11–13]. Purification was performed via column chromatography which led to products in high yields of 90% for Dx-PCA and 88% for Dx-TEMPO. These yields were significantly higher than previously reported reactions between steroids and spin labels [14].

Dexamethasone exhibits three alcohol groups that can undergo esterification reactions, as depicted in Scheme 1. It was reported that the acyl transfer catalyst DMAP also works for sterically demanding tertiary alcohols [12]. In the case of the three sterically different hydroxy groups of dexamethasone, Steglich-type conditions might potentially lead to the esterification of all three hydroxy groups of the steroid backbone. The conversion and reaction site were determined by mass spectroscopy (ESI-ToF) and NMR, respectively. ESI-ToF spectra only showed peaks that originated from the mono esterification, which indicated that one spin-label had been attached per dexamethasone molecule. In addition to ESI-ToF measurements, the successful binding of the spin label to dexamethasone could be shown by EPR spectroscopy. Figure 1 shows the EPR signal of both the free label TEMPO and the Dx-TEMPO conjugate. A minimization of the high field peak indicates a success in the labeling procedure. Using this spectroscopic technique, we further obtained information about the activity of the labels attached to the drug. Dx-PCA and Dx-TEMPO were compared to freshly prepared solutions of the free spin labels PCA and TEMPO, respectively. Both conjugates showed an EPR activity of 80% compared to the free drug. This may have been due to quenching by reactive species in solution.

Additionally, NMR analysis was used to determine the site of esterification. Prior to NMR measurements, the unpaired electron of the paramagnetic spin

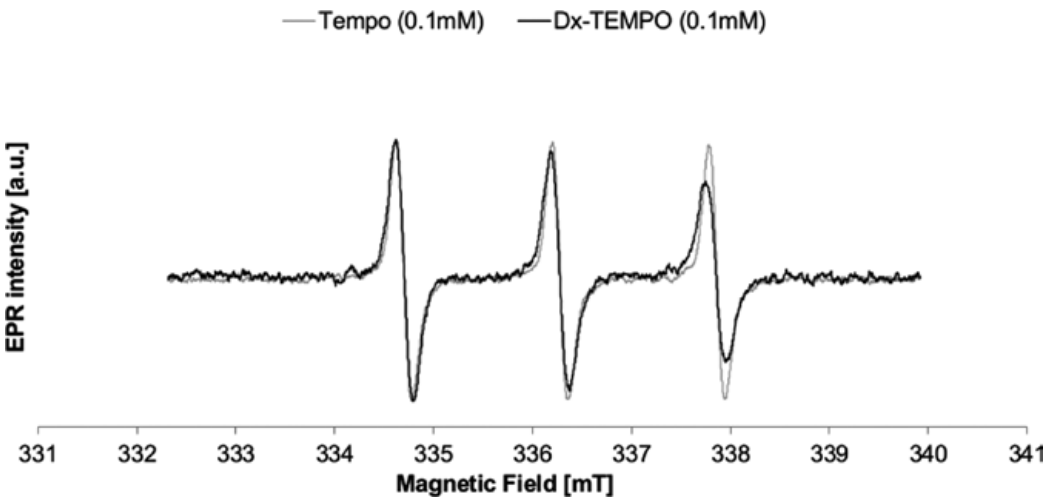

Fig. 1: X-band EPR spectra of TEMPO (gray) and Dx-TEMPO (black) dissolved in DMSO (0.1 mM), both normalized to the maximum height of the low field peak.

label was reduced. The mild reducing agent formic acid was used for the reduction of Dx-TEMPO, while the relatively strong reducing agent zinc powder in combination with ammonium chloride as a proton donor was used for the reduction of Dx-PCA to the respective hydroxylamine (see Scheme 2). Nevertheless, Dx-PCA showed a line broadening which indicates an incomplete reduction of the spin label. Even though the steroidal backbone of Dx-PCA could not be fully resolved, the resulting spectrum gave information on the spin label's binding site.

Based on the spectra in Figure 2, we determined the site of esterification. The essential information is given by the chemical shift of the protons in positions A (one proton) or C (two protons) that would change upon bond formation. The absence of a shift of peak A or C indicates a bond formation at the tertiary hydroxy group at position B. In both the PCA- as well as the TEMPO-labeled conjugates, there was only a significant shift of the two protons of position C. Thus, the coupling reactions performed under these conditions led to an esterification at the primary hydroxy group (C position), which is the sterically preferred position for the spin label attachment [14, 15]. The tertiary alcohol in the B position features the highest nucleophilicity and thus, by electronic character, best reactivity,

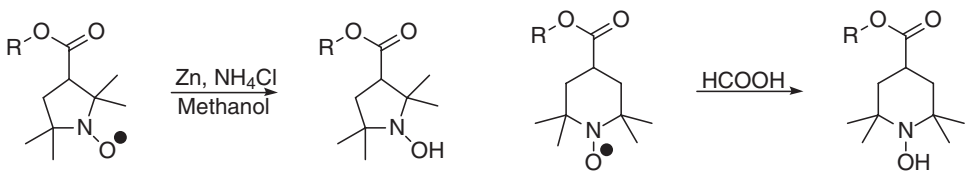

Scheme 2: Reduction of spin-labeled dexamethasone to the respective hydroxylamines.

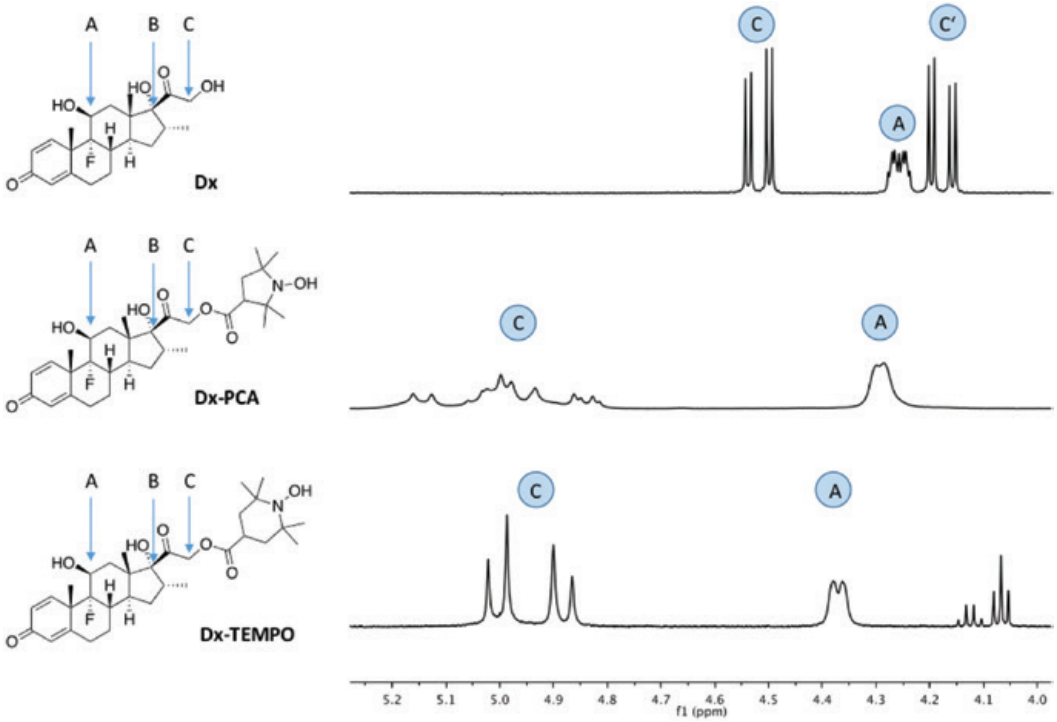

Fig. 2: Section of NMR spectra of Dx, Dx-PCA-NOH, and Dx-TEMPO-NOH (top to bottom) showing peak shift of CH^C, which indicates bond formation to the spin label at position C of dexamethasone. The strong line broadening in the second spectrum is caused by residual radicals in the sample. Dx-TEMPO: 4.07, 4.14 ppm solvent residues.

followed by the secondary alcohol in position A and the primary OH-group in position C. By steric demand, the reactivities are reversed, the tertiary alcohol is most hindered and the primary least. The esterification at position C indicates that our reaction conditions are controlled sterically rather than electronically.

For EPR measurements in *ex vivo* and cell studies for treatment of skin diseases, the molecular structure of the spin-labeled dexamethasone conjugates had to be stable for a few hours or days after application. We chose a HaCaT keratinocyte cell line as a test model. The stability of labeled conjugates was examined by treating HaCaT keratinocytes with a 0.1 mM Dx-TEMPO or Dx-PCA solution with PBS/glucose solution (2% DMSO content) for 180 min. PCA and TEMPO showed a stable EPR activity in a control experiment performed in cell medium in the same amount of time (for further details, see the SI). While Dx-TEMPO showed a fast EPR signal decay within 180 min, Dx-PCA showed a stable EPR signal with a marginal decrease to 93% of the initial EPR signal intensity (see Figure 3). This finding is in good agreement with previously published results reporting a limited stability and increased reactivity of TEMPO in comparison to PCA [6, 16].

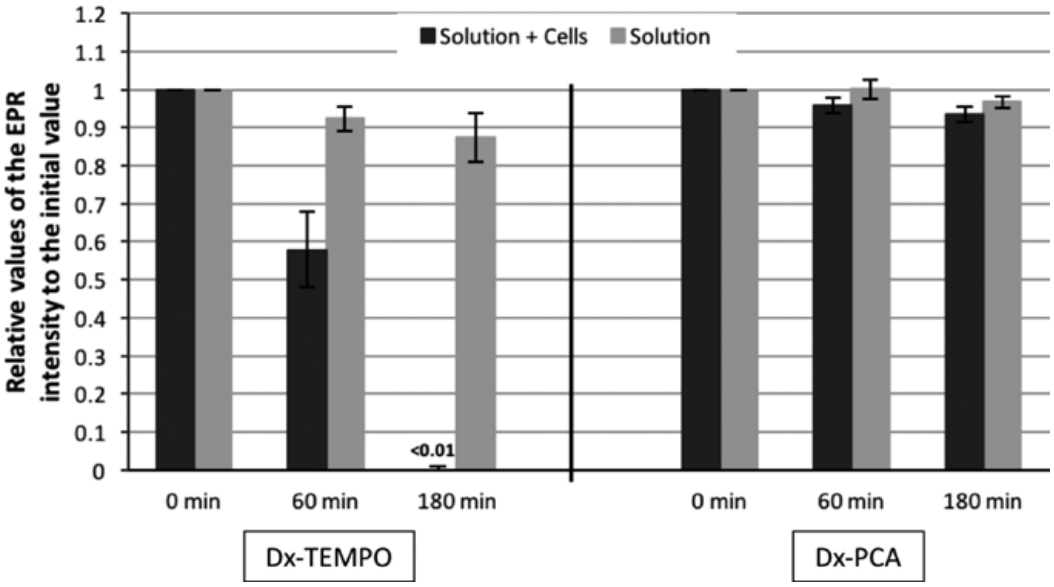

Fig. 3: Investigation of the time-dependent stability of Dx-TEMPO and Dx-PCA (0.1 mM) solution in PBS/glucose (2% DMSO content) after application to HaCaT cells (black bars). The EPR intensity was measured at different time points (0 min, 60 min, 180 min) and compared to the respective conjugates in PBS/glucose (2% DMSO content, gray bars) without HaCaT cells. Error bars represent standard errors with n = 3.

3 Conclusions

The applied protocols for spin-labeling dexamethasone lead to attachment of the spin labels PCA or TEMPO exclusively at the primary hydroxy group of dexamethasone in high yields, which renders the labeling protocol as highly reliable. EPR spectroscopy on HaCaT cells with a focus on the stability of the signal over time revealed that Dx-PCA was more suitable and stable than Dx-TEMPO for tracking the drug pathway over longer periods of time. While the EPR signal of Dx-TEMPO decreased to a non-detectable value within 180 min, Dx-PCA showed a slight decrease to only 93% of its initial intensity in the same period. We conclude that the more stable Dx-PCA is the conjugate of choice for biological studies on cells above 180 min. If studies are designed for observation periods below 60 min, Dx-TEMPO will lead to higher temporal resolution and should hence be chosen. EPR spectroscopy does allow not only to track dexamethasone in biological experiments, but also to investigate its chemical environment. Choosing the right stability of spin labels for EPR-based cellular uptake studies can lead to highly temporarily resolved results and give insights on the changing surrounding medium of dexamethasone upon uptake. The presented spin-labeled probe Dx-PCA is especially of high interest for drug delivery research, as it allows to gain deeper insight into the transport mechanisms of new drug delivery systems.

4 Experimental section

4.1 Synthesis of Dx-PCA

To a mixture of PCA in dry CH_2Cl_2, dexamethasone and DMAP were added under constant stirring. The resulting clear, pale orange solution was cooled to 0 °C for 10 min using an ice-bath. EDC was added, stirred for 5 min at 0 °C and afterwards allowed to reach r.t. The reaction mixture was refluxed for 4 h. Reaction was monitored using TLC (ethyl acetate). The reaction mixture was extracted with water three times. The collected organic phases were dried with Na_2SO_4, yielding a clear yellow solution that was afterwards evaporated to dryness under reduced pressure and redissolved in $CHCl_3$. The crude product was purified using hexane/ethyl acetate (gradient 1:1 to 1:2) as the mobile phase. Yield: 92%. For characterization see SI.

4.2 Synthesis of Dx-TEMPO

In an ACE pressure tube, carboxyl-TEMPO (43.5 mg, 0.217 mmol, 1.3 eq) was dissolved in dry CH_2Cl_2 (40 mL), followed by the addition of dexamethasone (66.0 mg, 0.166 mmol) and 4-DMAP (26.4 mg, 0.216 mmol, 1.3 eq) under constant stirring. The resulting clear, pale orange solution was cooled to 0 °C for 10 min using an ice-bath. EDC (41.7 mg, 0.218 mmol, 1.3 eq) was added, stirred for 5 min at 0 °C and afterwards allowed to reach r.t. The reaction mixture was stirred for 3 h and then heated under reflux. Reaction was monitored using TLC (hexane/ethyl acetate, 1:1). The reaction mixture was extracted with water three times. The collected organic phases were dried with Na_2SO_4, yielding a clear yellow solution which was afterwards evaporated to dryness under reduced pressure and dissolved in $CHCl_3$. The crude product was taken up on silica powder, charged into a chromatography column and purified using hexane/ethyl acetate (gradient 1:1 to 1:2) as the mobile phase. Yield: 88%. For characterization see SI.

4.3 Cell culture investigations

HaCaT (human adult low calcium high temperature, secondary keratinocytes) cells were cultivated in RPMI 1640 medium (Gibco, Invitrogen, Carlsbad, CA, USA) with supplements: 1% penicillin/streptomycin (Biochrom, Berlin, Germany), 2% glutamine (Biochrom) and 10% FCS (PAA Laboratories, Vienna, Austria). The cells were cultivated in an incubator at 37 °C, 5% CO_2 and 100% humidity until they reached a confluence of about 80% which was harvested by trypsination

(0.5% trypsin and 0.2% EDTA, Gibco), counted, seeded in new 75 cm^2 flasks, and/or used for further investigations [17]. To measure the EPR stability of Dx-TEMPO in cells, 1×10^6 cells were incubated in 1 mL PBS/glucose solution (2% DMSO content) with a 0.1 mM solution of the spin labeled drug in DMSO (final concentration of DMSO 2%) at 37 °C, 100% humidity, and 5% CO_2. After incubation, the cells were washed prior to EPR measurements. The baseline EPR intensity was measured by using glass capillaries (Hirschmann Laborgeräte GmbH & Co. KG, Eberstadt, Germany). TEMPO and PCA spin labels were tested for EPR signal stability in the above-described cell medium, and showed both no signal decay for 180 min. Hence, EPR measurements of TEMPO and PCA conjugates were performed over 180 min. Measurements for t = 0 min were started immediately after the application on HaCaT cells. EPR signal intensities represent intracellular spin levels. For further experimental details, see SI.

Acknowledgements: The authors acknowledge support from Deutsche Forschungsgemeinschaft (DFG)/German Research Foundation via SFB 1112, Projects A02 and B01.

References

1. M. C. Lukowiak, B. N. Thota, R. Haag, Biotechnol. Adv. **33** (2015) 1327.
2. I. N. Kurniasih, J. Keilitz, R. Haag, Chem. Soc. Rev. **44** (2015) 4145.
3. A. Ostrowski, D. Nordmeyer, A. Boreham, C. Holzhausen, L. Mundhenk, C. Graf, M. C. Meinke, A. Vogt, S. Hadam, J. Lademann, E. Rühl, U. Alexiev, A. D. Gruber, Beilstein J. Nanotechnol. **6** (2015) 263.
4. S. Hönzke, C. Gerecke, A. Elpelt, N. Zhang, M. Unbehauen, V. Kral, E. Fleige, F. Paulus, R. Haag, M. Schäfer-Korting, B. Kleuser, S. Hedtrich, J. Control Release **242** (2016) 50.
5. S. Saeidpour, S. B. Lohan, M. Anske, M. Unbehauen, E. Fleige, R. Haag, M. C. Meinke, R. Bittl, C. Teutloff, Eur. J. Pharm. Biopharm. **116** (2017) 94.
6. S. Lohan, A.-C. Lauer, S. Arndt, A. Friedrich, K. Tscherch, S. Haag, M. Darvin, H. Vollert, A. Kleemann, I. Gersonde, N. Groth, J. Lademann, S. Rohn, M. Meinke, Cosmetics **2** (2015) 286.
7. S. F. Haag, E. Fleige, M. Chen, A. Fahr, C. Teutloff, R. Bittl, J. Lademann, M. Schäfer-Korting, R. Haag, M. C. Meinke, Int. J. Pharm. **416** (2011) 223.
8. S. B. Lohan, N. Icken, C. Teutloff, S. Saeidpour, R. Bittl, J. Lademann, E. Fleige, R. Haag, S. F. Haag, M. C. Meinke, Int. J. Pharm. **501** (2016) 271.
9. B. P. Peters, F. G. Weissman, M. A. Gill, Am. J. Health Syst. Pharm. **57** (2000) 645.
10. A. Pyka, M. Babuska, M. Zachariasz, Acta Pol. Pharm. **63** (2006) 159.
11. G. Höfle, W. Steglich, Synthesis **11** (1972) 619.
12. W. Steglich, G. Höfle, Angew. Chem. Int. Ed. Engl. **8** (1969) 981.
13. W. Steglich, B. Neises, Angew. Chem. Int. Ed. Engl. **17** (1978) 522.
14. T. L. Kirley, H. B. Halsall, J. Steroid Biochem. **16** (1982) 133.
15. J. R. Dodd, A. E. Mathew, Steroids **42** (1983) 241.

16. T. Herrling, J. Fuchs, J. Rehberg, N. Groth, Free Radic. Biol. Med. **35** (2003) 59.
17. S. B. Lohan, S. Bauersachs, S. Ahlberg, N. Baisaeng, C. M. Keck, R. H. Müller, E. Witte, K. Wolk, S. Hackbarth, B. Roder, J. Lademann, M. C. Meinke, Eur. J. Pharm. Biopharm. **89** (2015) 201.

Supplemental Material: The online version of this article offers supplementary material (https://doi.org/10.1515/zpch-2017-1076).

Supporting Information

Spin-labeling of Dexamethasone: Radical Stability vs. Temporal Resolution of EPR-Spectroscopy on Biological Samples

Karolina A. Walker[†[a]], Michael L. Unbehauen[†[a]], Silke B. Lohan[b], Siavash Saeidpour[c], Martina C. Meinke[b], Reinhold Zimmer[a], Rainer Haag[a]*

[†]equal contribution

[a]Freie Universität Berlin, Institute for Chemistry and Biochemistry, Takustrasse 3, 14195 Berlin, Germany

[b]Department of Dermatology, Venerology and Allergology, Center of Experimental and Applied Cutaneous Physiology, Charité - Universitätsmedizin Berlin, Charitéplatz 1, 10117 Berlin, Germany

[c]Freie Universität Berlin, Department of Physics, Arnimallee 14, 14195 Berlin, Germany

*corresponding author: Rainer Haag, haag@chemie.fu-berlin.de

Materials: dexamethasone, PCA, TEMPO (Sigma Aldrich, Steinheim, Germany), 1-(3-dimethylaminopropyl)-3-ethylcarbodiimide hydrochloride (EDC, ≥ 99%, Carl Roth GmbH + Co. KG, Karlsruhe, Germany), 4-(dimethylamino)-pyridin (4-DMAP, 99%, Acros Organics, Acros Organics, Beel, Belgium) were used without further purification. Anhydrous DCM was taken from a MBraun MB SPS-800 solvent purification system.

Electron paramagnetic resonance spectroscopy: EPR spectroscopy of dexamethasone, Dx-TEMPO, and Dx-PCA was performed using an X-band EPR spectrometer (EPR spectrometer MiniScope MS 400, Magnettech, Berlin, Germany). The following parameter settings were used: microwave frequency (9.4 GHz), central magnetic field (336.12 mT), sweep width (7.59 mT), sweep time (20 s), modulation amplitude (0.05 mT), attenuation (30 dB), gain (200). Glass capillaries (Hirschmann Laborgeräte GmbH & Co. KG, Eberstadt, Germany) were completely filled with the liquid sample and sealed with a hematocrit sealing compound (Brandt, Wertheim, Germany). Mplot 2014-08-13 (Magnettech, Berlin, Germany) was used for the analysis of data.

Nuclear Magnetic Resonance Spectroscopy*:* ^{1}H and ^{13}C NMR spectra were recorded on a Bruker AMX 500 (Bruker Corporation, Billerica, MA, USA) or JEOL ECP 500 (JEOL GmbH, Freising, Germany). Tetramethylsilane was used for internal calibration at 125 MHz with complete proton decoupling.

Cell culture investigations: HaCaT (human adult low calcium high temperature, secondary keratinocytes) cells were cultivated in RPMI 1640 medium (Gibco, Invitrogen, Carlsbad, CA, USA) with supplements: 1% penicillin/ streptomycin (Biochrom, Berlin, Germany), 2% glutamine (Biochrom) and 10% FCS (PAA Laboratories, Vienna, Austria). The cells were cultivated in an incubator at 37 °C, 5% CO_2 and 100% humidity until they reached a confluence of about 80% which was harvested by trypsination (0.5% trypsin and 0.2% EDTA, Gibco), counted, seeded in new 75 cm^2 flasks, and/or used for further investigations.

To measure the EPR stability of Dx-TEMPO in cells, 1×10^6 cells were incubated in 1 ml PBS/ glucose solution (2% DMSO content) with a 0.1 mM solution of the spin labeled drug in DMSO (final concentration of DMSO 2%) at 37 °C, 100% humidity, and 5% CO_2. After incubation, the cells were washed prior to EPR measurements. The baseline EPR intensity was measured by using glass capillaries (Hirschmann Laborgeräte GmbH & Co. KG, Eberstadt, Germany). TEMPO and PCA spin labels were tested for EPR signal stability in the above-described cell medium, and showed both no signal decay for 180 min. Hence, EPR measurements of TEMPO and PCA conjugates were performed over 180 min. Measurements for t = 0 min were started immediately after the application on HaCaT cells. EPR signal intensities represent intracellular spin levels.

Synthesis of Dx-PCA

To a mixture of PCA in dry CH_2Cl_2, dexamethasone and DMAP were added under constant stirring. The resulting clear, pale orange solution was cooled to 0 °C for 10 min using an ice-bath. EDC was added, stirred for 5 min at 0 °C and afterwards allowed to reach r.t. The reaction mixture was refluxed for 4 h. Reaction was monitored using TLC (ethyl acetate). The reaction mixture was extracted with water three times. The collected organic phases were dried with Na_2SO_4, yielding a clear yellow solution that was afterwards evaporated to dryness under reduced pressure and redissolved in $CHCl_3$. The crude product was purified using hexane/ethyl acetate (gradient 1:1 to 1:2) as the mobile phase. Yield 92%.

mp: 230 °C

TLC R_f: 0.16 (Hex/EtOAc, 1:1)

MS (ESI-TOF): m/z calculated for $[M]^+$ 560.3024, found 560.3029, calculated for $[M+Na]^+$ 583.2916, found 583.2909, calculated for $[M+K]^+$ 599.2655, found 599.2644, calculated for $[2M+Na]^+$ 1143.5939, found 1143.5903, calculated for $[3M+Na]^+$ 1704.8996, found 1704.8964.

IR: ν = 1761, 1722 ($\nu_{C=O}$ ester), 1663 ($\nu_{C=O}$ Ring A), 1367 (ν_{N-O}), 1189, 1171, 1146 (ν_{C-O} ester), 984 cm^{-1} (ν_{C-F}).

Preparation for NMR Analysis: Dexa-PCA was reduced to its respective hydroxylamine by dissolving 19 mg (0.033 mmol) Dexa-PCA in 1 mL CD_3OD in a vial. NH_4Cl (11 mg, 0.2 mmol) and Zn powder (111 mg, 1.7 mmol) were added and the suspension was stirred for 2 h. Then the solution was filtered through a syringe filter, the solvent evaporated, and the compound redissolved in $CDCl_3$.

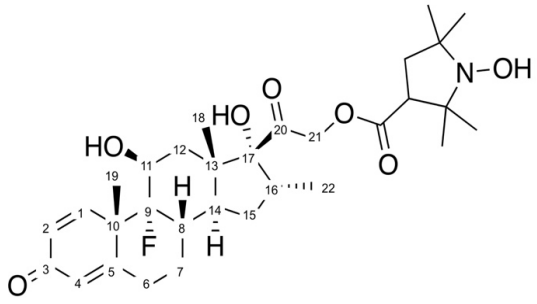

^{1}H-NMR (500 MHz, CD_3CN): δ (ppm) = 7.25 (d, J = 9.8 Hz, 1 H, C2-**H**), 6.23 (d, J = 9.8 Hz, 1 H, C1-**H**), 6.01 (m, 1 H, C4-**H**), 5.20 - 4.78 (m, 2H, C21**H**$_2$-OCO-PCA), 4.28 (m, 1 H, C11-**H** 3.32 (m, 2 H, C6-**H**), 3.00 (m, 1 H, C16-**H**), 2.64 (m, 1 H), 2.50 - 2.00 (7 H), 1.88-0.78 (26 H).

Synthesis of Dx-TEMPO

In an ACE pressure tube, carboxyl-TEMPO (43.5 mg, 0.217 mmol, 1.3 eq) was dissolved in dry CH_2Cl_2 (40 mL), followed by the addition of dexamethasone (66.0 mg, 0.166 mmol) and 4-DMAP (26.4 mg, 0.216 mmol, 1.3 eq) under constant stirring. The resulting clear, pale orange solution was cooled to 0 °C for 10 min using an ice-bath. EDC (41.7 mg, 0.218 mmol, 1.3 eq) was added, stirred for 5 min at 0 °C and afterwards allowed to reach r.t. The reaction mixture was stirred for 3 h and then heated under reflux. Reaction was monitored using TLC (hexane/ ethyl acetate, 1:1). The reaction mixture was extracted with water three times. The collected organic phases were dried with Na_2SO_4, yielding a clear yellow solution which was afterwards evaporated to dryness under reduced pressure and dissolved in $CHCl_3$. The crude product was taken up on silica powder, charged into a chromatography column and purified using hexane/ethyl acetate (gradient 1:1→ 1:2) as the mobile phase. Product was separated, yielding 84 mg (88% yield) of pure product.

mp: 259-263 °C

TLC R_f: 0.46 (Hex/EtOAc, 1:1)

MS (ESI-TOF): m/z calculated for $[M]^+$ 574.3175, found 574.3181, calculated for $[M+H]^+$ 575.3253, found 575.3252, calculated for $[M+Na]^+$ 597.3072, found 597.3091, calculated for $[M+K]^+$ 613.2812, found 576.2824.

IR: ν= 1742, 1719 ($\nu_{C=O}$ ester), 1664 ($\nu_{C=O}$ Ring A), 1380 (ν_{N-O}), 1194, 1171, 1159 (ν_{C-O} ester), 980 cm^{-1} (ν_{C-F}).

Preparation for NMR Analysis: A few drops of formic acid were added to the solution at least 30 minutes before analysis to reduce the radical to the respective hydroxylamine (reaction control via TLC).

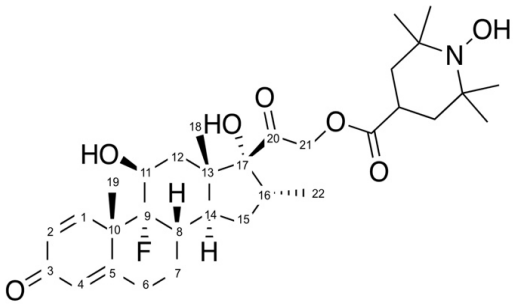

^{1}H-NMR (500 MHz, $CDCl_3$): δ = 7.30 (m, 1 H, C2-**H**), 6.40 (d, J = 9.4 Hz, 1 H, C1-**H**), 6.17 (m, 1 H, C4-**H**), 5.01, 4.88 (AB System, 2 H, J = 17 Hz, C21**H**$_2$-OCO-TEMPO), 4.39 - 4.38 (m, 1 H, C11-**H**), 4.07 (t, 1 H, -OCO-C**H**-(CH_2-$C(CH_3)_2$)$_2$-NOH), 3.10 - 3.00 (m, 2 H, C6-**H**), 2.66 - 2.60 (m, 1 H, C16-**H**), 2.40 (m, 3 H, C14-**H**, C12**H$_2$**), 2.25 - 2.10 (m, 5 H, C7-**H$_2$**, C15-**H$_2$**, C8-**H**), 2.06 (m, 3 H, C10-**Me**), 1.85 - 1.69, 1.44 - 1.42 (m, 12 H, TEMPO-**Me**), 1.04 (s, 3 H, C13-**Me**), 0.94 (s, 3 H, C16-**Me**) ppm.

3.3 Redox-sensitive Nanocarriers for the Controlled Release of Drugs in Inflammotory Skin Diseases

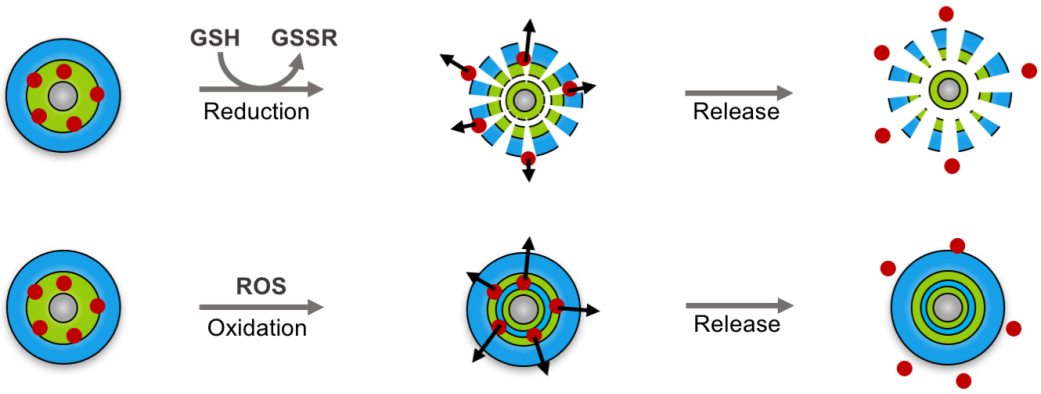

Author list:

Walker, K. A.; Rancan, F.; Mecking, S.; Quaas, E.; Vogt, A.; Haag, R.

Contribution:

Conception, synthesis, and analysis of the nanocarriers, experiments on performance and degradation behavior. Writing of manuscript and preparation of graphics and schemes.

Redox-sensitive Nanocarriers for Controlled Release of Drugs in Inflammotory Skin Diseases

Walker, K. A.; Rancan, F.; Mecking, S.; Quaas, E.; Vogt, A.; Haag, R.

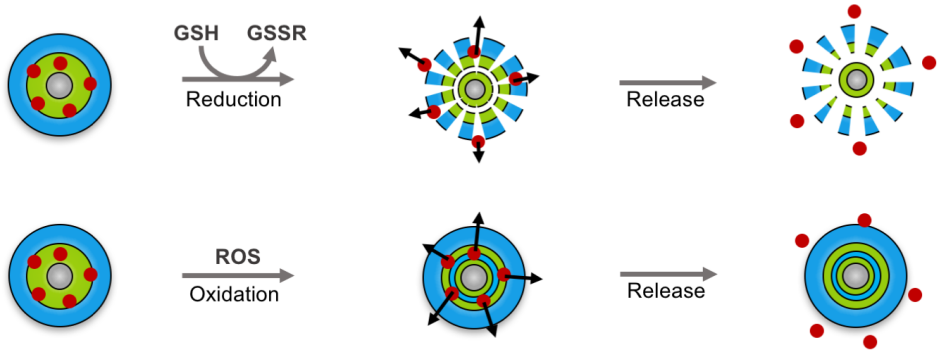

■ Introduction

Polymeric drug delivery systems aim at overcoming the limited solubility of drugs by entrapping them in a solubility-enhancing polymeric environment. Among the vast diversity of polymeric drug delivery systems, dendritic nanocarriers are considered as universal systems, as their architecture offers many benefits. Typically composed of a dendritic core molecule, surrounded by covalently attached linear amphiphilic molecules, i.e., the double shell, this Core Multishell nanocarrier (CMS) is a universal transporter, as its internal amphiphilic environment suits a wide range of both hydrophilic and hydrophobic drugs.[1] Furthermore, the internal cavities, the nanocarrier size, and flexibility are tunable by design, allowing for optimization of nanocarrier properties for specific drugs and controlled release adapted to the aimed biological target.[2] Drug release can be modified to achieve high local concentrations at the site of action and reduction of side effects by site-specific targeting, while chemical modifications of the nanocarrier can lead to a controlled or triggered mode of release. Whenever diseases are accompanied by pathological changes in endogenous chemical markers, nanocarriers can be designed to be responsive to these specific chemical markers. Skin has a natural compartmentalization of redox-active moieties, including thiols and disulfides, reactive oxygen species, and enzymes, which are relevant for maintaining the redox balance.[3] When skin diseases are accompanied by inflammation, biological and physical characteristic of the skin are altered, e.g., the skin barrier, its enzymatic activity, and the redox state.[4] In this work, we aimed at elucidating the potential of redox-gradients, which we hypothesized to have a different characteristic constitution compared to healthy skin. The redox gradient of the skin means the reductive and oxidative environment at different depths of the skin, represented mainly by the

molecules glutathione and various reactive oxygen species, respectively. The first case was chosen to be the targeted trigger for a reduction-sensitive CMS nanocarrier, capable of releasing encapsulated drugs at highly reductive sites in a triggered fashion. Glutathione is known to react with disulfides, resulting in the formation of a disulfide bond between GSH and one of the sulfur atoms of the disulfide, leaving back the other half of the disulfide as a thiol. This established reaction between GSH and a disulfide group was chosen as the basis for the reduction-sensitive CMS nanocarrier, as the disulfide has been reported to be an efficient functional group for reduction-sensitive drug delivery systems.[5-7] The complementary set of a reduction- and oxidation-sensitive CMS nanocarrier was intended to be chemically as similar as possible, to draw reliable conclusions when comparing both systems. For the complementary oxidation-sensitive CMS, we thus chose a thioether functional group as the oxidation-sensitive unit. Thioethers are sensitive to reactive oxygen species, and in studies with H_2O_2 as the oxidative species, thioether-based drug delivery systems have been successfully tested in vitro.[8-10] The oxidation of the thioether to sulfoxide is accompanied by a change in polarity from hydrophobic to hydrophilic, which is used as the mode of action for the oxidation-triggered release of drugs.[10-12]

■ Results and Discussion

Rational design of redox-sensitive nanocarriers

In this work, we synthesized a complementary pair of a reduction-sensitive and an oxidation-sensitive CMS nanocarrier for the triggered release of anti-inflammatory drugs at sites of inflammation. We hypothesize that these nanocarriers, both comprising sulfur-based redox-responsive functional groups, can release their cargo in a controlled fashion at the site of inflammation. We targeted at implementing the respective functional unit, disulfide or thioether, into the hydrophobic inner shell of the CMS nanocarriers (Fig.1).

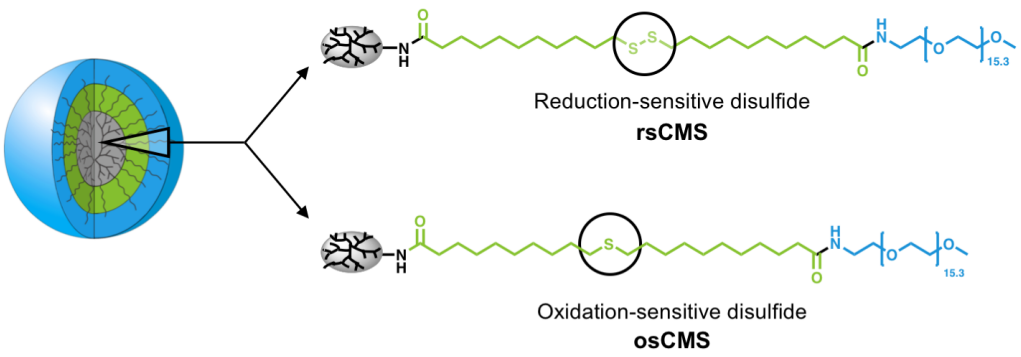

Fig. 1: Schematic represenation of a CMS nanocarrier and the complementary set of reduction-sensitive (rsCMS) and oxidation-sensitive osCMS with sulfur-based responsive groups.

The chosen anti-inflammatory drugs are hydrophobic, and in previous studies we observed hydrophobic drugs to be located preferably either at the interface between the inner shell and the outer shell or in between the hydrophobic inner shell building blocks. Locating the redox-sensitive moieties at the middle of the inner shell and thus close to the encapsulated drug, will allow a direct reaction of the encapsulated drugs to its changed environment.

Synthesis of building blocks and convergent synthesis of CMS nanocarriers

The CMS nanocarriers were synthesized by a convergent synthetic approach, combining two pre-synthesized building blocks. The outer shell mPEG-NH_2 **2** was obtained by a modification of the hydroxyl group of mPEG-OH via mesylation and reduction to the amine terminated equivalent. Subsequent amidation with a four-fold excess of previously dimerized disulfide **3** lead to the monoamide mPEG-C11-SS-C11-COOH **4** and its diamide side product. As the side product is a dead end to the following reaction steps, the purification approach was focused in removal of the unreacted starting material disulfide **3**, achieved by the repetitive sedimentation of the product in diethyl ether at 0°C. As the solubility of the product and its diamide equivalent is dominated by the solubility of mPEG, diamide could not be removed from the product, and the statistical fraction of 2 mol% diamide remained in the waxy product. After transformation of the carboxylic acid to an NHS-ester, the double shell building block was conjugated via amide bond formation to the core building block hPG-NH_2, leading to the respective rsCMS nanocarrier **9** (Scheme 1). Extensive purification via dialysis in methanol led to a CMS with narrow PDIs between 1.1 and 1.2 (see Table 1). Control nanocarrier cCMS **11** with an non-reductive inner shell as well as fluorescently labeled rsCMS-(FITC) **10** were synthesized analogous to rsCMS **9**. Thioether-containing osCMS **16** was synthesized by a photoinitiated thiol-ene reaction between the pre-made building blocks hPG-A-C8-ene **15** and mPEG-A-C11-SH **13**, while both building blocks were synthesized by amide bond formation between the respective NHS-activated acid and the aminated hPG-NH_2 or mPEG-NH_2 **2**. Even though thiol-ene reactions generally qualify as click reactions,[13] the photoinitiated thiol-ene reaction leading to osCMS had to be performed for 13 h to reach a conversion of 75 %. The reaction takes place at sterically demanding conditions, with the alkene covering 70 % of a 10 kDa hyperbranched polymeric scaffold and the complement thiol attached to the mPEG with 16 repeating units. Thus, the thiol-ene probably cannot be expected to take place under “click”-type conditions, as already discussed for the general consideration of radical thiol-ene between two polymers by Koo et al.[14] In agreement with literature, the thiol was used in excess and TCEP was added to reduce the disulfide of **13**, making the thiol accessible for the reaction. The resulting osCMS was extensively purified via dialysis in MeOH for 14 days, exchanging the solvent 18 times. Alternatively, the nanocarrier can be purified using ultrafiltration in 50% MeOH-DCM, which proved to be more efficient. The successful thiol-ene reaction was confirmed by ^{1}H NMR, and a peak broadening of the methylene-protons adjacent to the

thioether bond shows the lowered relaxation time of the methylene protons due to attachment to a polymer. The fluorescently-labeled analog osCMS-(FITC) **17** was obtained by post-synthesis functionalization of osCMS **16** with FITC in 10 % DMSO-PBS, as a labeling of the core building block prior to the photoinitiated thiol-ene reaction would have led to a bleaching of the dye during the UV irradiation in the synthesis of osCMS. Purification of osCMS-(FITC) using ultrafiltration in MeOH gave the product with a labeling ratio of 2-3 FITC molecules per osCMS.

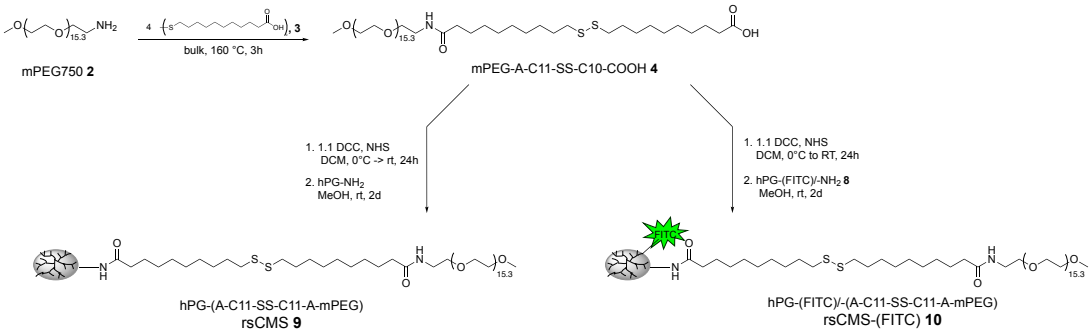

Scheme 1: Synthesis of rsCMS and rsCMS-(FITC).

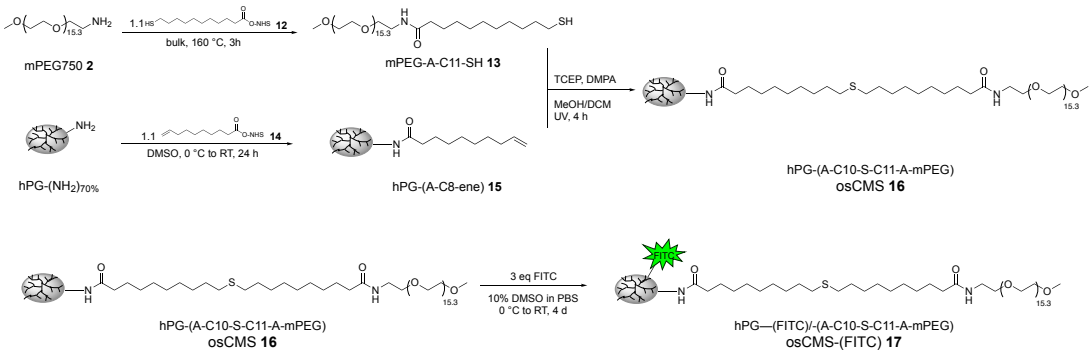

Scheme 2: Synthesis of osCMS and osCMS-(FITC).

The molar mass of the various CMS nanocarriers depend on the amount of conjugated double shell, reflected by the degree of functionalization D_f. Assuming a full conversion of all 95 amine groups of hPG-NH_2 and a resulting D_f of 100 %, all nanocarriers have a theoretical molar mass of above 100 kg mol^{-1} (see Table 1). However, these values were neither confirmed by GPC nor ^1H NMR (for calculation of M based on NMR measurements, please see SI), but instead indicated a lower degree of functionilization with lower molar masses. We also observed that the different synthesis approaches lead to different conjugation efficiencies. Reactions between the full double shell **4** and the highly aminated hPG results in poor conversions, reflected by the mediocre D_f value of 41 %. Introducting half of the inner shell to hPG on the one side and the other half to the mPEG outer shell results in a osCMS with signifcantly higher

conversions and a D_f of 75 %. The higher D_f value can be attributed to two effects: first, the introduction of the C11 half inner shell to hPG-NH_2 increases the distance between the terminal groups on the hPG surface, which facilitates parallel thiol-ene reactions at multiple functional groups. Second, the alkene-terminated spacer and its thiolated counterpart of double shell **13** have similar polarities, making an interaction of the reaction partners easier. Despite the deviant molar mass of osCMS **16** and rsCMS **9**, GPC analysis gave comparably similar M_n. This has been observed before and shows the frequent limitation of GPC performed with linear standards in the analysis of hyperbranched polymers.[15-16]

Table 1: Characterization data for redox and control CMS nanocarriers.

CMS	M, theor. [a] [$gmol^{-1}$]	M_n, NMR [b] [$gmol^{-1}$]	D_f, NMR [b] [%]	M_n, GPC [c] [$gmol^{-1}$]	M_w/M_n	$D_{H, vol}$ [d] [nm]
rsCMS **9**	120800	54700	41	39400	1.1	16
osCMS **16**	116400	89500	75	41500	1.2	6
cCMS **11**	116000	124000	77	39200	1.1	n.a.

a: assuming 100% conversion; b: determined via ^{1}H NMR; c: determined via GPC; d: measured at c = 5mg mL^{-1} in PBS at 25°C.

Despite osCMS having an almost twice as high functionalization as rsCMS, it shows a significantly smaller hydrodynamic diameter, as determined with DLS. This does not necessarily reflect a difference in diameter of the pure CMS molecule, as the distance of one terminal methoxy group to another on the opposite site of a perfectly stretched nanocarrier should be the same for both types of nanocarriers. The only difference in architecture is their degree of functionalization and the topology of their inner shell building blocks. The latter should not have a significant influence on the overall CMS size, as both the thioether and the disulfide based molecules have a comparable number of atoms and a comparably similar distance between the carboxylic end groups (2.67 nm and 2.66 nm, see Fig S17). Contrary to that, the difference in functionalization might influence the size. A higher amount of outer shell building blocks might lead to intramolecular interactions between the individual arms, making them coil and hence leading to a lower D_h, as seen in the case of osCMS. At a lower degree of functionalization, the arms can expand, increasing the electric double layer and leading to increased values of the apparent hydrodynamic diameter. Lederer et al. also reported hyperbranched molecules with a low number of arms to show off-sized hydrodynamic diameters in DLS, based on inaccurate assumptions related to the radii of hyperbranched molecules.[17]

Nanocarrier performance in vitro: Drug loading content, stimulus-triggered release and carrier integrity

The performance of the CMS nanocarriers in terms of drug loading and in vitro triggered release was tested with the fluorescent model drug Nile Red, and the anti-inflammatory drug dexamethasone. The drug loading content DLC was tested at various CMS concentrations and showed DLC values in the expected range. Independent of the type of CMS nanocarrier, a general trend can be observed depending on the drug. CMS nanocarriers strongly enhance the solubility of poorly water-soluble drugs like nile red, while the natural solubility of dexamethasone (natural solubility 0.085 mg mL^{-1}) is amplified by a factor of two to four.

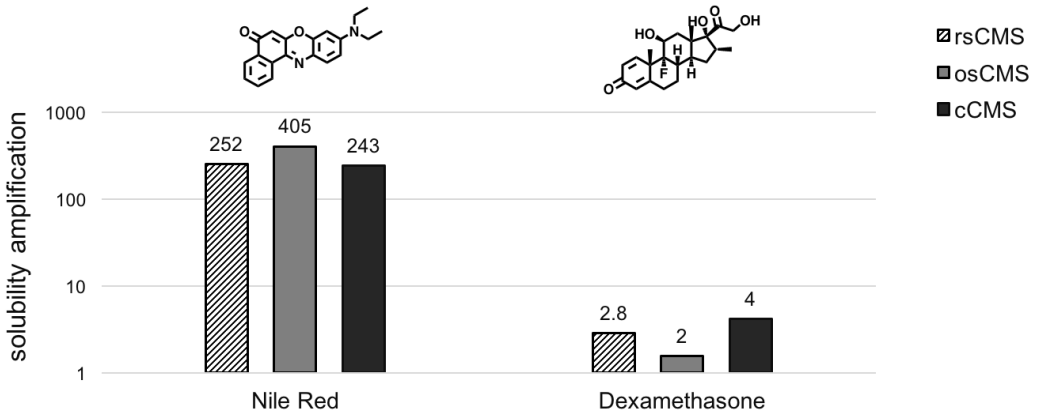

Fig. 2: Amplification of the natural solubility in water of nile red and dexamethasone by encapsulation in rsCMS (dashed), osCMS (grey), and cCMS (black). The solubility amplification was calculated as the ratio of the encapsulated drug to the drug's natural solubility. The natural solubility was determined by blank encapsulations in the absence of CMS nanocarriers. DLC values of dexamethasone were obtained by HPLC measurements of the CMS solutions and comparison with calibration curves. DLC of nile red was obtained by UV Vis in MeOH. Nile red and dexamethasone were encapsulated via film method.

In vitro screening of stimulus-triggered release of cargo from CMS

The proof of concept stimulus-triggered release of drugs from CMS nanocarriers was performed using nile red as a model drug. The fluorescent dye nile red is sensitive to its surrounding polarity and has a poor water solubility. Encapsulated into a nanocarrier, its water solubility can be enhanced, which results in a higher nile red fluorescence intensity compared to an aqueous solution of the dye. The release of the dye from the nanocarrier can thus be followed by measurement of the fluorescence intensity, and the wavelength of the emission maximum over time allows reports the dye's movement from the amphiphilic double shell to the surrounding medium.[18] The redox environment of a cell and its redox state in a biological context is a complex system, which still is not fully understood.[19-20] The most abundant redox-couple in a cell is the GSH/GSSG couple. With a ratio of 100:1, it is not at equilibrium, but constantly maintained in steady-state by enzymes, such as γ-glutamylcysteine synthetase or

glutathione synthetase.[19] The cytosolic concentration of glutathione reported varies between 1 and 11 mM. As depicted in Fig. 3, we chose a concentration of 10 mM for the proof-of-concept study of the triggered release. The curve shows a slight decrease in encapsulated NR, decreasing by 4 % within 24 h, as determined by fluorescence measurements. This is not the speed of release that we initially anticipated, but it reflects the limitation of using GSH in solution. We used a 10 mM GSH PBS solution (pH 7.4), with a GSH molarity cited as the cytosolic concentration of GSH, and a 10-fold concentration of PBS (pH 7.4), to balance the acidifying properties of GSH. However, the tested disulfide cleavage is a redox system, consisting of a thiol-disulfide interchange (GSH cleaving rsCMS disulfide) and the 2GSH/GSSG oxidation.[21] In the absence of enzymes, which in vivo maintain a constant concentration of free GSH, in vitro systems cannot reproduce the in vivo kinetics of the disulfide cleavage. Nevertheless, a higher release of NR by 10 mM GSH compared to the control in absence of GSH can be seen. The concept of triggered release by reducing agents from rsCMS is supported by the significantly faster release of NR by incubation with the reducing agent TCEP, leading to 70 % release of NR from rsCMS after 4 h, and overall 90 % within 24 h. The sigmoidal shape indicates an auto accelerated release process, as the reducing agent TCEP can access the disulfide easier, when the outer shell is cleaved.[12, 22-23] The oxidation-triggered release from osCMS was studied in a 1 % H_2O_2, solution in deionized water. Hydrogen peroxide was studied as an oxidant for polythioethers by Locatelli et al. and is reported to selectively oxidize thioethers to sulfoxide, whereas further oxidation to sulfones was not observed.[24] 80 % of the encapsulated NR was released within 24 h and the kinetics reflect a slower but sustained release, as compared to the exponential decrease of the NR decay curve in the case of rsCMS with TCEP. We also controlled the chemical composition of the nanocarriers to support the hypothesized stimulated chemical change of the CMS nanocarriers underlying the stimulus-triggered release. The chemical change of osCMS **11** was investigated with ^{1}H NMR after 24 h of incubation with 1 % H_2O_2. In line with previously published data, a shift of the methylene signal adjacent to the thioether group from 2.5 ppm downfield to 2.8 ppm was observed, indicating the oxidation to the respective sulfoxide (data not shown).[23] In contrast to a complete oxidation to sulfoxides within 3 h at comparable conditions as published by Herzberger et al.,[23] the complete oxidation of osCMS is not completed after 24 h. This might indicate a hindered access of H_2O_2 to the thioether, which is located in the hydrophobic inner shell. As the chemical integrity of the osCMS nanocarrier is not influenced by oxidation, the speed of NR release upon oxidation does not change with time, which contrasts with the auto accelerated reduction-triggered release of NR from rsCMS (Fig. 3). The osCMS sample remained clear even after complete oxidation, and UV Vis spectroscopy of the oxidized osCMS (oxCMS) in water shows a disappearance of the sulfide R-S-R absorption (Fig. S19).

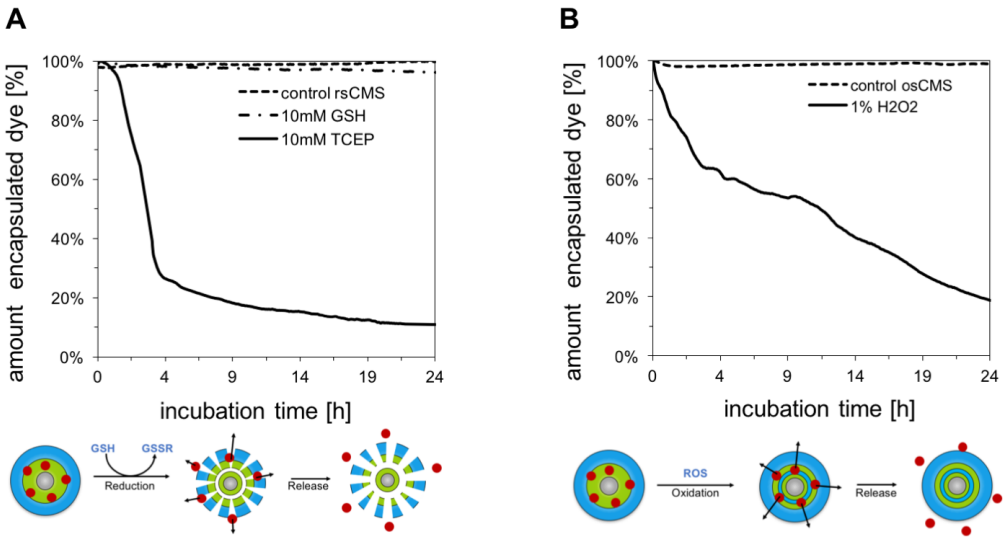

Fig. 3: Kinetics of stimulus-triggered release of nile red from rsCMS (A) and osCMS (B) measured with fluorescence spectroscopy over 24 h; NR release was followed by fluorescence intensity decay at NR emission maximum at 630 nm (A) or 639 nm (B); Inserts below release curves show respective mechanism of triggered release of nile red (red balls); release experiments of rsCMS (A) were performed in 10xPBS, pH 7.4, and release experiments of osCMS (B) were performed in diH_2O.

In the case of rsCMS, the reduction by TCEP leads to a partial degradation of the nanocarrier and possible crosslinking.After 24 h of TCEP incubation, the previously clear sample got turbid, and measurement of the size via DLS of the filtered sample showed only fragments with a size less than 1 nm (data not shown). Reduction by GSH, limited by the low fraction of reductive, non-oxidized GSH, as discussed above, was observed by following the methylene signal adjacent to disulfide at 2.8 ppm shifting to 2.6 ppm, assigned to the methylene group of the alkyl inner shell, adjacent to thiol (Fig. S18).

Skin Penetration experiments of rsCMS-(FITC) on ex vivo human skin

Nanoparticles which showed penetration of the skin barrier often contain surfactants for stabilization of the nanoparticles in solution or emulsion. The surfactants non-negligibly contribute to the enhanced skin permeation by widening pores and thus allowing the nanoparticles to pass hydrophilic pores or the lipid bilayer.[25] Our formulation is free of additional surfactant and does not use skin penetration enhancers, such as dimethyl sulfoxide or ethanol. Penetration of reduction-sensitive rsCMS-(FITC), covalently labelled with fluorescein molecules, and loaded with red-fluorescent NR was tested. Ex vivo human skin from the abdomen was incubated with an aqueous solution of rsCMS-(FITC) for 16 h and the FITC and NR distribution in skin sections was analyzed with a confocal laser scanning microscope. Post-operative skin was either used fresh after removal or treated with UV for 3 min to induce depletion of the antioxidant defense. Uptake of NR is different for UV treated

and non-treated skin. In line with previous publications, a decreasing concentration from SC to dermis is observed in both cases (Fig. 4).

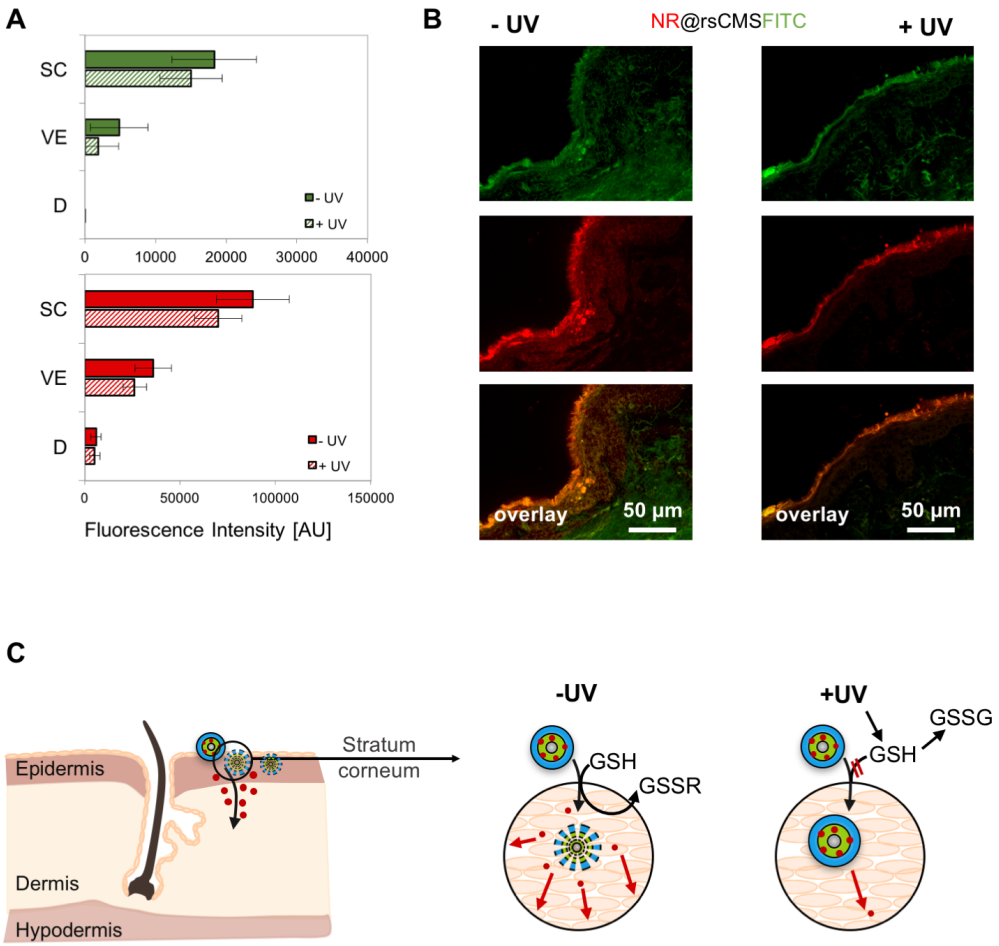

Fig. 4: Skin penetration of nile red-loaded (NR) rsCMS-(FITC). The penetration of NR in CMS nanocarriers as aq. solution was assessed 16 h after topical application on excised human ex vivo skin; **A:** Skin sections were analyzed with confocal laser scanning microscopy; Investigations on CMS nanocarriers covalently labeled with FITC (B, green) and loaded with NR (B, red) revealed that most nanocarriers remained on the skin surface and in the upper stratum corneum, while free NR diffused into the epidermis, and dermis. Nanocarrier-associated FITC fluorescence dropped towards deeper layers of the skin; error bars show SD, n=8; **B:** representative skin section for –UV and +UV; **C**: Hypothesized mode of NR@rsCMS-(FITC) triggered release, depending on tested skin type (fresh skin, -UV; irradiated skin, +UV); GSH cleaves rsCMS disulfide, triggering release of NR (-UV); upon irradiation with UV, GSH is oxidized to GSSG by generated ROS, and thus rsCMS disulfide cleavage is limited, and less NR is released from rsCMS (+UV).

However, in UV-treated skin a lower fluorescence of NR in the epidermis is observed. In healthy skin, epidermis is reported to have a high amount of glutathione reductase, with a decrease going to deeper layers.[26] If skin is irradiated with UV and compounds containing free thiols are oxidized, their role as reductants for disulfides is diminished. Thus, rsCMS is expected to be cleaved in a slower rate in the epidermis of UV-treated skin compared to non-

treated skin. Our observation supports this hypothesis that the cleavage of rsCMS and successive release of NR is slowed down in a skin environment with a depleted reductive capacity.

■ Conclusion

Synthesis of rsCMS and osCMS resulted in chemically comparable CMS nanocarriers with similar sized and narrow molecular weight distributions. The proof of concept in vitro study supported the hypothesized triggered release of the fluorescent model drug nile red, analyzed by time-dependent fluorescence spectroscopy measurements. The reduction-triggered release of nile red from rsCMS was shown with glutathione, but the release with TCEP was more pronounced and lead to 90 % release of the encapsulated dye within 24 h. Oxidation-triggered release of nile red from osCMS was observed after incubation with 1% H_2O_2 and reflected a more sustained release upon oxidation of the nanocarrier. Preliminary penetration experiments of NR@rsCMS-(FITC) were performed on both fresh ex vivo human skin and UV-irradiated human skin. UV irradiation triggers formation of ROS species, thus mimicking the change in the physicochemical penetration barrier of inflammed skin. A limited penetration into skin by NR@rsCMS-(FITC) was observed when the skin was previously irradiated. The ROS generation by UV irradiation dimerizes free GSH, and so less GSH is available for the reduction of rsCMS, resulting in a less pronounced Nile Red release in deeper stratum corneum skin layers. This is in line with our expectations, and shows that a layer of increased GSH concentration is present in deeper layers of the stratum corneum (SC), which triggers a release of NR in the case of the non-irradiated skin, but prevents deeper penetration of the rsCMS for the case of irradiation. Nevertheless, a study for the comparison of rsCMS to osCMS penetration needs to be performed to give conclusive results on the hypothesized natural gradients of reductants and oxidants in skin.

■ Materials and Methods

Materials

All chemicals were purchased from Sigma Aldrich (Sigma Aldrich, Steinheim, Germany) or Carl Roth (Carl Roth GmbH + Co. KG, Karlsruhe, Germany) and used without further purification, unless otherwise stated. hPG-NH_2 was synthesized in the group of Prof. Rainer Haag by Anja Stöshel and Cathleen Schlesener according to Roller et al.[27] Solvents were purchased as HPLC grade and used without further purification. Anhydrous solvents were either purchased as ultra-dry solvents from Acros Organics, or taken from a MBraun MB SPS-800 solvent purification system. Dialysis was performed in benzoylated cellulose dialysis tubes from Sigma-Aldrich (width: 32 mm, MWCO = 1000 g/mol).

Instruments

GPC

Chromatography was performed using a Shimadzu (Kyoto, Japan) liquid chromatography (LC) set up with degasser, pump, auto sampler, column oven, and differential refractometer. Three PolarSil columns (PSS Polymer Standards Service GmbH, Mainz, Germany; PolarSil 8 mm × 300 mm, 100, 1000, 3000 Å with 5 µm particle size) using DMF with 0.3% LiBr and 0.6% acetic acid as the mobile phase at a flow rate of 1 $mL \cdot min^{-1}$ were used to analyze polymer samples. The columns were operated at 40 °C with the RI detector set to the same temperature. The calibration was performed by using polystyrene standard (PSS, Mainz, Germany). Samples were measured at a concentration of 10 $mg \cdot mL^{-1}$ injecting 100 µL. LC solution software from Shimadzu was used for data acquirement and interpretation.

HPLC

Chromatography for the analysis of dexamethasone content was performed on a Knauer Smartline-HPLC system with an internal UV absorption detector (λ = 254 nm), equipped with a Gemini RP C18 column (Phenomenix, 250 nm × 4.6 mm, particle size: 5 µm) and run with an acetonitrile-water (40:60) mixture as the mobile phase at a flow rate of 1.0 $mL \cdot min^{-1}$ under isocratic regime. The data were analyzed with Chromgate software (Knauer, Berlin, Germany).

^{1}H NMR, ^{13}C NMR

Spectra were recorded on a Bruker AMX 500 (Bruker Corporation, Billerica, MA, USA), Jeol ECP 500 (JEOL (Germany) GmbH, Freising, Germany), or a Bruker Avance 400 spectrometer (Bruker Corporation, Billerica, MA, USA) (at 295 K). ^{13}C NMR and overnight measurements spectra were recorded on a Bruker Avance 500 spectrometer, or a Bruker Avance III 700 (Bruker Corporation, Billerica, MA, USA). Tetramethylsilane was used for internal calibration at 125 MHz with complete proton decoupling. Spectra were analyzed with MestReNova 7 (Mestrelab Research S.L., Santiago de Compostela, Spain). Chemical shifts of impurities were assigned based literature.[28] MestreNova 7.11 was used for data analysis and interpretation.

DLS

Measurements were performed using a Malvern Zetasizer Nano instrument (Malvern Instruments Ltd, Worcestershire, UK) equipped with a He-Ne laser (633 nm) using backscattering mode (detector angle 173°). The CMS nanocarriers were dissolved in diH_2O, PBS or MEOH mixed by a Vortex shaker for 2 min, and 100 µL of the solution was added to a disposable Plastibrand® micro cuvette (Brand GmbH + Co KG, Wertheim, Germany) with a round aperture. The autocorrelation functions of the backscattered light fluctuation were analyzed using Zetasizer DLS software from Malvern Instruments Ltd (Worcestershire, UK) to determine the size distribution by intensity and volume. The measurements were performed at

25 °C, equilibrating the system on this temperature for 120 s. Mean diameter values were obtained from three different runs of 12 measurements each, and 12 s each measurement.

UV Vis

Measurements were performed on an Agilent Cary 8454 UV-Visible spectrophotometer using Suprasil® (Hellma analytics) or Spectrosil® (Carl Roth) half-micro quartz cuvettes with a 4 x 10 mm light path. Data was collected using the UV-Vis ChemStation Software.

Fluorescence

Measurements were performed on a Scinco S-3100 spectrometer at 37 °C or 25 °C, maintained with a Haake F3 thermostat. Measurements were performed using Suprasil® (Hellma analytics) half-micro quartz cuvettes with a 4 x 10 mm light path and stopper, and an excitation band width of 3 nm and emission band width of 5 nm was chosen for the measurements.

Confocal Laser Scan Microscopy of Skin Sections

Skin sections were observed at a magnification of × 200 with a confocal laser microscope (LSM 700, Zeiss, Germany). Pictures of at least 15 sections per donor were taken with a charge coupled device (CCD) camera using always the same settings. Pictures were then analyzed using the ImageJ software. The mean fluorescence intensity (MFI) of areas in SC, viable epidermis, and dermis was measured. At least 10 MFI values for each samples and control from three different donors were calculated. Similar results were obtained in all experiments with skin from different donors. Representative results from one donor are shown in Figure 4. Averages and standard deviations were reported in the diagrams using Microsoft Excel.

Methods

Skin Penetration Experiments

Abdominal skin was obtained from Caucasian donors after written informed consent and approval from the institutional review board of Charité-Universitätsmedizin Berlin (approval EA1/135/06, renewed on January 2018) in adherence with the Declaration of Helsinki principles. The skin samples were examined macroscopically and microscopically to be intact without damage, scars or stretch marks. Subcutaneous fat was partially removed and skin pieces of 1x1 cm were stretched on polystyrene plates covered with parafilm. Part of the skin pieces were irradiated with a UV lamp (switched on 5 min before irradiation) for 3 min at 2.5 cm distance, which corresponds to a dose of 1.59 mW/cm^2 UV and 2.1 mW/cm^2 UVB. This dose is supposed to induce a sun burn *in vivo* and thus to produce an amount of free radicals that is enough to deplete all GSH in SC.

Thereafter, 10 µL of a 5 mg/mL of NR@rsCMS-(FITC) suspension was applied on the surface of 0.5x0.5 cm of skin. The skin was placed in a humidified chamber and incubated at 37°C for 16 h. After incubation, the non-penetrated suspension was carefully removed with a paper towel and one tape stripping. Samples were frozen in liquid nitrogen and skin cryosections of 5 µm thickness were prepared using a microtome (2800 Frigocut-N, Reichert-Jung, Heidelberg, Germany).

Synthesis of rsCMS and cCMS

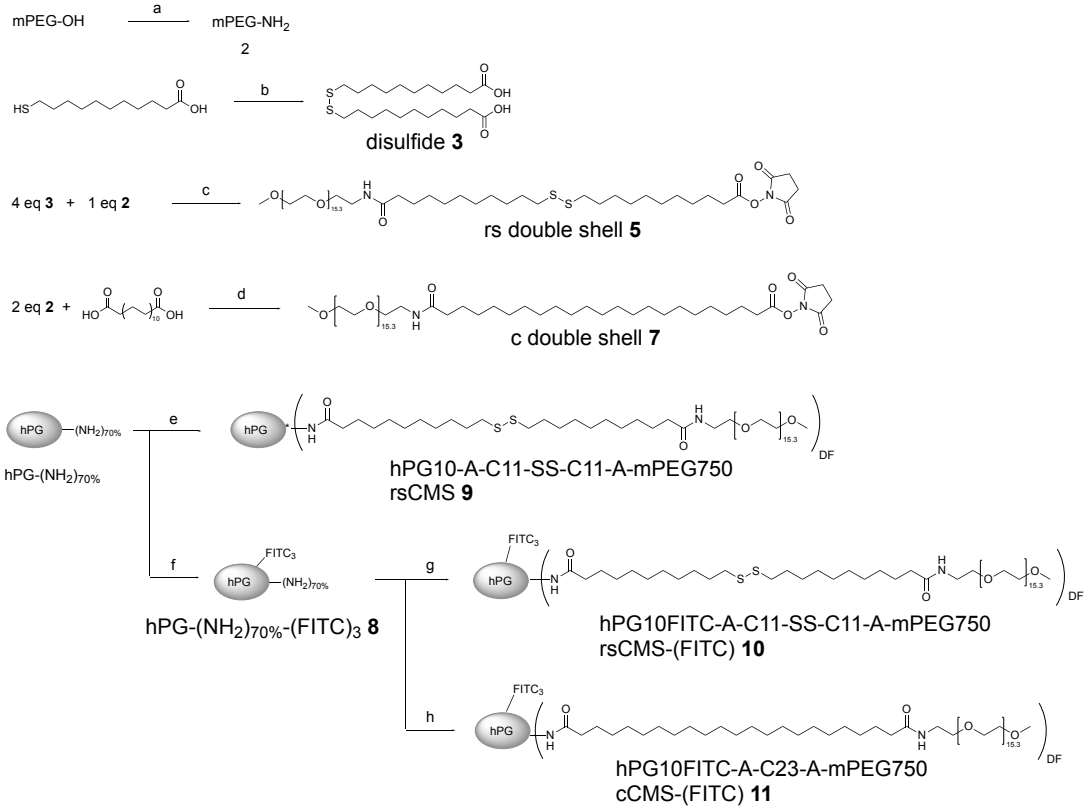

Scheme 3: Detailed synthesis of rsCMS, rsCMS-(FITC) and cCMS-(FITC); **a**: 1. MsCl, TEA, 0 °C to rt, 4 d; 2. aq. NH_3, 2 d; **b**: I_2, KI, NaOH, MeOH, rt, 30 min; **c**: 1. bulk, 190 °C, 3 h, 2. DCC, NHS, DCM, 0 °C to rt, 24 h; **d**: 1. bulk, 160 °C, 3 h, 2. DCC, NHS, DCM, 0 °C to rt, 24 h; **e**: 1.6 eq **5**, MeOH, rt, 2 d; **f:** 0.03 eq FITC, DMSO, rt, 2 d; **g**: 1.1 eq **5**, MeOH, rt, 2 d; **h**: 1.1 eq **7**, MeOH, rt, 24 h.

α-Methoxy ω–methane sulfonyl poly (ethylene glycol)

Methoxy poly (ethylene glycol) (14.1 g) was dried at 50°C in high vacuum for 1.5 h to remove traces of H_2O, then 150 mL anhydrous DCM was added to the melt and the clear solution was cooled with an ice bath. Mesylchloride (2.584 g, 1.2 eq) was added dropwise, followed by slow addition of triethylamine (11.434 g, 15.7 mL, 5 eq) using a dropping funnel, and the ice bath was removed. The reaction was quenched with H_2O after stirring for four days at rt. Extraction of the organic phase with Brine (3 x 30 mL) under addition of a few drops of EtOH for emulsion separation, followed by washing of the organic phase with diH_2O (7x 20 mL), drying with Na_2SO_4 and evaporation of the solvent under reduced pressure yielded a wax-like product (11.06 g, 71% yield). ^{1}H NMR (500 MHz, DCM-d2): δ = 4.35 (C**H$_2$**-OSO_2CH_3), 3.73 (C**H$_2$**-CH2-OSO_2CH_3), 3.56-3.66 (PEG backbone), 3.50 (C**H$_2$**-O-CH_3), 3.33 (O-C**H$_3$**), 3.06 (OSO_2-C**H$_3$**), 1.69 (impurity) ppm.

α-Methoxy ω–amino poly (ethylene glycol) ***2***

Terminally aminated PEG was synthesized following the protocol of Elbert et al.[29] Mesylated mPEG **1** (4.535 g, 5.5 mmol) was dissolved in 40 mL aq. NH_3 (25%) and the flask was sealed with a rubber septum. For a full conversion, the solution was stirred for two days at rt. The flask was left opened to let ammonia evaporate over the weekend. After raising the pH of the solution to 13 using aq. NaOH (1M), the product was extracted with DCM (3 x 100 mL). The organic phases were collected, dried with Na_2SO_4, and filtered using a cellulose filter. The solvent was evaporated under reduced pressure at 40 °C. The product mPEG-NH2 **2** was obtained as a white wax-like solid (3.739 g, 91% yield). ^{1}H NMR (500 MHz, DCM-d2): δ = 3.4-3.9 (C**H$_2$** PEG backbone), 3.3 (PEG-OC**H$_3$**), 2.8 (PEG-CH_2-C**H$_2$**-NH_2) ppm.

11-(10'-carboxy-decyldisulfanyl) undecanoic acid ***3***

Disulfide **3** was synthesized following the protocol of T. Belser et al. (J. Am. Chem. Soc. **2005**, 127, 8720-8731). HS-$C_{10}H_{20}$-COOH (7.32 g, 34 mmol) was dissolved in 200 mL MeOH and solid NaOH (1.34 g, 1 eq), I_2 (4.254 g, 0.5 eq) and KI (166 mg, 0.03 eq) were added under stirring. The milky yellow solution was stirred for 2 h at rt and then decolored with 20 mL saturated aq. Na_2SO_3. The solvents were removed under reduced pressure at 50 °C and the resulting aq. slurry was dispersed in DCM, acidified to pH 1 with 1M HCl. The aqueous phase was decanted, and the organic phase was extracted four times with diH_2O using a separation funnel. The organic phases were combined and dried, yielding a white powdered product. The separated aqueous phases were combined, extracted thrice with DCM and the organic phases were combined and dried, yielding additional white powdered product. The two fractions were combined to one product **3** after ^{1}H NMR confirmed purity of both fractions (6.367 g, 87% yield). ^{1}H NMR (500 MHz, Aceton-d_6): δ = 2.72 (-C**H$_2$**-SS-C**H$_2$**-), 2.28 (-C**H$_2$**-COOH), 1.72-1.32 (-S-CH_2-(C**H$_2$**)$_8$-CH_2-COOH) ppm.

Double shell mPEG-C_{11}-SS-C_{10}-COOH ***4***

mPEG-NH_2 **2** (2.614 g, 3.5 mmol) was dried at 150 °C in high vacuum for 4h, then disulfide **3** (6.067 g, 4 eq) was added to the melt. After stirring the bulk mixture at 190°C in high vacuum under vigorous stirring for 3.5 h, the mixture was cooled and at 70 °C 70 mL toluene was added under stirring. After the resulting dispersion reached rt, it was centrifuged at 4000 U min^{-1} for 10 min to increase sedimentation. The supernatants were collected and the centrifugation protocol was repeated twice. The solvent of the collected supernatants was removed under reduced pressure at 40°C, the solid was dissolved in Et_2O at 35 °C and then cooled down to 4 °C, leading to a dispersion. The solid was filtered off using a folded cellulose filter, dissolved in $CHCl_3$ and then dried again, dissolved in Et_2O at 35°C again and the cold extraction protocol was repeated twice. The solid product was finally solubilized in $CHCl_3$, and the solvent was removed at reduced pressure to yield a wax-like dishell **4** (m=1.253 g, 30% yield, contains

max. 2 mol% diamide product mPEG-C_{11}-SS-C_{11}-mPEG). ^{1}H NMR (400 MHz, MeOH-d_4): δ = 3.82 (CONH-CH_2-C**H$_2$**-), 3.54-3.64 (PEG backbone), 3.36 (O-C**H$_3$**), 2.68 (C**H$_2$**-S-S-C**H$_2$**), 2.45 (C**H$_2$**-SH, traces of disulfide cleavage product), 2.28 (C**H$_2$**-COOH), 2.19 (C**H$_2$**-CONH), 1.33-1.72 (HOOC-CH_2-(C**H$_2$**)$_8$-C**H$_2$**-SS-C**H$_2$**-(C**H$_2$**)$_8$-CH_2-CONH) ppm.

mPEG-C_{11}-SS-C_{10}-CO-NHS ***5***

Dishell **4** (1.253 g) was dried at high vacuum for 20 min, dissolved in 10 mL anhydrous DCM, N-hydroxysuccinimid (138 mg, 1.1 eq) was added under dry conditions (Schlenk technique) and then the solution was cooled to 0 °C. Dicyclohexylurea (0.244 g, 1.1 eq) and 10 mL anhydrous DCM were added and the solution was stirred over night at rt. Solid DCU was filtered off, and the filtrate was concentrated under reduced pressure to yield wax-like NHS-activated dishell **5** (1.344 g, 100% yield). ^{1}H NMR (500 MHz, MeOH-d_4): δ = 3.77 (CONH-CH_2-C**H$_2$**-O), 3.54-3.64 (PEG backbone), 3.36 (O-C**H$_3$,** CONH-C**H$_2$**-CH_2-O), 2.84 (-N-(CO-C**H$_2$**-C**H$_2$**-CO)-), 2.79 (impurity), 2.69 (C**H$_2$**-S-S-C**H$_2$**), 2.62 (C**H$_2$**-COO-NHS), 2.47 (CH2-SH from disulfide cleavage), 2.19 (C**H$_2$**-CONH-PEG), 1.33-1.76 (NHS-OOC-CH_2-(C**H$_2$**)$_8$-C**H$_2$**-SS-C**H$_2$**-(C**H$_2$**)$_8$-CH_2-CONH) ppm.

mPEG-C_{22}-COOH ***6***

mPEG-NH_2 **2** (0.533 g, 1.3 mmol) was dried at 80 °C in high vacuum overnight in a Schlenk flask, HOOC-$C_{21}H_{42}$-COOH (0.5 g, 2 eq) was added under Argon flow, and the bulk mixture was heated to 160 °C. When ninhydrin staining of the amine group indicated full conversion of the amine after 3 h, the bulk mixture was cooled down and MeOH was added under stirring at rt. The dispersion was repeatedly separated under centrifugation at 4000 U min^{-1} at 4 °C, and the collected supernatants were concentrated under reduced pressure. After short column purification (DCM-MeOH 9:1, R_f=0.7) the wax-like product dishell **6** was obtained, containing 10 mol% dimer by-products (223 mg, 28%). ^{1}H NMR (500 MHz, DMSO-d_6): δ = 7.79 (CON**H**), 3.37-3.66 (PEG backbone), 3.24 (O-C**H$_3$**), 2.18 (C**H$_2$**-COOH), 2.04 (C**H$_2$**-CONH), 1.23-1.46 (HOOC-CH_2-(C**H$_2$**)$_{19}$-CH_2-CONH) ppm.

mPEG-C_{22}-CO-NHS ***7***

Dishell **6** (0.223 g, 0.2 mmol) and N-hydroxysuccinimid (0.025 g, 1.1 eq) were dissolved in 10 mL anhydrous DCM, cooled to 0 °C and DCC (0.045 g, 1.1 eq) was added under stirring, and the ice bath was removed. After stirring for 24 h, formed DCU was filtered off and the filtrate was concentrated under reduced pressure and dried under high vacuum, yielding NHS-activated dishell **7** (0.204 g, 90% conversion, 85% yield).

^{1}H NMR (400 MHz, DMSO-d_6): δ = 3.68 (PEG backbone), 3.38 (O-C**H$_3$,** CONH-C**H$_2$**-CH_2-O), 2.80 (-N-(CO-C**H$_2$**-C**H$_2$**-CO)-), 2.64 (C**H$_2$**-COO-NHS), 2.17 (C**H$_2$**-CONH-PEG), 1.45–1.71 (NHS-OOC-CH_2-(C**H$_2$**)$_{19}$-CH_2-CONH) ppm.

hPG-$(NH_2)_{0.7}$/-$(FITC)_{0.06}$ ***8***

A stock solution of FITC in DMSO (700 µL, 0.0089 mmol, 0.03 eq) was added under stirring to 1.5 mL of a hPG-NH_2 solution in DMSO. The clear orange solution was stirred for 24 h in dark. Purification by dialysis in the dark (RC, MWCO 1-2 kDa) against MeOH for 7 days gave a pure product, and the absence of unbound FITC was confirmed with TLC (20% MeOH in DCM).

rsCMS ***9*** *& rsCMS-(FITC)* ***10*** *& cCMS-(FITC)* ***11***

Synthesis of nanocarriers was conducted in analogue reactions, and is exemplified for synthesis of rsCMS. To a solution of NHS-activated dishell **5** (1.444 g, 1.6 eq) in 5 mL MeOH, 3.259 mL of a of hPG-NH_2 solution in MeOH (c=20 mg/mL, 65 mg, 1 eq amine groups) was added. The solution was stirred for two days at rt, transferred to a dialysis tubing (RC, MWCO 1-2 kDa) and dialysis was performed for three days against 600 mL MeOH, exchanging MeOH five times. ^{1}H NMR (500 MHz, MeOH-d_4): δ = 7.89 (N**H**CO), 3.49-3.78 (hPG and PEG backbone C**H$_2$** and C**H**), 3.36 (OC**H$_3$**), 3.31 (MeOH), 2.71 (C**H$_2$**-S-S-C**H$_2$**), 2.45 (C**H$_2$**-SH), 2.24 (hPG-NHCO-C**H$_2$**), 2.20 (C**H$_2$**-CONH-PEG-Ome), 1.34-1.70 ppm.

Synthesis of osCMS and osCMS-(FITC)

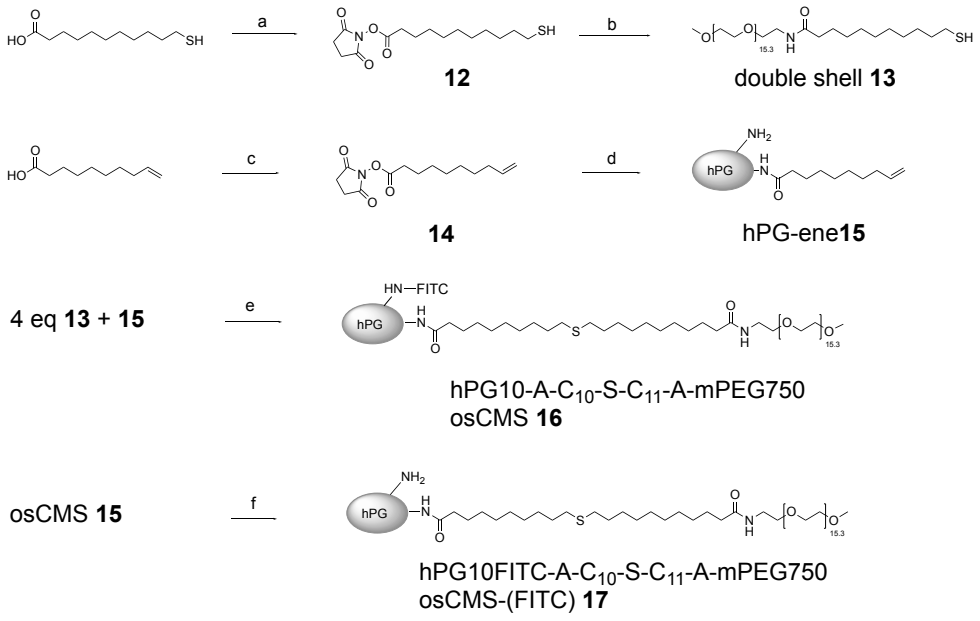

Scheme 4: Detailed synthesis of osCMS and osCMS-(FITC); **a**: NHS, EDCI, dry DCM, o.n.; **b**: 0.9 eq mPEG-NH_2 **2**, DMSO, 0 °C to rt, 24 h; **c**: NHS, EDCI, dry DCM, o.n.; **d**: 0.9 eq hPG-NH_2, DMSO, 0 °C to rt, 24 h; **e**: TCEP, DMPA, MeOH/DCM, UV, 4 h; **f**: 0.03 eq FITC, 10% DMSO in PBS, rt, 2 d.

α-mercapto ω–NHS dodecanoic acid SH-C10-CO-NHS ***12***

N-hydroxysuccinimid (1.740 g, 1.1 eq) was added to a solution of 11-mercaptoundecanoic acid (3.066 g, 14 mmol) in anhydrous DCM (200 mL). While cooling the mixture with an ice bath, EDCI (2.895 g, 1.1 eq) was added, the mixture was stirred at 0°C for 15 min, and subsequently

allowed to reach rt. After 18 h, measurement of ^{1}H NMR confirmed quantitative conversion and the product in DCM was extracted with aq. $NaHSO_4$ (2.5%) seven times, followed by washing of the collected organic phases with Brine and diH_2O. The collected organic phase was dried with $MgSO_4$, filtered with a folded cellulose filter and the solvent was removed under reduced pressure, yielding a white solid (4.143 g, 94% yield). ^{1}H NMR (500 MHz, DCM-d_2): δ = 3.54 (impurity), 2.80 (-N-(CO-C**H$_2$**-C**H$_2$**-CO)-), 2.68 (C**H$_2$**-SS-C**H$_2$**), 2.59 (NHS-OCO-C**H$_2$**), 2.50 (C**H$_2$**-SH), 2.33 (C**H$_2$**-COOH), 1.72 (NHS-OCO-C**H$_2$**-C**H$_2$**), 1.61 (C**H$_2$**-C**H$_2$**-SH), 1.29-1.37 (NHS-OCO-CH_2-CH_2-(C**H$_2$**)$_6$-CH_2-CH_2-SH) ppm.

*Double shell mPEG-C11-SH **13***

To a solution of activated acid **12** in DMF-H_2O (1:1, 5 mL), amine **2** (5 g, 6.7 mmol) in a satured $NaHCO_3$ solution in DMF-H_2O (1:1, 15 mL) was added dropwise over 20 min under stirring. 1H NMR measurement confirmed quantitative conversion after 48h. The solvent of the reaction mixture was removed under reduced pressure, the resulting crude product was dissolved in 100 mL $CHCl_3$ and the organic phase was washed with Brine seven times (20 mL each), and four times with diH_2O (20 mL each). After extracting further product from the collected aq. phases with $CHCl_3$, the combined organic phases were dried with MgSO4, filtered with a folded cellulose filter and the solvent was removed under reduced pressure, yielding a wax-like yellow product, consisting of a mixture of the targeted product and its dimer form (6.246 g, 99% yield). ^{1}H NMR (500 MHz, CDCl3): δ = 3.42-3.76 (PEG backbone CH2), 3.36 (PEG-OMe) 2.65 (C**H$_2$**-SS-C**H$_2$**), 2.50 (C**H$_2$**-SH), 2.15 (C**H$_2$**-CONH), 1.59 (CH_2-C**H$_2$**-CONH, C**H$_2$**-CH_2-SH), 1.35-1.25 (NHCO-CH_2-CH_2-(C**H$_2$**)$_6$-CH_2-CH_2-SH) ppm.

*NHS-activated decenoic acid **14***

To a solution of NHS (3.722 g, 1.1 eq) and 9-decenoic acid (5.049 g, 30 mmol) in 5% DMSO-DCM (130 mL), EDCI (11.27 g, 2 eq) was added under stirring at 0°C. Full conversion was reached after 24h, as confirmed by 1H NMR. The reaction mixture was extracted with aq. $NaHSO_4$ (2.5%), and the organic phase was washed repeatedly to remove DMSO from the organic phase. After five cycles of aq. NaHSO4 wash (20-40 mL each), the collected organic phases were washed twice with Brine and twice with diH_2O. The collected organic phases were subsequently dried with $MgSO_4$, filtered, and the solvent was removed under reduced pressure, yielding clear, light yellow crystal needles with a smell of rotten potatoes (4.654 g, 59% yield). ^{1}H NMR (500 MHz, CD_2Cl_2): δ= 5.81 (C**H**=CH_2), 4.91-5.01 (CH=C**H$_2$**), 2.80 (-N-(CO-C**H$_2$**-C**H$_2$**-CO)-), 2.71 (impurity), 2.59 (OCO-C**H$_2$**-), 2.42, 2.30 (impurity), 2.04 (C**H$_2$**-CH=CH_2), 1.72 (OCO-CH_2-C**H$_2$**-), 1.33- 1.40 (OCO-CH_2-CH_2-(C**H$_2$**)$_4$-CH_2-CH=CH_2) ppm. ^{13}C NMR (126 MHz, CD_2Cl_2) = 169.84 (N-(**C**O-CH_2-CH_2-**C**O)-), 169.40 (**C**OO), 139.78 (**C**H=CH_2**)**, 114.46 (CH=**C**H_2), 34.29 (**C**H_2-CH=CH_2), 31.45 (OCO-**C**H_2-), 29.46, 29.39, 29.26

(OCO-CH_2-CH_2-(**C**H_2)$_4$-CH_2-CH=CH_2), 26.20 (N-(CO-**C**H_2-**C**H_2-CO)-), 25.15 (OCO-CH_2-**C**H_2-) ppm.

hPG-(NHCO-C_7H_{14}-CH=CH_2)$_{0.7}$ ***15***

A solution of hPG-NH_2 (0.1 g, 0.945 mmol NH_2) and $NaHCO_3$ (0.08 g) in DMSO (5 mL) was added dropwise to a solution of activated acid **14** in DMSO (2.5 mL). The clear yellow solution with dispersed $NaHCO_3$ was stirred at rt for five days, during which a yellow slur precipitated. The solvent was decanted. The slur was dissolved in 10% THF-MeOH (15 mL) and the crude product was purified by dialysis for three days against 10% THF-MeOH using a benzoylated dialysis tubing (MWCO 1-2 kDa). The solvent was removed under reduced pressure, and the product was obtained as a clear yellow viscous melt (0.165 g, 75% conversion, 68% yield). The product was stored as a solution in 20% DCM-MeOH. ^{1}H NMR (500 MHz, MeOH-d_4): δ = 5.81 (CH=C**H$_2$**), 4.96 (C**H**=CH_2), 3.53 (hPG backbone), 2.22 (NHCO-C**H$_2$**), 2.05 (C**H$_2$**-CH=CH_2), 1.59 (NHCO-CH_2-C**H$_2$**), 1.33 (NHCO-CH_2-CH_2-(**C**H_2)$_4$-CH_2-CH=CH_2) ppm.

osCMS ***16***

Reducing agent TCEP (0.454 g, 1.7 eq) was added to a solution of alkene **15** (0.145 g, 0.93 mmol ene) and thiol **13** (3.728 g, 4 eq) in 20% DCM-MeOH (12 mL) and the resulting mixture was degassed by an Argon flow through the solution for 2h. Initiator DMPA (0.121 g, 0.5 eq) was added under Argon and the solution was degassed for another 15 min. Closed with a septum and equipped with an Argon balloon, the flask was placed in the focal point of an UV lamp and the reaction mixture was irradiated at 80 W under stirring for 6 h. ^{1}H NMR measurements showed incomplete conversion, and so TCEP (400 mg) and DMPA (60 mg) were added and the reaction was irradiated once more under the same conditions for 7h. DCM was removed from the reaction mixture at reduced pressure and the resulting mixture in 20 mL MeOH was transferred to a benzoylated RC dialysis tubing (MWCO 1-2 kDa) and the product was dialyzed against 500 mL MeOH for 14 days, exchanging the solvent 18 times. After GPC confirmed high purity of the product, the product was removed from the dialysis bag, MeOH was removed and exchanged for diH_2O (3mL), yielding 5 mL of a yellow product stock solution with c=40 mg/mL (200 mg in total, 20% yield). ^{1}H NMR (500 MHz, MeOH-d4) = 3.43-3.85 (hPG and PEG backbone) 3.36 (OC**H$_3$**), 2.52 (C**H$_2$**-S-C**H$_2$**), 2.20 (broadened: hPG-NHCO-C**H$_2$**, defined triplet: C**H$_2$**-CONH-mPEG), 2.06 (impurity), 1.33-1.78 (NHCO-CH_2-(C**H$_2$**)$_7$-CH_2-S-CH_2-(C**H$_2$**)$_8$-CH_2-CONH) ppm. ^{13}C NMR (126 MHz, MeOH-d_4, 1024 scans) = 71.57 (PEG backbone), 40.39 (hPG backbone), 30.49 (alkyl backbone).

osCMS-(FITC) ***17***

FITC stock solution in DMSO (104 µL, 5 mg/mL, 520 µg, 3 molecules per CMS) was added to a stirring solution of osCMS **16** in PBS (1.111 µL, 36 mg/mL, 40 mg) at 4°C, and the mixture was stirred at rt in the dark for 4 days. Purification of the product by column chromatography

(Sephadex G25), followed by ultrafiltartion in MeOH (RC membrane, MWCO 3 kDa) gave the fluorescently-labelled product osCMS-(FITC) in quantitative yields. The product was free of unbound FITC, as shown by TLC and stored in the dark as a stock solution in MeOH.

Characterization of nanocarriers

GPC

Molar mass distributions of dishell, hPG-NH_2 and CMS were analyzed by GPC with DMF as the mobile phase. Compounds were dried, dissolved in DMF to a final concentration of 10 mg/mL and filtered using a 0.45 µm RC syringe filter.

DLS

Sizes of nanocarriers were measured with dynamic light scattering (DLS) at 25 °C. Samples in PBS or MeOH were measured directly after dissolution of dry samples to final concentrations of 1 mg/mL and 5 mg/mL, without filtration of the sample. Samples were stored at rt in glass vials.

Quantification of FITC labeling

The amount of covalently bound FITC molecules to hPG-NH_2 was determined via UV Vis measurements of the hPG-$(NH_2)_{0.7}$/-$(FITC)_{0.06}$ conjugate **8**. The conjugate was dissolved in PB buffer pH 9.0 (0.1 M KH_2PO_4, 300 mM KCl, 1 M KOH until pH 9.0, and 10 % DMSO to ensure solubilization of hPG, to a final concentration of c (hPG-$(NH_2)_{0.7}$-$(FITC)_{0.06}$) = 1.76 mg/mL or c (amine) = 16.7 mM and the absorption spectrum was measured at 25 °C in a glass cuvette. Comparison of the absorption maximum of FITC at 499 nm to the calibration curve of FITC in the identical PB buffer pH 9.0 gave a FITC concentration of c (FITC)= 1.41 mM, or 7.6 FITC molecules per hPG-NH_2 molecule. The conjugate and free FITC were dissolved in a PB buffer at pH 9.0 to maintain an equilibrium shift of the pH-sensitive FITC molecule to its dianion form. To prevent effects of the local pH buffer capacity of amine groups of hPG-NH_2 on the absorption of FITC, a high salt concentration of 300 mM KCl was chosen.[30]

Drug Encapsulation

Encapsulation of NR and Dexamethasone via the film method

The solvent of a 200 µL NR stock solution (5 mg/mL in EtOH, 1 mg drug) was slowly evaporated under reduced pressure. The thin film was covered with 3 mL of a CMS stock solution in diH_2O (1 mg/mL or 5 mg/mL), and the mixture was stirred at rt and 1200 rpm for 24 h. The dispersion was filtered using a 0.45µm RC syringe filter to remove insoluble NR. The filtered sample was stored at 4 °C in the dark. Blank encapsulations were conducted analogue to drug encapsulation, but using diH_2O instead of aq. CMS samples.

DLC via UV-Vis

For the determination of the drug loading content, 200 µL NR@CMS solution were freeze-dried in an Eppendorf tube, dissolved in 1 mL MeOH and the absorption spectrum of the diluted sample was measured. If the intensity of the absorption maximum was E>1, the sample was further diluted. The concentration of NR in the sample was determined using Lambert-Beer Law. Drug loading content (DLC) is calculated as shown in SI.

DLC via HPLC

60 µL of the filtered DXM@CMS solutions were diluted with 40% acetonitrile. The concentration of the drug in solution was determined using a calibration curve of Dexamethasone in 60 % H_2O-ACN (concentration range: 0.5-0.0039 mg/mL, with linear fit R^2>99.9%). Calibration curves were freshly prepared and measured prior to sample measurements.

In vitro Proof of Concept: Triggered Release

Release of Cargo: NR@rsCMS + 10 mM TCEP

500 µL of a 5 mg/mL NR@rsCMS solution in diH_2O was diluted 1:1 with a 20 mM TCEP in 20-fold concentrated PBS (set to pH 6.4 with 310 µL 1M KOH) to yield 1 mL of a 2.5 mg/mL NR@rsCMS with 10 mM TCEP (8-fold excess of TCEP towards SS bonds) in 10-fold concentrated PBS at pH 6.4. The fluorescence measurement at 37 °C was started directly after dissolution, and spectra were taken every 300 s for 24 h.

Release of Cargo: NR@rsCMS + 10 mM GSH

500 µL of a 5 mg/mL NR@rsCMS solution in diH_2O was diluted 1:1 with a 20 mM GSH in 20-fold concentrated PBS (set to pH 7.4 with 220 µL 1M KOH) to yield 1 mL of a 2.5 mg/mL NR@rsCMS with 10 mM GSH (8-fold excess of GSH towards SS bonds) in 10-fold concentrated PBS at pH 7.4. The fluorescence measurement at 37 °C was started directly after dissolution, and spectra were taken every 300 s for 24 h.

Release of Cargo: NR@osCMS + 1 % H_2O_2

500 µL of a 5 mg/mL NR@osCMS solution in diH_2O was diluted 1:1 with a 2 % H_2O_2 in diH_2O to yield 1 mL of a 2.5 mg/mL NR@rsCMS with 1 % H_2O_2. The fluorescence measurement at 37 °C was started directly after dissolution, and spectra were taken every 300 s for 24 h.

Controlled release experiments

Controllled release experiments were conducted with the respective nanocarriers at a concentration of 2.5 mg/mL in the respective identical solvent, but in absence of the reducing or oxidating agent. The respective fluorescence measurements at 37 °C were started directly after dissolution, and spectra were taken every 300 s for 24 h.

References

1. Radowski, M. R.; Shukla, A.; von Berlepsch, H.; Böttcher, C.; Pickaert, G.; Rehage, H.; Haag, R., Supramolecular aggregates of dendritic multishell architectures as universal nanocarriers. *Angew Chem Int Edit* **2007,** *46* (8), 1265-1269.
2. Kurniasih, I. N.; Keilitz, J.; Haag, R., Dendritic nanocarriers based on hyperbranched polymers. *Chemical Society Reviews* **2015,** *44* (12), 4145-4164.
3. Ogura, R.; Knox, J. M.; Griffin, A. C.; Kusuhara, M., The concentration of sulfhydryl and disulfide in human epidermis, hair and nail. *The Journal of investigative dermatology* **1962,** *38*, 69.
4. Fuchs, J.; Zollner, T.; Kaufmann, R.; Podda, M., Redox-modulated pathways in inflammatory skin diseases. *Free Radical Biology and Medicine* **2001,** *30* (4), 337-353.
5. Etrych, T.; Kovář, L.; Šubr, V.; Braunová, A.; Pechar, M.; Chytil, P.; Říhova, B.; Ulbrich, K., High-molecular-weight Polymers Containing Biodegradable Disulfide Bonds: Synthesis and In Vitro Verification of Intracellular Degradation. *Journal of Bioactive and Compatible Polymers* **2010,** *25* (1), 5-26.
6. de Vries, W. C.; Grill, D.; Tesch, M.; Ricker, A.; Nusse, H.; Klingauf, J.; Studer, A.; Gerke, V.; Ravoo, B. J., Reversible Stabilization of Vesicles: Redox-Responsive Polymer Nanocontainers for Intracellular Delivery. *Angew Chem Int Ed Engl* **2017,** *56* (32), 9603-9607.
7. Xia, J.; Du, Y.; Huang, L.; Chaurasiya, B.; Tu, J.; Webster, T. J.; Sun, C., Redox-responsive micelles from disulfide bond-bridged hyaluronic acid-tocopherol succinate for the treatment of melanoma. *Nanomedicine* **2018,** *14* (3), 713-723.
8. Casado, N.; Hernández, G.; Sardon, H.; Mecerreyes, D., Current trends in redox polymers for energy and medicine. *Progress in Polymer Science* **2016,** *52*, 107-135.
9. Song, C.-C.; Du, F.-S.; Li, Z.-C., Oxidation-responsive polymers for biomedical applications. *J. Mater. Chem. B* **2014,** *2* (22), 3413-3426.
10. Lee, S. H.; Gupta, M. K.; Bang, J. B.; Bae, H.; Sung, H. J., Current progress in Reactive Oxygen Species (ROS)-Responsive materials for biomedical applications. *Adv Healthc Mater* **2013,** *2* (6), 908-915.
11. Lallana, E.; Tirelli, N., Oxidation-Responsive Polymers: Which Groups to Use, How to Make Them, What to Expect From Them (Biomedical Applications). *Macromolecular Chemistry and Physics* **2013,** *214* (2), 143-158.
12. Khutoryanskiy, V. V.; Tirelli, N., Oxidation-responsiveness of nanomaterials for targeting inflammatory reactions. *Pure and Applied Chemistry* **2008,** *80* (8), 1703-1718.
13. Hoyle, C. E.; Bowman, C. N., Thiol–ene click chemistry. *Angewandte Chemie International Edition* **2010,** *49* (9), 1540-1573.

14. Koo, S. P.; Stamenović, M. M.; Prasath, R. A.; Inglis, A. J.; Du Prez, F. E.; Barner-Kowollik, C.; Van Camp, W.; Junkers, T., Limitations of radical thiol-ene reactions for polymer–polymer conjugation. *Journal of Polymer Science Part A: Polymer Chemistry* **2010,** *48* (8), 1699-1713.
15. Mangold, C.; Dingels, C.; Obermeier, B.; Frey, H.; Wurm, F., PEG-based multifunctional polyethers with highly reactive vinyl-ether side chains for click-type functionalization. *Macromolecules* **2011,** *44* (16), 6326-6334.
16. Niederer, K.; Schüll, C.; Leibig, D.; Johann, T.; Frey, H., Catechol Acetonide Glycidyl Ether (CAGE): A Functional Epoxide Monomer for Linear and Hyperbranched Multi-Catechol Functional Polyether Architectures. *Macromolecules* **2016,** *49* (5), 1655-1665.
17. Lederer, A.; Burchard, W.; Khalyavina, A.; Lindner, P.; Schweins, R., Is the universal law valid for branched polymers? *Angewandte Chemie International Edition* **2013,** *52* (17), 4659-4663.
18. Swain, J.; Mishra, A. K., Nile red fluorescence for quantitative monitoring of micropolarity and microviscosity of pluronic F127 in aqueous media. *Photochemical & Photobiological Sciences* **2016,** *15* (11), 1400-1407.
19. Schafer, F. Q.; Buettner, G. R., Redox environment of the cell as viewed through the redox state of the glutathione disulfide/glutathione couple. *Free Radical Biology and Medicine* **2001,** *30* (11), 1191-1212.
20. Comini, M. A., Measurement and meaning of cellular thiol:disufhide redox status. *Free Radical Research* **2016,** *50* (2), 246-271.
21. Nagy, P., Kinetics and mechanisms of thiol–disulfide exchange covering direct substitution and thiol oxidation-mediated pathways. *Antioxidants & redox signaling* **2013,** *18* (13), 1623-1641.
22. d'Arcy, R.; Burke, J.; Tirelli, N., Branched polyesters: Preparative strategies and applications. *Adv Drug Deliv Rev* **2016,** *107*, 60-81.
23. Herzberger, J.; Fischer, K.; Leibig, D.; Bros, M.; Thiermann, R.; Frey, H., Oxidation-Responsive and "Clickable" Poly(ethylene glycol) via Copolymerization of 2-(Methylthio)ethyl Glycidyl Ether. *J Am Chem Soc* **2016,** *138* (29), 9212-9223.
24. Jeanmaire, D.; Laliturai, J.; Almalik, A.; Carampin, P.; d'Arcy, R.; Lallana, E.; Evans, R.; Winpenny, R. E.; Tirelli, N., Chemical specificity in REDOX-responsive materials: the diverse effects of different Reactive Oxygen Species (ROS) on polysulfide nanoparticles. *Polymer Chemistry* **2014,** *5* (4), 1393-1404.
25. Cevc, G.; Vierl, U., Nanotechnology and the transdermal route: A state of the art review and critical appraisal. *Journal of Controlled Release* **2010,** *141* (3), 277-299.

26. Wagener, F. A. D. T. G.; Carels, C. E.; Lundvig, D. M. S., Targeting the Redox Balance in Inflammatory Skin Conditions. *International Journal of Molecular Sciences* **2013,** *14* (5), 9126-9167.
27. Roller, S.; Zhou, H.; Haag, R., High-loading polyglycerol supported reagents for Mitsunobu-and acylation-reactions and other useful polyglycerol derivatives. *Molecular diversity* **2005,** *9* (4), 305-316.
28. Fulmer, G. R.; Miller, A. J.; Sherden, N. H.; Gottlieb, H. E.; Nudelman, A.; Stoltz, B. M.; Bercaw, J. E.; Goldberg, K. I., NMR chemical shifts of trace impurities: common laboratory solvents, organics, and gases in deuterated solvents relevant to the organometallic chemist. *Organometallics* **2010,** *29* (9), 2176-2179.
29. Elbert, D. L.; Hubbell, J. A., Conjugate Addition Reactions Combined with Free-Radical Cross-Linking for the Design of Materials for Tissue Engineering. *Biomacromolecules* **2001,** *2* (2), 430-441.
30. Möller, M.; Alexiev, U., Surface charge changes upon formation of the signaling state in visual rhodopsin. *Photochemistry and photobiology* **2009,** *85* (2), 501-508.

Supporting Information

Redox-sensitive Nanocarriers for Controlled Release of Drugs in Inflammotory Skin Diseases

Walker, K. A.; Rancan, F.; Mecking, S.; Quaas, E.; Vogt, A.; Haag, R.

Table of Contents

Characterization of nanocarriers

NMR spectra

α-Methoxy-ω–methanesulfonyl-poly(ethylene glycol) ***1***

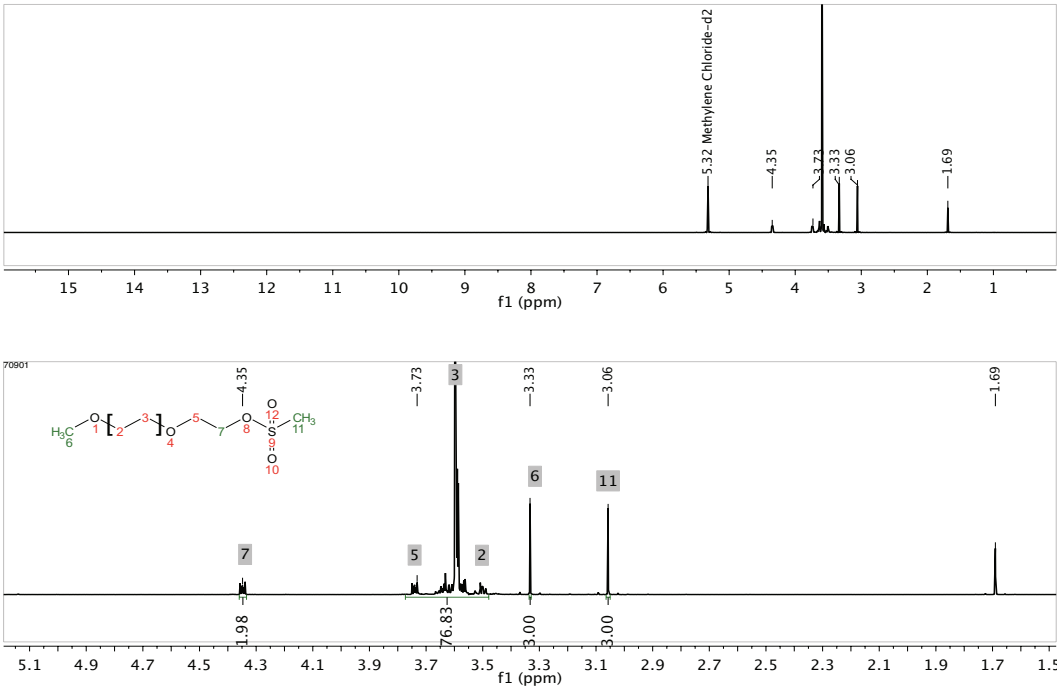

Figure S 1: ^{1}H NMR spectrum of α-Methoxy ω–methane sulfonyl poly(ethylene glycol) (DCM-d_2, 500 MHz, 297 K) with zoom into 1.5 – 5.1 ppm (bottom).

11-(10'-carboxy-decyldisulfanyl) undecanoic acid ***3***

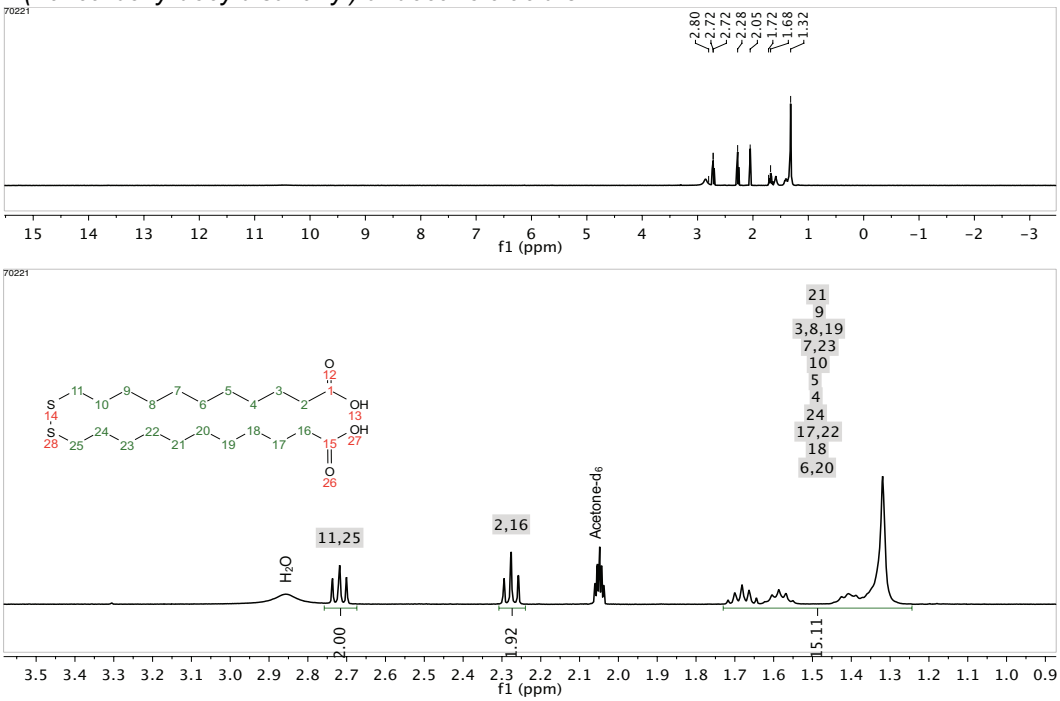

Figure S 2: ^{1}H NMR spectrum of 11-(10'-carboxy-decyldisulfanyl) undecanoic acid (Acetone-d_6, 400 MHz, 390 K) with zoom into 1.0 – 4.2 ppm (bottom).

Double shell mPEG-C_{11}-SS-C_{10}-COOH ***4***

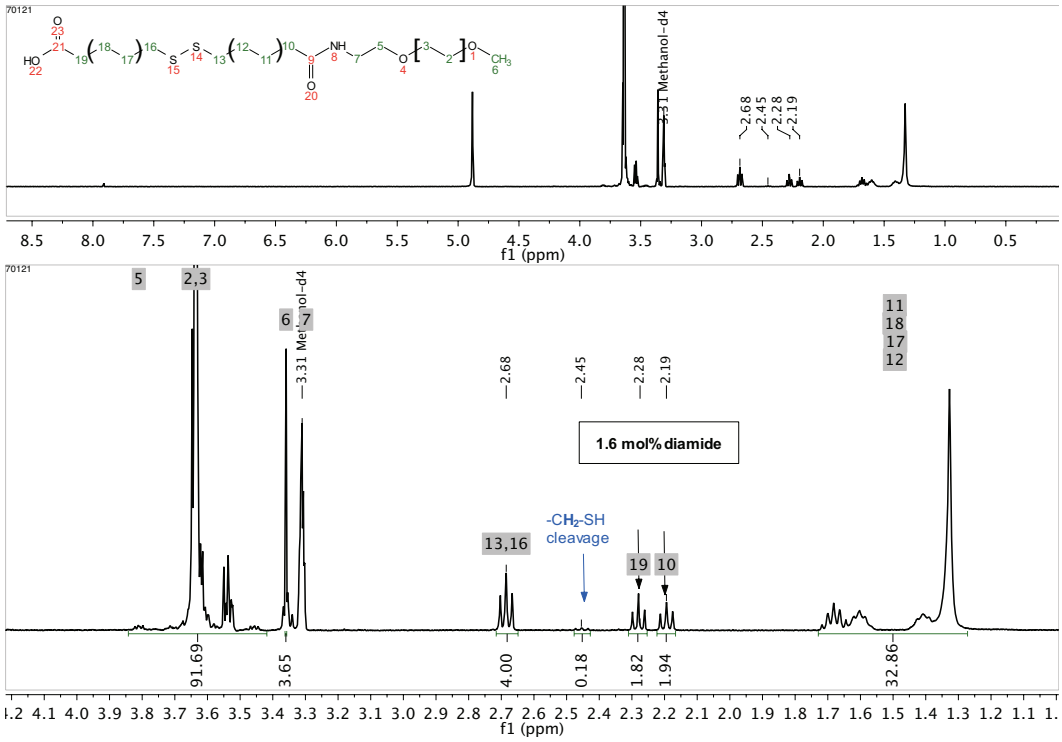

Figure S 3: ^{1}H NMR spectrum of mPEG-C_{11}-SS-C_{10}-COOH (MeOH-d_4, 400 MHz, 390 K) with zoom into 1.0 – 4.2 ppm (bottom).

mPEG-C_{11}-SS-C_{10}-CO-NHS ***5***

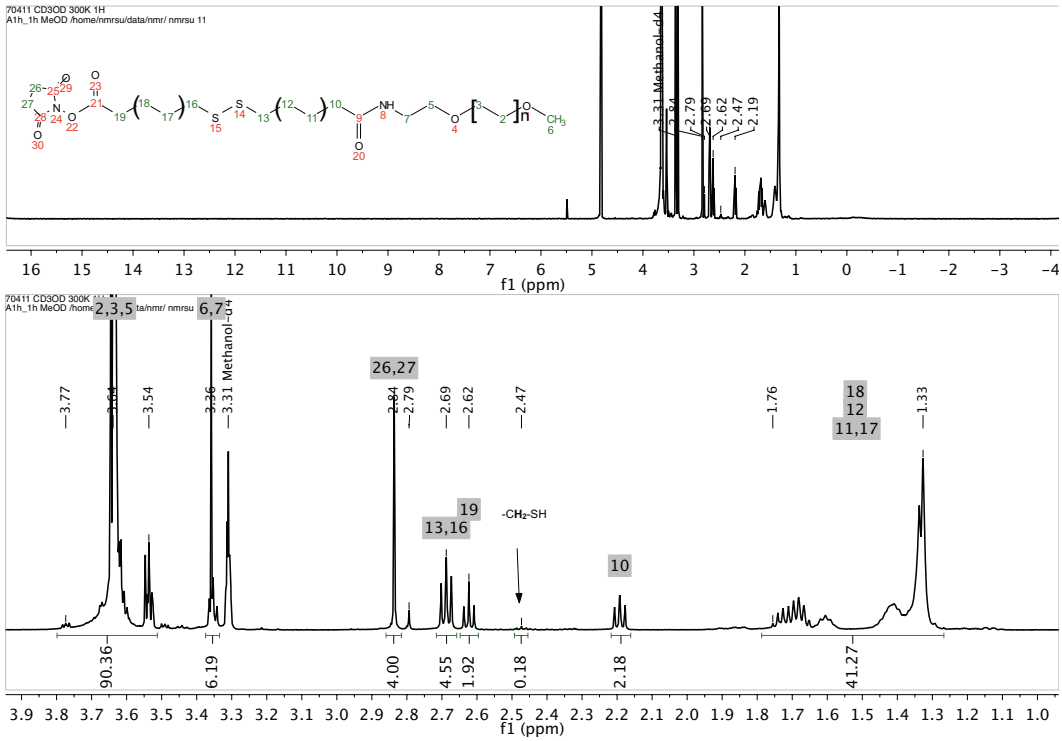

Figure S 4: ^{1}H NMR spectrum of mPEG-C11-SS-C10-CO-NHS (MeOH-d_4, 500 MHz, 302 K) with zoom into 1.0 – 3.9 ppm (bottom).

mPEG-C_{22}-COOH ***6***

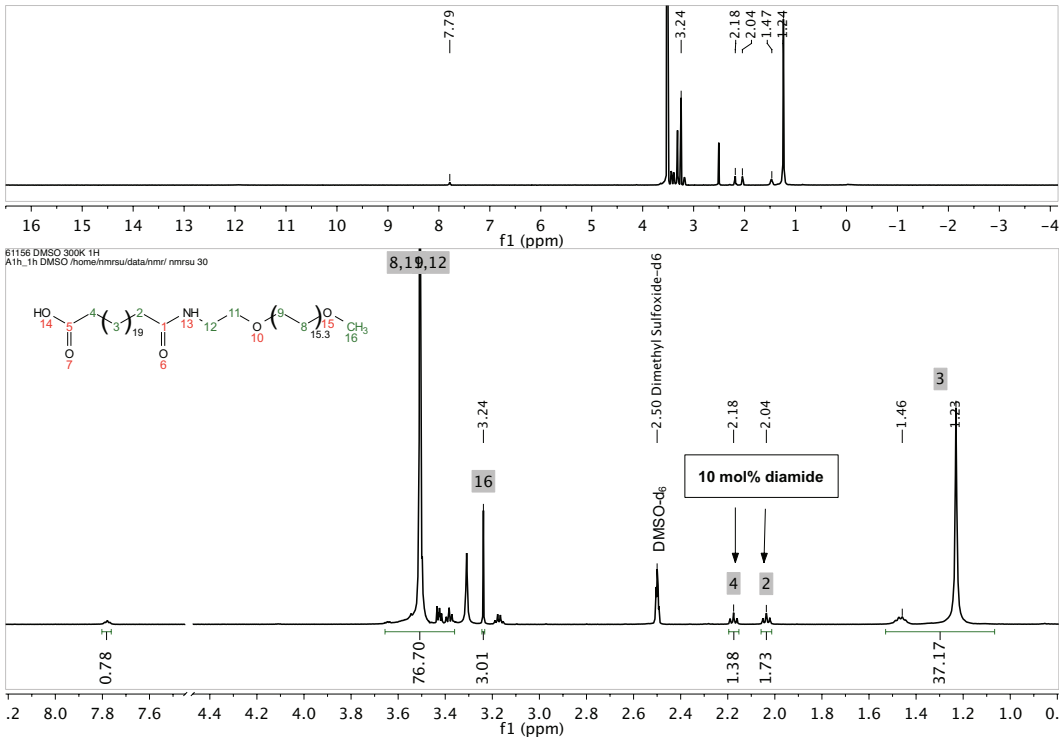

Figure S 5: ^{1}H NMR spectrum of mPEG-C_{22}-COOH (DMSO-d_6, 500 MHz, 300 K) with zoom into 1.0 – 4.4 and 7.6-8.2 ppm (bottom).

mPEG-C_{22}-CO-NHS ***7***

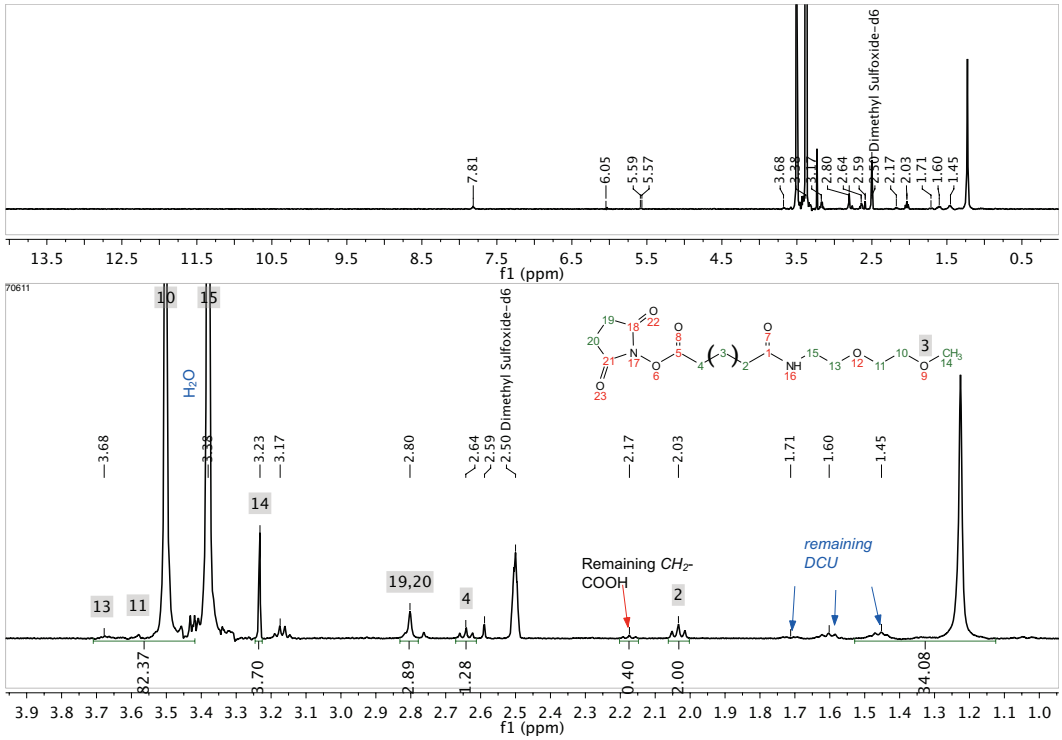

Figure S 6: ^{1}H NMR spectrum of mPEG-C_{22}-CO-NHS (DMSO-d_6, 400 MHz, 391 K) with zoom into 1 – 3.9 ppm (bottom).

rsCMS ***9***

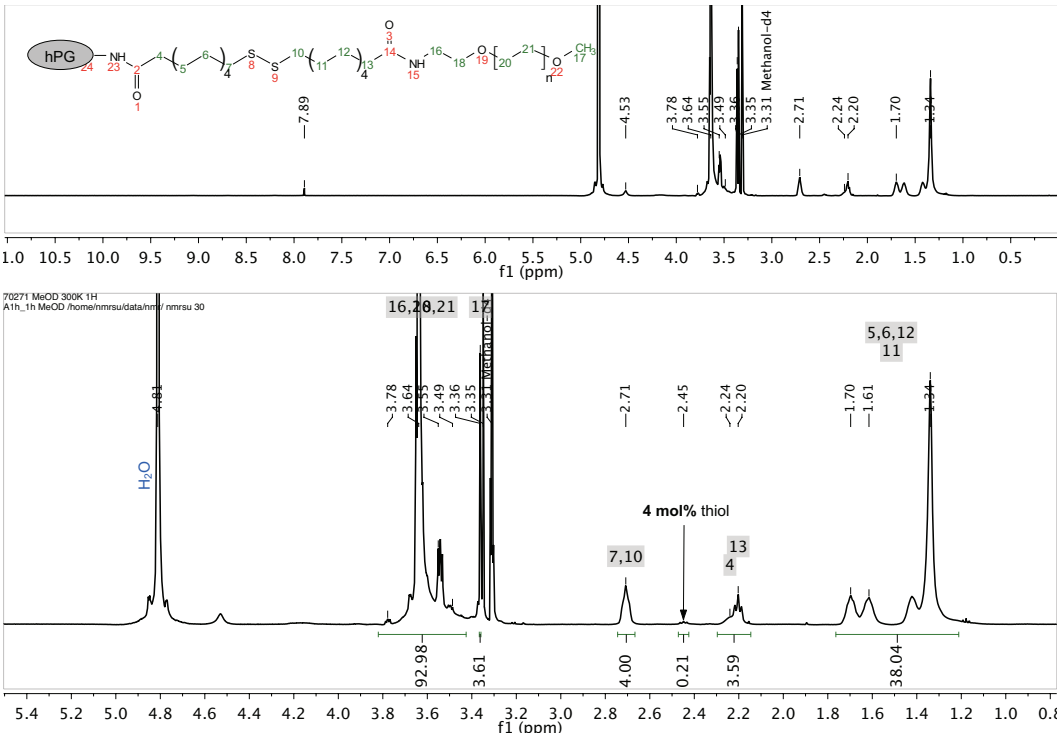

Figure S 7: ^{1}H NMR spectrum of purified product rsCMS (MeOH-d_4, 500 MHz, 305 K) with zoom into 0.5 - 5.4 ppm (bottom). For the ease of display, hPG atoms are not explicitly displayed in molecule representation.

α-mercapto ω–NHS dodecanoic acid SH-C_{10}-CO-NHS ***12***

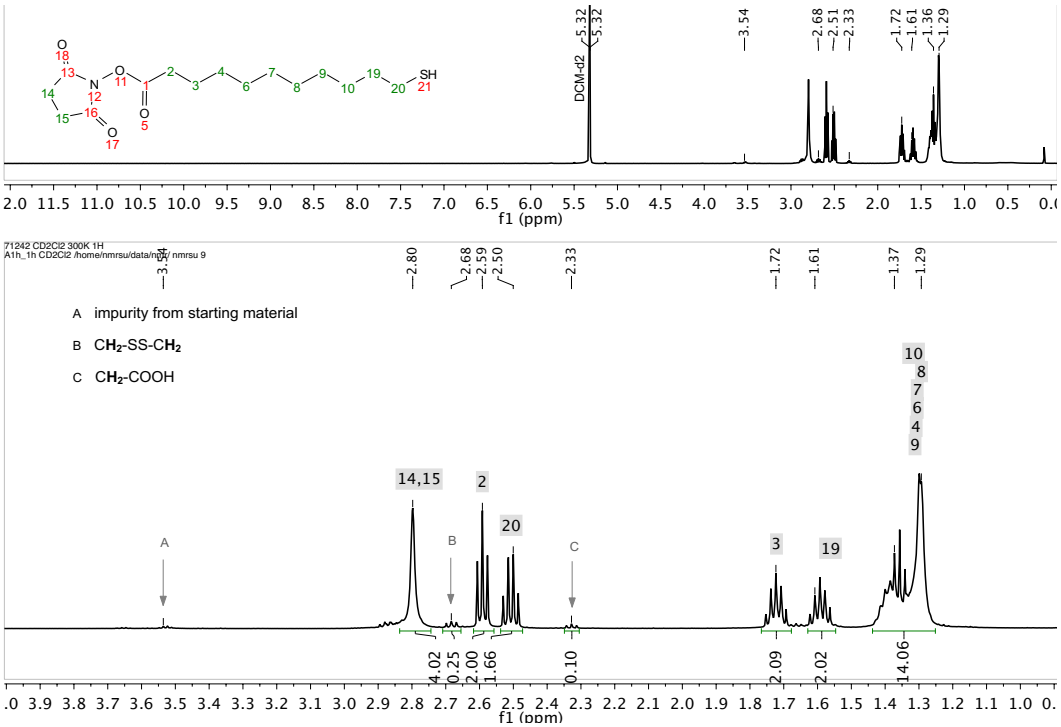

Figure S 8: ^{1}H NMR spectrum of SH-C_{11}-CO-NHS **12** (500 MHz, DCM-d_2) with zoom into 1.0 to 4.0 ppm (bottom).

Double shell mPEG-C_{11}-SH ***13***

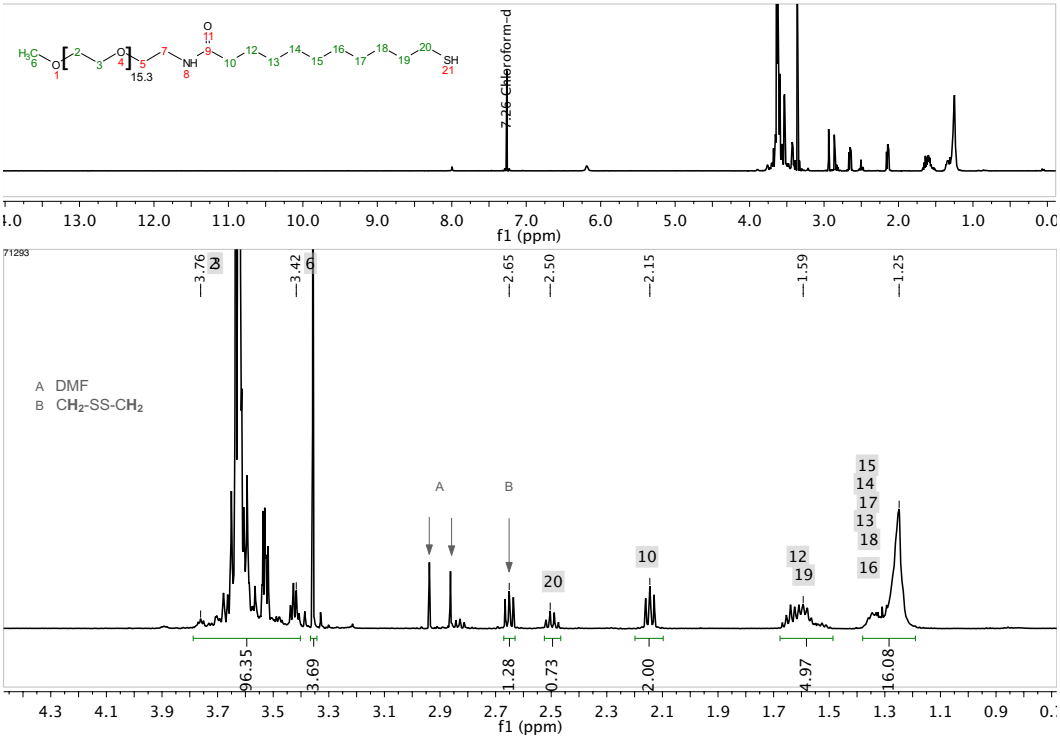

Figure S 9: ^{1}H NMR spectrum of mPEG-C_{11}-SH **13** (500 MHz, $CDCl_3$) with zoom into 0.8 to 4.3 ppm (bottom).

NHS-activated decenoic acid ***14***

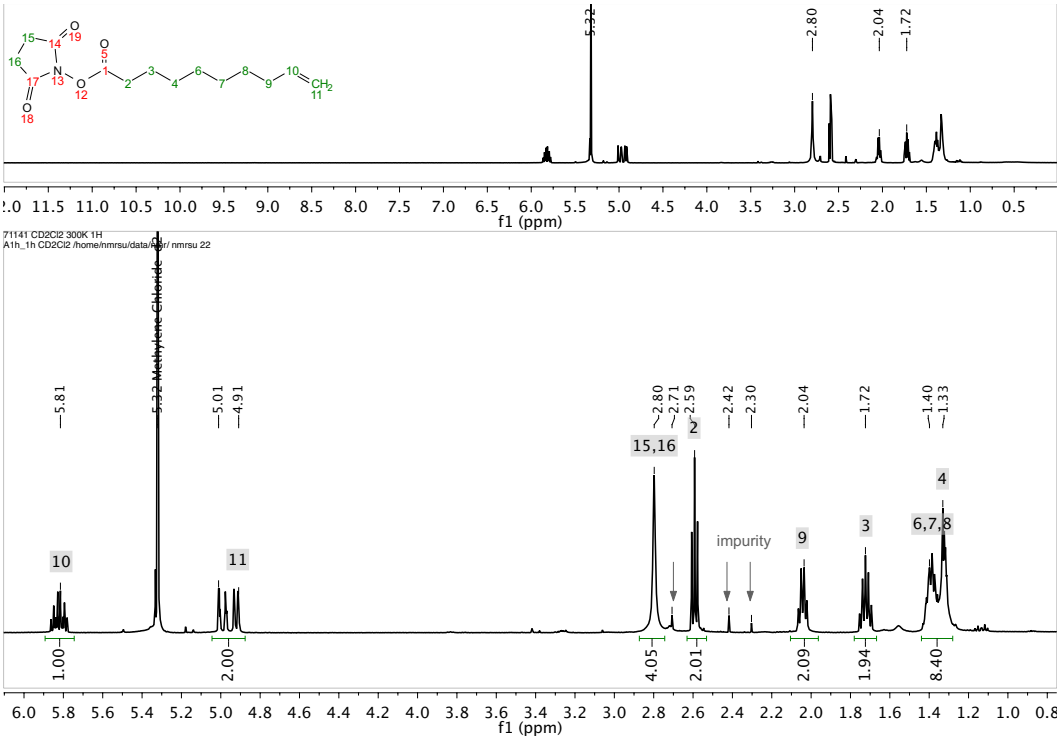

Figure S 10: ^{1}H NMR spectrum of NHS-activated decenoic acid **14** (500 MHz, CD_2Cl_2) with zoom into 0.8 to 6.0 ppm.

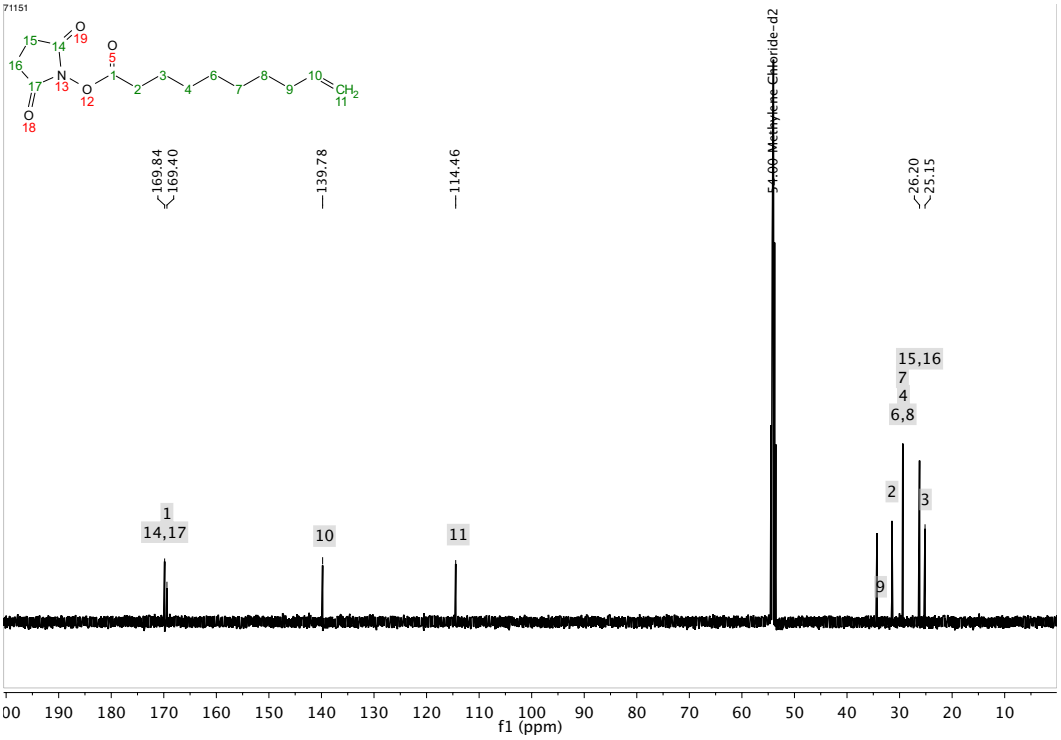

Figure S 11: ^{13}C NMR spectrum of NHS-activated decenoic acid **14** (126 MHz, CD_2Cl_2).

hPG-(NHCO-C_7H_{14}-CH=CH_2)$_{0.7}$ ***15***

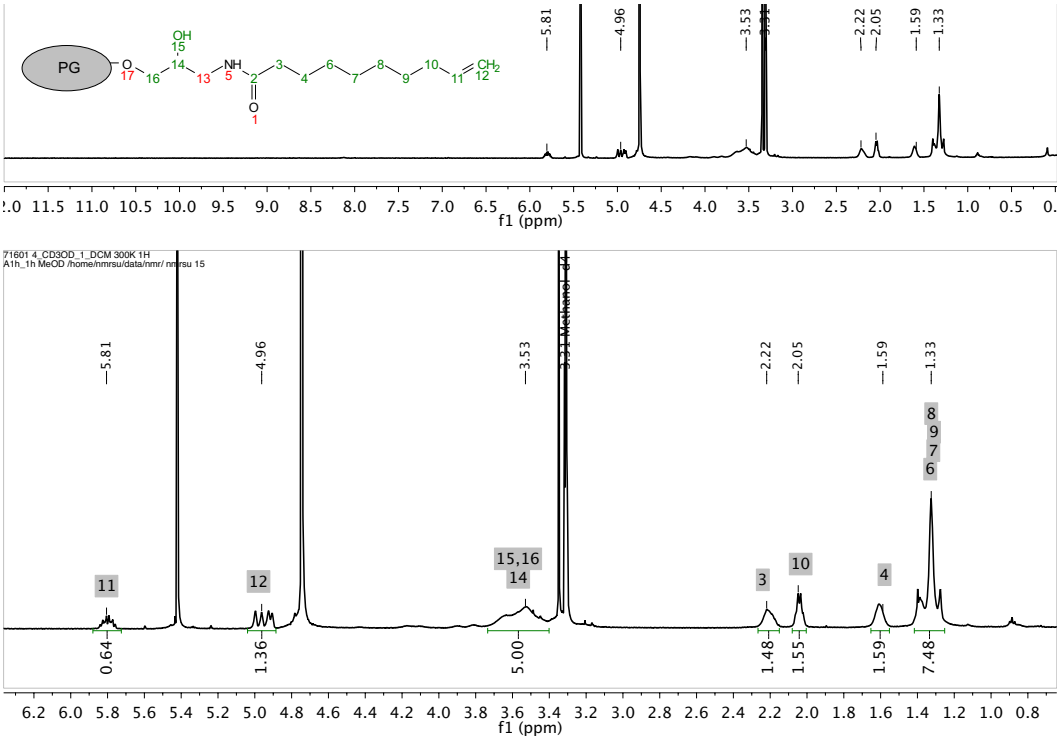

Figure S 12: ^{1}H NMR spectrum of hPG-(NHCO-C_7H_{14}-CH=CH_2)$_{0.7}$ **15** (500 MHz, MeOH-d_4) with zoom into 0.8 to 6.2 ppm; for the ease of display, hPG atoms are not explicitly displayed in molecule representation.

*osCMS **16***

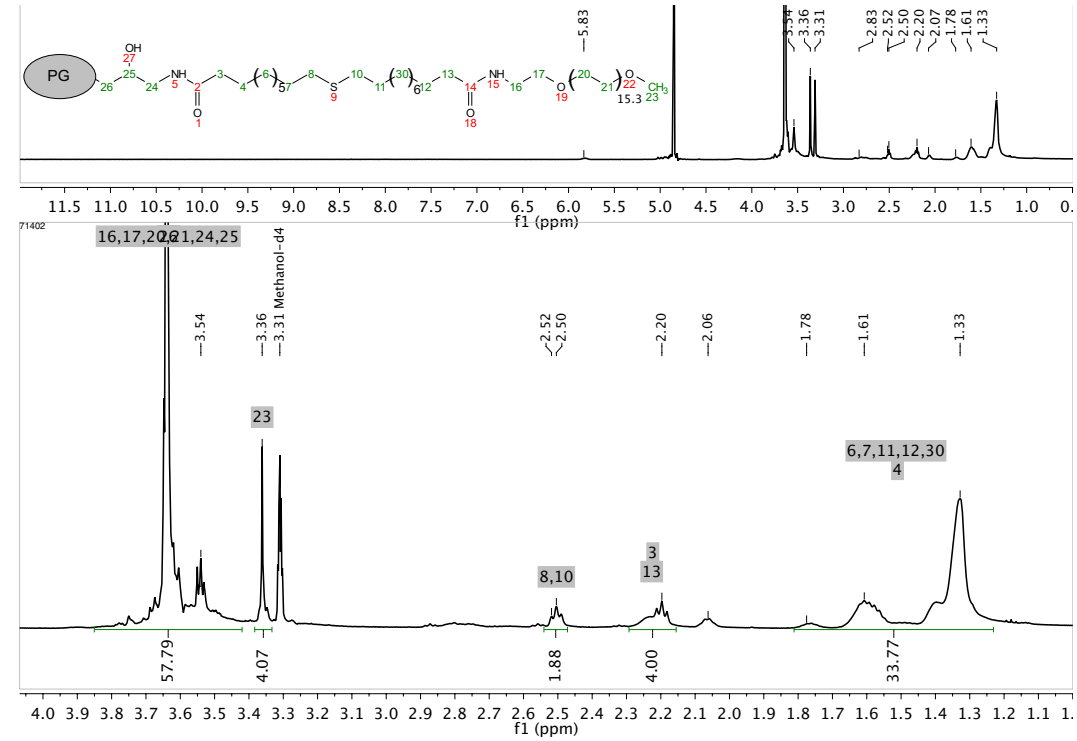

Figure S 13: ^{1}H NMR spectrum of osCMS **16** (500 MHz, MeOH-d_4) with zoom into 1.0 to 4.0 ppm (bottom); for the ease of display, hPG atoms are not explicitly displayed in molecule representation.

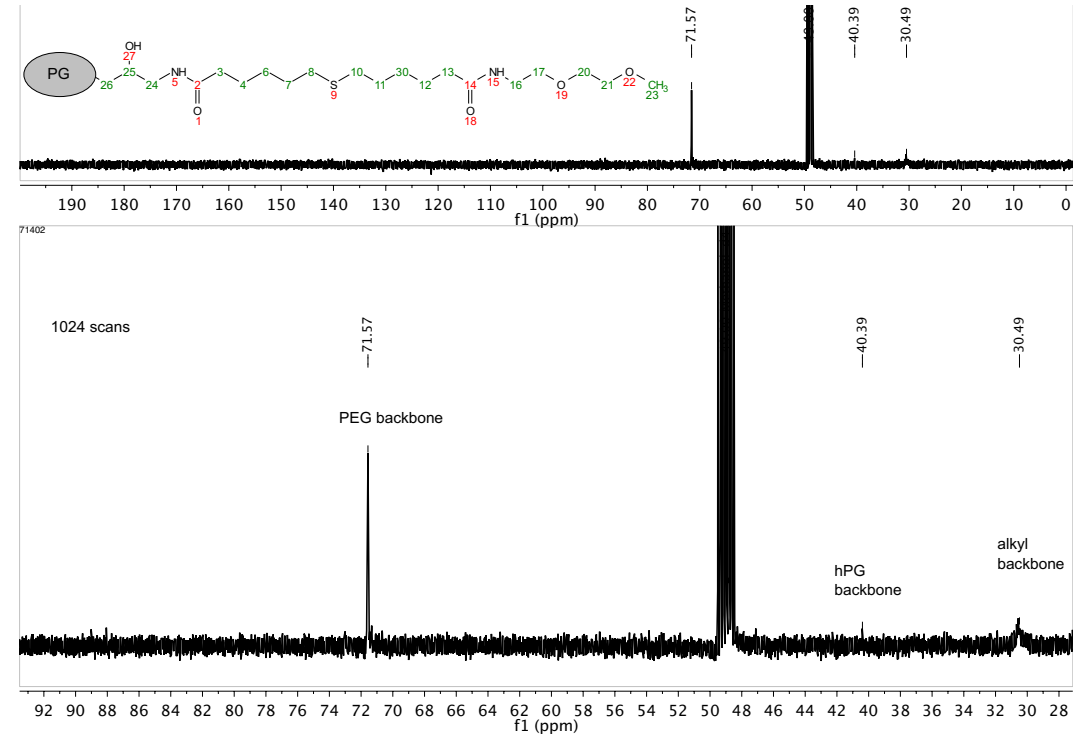

Figure S 14: ^{13}C NMR spectrum of osCMS **16** (126 MHz, MeOH-d_4, 1024 scans) with zoom into 28 to 92 ppm (bottom); for the ease of display, hPG atoms are not explicitly displayed in molecule representation.

Molecular weight distribution – GPC

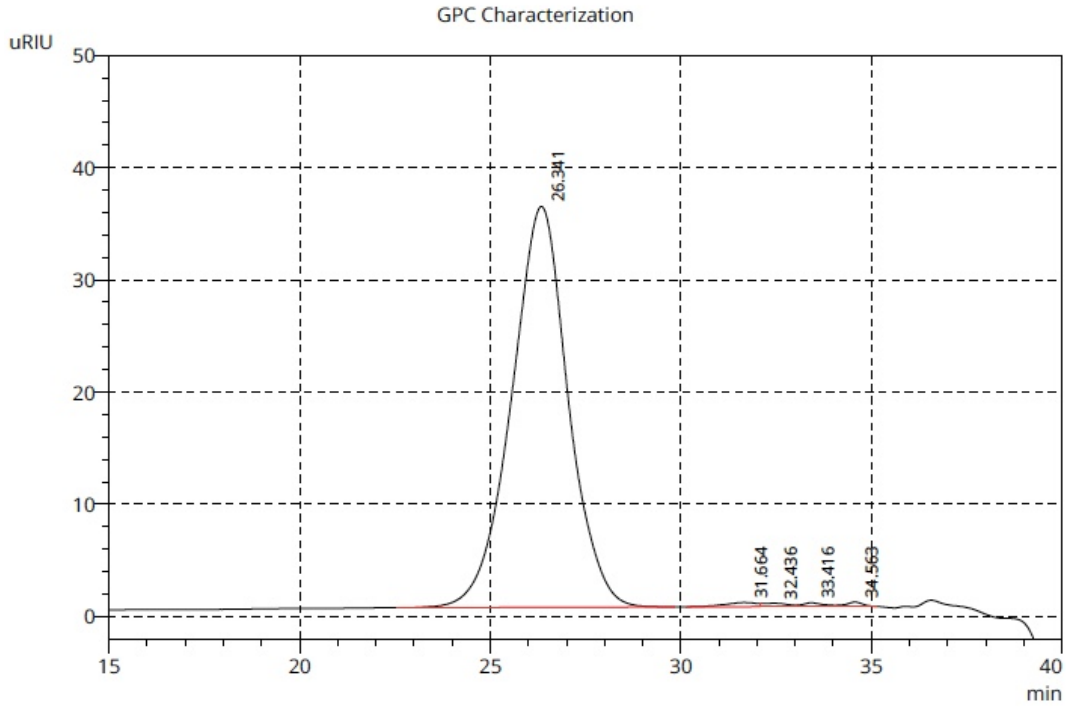

Figure S 15: GPC elugram of purified product rsCMS (DMF, RI detector, PS standards). Peak at 26.341 min refers to product, while peaks with longer elution time refer to MeOH traces in measured sample.

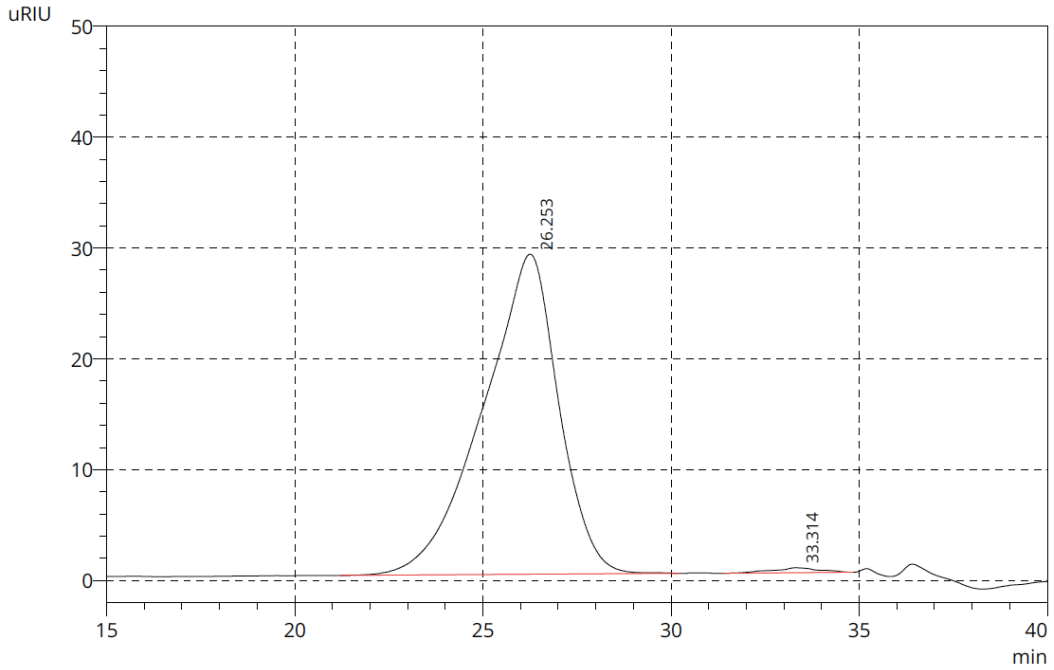

Figure S 16: GPC elugram of purified product osCMS (DMF, RI detector, PS standards). Peak at 26.253 min refers to product, while peaks with longer elution time refer to MeOH traces in measured sample.

Molar mass calculation via ^{1}H NMR

The calculation of the molar mass by ^{1}H NMR spectroscopy is based on the calculation of the degree of functionalization D_f, reflecting the fraction of double shell conjugation to the hyperbranched hPG scaffold. Comparison of the polymeric hPG and PEG methylene and methine signals (around 3.7 ppm) to the respective alkyl backbone peaks of the double shell at around 1.2 ppm leads to the D_f value.[1] The following calculation is exemplary and shows the analysis of the molar mass of rsCMS.

Predefinitions:

- D_f: Degree of functionalization
- $\sum_{3.7ppm}$: sum of hPG and PEG C**H$_2$** and C**H**, in which hPG contributes five protons and PEG $63 - 2 \cdot D_f$ (M_{PEG}=750 gmol^{-1}, two protons adjacent to amide shifted to higher ppm and thus substracted).
- Aliphatic C**H$_2$** set to 32

Calculation of D_f

$\sigma_{3,7} = 5 + 61 \cdot D_f$

$\sigma_{1,2} = 32 \cdot D_f$

$$\sum_{3,7} = \frac{\sigma_{3,7}}{\sigma_{1,2}} \cdot 32 = \frac{5 + 61 \cdot D_f}{D_f}$$

$$\sum_{3,7} = \frac{5}{D_f} + 61$$

$$D_f = \frac{5}{\sum_{3,7} - 61} = \frac{5}{78.2 - 61} = \mathbf{0.29}$$

Calculation of the molar mass

$$M\ (rsCMS)$$
$$= \left(D_f \cdot 135\right) \cdot M(mPEG - A - C11 - SS - C11 - COOH) - \left(D_f \cdot 135\right) \cdot M(H_2O) + M\ (hPG)$$
$$= 55466.2\ g\ mol^{-1}$$

Calculation of the theoretical molar mass of CMS nanocarriers are done assuming full conversion of the available 70% amine groups of hPG-NH_2.

Disulfide vs Thioether inner shell 3D model

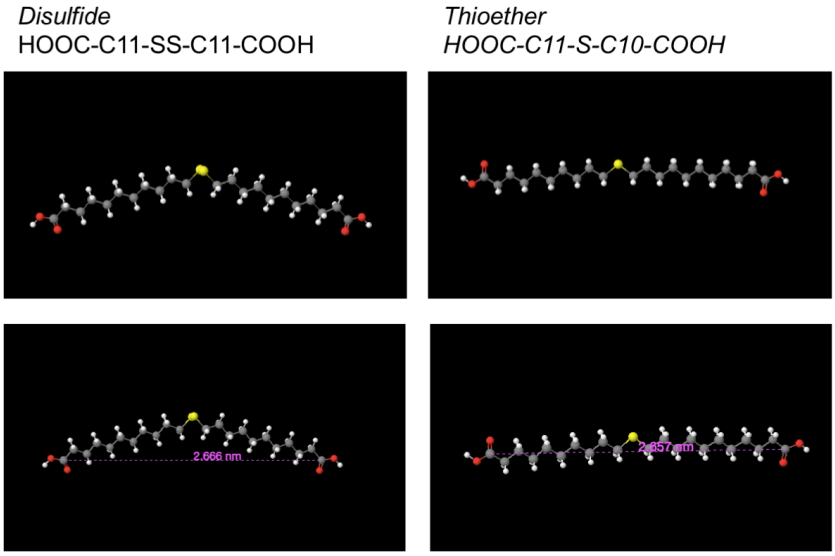

Figure S 17: 3D models of thioether and disulfide inner shell building blocks generated with molView.org (accessed on 06.05.18).

Link to disulfide model:

https://embed.molview.org/v1/?mode=balls&cid=15748524

Link to thioether model:

https://embed.molview.org/v1/?mode=balls&smiles=C(CCCCCCCCSCCCCCCCCCC(=O)O)CC(=O)O

Hydrodynamic diameter – CMS

Table S 1: Hydrodynamic diameter of rsCMS in various solvents.

c [mg/mL]	Size in MeOH		Size in PBS	
	$d_{H_{Int}}$	$d_{H_{Vol}}$	$d_{H_{Int}}$	$d_{H_{Vol}}$
1	260 nm (99%)	285 nm (93%) 5400 nm (7%)	18 nm (44%) 2300 nm (56%)	17 nm (99%)
5	10 nm (3%) 160 nm (97%)	9 nm (65%) 145 nm (35%)	19 (77%) 2300 (23%)	16 nm (99%)

In vitro Proof of Concept: Triggered Release

Triggered release of drug by reduction of rsCMS

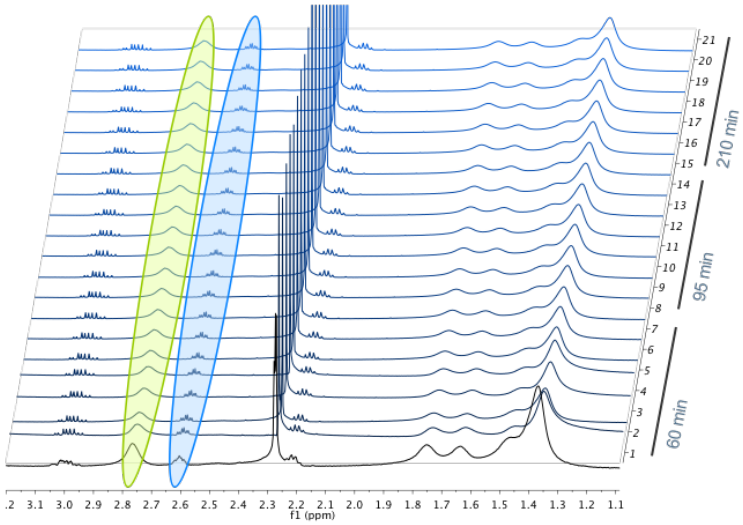

Figure S 18: Stacked ^{1}H NMR spectra of interval measurement, 80 scans per measurement; incubation with 10 mM GSH solution in PBS pH 7.4 at 37 °C; Ratio of 2.8 ppm (C*H*$_2$-SS-C*H*$_2$) vs 2.6 ppm (C*H*$_2$-SH).

Oxidation of osCMS by H_2O_2

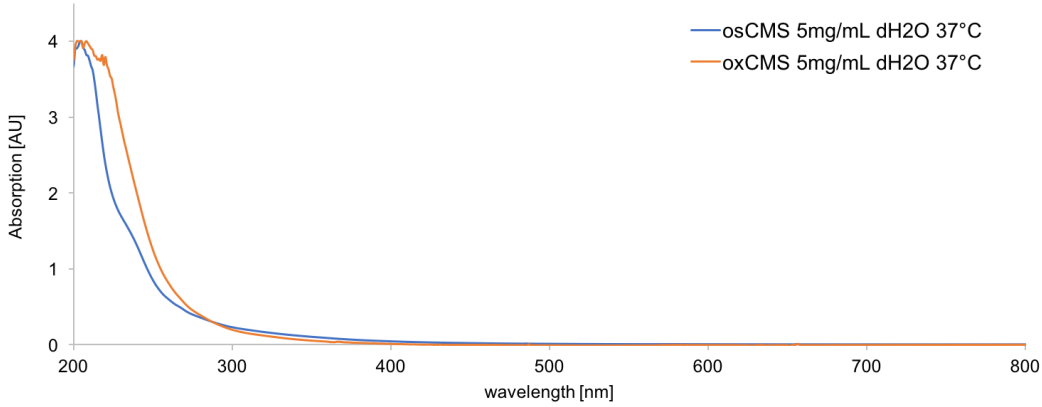

Figure S 19: UV-Vis absorption of osCMS before oxidation (osCMS, red) and after oxidation (oxCMS, black).

References

1. Unbehauen, M. L.; Fleige, E.; Paulus, F.; Schemmer, B.; Mecking, S.; Moré, S. D.; Haag, R., Biodegradable Core–Multishell Nanocarriers: Influence of Inner Shell Structure on the Encapsulation Behavior of Dexamethasone and Tacrolimus. *Polymers* **2017,** *9* (8), 316.

4 Summary and Outlook

The development of new drug delivery systems is driven by application-inspired responsive features of the system. In my PhD work, the goal was to develop stimuli-responsive polymeric nanocarriers consisting of linear amphiphiles, core-crosslinked by a hyperbranched polymeric scaffold, forming the so-called core multishell (CMS) nanotransporter. The chemical features for stimulus-responsiveness reflects the need predetermined by the application. Here, the treatment of inflammatory skin conditions was targeted, and so CMS nanocarriers were envisioned to feature stimulus-responsiveness for dermal drug delivery. In a simplified way, the skin is a layer cake of individual physical and biochemical barriers, which renders the penetration of the skin a highly demanding target. Previous CMS nanocarriers, consisting of hyperbranched polyglycerol (hPG) as the core molecule, an alkyl inner shell, and a water-soluble mPEG outer shell, were tested for dermal drug delivery and showed increased penetration up to deeper layers of stratum corneum. However, hyperbranched polyglycerol is biocompatible, but not biodegradable. A possible accumulation of the hPG-based CMS nanocarrier might thus lead to toxicity, especially in diseased skin with an upregulated inflammatory response due to chronic inflammation. To circumvent this accumulation-related toxicity, a biodegradable CMS nanocarrier was synthesized in the first project. As discussed in chapter *1.4.1 Forms of Biodegradability*, biodegradable polymers which degrade to bioresorbable moieties are considered a special case of biodegradability, and thus poly(lactic acid), degrading to endogenous lactic acid, is considered a safe biodegradable polymer. In analogy, adipic acid and glycerol were chosen as the A_2 and B_3 building blocks for a bulk polycondensation synthesis of a hyperbranched polyester. According to literature, this polymer is expected to hydrolytically degrade to bioresorbable 6-hydroxycaproic acid and glycerol. The hyperbranched polyester is terminated with both carboxylic acids and hydroxy groups, and selective modification of one or the other functional group gives either homofunctional hydroxy-terminated or carboxylic acid-terminated hyperbranched polyesters. In a previous *grafting to* approach, a CMS nanocarrier was synthesized by reacting the carboxylic-acid terminated hyperbanched polyester with an amphiphilic mPEG-OCL_7-NH_2 building block. However, instead of the amine reacting with the core carboxylic acid groups, intramolecular backbiting of the amphiphilic double shell led to cyclic amide formation. Changing the synthetic strategy to a *grafting from* approach finally resulted in the targeted structure. To this end, the hyperbranched polyester with terminal hydroxy groups was used as a macroinitiator for the ring-opening polymerization of ε-caprolactone, leading to linear oligocaprolactone (OCL) with nine repeating units, on average. Ester bond formation between the hydroxy end groups of the OCL arms and a carboxylic acid-terminated mPEG gave the targeted CMS nanocarrier. Starting with the crude hyperbranched polyester, the polymer underwent three further steps of

modification, each being limited by the sterically demanding circumstance of being conducted at a polyfunctional molecule. Considering the complete synthesis of the CMS nanocarrier, the overall conversion of one polyester terminal group is only 40 %. The low conversion is reflected by the low degree of branching of 52 %. The low overall conversion, coupled with a comparably low molecular weight of the polymeric core (M_n = 900 Da) resulted in a nanocarrier with a poor encapsulation performance. It showed a drug loading capacity of 1.8 wt% for dexamethasone, which translates to one molecule of dexamethasone per one nanocarrier. This low loading capacity probably arises from the low number of arms present on the nanocarrier. A hyperbranched polyester with a higher molecular weight and degree of branching would offer more functional groups for the attachment of the double shell, and hence, a higher density of the double shell could be reached. The encapsulation of a drug by physical entrapment is based on weak van der Waals forces, and hence a shorter distance between drug and entrapping polymer results in stronger encapsulation. Consequently, a higher arm density generally results in a higher drug loading capacity. The biodegradability of the CMS nanocarrier was expected to take place upon hydrolytic degradation at acidic conditions. The hydrolysis of the nanocarrier was tested at pH 5.0, as this value is associated with pathological changes of physiological pH values. In contrast to the expectations backed up by literature, this polymer surprisingly did not hydrolyse even after seven days, as shown by a kinetic study based on NMR analysis. Control experiments of the degradtion by incubation of the polymer in PBS buffer at pH 7.4 showed no degradation as well. In contrast, incubation of the nanocarrier with lipase resulted in complete enzymatic degradation within five days. Despite the unrealistically high amount of enzyme (200 wt%) and the nature of the enzyme itself, being a yeast lipase, this degradation mechanism is expetced to take place in vivo at physiological conditions, as lipases are also present in the human body. Nevertheless, if a drug delivery system is meant to degrade within a reasonable time, simple ester bonds are not the right choice if the degradation is supposed to take place under acidic conditions. Alternatively, polyacetals or –ketals can be used as the hydrolytically degradable polymeric scaffold. During my ongoing work on polyesters, however, it turned out that chronically inflammed skin has a pH value of 5.5 on the surface, and the pH value reaches neutral pH with increasing depth. This is opposed to our initial hypothesis on inflamed skin having a neutral pH and reaching acidic values in inflamed areas. Hence, the hydrolytic degradability in the acidic regime as a feature for controlled delivery of drugs into skin became redundant. Still, skin remained the target for the next project on responsive nanocarriers for the triggered-release of drugs. Skin has a natural compartmentalization of redox-active moieties, including thiols and disulfides, reactive oxygen species, and enzymes, which are releavant for maintaining the redox balance. We hypothesize the redox environment to be a major indicator for inflammation during inflammatory skin diseases, and pathological changes of the redox environment can thus be

used as a selective trigger for stimulus-triggered release of drugs in areas of inflammation. To test this hypothesis, a complementary pair of a reduction-sensitive (rsCMS) and an oxidation-sensitive CMS nanocarrier (osCMS) was synthesized. The glutathione-glutathione disulfide (2GSH/GSSG) redox pair is the major redox buffer in the body and it is responsible for the control of peptide folding by oxidation and reduction of the peptide's cysteines. Inspired by the natural disulfide bond formation and scission, we focussed on sulfur as the basis for the reduction- and oxidation sensitive groups within the CMS nanocarrier. The reduction-sensitive CMS was conseqently planned to contain a reduction-sensitive disulfide group within the double shell. As most drugs encapsulated by CMS are reported to be located at the interphase between the hydrophilic outer shell and the hydrophobic inner shell, the reduction was intended to lead to a shell scission, leading to release of the encapsulated drug. Thus, the disulfide group was synthetically placed in the middle of the inner shell. Retrosynthesis of the targeted rsCMS gives three major building blocks: hPG as the core building block, a symmetrical disulfide as the inner shell, and the mPEG outer shell. The disulfide inner shell building block was reacted with a mPEG-NH_2 by amide bond formation using a four-fold excess of the disulfide to prevent diamide formation. The resulting double shell building block was connected to an aminated hPG-NH_2 of 10 kDa, containing 95 NH_2 groups per hPG scaffold, via amide bond formation. Amide bonds between the three major building blocks were chosen as biologically relative inert groups, which are not expected to undergo significant degradation within the expected residing time of the nanocarriers on the skin. Thus, release upon degradation of the nanocarrier is expected to occur primarily due to disulfide bond scission. The oxidation-responsive counterpart was designed to have the same number of atoms in the linear double shell as rsCMS. Here, the synthesis was accomplished by connecting a thiolated hPG to a mPEG-ene building block. The oxidation-sensitive thioether was located at the same position as the disulfide in the rsCMS, i.e., the middle of the inner shell building block. Thus, a linear thiol building block was conntected to mPEG-NH_2 via amide bond formation, whereas amide bond formation between 9-decenoic acid and hPG-NH_2 gave the hyperbranched scaffold. The resulting building blocks were subsequently connected in a UV-initiated radical thiol-ene reaction. Radical thiol-ene generally qualifies for being a "click-type" reaction, and so quick reactions with high yields were expected. However, the thiol-ene reaction between the linear amphiphilic PEG-alkyl-thiol and hPG-alkene was conducted for 13 h to reach 75 % functionalization. As the alkene has an expected medium range reactivity, the reaction rate is probably dominated by the less reactive alkyl-thiol. A limited H-abstraction rate of the thiol leads to reduced chain transfer rates, and thus the chain transfer becomes the rate limiting step of the thiol-ene reaction.[158] Further limitations of the radical thiol-ene reaction arises from the reaction set-up. For the generation of radicals throughout bigger reaction volumes, uniform exposure of the complete reaction volume to the light source is necessary. However, being

limited by the design of reaction flasks or tubes, and the light attenuation within the reaction volume, radicals are probably predominantly formed at the focal point of the light. Alternatively, thermal thiol-ene reactions, initiated by azobisisobutyronitrile (AIBN), could lead to more efficient thiol-ene reactions and higher conversions in shorter time. Both rsCMS and osCMS were purified by dialysis or ultrafiltration, giving products with narrow polydispersitiy values of 1.1 and 1.2, respectively. Their drug loading capacities were assessed for nile red, dexamethasone, and tacrolimus. Nile red and dexamethasone encapsulation gave loading capacities within the expected range, whereas the appllied film uptake method did not give significant encapsulation for tacrolimus. Encapsulation of tacrolimus with a sonication-assisted uptake of the drug gave significantly increased encapsulation capacities. However, CMS solutions with tacrolimus, encapsulated by sonication, are stable for several days at 4 °C, after which the clear solutions became turbid, indicating a precipitation of the drug. This observation indicates that an instable formulation with CMS acting as a surfactant for tacrolimus might have been formed. This hypothesis needs to be further investigated. Prior to testing of the carriers as dermal drug delivery agents, a proof of concept study on the stimulus-triggered release of encapsulated model drug nile red was performed with both carriers. As hypothesized for the skin, upregulation of reactive oxygen species ROS and glutathione might act as triggers for the release. For the in vitro study, NR@rsCMS was incubated with a 10 mM GSH solution, whereas NR@osCMS was incubated simultaneously with a 1 % H_2O_2 concentration. The GSH-triggered release of nile red did not occur at an expected rate, as NR showed a release of < 5 % within 24 h. However, the inefficient scission of the rsCMS disulfide bond probably arises from the poor reduction capacity of 10 mM GSH solutions. As discussed in chapter *1.3.1 Definition of the Redox Potential in Biological Environment*, the reduction capacity of the 10 mM GSH solution is not equivalent to the reduction capacity of a 10 mM GSH environment in vivo. When performing in vitro GSH studies, the lack of redox enzymes limits the comparability of the in vitro to the in vivo situation. Thus, to proof the concept of the reduction-triggered release of the encapsulated NR, TCEP was used. In this case, 90 % of the encapsulated drug were released within 24 h, proving the general applicability of disulfide-containing rsCMS as reduction-responsive CMS nanocarrier. Incubation of osCMS with 1 % H_2O_2, mimicking the oxidative in vivo environment, resulted in 80 % release of drug in 24 h. The osCMS nanocarrier is not degraded, but its thioether moiety is oxidized to sulfoxide, thus changing its polarity from a completely hydrophobic inner shell to an inner shell with one sphere of higher polarity and increased hydrophilicity. This change in polarity triggers also a conformational change, and the hydrophobic drug nile red was released from the oxidized osCMS in a sustained fashion. The dermal drug delivery was tested for rsCMS on both fresh ex vivo human skin and UVA-irradiated human skin. UVA irradiation triggers formation of ROS species, and thus one pathological change in the penetration barrier of inflammed skin is

mimicked. We observed a limited penetration into skin by NR@rsCMS^{FITC} when the skin was previously irradiated. The ROS generation by UVA irradiation dimerizes free GSH, and so less GSH is available for the reduction of rsCMS, hence less pronounced Nile Red release in deeper skin layers is observed. This is in line with our expectations, and shows that a layer of increased GSH concentration is present in deeper layers of the SC, which triggers a release of NR in the case of the non-irradiated skin, but prevents deeper penetration of the rsCMS for the case of irradiation. The observations from the skin experiments can be further supported, or disproved, by electron paramagnetic resonance (EPR) spectroscopy. In my paper “Radical Stability vs. Temporal Resolution of EPR-Spectroscopy on Biological Samples”, a spin-labelled, EPR-active version of dexamethasone was synthesized. Selective esterification of the primary hydroxy group of dexamethasone by EDCI-mediated ester bond formation gave one of possibly three regioisomers in high yields. Dexamethasone labelled with the spin label PCA was compared with a TEMPO-labelled version, and radical stability tests in cell culture showed that the concentration of TEMPO radicals decreases to non-detectable values in 180 min, while PCA remained stable over the same period. Encapsulating PCA-labelled dexamethasone into rsCMS and osCMS and incubation of non-irradiated and UVA-irradiated skin with the respective nanocarriers, we might be able to follow the distribution of ROS radicals and GSH thiols throughout the different skin layers by EPR spectroscopy on skin sections. PCA remains stable for longer periods of time, and so dexamethasone-PCA released from CMS might show different kinetics of nitroxide spin reduction throughout the skin layers, depending on whether the skin was irradiated or not. This study will be conducted in near future.

The biochemical and physical environment of skin is highly complex. Using CMS nanocarriers, various aspects of the skin barrier in healthy and diseased state can be investigated. Once the basics of the physico-chemical barriers of skin are understood, nanocarriers for the stimulus-triggered release of highly potent drugs at sites of inflammation can be designed. So far, CMS nanocarriers appear to be limited in terms of the molar mass of drugs to be encapsulated. When therapeutic proteins are to be transported by CMS nanocarriers, a physical entrapment within one CMS, the limited size within one CMS makes the classical encapsulation impossible. CMS aggregates, however, could transport bigger molecules in between the individual, intermolecularly entangled CMS nanocarriers. CMS nanocarriers were previously presented as “universal” carriers. While this holds true for the CMS nanocarrier being a broadly applicable nanocarrier for drug delivery, application-oriented design of specialized features, such as degradability, triggered release, or polarity switches, allows to translate the CMS from a platform to a tailored drug delivery system.

5 Short Summary

5.1 Kurzzusammenfassung

Diese Dissertation fasst meine Forschung im Gebiet der Kern-Multischale Nanotransporter als dermale Wirkstoff-Transportsysteme zusammen. Da der Kern-Multischale Nanotransporter als Plattform für den Wirkstofftransport bereits in einigen Veröffentlichungen etabliert wurde, war das Ziel meiner Doktorarbiet den Nanotransporter als bioresponsiven Nanotransporter für den Transport in Haut zu spezialisieren. Hinsichtlich der chemischen Umgebung ist Haut, bzw. besonders erkrante Haut, ein bisher wenig charaktersiertes Gewebe. Die erhöhte Penetration des Fluoreszenzfarbstoffs Nilrot durch Kern-Multischale Nanotransporter in tiefere Hautschichten im Vergleich zu einer Nilrot-Creme wurde bereits in vorangegangenen Arbeiten veröffentlicht. Die erhöhte Penetration war der Ausgangspunkt für die Hypothese hinsichtlich der potentiellen Anwendung des Kern-Multishale Nanotransporters als Wirkstoff-transportsystem. Allerdings wurde der Verbleib der Nanotransporter in der Haut als potentielle Ursache von Toxizitätsproblemen erachtet. Daher war das erste Projekt dieser Doktorarbeit darauf ausgerichtet, einen biologisch abbaubaren CMS-Nanotransporter zu etablieren. Basierend auf einer Disäure und einem Triol wurde ein hyperverzweigter Polyester als Kernmolekül eines CMS-Nanotransporters synthetisiert und als Makroinitiator für die ringöffnende Polymerisation von ε-Caprolacton verwendet. Umgeben von einer wasser-löslichen mPEG-Außenhülle zeigte dieser Nanotransporter in sieben Tagen einen vollständigen enzymatischen Abbau, während die Hydrolyse des Ester-basierten CMS-Nanotransporters überraschenderweise unter physiologisch relevanten Bedingungen nicht stattfand. Das niedrige Molekulargewicht des Kernmoleküls und die geringe Verzweigung des resultierenden CMS-Nanotransporters sind vermutlich der Grund für die schlechte Kapazität der Wirkstoffbeladung dieses biologisch abbaubaren Nanotransporters. Mit Blick auf die Redoxbarriere der Haut stellten wir die Hypothese auf, dass der natürliche Gradient an Reduktionsmitteln und Oxidantien in der Haut ein geeigneter Auslöser für eine stimulusinitiierte Freisetzung von Wirkstoffen an Entzündungsherden sein könnte. Zwei komplementäre CMS nanocarrier, einerseits ein reduktionssensitiv und andererseits oxidationsempfindlich, wurden synthetisiert. Basierend auf einem hyperverzweigten Polyglycerol als Kernbaustein und einer wasserlöslichen mPEG-Außenhülle enthielt die innere Alkylhülle entweder eine Disulfideinheit oder eine Thioethereinheit. Das reduktionsempfindliche Disulfid-haltige rsCMS und sein oxidationsempfindliches Thioether-haltiges osCMS-Gegenstück wurden in vitro auf die stimulierte Freisetzung des eingekapselten Farbstoffs Nilrot getestet. Eine physiologisch relevante Konzentration von 10 mM GSH war nicht in der Lage, eine schnelle Freisetzung von NR auszulösen, möglicherweise aufgrund der begrenzten Reduktionskapazität von GSH in Abwesenheit von Redox-vermittelnden Enzymen. Das Reduktionsmittel TCEP führte dagegen

zu einer Freisetzung von 90% innerhalb von 24 Stunden. Die Inkubation von osCMS mit 1% H_2O_2 führte zu einer anhaltenden Freisetzung von 80% NR im gleichen Zeitraum. Hautpenetrationsexperimente von NR@rsCMS an ex vivo humaner Haut stützten unsere Hypothese zum natürlichen GSH-Gradienten in der Haut. Die Synthese eines EPR-markierten Dexamethasons wurde ebenfalls etabliert, und die PCA-markierte Version wird in zukünftigen Studien zur Verteilung von ROS in der Haut als Auslöser für die stimulierte Freisetzung von Medikamenten aus osCMS verwendet.

5.2 Short Summary

This thesis summarizes the research conducted in the field of core-multishell nanocarriers for the application in dermal drug delivery. While the CMS nanocarrier as a platform for drug delivery has been established by several publications, the goal of my thesis was to specialize the CMS nanocarrier as a bioresponsive nanocarrier for applications in the skin. The skin is a yet poorly characterized biological environment regarding its chemistry, especially in the state of disease. However, the penetration and successful delivery of the fluorescent model drug nile red into deeper skin layers, compared to a standard nile red cream, has been stated in a previous study. The increased penetration was the starting point for the general hypothesis on the CMS nanocarrier being a potential drug delivery platform. However, the fate of the nanocarrier inside the skin was identified as a potential toxicity issue. Hence, the first project of this PhD work aimed at establishing a biodegradable CMS nanocarrier. Based on a diacid and a triol, a hyperbranched polyester as the core molecule of a CMS nanocarrier was synthesized and used as a macroiniiator for the ring-opening polymerization of ε-caprolactone. Surrounded by a water-soluble mPEG outer shell, this nanocarrier showed a complete enzymatic degradation in seven days, while surprisingly, hydrolysis of the ester-based CMS nanocarrier did not take place under physiologically relevant conditions. The low molecular weight of the core molecule and the low branching of the resulting CMS nanocarrier are hypothesized to be the reason for the poor drug loading capacity of this biodegradable nanocarrier. Aiming at the redox-barrier of skin, we hypothesized the natural gradient of reductants and oxidants in the skin to be a suitable trigger for stimulus-initiated release of drugs at sites of inflammation. A complementary set of a reduction-sensitive and an oxidation-sensitive CMS nanocarrier has been synthesized. Based on a hyperbranched polyglycerol as a core building block, and a water-soluble mPEG outer shell, the alkyl inner shell contained either a disulfide moiety, or a thioether moiety. The reduction-sensitive disulfide-containing rsCMS and its oxidation-sensitive thioether-containing osCMS counterpart were tested for the triggered release of the encapsulated dye nile red in vitro. A physiologically relevant concentration of 10 mM GSH was not able to trigger a fast release of NR, possibly due to the limited reduction capacity of GSH in the absence of redox-mediating enzymes. However, the reductant TCEP led to 90 % release in 24 h. The incubation of osCMS with 1 % H_2O_2 triggered

a sustained release of 80 % NR over the same period. Skin penetration experiments of NR@rsCMS on ex vivo human skin supported our hypothesis on the natural GSH gradient in the skin. Also, the synthesis of an EPR-labelled dexamethasone was established, and the PCA-labelled version will be used in future studies on the distribution of ROS in skin as the trigger for stimulated release of drugs from osCMS.

6 References

1. Ringsdorf, H. In *Structure and properties of pharmacologically active polymers*, Journal of Polymer Science: Polymer Symposia, Wiley Online Library: 1975; 135-153.
2. Duncan, R., The dawning era of polymer therapeutics. *Nat Rev Drug Discov* **2003,** *2* (5), 347-360.
3. Webber, M. J.; Langer, R., Drug delivery by supramolecular design. *Chemical Society Reviews* **2017,** *46* (21), 6600-6620.
4. Jansen, J. F.; de Brabander-van den Berg, E. M.; Meijer, E. W., Encapsulation of guest molecules into a dendritic box. *Science* **1994,** *266*, 1226-1229.
5. Tomalia, D. A.; Naylor, A. M.; Goddard, W. A., Starburst dendrimers: Molecular-level control of size, shape, surface chemistry, topology, and flexibility from atoms to macroscopic matter. *Angewandte Chemie International Edition in English* **1990,** *29* (2), 138-175.
6. Radowski, M. R.; Shukla, A.; von Berlepsch, H.; Böttcher, C.; Pickaert, G.; Rehage, H.; Haag, R., Supramolecular aggregates of dendritic multishell architectures as universal nanocarriers. *Angew Chem Int Edit* **2007,** *46* (8), 1265-1269.
7. Calderón, M.; Quadir, M. A.; Strumia, M.; Haag, R., Functional dendritic polymer architectures as stimuli-responsive nanocarriers. *Biochimie* **2010,** *92* (9), 1242-1251.
8. Fleige, E.; Ziem, B.; Grabolle, M.; Haag, R.; Resch-Genger, U., Aggregation phenomena of host and guest upon the loading of dendritic core-multishell nanoparticles with solvatochromic dyes. *Macromolecules* **2012,** *45* (23), 9452-9459.
9. Haag, R.; Kratz, F., Polymer therapeutics: Concepts and applications. *Angew Chem Int Ed Engl* **2006,** *45* (8), 1198-1215.
10. Kratz, F.; Müller, I. A.; Ryppa, C.; Warnecke, A., Prodrug strategies in anticancer chemotherapy. *ChemMedChem* **2008,** *3* (1), 20-53.
11. Dragojevic, S.; Ryu, J. S.; Raucher, D., Polymer-based prodrugs: Improving tumor targeting and the solubility of small molecule drugs in cancer therapy. *Molecules* **2015,** *20* (12), 21750-21769.
12. Fleige, E.; Quadir, M. A.; Haag, R., Stimuli-responsive polymeric nanocarriers for the controlled transport of active compounds: Concepts and applications. *Advanced Drug Delivery Reviews* **2012,** *64* (9), 866-884.
13. Wong, P. T.; Choi, S. K., Mechanisms of drug release in nanotherapeutic delivery systems. *Chemical Reviews* **2015,** *115* (9), 3388-3432.
14. Vaupel, P.; Kallinowski, F.; Okunieff, P., Blood flow, oxygen and nutrient supply, and metabolic microenvironment of human tumors: A review. *Cancer Res* **1989,** *49* (23), 6449-6465.

15. Kato, Y.; Ozawa, S.; Miyamoto, C.; Maehata, Y.; Suzuki, A.; Maeda, T.; Baba, Y., Acidic extracellular microenvironment and cancer. *Cancer Cell International* **2013,** *13*, 89-89.
16. Pistolis, G.; Malliaris, A.; Tsiourvas, D.; Paleos, C. M., Poly(propyleneimine) dendrimers as ph-sensitive controlled-release systems. *Chemistry - A European Journal* **1999,** *5* (5), 1440-1444.
17. Vartak, D. G.; Gemeinhart, R. A., Matrix metalloproteases: Underutilized targets for drug delivery. *Journal of drug targeting* **2007,** *15* (1), 1-20.
18. Peng, Z. H.; Kopecek, J., Enhancing accumulation and penetration of hpma copolymer-doxorubicin conjugates in 2d and 3d prostate cancer cells via irgd conjugation with an mmp-2 cleavable spacer. *J Am Chem Soc* **2015,** *137* (21), 6726-6729.
19. Schafer, F. Q.; Buettner, G. R., Redox environment of the cell as viewed through the redox state of the glutathione disulfide/glutathione couple. *Free Radical Biology and Medicine* **2001,** *30* (11), 1191-1212.
20. Saito, G.; Swanson, J. A.; Lee, K.-D., Drug delivery strategy utilizing conjugation via reversible disulfide linkages: Role and site of cellular reducing activities. *Advanced Drug Delivery Reviews* **2003,** *55* (2), 199-215.
21. Meng, F.; Hennink, W. E.; Zhong, Z., Reduction-sensitive polymers and bioconjugates for biomedical applications. *Biomaterials* **2009,** *30* (12), 2180-2198.
22. Matsumoto, S.; Christie, R. J.; Nishiyama, N.; Miyata, K.; Ishii, A.; Oba, M.; Koyama, H.; Yamasaki, Y.; Kataoka, K., Environment-responsive block copolymer micelles with a disulfide cross-linked core for enhanced sirna delivery. *Biomacromolecules* **2009,** *10* (1), 119-127.
23. Fritsch, P., *Dermatologie und venerologie für das studium*. 2009.
24. Prausnitz, M. R.; Elias, P. M.; Franz, T. J.; Schmuth, M.; Tsai, J.-C.; Menon, G. K.; Holleran, W. M.; Feingold, K. R., Skin barrier and transdermal drug delivery. In *Drug delivery: Fundamentals and applications*, Hillery, A. M.; Park, K., Eds. CRC Press: 2016; pp 2065-2073.
25. Elias, P. M., Epidermal lipids, barrier function, and desquamation. *Journal of Investigative Dermatology* **1983,** *80*, 44-49.
26. Pappas, A., Epidermal surface lipids. *Dermato-endocrinology* **2009,** *1* (2), 72-76.
27. Richter, T.; Peuckert, C.; Sattler, M.; Koenig, K.; Riemann, I.; Hintze, U.; Wittern, K. P.; Wiesendanger, R.; Wepf, R., Dead but highly dynamic – the stratum corneum is divided into three hydration zones. *Skin Pharmacology and Physiology* **2004,** *17* (5), 246-257.
28. Groen, D.; Poole, D. S.; Gooris, G. S.; Bouwstra, J. A., Is an orthorhombic lateral packing and a proper lamellar organization important for the skin barrier function? *Biochimica et Biophysica Acta (BBA) - Biomembranes* **2011,** *1808* (6), 1529-1537.

29. Menon, G. K.; Bommannan, D. B.; Elias, P. M., High-frequency sonophoresis: Permeation pathways and structural basis for enhanced permeability. *Skin Pharmacology and Physiology* **1994,** *7* (3), 130-139.
30. Cevc, G.; Vierl, U., Nanotechnology and the transdermal route: A state of the art review and critical appraisal. *Journal of Controlled Release* **2010,** *141* (3), 277-299.
31. Vogt, A.; Wischke, C.; Neffe, A. T.; Ma, N.; Alexiev, U.; Lendlein, A., Nanocarriers for drug delivery into and through the skin - do existing technologies match clinical challenges? *J Control Release* **2016**.
32. Schmuth, M.; Blunder, S.; Dubrac, S.; Gruber, R.; Moosbrugger-Martinz, V., Epidermal barrier in hereditary ichthyoses, atopic dermatitis, and psoriasis. *JDDG: Journal der Deutschen Dermatologischen Gesellschaft* **2015,** *13* (11), 1119-1123.
33. van Smeden, J.; Bouwstra, J. A., Stratum corneum lipids: Their role for the skin barrier function in healthy subjects and atopic dermatitis patients. *Curr Probl Dermatol* **2016,** *49*, 8-26.
34. Callen, J.; Chamlin, S.; Eichenfield, L. F.; Ellis, C.; Girardi, M.; Goldfarb, M.; Hanifin, J.; Lee, P.; Margolis, D.; Paller, A. S.; Piacquadio, D.; Peterson, W.; Kaulback, K.; Fennerty, M.; Wintroub, B. U., A systematic review of the safety of topical therapies for atopic dermatitis. *British Journal of Dermatology* **2007,** *156* (2), 203-221.
35. Prow, T. W.; Grice, J. E.; Lin, L. L.; Faye, R.; Butler, M.; Becker, W.; Wurm, E. M. T.; Yoong, C.; Robertson, T. A.; Soyer, H. P.; Roberts, M. S., Nanoparticles and microparticles for skin drug delivery. *Advanced Drug Delivery Reviews* **2011,** *63* (6), 470-491.
36. Vogt, A.; Mandt, N.; Lademann, J.; Schaefer, H.; Blume-Peytavi, U., Follicular targeting-a promising tool in selective dermatotherapy. *Journal of Investigative Dermatology Symposium Proceedings* **2005,** *10* (3), 252-255.
37. Toll, R.; Jacobi, U.; Richter, H.; Lademann, J.; Schaefer, H.; Blume-Peytavi, U., Penetration profile of microspheres in follicular targeting of terminal hair follicles. *Journal of Investigative Dermatology* **2004,** *123* (1), 168-176.
38. Otberg, N.; Richter, H.; Schaefer, H.; Blume-Peytavi, U.; Sterry, W.; Lademann, J., Variations of hair follicle size and distribution in different body sites. *Journal of Investigative Dermatology* **2004,** *122* (1), 14-19.
39. Lademann, J.; Otberg, N.; Jacobi, U.; Hoffman, R. M.; Blume-Peytavi, U. In *Follicular penetration and targeting*, Journal of Investigative Dermatology Symposium Proceedings, Elsevier: 2005; 301-303.
40. Schäfer-Korting, M.; Mehnert, W.; Korting, H.-C., Lipid nanoparticles for improved topical application of drugs for skin diseases. *Advanced drug delivery reviews* **2007,** *59* (6), 427-443.

41. Mortensen, L. J.; Jatana, S.; Gelein, R.; De Benedetto, A.; De Mesy Bentley, K. L.; Beck, L. A.; Elder, A.; DeLouise, L. A., Quantification of quantum dot murine skin penetration with uvr barrier impairment. *Nanotoxicology* **2013,** *7* (8), 1386-1398.
42. Gamer, A.; Leibold, E. v.; Van Ravenzwaay, B., The in vitro absorption of microfine zinc oxide and titanium dioxide through porcine skin. *Toxicology in vitro* **2006,** *20* (3), 301-307.
43. Lademann, J.; Weigmann, H.-J.; Rickmeyer, C.; Barthelmes, H.; Schaefer, H.; Mueller, G.; Sterry, W., Penetration of titanium dioxide microparticles in a sunscreen formulation into the horny layer and the follicular orifice. *Skin Pharmacology and Physiology* **1999,** *12* (5), 247-256.
44. Graf, C. M.; Meinke, M. C.; Gao, Q.; Hadam, S.; Raabe, J.; Sterry, W.; Blume-Peytavi, U.; Lademann, J. M.; Rühl, E.; Vogt, A., Qualitative detection of single submicron and nanoparticles in human skin by scanning transmission x-ray microscopy. *Journal of Biomedical Optics* **2009,** *14* (2), 021015.
45. Larese, F. F.; D'Agostin, F.; Crosera, M.; Adami, G.; Renzi, N.; Bovenzi, M.; Maina, G., Human skin penetration of silver nanoparticles through intact and damaged skin. *Toxicology* **2009,** *255* (1-2), 33-37.
46. Jenning, V.; Gysler, A.; Schäfer-Korting, M.; Gohla, S. H., Vitamin a loaded solid lipid nanoparticles for topical use: Occlusive properties and drug targeting to the upper skin. *European Journal of Pharmaceutics and Biopharmaceutics* **2000,** *49* (3), 211-218.
47. Alvarez-Román, R.; Naik, A.; Kalia, Y.; Guy, R. H.; Fessi, H., Skin penetration and distribution of polymeric nanoparticles. *Journal of Controlled Release* **2004,** *99* (1), 53-62.
48. Abraham, W.; Downing, D. T., Interaction between corneocytes and stratum corneum lipid liposomes in vitro. *Biochimica et Biophysica Acta (BBA)-Biomembranes* **1990,** *1021* (2), 119-125.
49. Boncheva, M.; De Sterke, J.; Caspers, P. J.; Puppels, G. J., Depth profiling of stratum corneum hydration in vivo: A comparison between conductance and confocal raman spectroscopic measurements. *Experimental dermatology* **2009,** *18* (10), 870-876.
50. Yamamoto, K.; Klossek, A.; Flesch, R.; Ohigashi, T.; Fleige, E.; Rancan, F.; Frombach, J.; Vogt, A.; Blume-Peytavi, U.; Schrade, P., Core-multishell nanocarriers: Transport and release of dexamethasone probed by soft x-ray spectromicroscopy. *Journal of Controlled Release* **2016,** *242*, 64-70.
51. Chilcott, R.; Price, S., *Principles and practice of skin toxicology*. John Wiley & Sons: 2008.

52. Zhang, L.; Monteiro-Riviere, N., Assessment of quantum dot penetration into intact, tape-stripped, abraded and flexed rat skin. *Skin pharmacology and physiology* **2008,** *21* (3), 166-180.
53. Prow, T. W.; Monteiro-Riviere, N. A.; Inman, A. O.; Grice, J. E.; Chen, X.; Zhao, X.; Sanchez, W. H.; Gierden, A.; Kendall, M. A.; Zvyagin, A. V., Quantum dot penetration into viable human skin. *Nanotoxicology* **2012,** *6* (2), 173-185.
54. Prausnitz, M. R., Microneedles for transdermal drug delivery. *Advanced drug delivery reviews* **2004,** *56* (5), 581-587.
55. Rancan, F.; Blume-Peytavi, U.; Vogt, A., Utilization of biodegradable polymeric materials as delivery agents in dermatology. *Clinical, cosmetic and investigational dermatology* **2014,** *7*, 23-34.
56. Papakostas, D.; Rancan, F.; Sterry, W.; Blume-Peytavi, U.; Vogt, A., Nanoparticles in dermatology. *Archives of dermatological research* **2011,** *303* (8), 533-550.
57. Vogt, A.; Combadiere, B.; Hadam, S.; Stieler, K. M.; Lademann, J.; Schaefer, H.; Autran, B.; Sterry, W.; Blume-Peytavi, U., 40nm, but not 750 or 1,500nm, nanoparticles enter epidermal cd1a+ cells after transcutaneous application on human skin. *Journal of Investigative Dermatology* **2006,** *126* (6), 1316-1322.
58. Rancan, F.; Gao, Q.; Graf, C.; Troppens, S.; Hadam, S.; Hackbarth, S.; Kembuan, C.; Blume-Peytavi, U.; Rühl, E.; Lademann, J.; Vogt, A., Skin penetration and cellular uptake of amorphous silica nanoparticles with variable size, surface functionalization, and colloidal stability. *ACS Nano* **2012,** *6* (8), 6829-6842.
59. Mortensen, L. J.; Oberdörster, G.; Pentland, A. P.; DeLouise, L. A., In vivo skin penetration of quantum dot nanoparticles in the murine model: The effect of uvr. *Nano Letters* **2008,** *8* (9), 2779-2787.
60. Flohé, L., The fairytale of the gssg/gsh redox potential. *Biochim Biophys Acta* **2013,** *1830* (5), 3139-3142.
61. Misra, H. P., Generation of superoxide free radical during the autoxidation of thiols. *Journal of Biological Chemistry* **1974,** *249* (7), 2151-2155.
62. Comini, M. A., Measurement and meaning of cellular thiol:Disufhide redox status. *Free Radical Research* **2016,** *50* (2), 246-271.
63. Chen, X.; Zhou, Y.; Peng, X.; Yoon, J., Fluorescent and colorimetric probes for detection of thiols. *Chemical Society Reviews* **2010,** *39* (6), 2120-2135.
64. Deponte, M., The incomplete glutathione puzzle: Just guessing at numbers and figures? *Antioxid Redox Signal* **2017,** *27* (15), 1130-1161.
65. Wagener, F. A. D. T. G.; Carels, C. E.; Lundvig, D. M. S., Targeting the redox balance in inflammatory skin conditions. *International Journal of Molecular Sciences* **2013,** *14* (5), 9126-9167.

66. Kamata, H.; Hirata, H., Redox regulation of cellular signalling. *Cellular signalling* **1999,** *11* (1), 1-14.
67. Ogura, R.; Knox, J. M.; Griffin, A. C.; Kusuhara, M., The concentration of sulfhydryl and disulfide in human epidermis, hair and nail. *The Journal of investigative dermatology* **1962,** *38*, 69.
68. Yamada, H.; Takamori, K.; Ogawa, H., Localization and some properties of skin sulfhydryl oxidase. *Archives of dermatological research* **1987,** *279* (3), 194-197.
69. Weber, S. U.; Thiele, J. J.; Packer, L.; Cross, C. E., Vitamin c, uric acid, and glutathione gradients in murine stratum corneum and their susceptibility to ozone exposure. *Journal of Investigative Dermatology* **1999,** *113* (6), 1128-1132.
70. Fuchs, J.; Zollner, T.; Kaufmann, R.; Podda, M., Redox-modulated pathways in inflammatory skin diseases. *Free Radical Biology and Medicine* **2001,** *30* (4), 337-353.
71. Şikar Aktürk, A.; Özdoğan, H.; Bayramgürler, D.; Çekmen, M.; Bilen, N.; Kıran, R., Nitric oxide and malondialdehyde levels in plasma and tissue of psoriasis patients. *Journal of the European Academy of Dermatology and Venereology* **2012,** *26* (7), 833-837.
72. Zhang, X.; Han, L.; Liu, M.; Wang, K.; Tao, L.; Wan, Q.; Wei, Y., Recent progress and advances in redox-responsive polymers as controlled delivery nanoplatforms. *Materials Chemistry Frontiers* **2017,** *1* (5), 807-822.
73. Gyarmati, B.; Némethy, Á.; Szilágyi, A., Reversible disulphide formation in polymer networks: A versatile functional group from synthesis to applications. *European Polymer Journal* **2013,** *49* (6), 1268-1286.
74. Neves, R. P.; Fernandes, P. A.; Ramos, M. J., Mechanistic insights on the reduction of glutathione disulfide by protein disulfide isomerase. *Proceedings of the National Academy of Sciences* **2017**, 201618985.
75. Beld, J.; Woycechowsky, K. J.; Hilvert, D., Selenoglutathione: Efficient oxidative protein folding by a diselenide. *Biochemistry* **2007,** *46* (18), 5382-5390.
76. Cheng, G.; He, Y.; Xie, L.; Nie, Y.; He, B.; Zhang, Z.; Gu, Z., Development of a reduction-sensitive diselenide-conjugated oligoethylenimine nanoparticulate system as a gene carrier. *Int J Nanomedicine* **2012,** *7*, 3991-4006.
77. Xu, Q.; He, C.; Xiao, C.; Chen, X., Reactive oxygen species (ros) responsive polymers for biomedical applications. *Macromol Biosci* **2016,** *16* (5), 635-646.
78. Song, C.-C.; Du, F.-S.; Li, Z.-C., Oxidation-responsive polymers for biomedical applications. *J. Mater. Chem. B* **2014,** *2* (22), 3413-3426.
79. Lee, S. H.; Gupta, M. K.; Bang, J. B.; Bae, H.; Sung, H. J., Current progress in reactive oxygen species (ros)-responsive materials for biomedical applications. *Adv Healthc Mater* **2013,** *2* (6), 908-915.

80. Xu, H.; Cao, W.; Zhang, X., Selenium-containing polymers: Promising biomaterials for controlled release and enzyme mimics. *Accounts of Chemical Research* **2013,** *46* (7), 1647-1658.
81. Casado, N.; Hernández, G.; Sardon, H.; Mecerreyes, D., Current trends in redox polymers for energy and medicine. *Progress in Polymer Science* **2016,** *52*, 107-135.
82. Finkel, T., Signal transduction by reactive oxygen species. *J Cell Biol* **2011,** *194* (1), 7-15.
83. Kumar, R.; Sinha, V. R., Thiomer: A potential carrier for therapeutic delivery. *Reactive and Functional Polymers* **2013,** *73* (8), 1156-1166.
84. Neu, M.; Germershaus, O.; Mao, S.; Voigt, K.-H.; Behe, M.; Kissel, T., Crosslinked nanocarriers based upon poly (ethylene imine) for systemic plasmid delivery: In vitro characterization and in vivo studies in mice. *Journal of Controlled Release* **2007,** *118* (3), 370-380.
85. Matsumoto, S.; Christie, R. J.; Nishiyama, N.; Miyata, K.; Ishii, A.; Oba, M.; Koyama, H.; Yamasaki, Y.; Kataoka, K., Environment-responsive block copolymer micelles with a disulfide cross-linked core for enhanced sirna delivery. *Biomacromolecules* **2008,** *10* (1), 119-127.
86. Oupický, D.; Parker, A. L.; Seymour, L. W., Laterally stabilized complexes of DNA with linear reducible polycations: Strategy for triggered intracellular activation of DNA delivery vectors. *Journal of the American Chemical Society* **2002,** *124* (1), 8-9.
87. You, Y. Z.; Yu, Z. Q.; Cui, M. M.; Hong, C. Y., Preparation of photoluminescent nanorings with controllable bioreducibility and stimuli-responsiveness. *Angewandte Chemie International Edition* **2010,** *49* (6), 1099-1102.
88. Liu, J.; Pang, Y.; Huang, W.; Zhu, Z.; Zhu, X.; Zhou, Y.; Yan, D., Redox-responsive polyphosphate nanosized assemblies: A smart drug delivery platform for cancer therapy. *Biomacromolecules* **2011,** *12* (6), 2407-2415.
89. Steinhilber, D.; Sisson, A. L.; Mangoldt, D.; Welker, P.; Licha, K.; Haag, R., Synthesis, reductive cleavage, and cellular interaction studies of biodegradable, polyglycerol nanogels. *Advanced Functional Materials* **2010,** *20* (23), 4133-4138.
90. Zhang, R.; Li, X.; He, K.; Sheng, X.; Deng, S.; Shen, Y.; Chang, G.; Ye, X., Preparation and properties of redox responsive modified hyaluronic acid hydrogels for drug release. *Polymers for Advanced Technologies* **2017,** *28* (12), 1759-1763.
91. Cuchelkar, V.; Kopečková, P.; Kopeček, J., Synthesis and biological evaluation of disulfide-linked hpma copolymer-mesochlorin e6 conjugates. *Macromolecular bioscience* **2008,** *8* (5), 375-383.
92. de Vries, W. C.; Grill, D.; Tesch, M.; Ricker, A.; Nusse, H.; Klingauf, J.; Studer, A.; Gerke, V.; Ravoo, B. J., Reversible stabilization of vesicles: Redox-responsive polymer

nanocontainers for intracellular delivery. *Angew Chem Int Ed Engl* **2017,** *56* (32), 9603-9607.

93. Bernkop-Schnürch, A., Thiomers: A new generation of mucoadhesive polymers. *Advanced Drug Delivery Reviews* **2005,** *57* (11), 1569-1582.
94. Köllner, S.; Dünnhaupt, S.; Waldner, C.; Hauptstein, S.; de Sousa, I. P.; Bernkop-Schnürch, A., Mucus permeating thiomer nanoparticles. *European Journal of Pharmaceutics and Biopharmaceutics* **2015,** *97*, 265-272.
95. Napoli, A.; Valentini, M.; Tirelli, N.; Müller, M.; Hubbell, J. A., Oxidation-responsive polymeric vesicles. *Nature Materials* **2004,** *3*, 183-189.
96. Lallana, E.; Tirelli, N., Oxidation-responsive polymers: Which groups to use, how to make them, what to expect from them (biomedical applications). *Macromolecular Chemistry and Physics* **2013,** *214* (2), 143-158.
97. Velluto, D.; Demurtas, D.; Hubbell, J. A., Peg-b-pps diblock copolymer aggregates for hydrophobic drug solubilization and release: Cyclosporin a as an example. *Molecular Pharmaceutics* **2008,** *5* (4), 632-642.
98. Hu, P.; Tirelli, N., Scavenging ros: Superoxide dismutase/catalase mimetics by the use of an oxidation-sensitive nanocarrier/enzyme conjugate. *Bioconjugate Chemistry* **2012,** *23* (3), 438-449.
99. Borges, F.; Fernandes, E.; Roleira, F., Progress towards the discovery of xanthine oxidase inhibitors. *Curr Med Chem* **2002,** *9* (2), 195-217.
100. Reddy, S. T.; Rehor, A.; Schmoekel, H. G.; Hubbell, J. A.; Swartz, M. A., In vivo targeting of dendritic cells in lymph nodes with poly(propylene sulfide) nanoparticles. *Journal of Controlled Release* **2006,** *112* (1), 26-34.
101. Napoli, A.; Tirelli, N.; Wehrli, E.; Hubbell, J. A., Lyotropic behavior in water of amphiphilic aba triblock copolymers based on poly(propylene sulfide) and poly(ethylene glycol). *Langmuir* **2002,** *18* (22), 8324-8329.
102. Hu, P.; Tirelli, N., Inter-micellar dynamics in block copolymer micelles: Fret experiments of macroamphiphile and payload exchange. *Reactive and Functional Polymers* **2011,** *71* (3), 303-314.
103. Scott, E. A.; Stano, A.; Gillard, M.; Maio-Liu, A. C.; Swartz, M. A.; Hubbell, J. A., Dendritic cell activation and t cell priming with adjuvant-and antigen-loaded oxidation-sensitive polymersomes. *Biomaterials* **2012,** *33* (26), 6211-6219.
104. Poole, K. M.; Nelson, C. E.; Joshi, R. V.; Martin, J. R.; Gupta, M. K.; Haws, S. C.; Kavanaugh, T. E.; Skala, M. C.; Duvall, C. L., Ros-responsive microspheres for on demand antioxidant therapy in a model of diabetic peripheral arterial disease. *Biomaterials* **2015,** *41*, 166-175.

105. Deming, T. J., Functional modification of thioether groups in peptides, polypeptides, and proteins. *Bioconjug Chem* **2017,** *28* (3), 691-700.
106. Levine, R. L.; Mosoni, L.; Berlett, B. S.; Stadtman, E. R., Methionine residues as endogenous antioxidants in proteins. *Proceedings of the National Academy of Sciences* **1996,** *93* (26), 15036-15040.
107. Levine, R. L.; Moskovitz, J.; Stadtman, E. R., Oxidation of methionine in proteins: Roles in antioxidant defense and cellular regulation. *IUBMB life* **2000,** *50* (4-5), 301-307.
108. Dado, G. P.; Gellman, S. H., Redox control of secondary structure in a designed peptide. *Journal of the American Chemical Society* **1993,** *115* (26), 12609-12610.
109. Schenck, H. L.; Dado, G. P.; Gellman, S. H., Redox-triggered secondary structure changes in the aggregated states of a designed methionine-rich peptide. *Journal of the American Chemical Society* **1996,** *118* (50), 12487-12494.
110. Herzberger, J.; Fischer, K.; Leibig, D.; Bros, M.; Thiermann, R.; Frey, H., Oxidation-responsive and "clickable" poly(ethylene glycol) via copolymerization of 2-(methylthio)ethyl glycidyl ether. *J Am Chem Soc* **2016,** *138* (29), 9212-9223.
111. Jeanmaire, D.; Laliturai, J.; Almalik, A.; Carampin, P.; d'Arcy, R.; Lallana, E.; Evans, R.; Winpenny, R. E.; Tirelli, N., Chemical specificity in redox-responsive materials: The diverse effects of different reactive oxygen species (ros) on polysulfide nanoparticles. *Polymer Chemistry* **2014,** *5* (4), 1393-1404.
112. Carampin, P.; Lallana, E.; Laliturai, J.; Carroccio, S. C.; Puglisi, C.; Tirelli, N., Oxidant-dependent redox responsiveness of polysulfides. *Macromolecular Chemistry and Physics* **2012,** *213* (19), 2052-2061.
113. Allen, B. L.; Johnson, J. D.; Walker, J. P., Encapsulation and enzyme-mediated release of molecular cargo in polysulfide nanoparticles. *ACS nano* **2011,** *5* (6), 5263-5272.
114. d'Arcy, R.; Siani, A.; Lallana, E.; Tirelli, N., Influence of primary structure on responsiveness. Oxidative, thermal, and thermo-oxidative responses in polysulfides. *Macromolecules* **2015,** *48* (22), 8108-8120.
115. d'Arcy, R.; Tirelli, N., Branched amphiphilic polysulfides: Influence of macromolecular architecture on self-assembly and oxidation responsiveness. *MRS Proceedings* **2015,** *1718*, 55-63.
116. Heller, J., Controlled release of biologically active compounds from bioerodible polymers. *Biomaterials* **1980,** *1* (1), 51-57.
117. Ulery, B. D.; Nair, L. S.; Laurencin, C. T., Biomedical applications of biodegradable polymers. *Journal of Polymer Science Part B: Polymer Physics* **2011,** *49* (12), 832-864.
118. Binauld, S.; Stenzel, M. H., Acid-degradable polymers for drug delivery: A decade of innovation. *Chemical communications (Cambridge, England)* **2013,** *49* (21), 2082-2102.

119. Huang, Y.; Wang, D.; Zhu, X.; Yan, D.; Chen, R., Synthesis and therapeutic applications of biocompatible or biodegradable hyperbranched polymers. *Polym. Chem.* **2015,** *6* (15), 2794-2812.
120. Marin, E.; Briceno, M. I.; Caballero-George, C., Critical evaluation of biodegradable polymers used in nanodrugs. *Int. J. Nanomed.* **2012,** *8*, 3071-3091.
121. Ikada, Y.; Tsuji, H., Biodegradable polyesters for medical and ecological applications. *Macromolecular rapid communications* **2000,** *21* (3), 117-132.
122. Nair, L. S.; Laurencin, C. T., Biodegradable polymers as biomaterials. *Progress in Polymer Science* **2007,** *32* (8), 762-798.
123. Gilding, D. K. In *Biodegradable polymers* CRC: 1981; 209-232.
124. Merkli, A.; Tabatabay, C.; Gurny, R.; Heller, J., Biodegradable polymers for the controlled release of ocular drugs. *Progress in Polymer Science* **1998,** *23* (3), 563-580.
125. Bauer, K. N.; Tee, H. T.; Velencoso, M. M.; Wurm, F. R., Main-chain poly(phosphoester)s: History, syntheses, degradation, bio-and flame-retardant applications. *Progress in Polymer Science* **2017,** *73*, 61-122.
126. Ceonzo, K.; Gaynor, A.; Shaffer, L.; Kojima, K.; Vacanti, C. A.; Stahl, G. L., Polyglycolic acid-induced inflammation: Role of hydrolysis and resulting complement activation. *Tissue engineering* **2006,** *12* (2), 301-308.
127. Zhang, X.; Hu, H.; Liu, T.; Yang, Y.; Peng, Y.; Cai, Q.; Fang, L., Multi-armed poly(l-glutamic acid)-graft-polypropyleneinime as effective and serum resistant gene delivery vectors. *International Journal of Pharmaceutics* **2014,** *465* (1), 444-454.
128. Jessel, N.; Oulad-Abdelghani, M.; Meyer, F.; Lavalle, P.; Haikel, Y.; Schaaf, P.; Voegel, J.-C., Multiple and time-scheduled in situ DNA delivery mediated by β-cyclodextrin embedded in a polyelectrolyte multilayer. *Proceedings of the National Academy of Sciences* **2006,** *103* (23), 8618-8621.
129. Pilbat, A.-M.; Ball, V.; Schaaf, P.; Voegel, J.-C.; Szalontai, B., Partial poly (glutamic acid)↔ poly (aspartic acid) exchange in layer-by-layer polyelectrolyte films. Structural alterations in the three-component architectures. *Langmuir* **2006,** *22* (13), 5753-5759.
130. Xu, Q.; He, C.; Zhang, Z.; Ren, K.; Chen, X., Injectable, biomolecule-responsive polypeptide hydrogels for cell encapsulation and facile cell recovery through triggered degradation. *ACS Applied Materials & Interfaces* **2016,** *8* (45), 30692-30702.
131. Malikmammadov, E.; Tanir, T. E.; Kiziltay, A.; Hasirci, V.; Hasirci, N., Pcl and pcl-based materials in biomedical applications. *Journal of Biomaterials Science, Polymer Edition* **2018,** *29* (7-9), 863-893.
132. McKee, M. G.; Unal, S.; Wilkes, G. L.; Long, T. E., Branched polyesters: Recent advances in synthesis and performance. *Progress in Polymer Science* **2005,** *30* (5), 507-539.

133. Tande, B. M.; Wagner, N. J.; Mackay, M. E.; Hawker, C. J.; Jeong, M., Viscosimetric, hydrodynamic, and conformational properties of dendrimers and dendrons. *Macromolecules* **2001,** *34* (24), 8580-8585.
134. Stumbé, J. F.; Bruchmann, B., Hyperbranched polyesters based on adipic acid and glycerol. *Macromolecular Rapid Communications* **2004,** *25* (9), 921-924.
135. Fréchet, J. M.; Hawker, C. J., Hyperbranched polyphenylene and hyperbranched polyesters: New soluble, three-dimensional, reactive polymers. *Reactive and Functional Polymers* **1995,** *26* (1-3), 127-136.
136. Voit, B. I.; Lederer, A., Hyperbranched and highly branched polymer architectures--synthetic strategies and major characterization aspects. *Chemical reviews* **2009,** *109* (11), 5924-5973.
137. Twibanire, J. d. A. K.; Grindley, T. B., Polyester dendrimers: Smart carriers for drug delivery. *Polymers* **2014,** *6* (1), 179-213.
138. Reul, R.; Renette, T.; Bege, N.; Kissel, T., Nanoparticles for paclitaxel delivery: A comparative study of different types of dendritic polyesters and their degradation behavior. *International Journal of Pharmaceutics* **2011,** *407* (1), 190-196.
139. Smet, M.; Gottschalk, C.; Skaria, S.; Frey, H., Aliphatic hyperbranched copolyesters by combination of rop and ab2-polycondensation. *Macromolecular Chemistry and Physics* **2005,** *206* (24), 2421-2428.
140. Skaria, S.; Smet, M.; Frey, H., Enzyme-catalyzed synthesis of hyperbranched aliphatic polyesters. *Macromolecular rapid communications* **2002,** *23* (4), 292-296.
141. Satoh, T.; Kakuchi, T., Synthesis of hyperbranched carbohydrate polymers by ring-opening multibranching polymerization of anhydro sugar. *Macromolecular bioscience* **2007,** *7* (8), 999-1009.
142. Rodríguez-Hernández, J.; Gatti, M.; Klok, H.-A., Highly branched poly (l-lysine). *Biomacromolecules* **2003,** *4* (2), 249-258.
143. Jikei, M.; Chon, S.-H.; Kakimoto, M.-a.; Kawauchi, S.; Imase, T.; Watanebe, J., Synthesis of hyperbranched aromatic polyamide from aromatic diamines and trimesic acid. *Macromolecules* **1999,** *32* (6), 2061-2064.
144. Scholl, M.; Nguyen, T. Q.; Bruchmann, B.; Klok, H.-A., Controlling polymer architecture in the thermal hyperbranched polymerization of l-lysine. *Macromolecules* **2007,** *40* (16), 5726-5734.
145. Liu, J.; Huang, W.; Zhou, Y.; Yan, D., Synthesis of hyperbranched polyphosphates by self-condensing ring-opening polymerization of heep without catalyst. *Macromolecules* **2009,** *42* (13), 4394-4399.

146. Iwasaki, Y.; Nakagawa, C.; Ohtomi, M.; Ishihara, K.; Akiyoshi, K., Novel biodegradable polyphosphate cross-linker for making biocompatible hydrogel. *Biomacromolecules* **2004,** *5* (3), 1110-1115.
147. Wang, D.; Zhao, T.; Zhu, X.; Yan, D.; Wang, W., Bioapplications of hyperbranched polymers. *Chemical Society Reviews* **2015,** *44* (12), 4023-4071.
148. Schwarzl, R.; Du, F.; Haag, R.; Netz, R. R., General method for the quantification of drug loading and release kinetics of nanocarriers. *European Journal of Pharmaceutics and Biopharmaceutics* **2017,** *116*, 131-137.
149. Döge, N.; Hönzke, S.; Schumacher, F.; Balzus, B.; Colombo, M.; Hadam, S.; Rancan, F.; Blume-Peytavi, U.; Schäfer-Korting, M.; Schindler, A.; Rühl, E.; Skov, P. S.; Church, M. K.; Hedtrich, S.; Kleuser, B.; Bodmeier, R.; Vogt, A., Ethyl cellulose nanocarriers and nanocrystals differentially deliver dexamethasone into intact, tape-stripped or sodium lauryl sulfate-exposed ex vivo human skin - assessment by intradermal microdialysis and extraction from the different skin layers. *Journal of Controlled Release* **2016,** *242*, 25-34.
150. Baroli, B.; Ennas, M. G.; Loffredo, F.; Isola, M.; Pinna, R.; López-Quintela, M. A., Penetration of metallic nanoparticles in human full-thickness skin. *Journal of Investigative Dermatology* **2007,** *127* (7), 1701-1712.
151. Grant, C. A.; Twigg, P. C.; Baker, R.; Tobin, D. J., Tattoo ink nanoparticles in skin tissue and fibroblasts. *Beilstein journal of nanotechnology* **2015,** *6*, 1183-1191.
152. Yamamoto, K.; Flesch, R.; Ohigashi, T.; Hedtrich, S.; Klossek, A.; Patoka, P.; Ulrich, G.; Ahlberg, S.; Rancan, F.; Vogt, A., Selective probing of the penetration of dexamethasone into human skin by soft x-ray spectromicroscopy. *Analytical chemistry* **2015,** *87* (12), 6173-6179.
153. Honeywell-Nguyen, P. L.; Gooris, G. S.; Bouwstra, J. A., Quantitative assessment of the transport of elastic and rigid vesicle components and a model drug from these vesicle formulations into human skin in vivo. *J Invest Dermatol* **2004,** *123* (5), 902-910.
154. Caspers, P. J.; Lucassen, G. W.; Carter, E. A.; Bruining, H. A.; Puppels, G. J., In vivo confocal raman microspectroscopy of the skin: Noninvasive determination of molecular concentration profiles. *J Invest Dermatol* **2001,** *116* (3), 434-442.
155. Krüger, H. R.; Nagel, G.; Wedepohl, S.; Calderón, M., Dendritic polymer imaging systems for the evaluation of conjugate uptake and cleavage. *Nanoscale* **2015,** *7* (9), 3838-3844.
156. Boreham, A.; Brodwolf, R.; Walker, K.; Haag, R.; Alexiev, U., Time-resolved fluorescence spectroscopy and fluorescence lifetime imaging microscopy for characterization of dendritic polymer nanoparticles and applications in nanomedicine. *Molecules* **2016,** *22* (1), 17.

157. Saeidpour, S.; Lohan, S. B.; Anske, M.; Unbehauen, M.; Fleige, E.; Haag, R.; Meinke, M. C.; Bittl, R.; Teutloff, C., Localization of dexamethasone within dendritic core-multishell (cms) nanoparticles and skin penetration properties studied by multi-frequency electron paramagnetic resonance (epr) spectroscopy. *European Journal of Pharmaceutics and Biopharmaceutics* **2017,** *116*, 94-101.
158. Hoyle, C. E.; Bowman, C. N., Thiol–ene click chemistry. *Angewandte Chemie International Edition* **2010,** *49* (9), 1540-1573.

7 List of Publications and Conference Contributions

Peer Reviewed Publications

1. **Walker, K.A.;** Unbehauen, M.L.; Lohan, S.B.; Saeidpour, S; Meinke, M.C.; Zimmer, R.; Haag, R., Spin-labeling of Dexamethasone: Radical Stability vs. Temporal Resolution of EPR-Spectroscopy on Biological Samples. ZPC **2018**, DOI: https://doi.org/10.1515/zpch-2017-1076 (epub ahead of print).

2. González-Rodríguez, S; Quadir, M.A.; Gupta, S.; **Walker, K.A**.; Zhang, X.; Spahn, V.; Labuz, D.; Rodriguez-Gaztelumendi, A.; Schmelz, M.; Joseph, J.; Parr, M.K.; Machelska, H.; Haag, R.; Stein, C., Polyglycerol-opioid conjugates – a novel generation of painkillers designed to preclude side effects. *eLife* **2017**, 6: e27081.

3. Boreham, A.; Brodwolf, R.; **Walker, K.**; Haag, R.; Alexiev, U. Time-Resolved Fluorescence Spectroscopy and Fluorescence Lifetime Imaging Microscopy for Characterization of Dendritic Polymer Nanoparticles and Applications in Nanomedicine. *Molecules* **2017**, *22*, 17.

4. **Walker, K.A.**; Stumbé, J.-F.; Haag, R. Polyester-Based, Biodegradable Core-Multishell Nanocarriers for the Transport of Hydrophobic Drugs. *Polymers* **2016**, *8*, 192.

5. Fleige, E.; Achazi, K.; **Schaletzki, K.**; Triemer, T.; Haag, R., pH-Responsive Dendritic Core–Multishell Nanocarriers. *Journal of Controlled Release* **2014,** *185*, 99-108.

Conference Contribution with Talks

6. **Walker, K.**; Klinger, D. Integrated Research Training Group: Transforming Students and Post-Docs into Independent Researchers, Verteidigung der 2. Förderperiode des Sonderforschungsbereiches 1112, Berlin, **2017**.

7. **Walker, K.**; Haag, R. Nanopartikel für die Schmerztherapie, Präsentation beim 18. Hauptstadtkongress der DGAI für Anästhesiologie und Intensivtherapie, Berlin, **2016**.

8. **Walker, K.**; Unbehauen, M. CMS Nanocarriers: Loading and Characterisation, Organisation und Durchführung eines Methodenforums im Rahmen des Graduiertenkollegs *Nanocarrier*, **2016** und **2015**.

Conference Contribution with Poster Presentations

9. Unbehauen, M.*; **Walker, K.***; Fleige; E.; Hönzke, S.; Hedtrich, S.; Haag, R. Ester-Based Core-Multishell Nanocarriers for the Encapsulation of Hydrophobic Drugs, 11th Intl. Symposium Polymer Therapeutics Lab to Clinic, Valencia, Spanien, **2016**.

10. Fleige, E.; Unbehauen, M.; **Schaletzki, K.**; Radowski, M.; Küchler, S.; Haag, R. Dendritic Core Multishell Nanocarriers for the Delivery of Active Compounds, Intl. Conference and Workshop on Biological Barriers: Non-Cellular Barriers: Mucus and Surfactant, Saarbrücken, **2014**.

8 Curriculum Vitae

For reasons of data protection, my CV is not published in the electronic version of my thesis.